Institut für Geodäsie und Geoinformation der Universität Bonn

Retrieval of Sea Level and Surface Loading Variations from Geodetic Observations and Model Simulations: an Integrated Approach

Dissertation
zur Erlangung des akademischen Grades
Doktor-Ingenieur (Dr.-Ing.)
der Landwirtschaftlichen Fakultät
der Rheinischen Friedrich-Wilhelms-Universität Bonn

vorgelegt am 8. Januar 2014 von

Msc. Roelof Rietbroek

aus 's-Gravenhage, Niederlande

Retrieval of Sea Level and Surface Loading Variations from Geodetic Observations and Model Simulations: an Integrated Approach

Summary

The mass distribution in the system Earth changes dynamically over time. Time-variable mass transport mainly arises from the interplay between the terrestrial hydrological water cycle, the ocean and atmosphere, and the Earth's cryosphere. To understand the dynamics of the system Earth and its climate, it is of paramount importance to establish and maintain an accurate observational basis of these surface processes, against which models and theories can be tested.

A variety of observational techniques are used today. The time-variable gravity is measured from space by the Gravity Recovery and Climate Experiment (GRACE), Earth deformation processes are monitored by a permanent global network of GPS stations, and sea surface changes are detected by a family of satellite altimeters. The underlying motivation of this work is that the combination of the different observation types allows the mitigation of some of the technique-specific limitations.

In the framework of this dissertation, several types of geodetic observations have been combined in a least-squares sense to estimate present-day changes of surface mass storage in the Earth system, using dynamically consistent surface loading theory.

Two types of inversion schemes have been designed and implemented. In the first scheme, time variable gravity from GRACE, deformations of a permanent GPS station network, and simulated ocean bottom pressure changes from an ocean model, are used to estimate weekly surface loading changes covering the entire globe. In the second inversion scheme, (inter-)annual changes of the Earth's cryosphere, ocean and terrestrial water cycle, are parameterized by a predefined set of standing waves, whose time variations are estimated by combining GRACE gravimetry with satellite altimetry from Jason-1 and Jason-2.

Ein kombinierter Ansatz zur Bestimmung von Meeresspiegelschwankungen und Auflastsveränderungen aus geodätischen Beobachtungen und Modellsimulationen

Zusammenfassung

Die Verteilung der Massen im System Erde verändert sich dynamisch über die Zeit. Zeitvariable Massentransporte entstehen vor allem durch das Zusammenspiel von terrestrischem hydrologischem Wasserkreislauf, Cryosphäre, sowie Ozeanen und Atmosphäre. Das Verständis der Dynamik des Systems Erde sowie damit im Zusammenhang stehender Klimaveränderungen erfordert ein umfassendes Beobachtungssystem dieser Oberflächenprozesse, gegen welches Modelle und Theorien getestet werden können.

Heutzutage gibt es eine Vielzahl von Erdbeobachtungstechniken. Das zeitvariable Gravitationsfeld wird aus dem Weltall durch die GRACE-Mission (Gravity Recovery and Climate Experiment) vermessen. Deformationsprozesse der Erdoberfläche können mit Hilfe eines globalen Netzwerkes permanenter GPS-Stationen überwacht und Änderungen der Meeresoberfläche von Altimetersatelliten detektiert werden. Dieser Arbeit liegt die Motivation zugrunde, dass die Kombination verschiedener Beobachtungstypen die technisch-spezifischen Einschränkungen einzelner Beobachtungstechniken verringern kann. Im Rahmen der vorliegenden Dissertation werden verschiedene geodätische Beobachtungen in einem Kleinste-Quadrate Ansatz kombiniert, um unter Ausnutzung einer dynamisch konsistenten Auflasttheorie die heutigen Veränderungen der Oberflächenspeicher im Erdsystem zu bestimmen.

Zwei verschiedene Inversionsschemata wurden dazu entworfen und implementiert. In einem ersten Schema werden zeitvariable Schwerefelder von GRACE, Deformationen eines Netzwerkes permanenter GPS-Stationen und durch ein Ozeanmodell simulierte Ozeanbodendruckvariationen verwendet, um wöchentliche Auflastveränderungen für die gesamte Erde zu bestimmen. Im zweiten Inversionsschema werden (inter-)annuale Veränderungen von Cryosphäre, Ozean und terrestrischem Wasserkreislauf durch einen vordefinierten Satz stehender Wellen parametrisiert, deren Zeitvariationen aus einer Kombination von GRACE und Altimetriebeobachtungen der Satelliten Jason-1 und Jason-2 geschätzt werden.

Acknowlegdments

Contents

List of Figures

List of Tables

1 Introduction

1.1 Motivation and Objectives

On Earth, everything moves. Air and water are carried through the atmosphere and ocean by currents. And over land, precipitation and rivers participate in the endless hydrological watercycle. On geological timescales, even the firm foundation we stand on does not remain in place. Mantle convection causes the tectonic plates to drift, and the Earth's crust is still rebounding back into place in response to the massive ice loads from the last glacial maximum.

A major force in all these phenomena is the gravity field as generated by the Earth. Clearly, since the gravitational field of the Earth will change once masses move from A to B, it makes sense to closely monitor gravity. Measuring gravity is one of the key aspects of geodesy. In addition, the shape of the Earth and its orientation in space are also important observables used in the field of geodesy.

Now measuring is one thing, but modelling (and ultimately predicting) is another. Many aspects of the system Earth can be modelled and its physics understood. Capable general circulation models of the ocean and atmosphere exist, and hydrological models are able to model important aspects of the watercycle. However, remaining shortcomings are present in the models. For example, when adding the land, ocean and atmospheric masses from the models, one will find that they will not conserve mass on a global scale.

Combining the best of the measuring and observing world is that what provides valuable insights. Afterall, without models, a geodesist will have a lot of trouble explaining what part of the measurement is noise and what part is signal. And without measurements, a modeller has no way of saying whether his model has any relation to what is happening on the actual Earth.

From an observational perspective, it makes sense to use measurements from multiple techniques to estimate geophysical parameters in inverse problems. Shortcomings in one technique are often compensated by the strength of another. Furthermore, the estimated parameters from joint inversions are generally associated with an increased accuracy. The above idea is fundamental to my work and may be put into the form of a working hypothesis:

The combination of existing geodetic observations in joint inversions can significantly improve the current accuracy and separability of surface loading phenomena, compared to single-technique inversions.

My original contribution to this exciting and dynamic research field consequently consists of the design and implementation of a multi-sensor inverse methodology, solving for surface mass loads and sea level, using data from satellite gravimetry, altimetry, GPS-derived network deformations and simulated ocean bottom pressure. More specifically, I consistently combine different and complementary types of data by invoking a range of dynamical theories such as mass conservation, response of the passive ocean, surface loading on a SNREI Earth, and reference frame theory. I demonstrate that, without the need for assimilating the data in a (yet to be build) 'complete' Earth system model, the joint inversion results have more added value, compared to the situation where all the data types are considered as isolated entities.

Like many geophysical inverse problems, the inverse problems in this thesis are either severely or, in the best case, weakly ill-posed. Each observational type is sensitive to particular combinations of the parameters. To enable the computation of meaningful solutions, I designed new methods which mitigate the ill-posedness at hand.

The results of the joint inversions shed more light on a wide spectrum of contemporary changes in the system Earth, ranging from the terrestrial hydrological water cycle, continental ice mass changes to global and regional sea level induced by mass transport and thermo- and halo-steric expansion/contraction.

Two types of joint inversions are considered in this thesis. The first inversion type, schematically depicted in Fig. 1.1, combines time-variable gravity from the Gravity Recovery and Climate Experiment (GRACE), GPS derived network deformations and ocean bottom pressure from a global ocean model. The most important sought-for parameters in this inversion are weekly changes of surface loading, expressed as spherical harmonic coefficients. The green textboxes of Fig. 1.1 describe the external data, which are entering the processing chains of this thesis. The original contribution of this work is enclosed in the blue boxes. They contain the tasks for which methods have been developed and implemented.

The schematics of the second type of inversion, where GRACE data and measurements from radar altimetry are combined, can be found in Fig. 1.2. Compared to the first inversion type, where a generic surface load is parametrized in spherical harmonic coefficients, the solution space is much more restricted. Only a limited amount of geophysical effects (e.g. a mass change in a certain drainage basin in Greenland or Antarctica) are parametrized by time series (the sought-for parameters), multiplied by time-invariant spatial patterns, which are determined beforehand from auxiliary data.

In previous years, I published early versions of methods and results of this thesis work in journal papers. The results of a joint inversion, using GRACE, GPS derived network deformations from the IGS (International GNSS Service), and simulated ocean bottom pressure was published in Rietbroek et al. (2009). In Rietbroek et al. (2012b), reprocessed GPS data were introduced in the form of normal equation systems, and an improved ocean model with updated errors was used. Just recently, a paper has been accepted (Rietbroek et al., 2014), which concerns the use of GPS network deformations to bridge the gap which is expected at the approaching end of life of the (aging) GRACE mission.
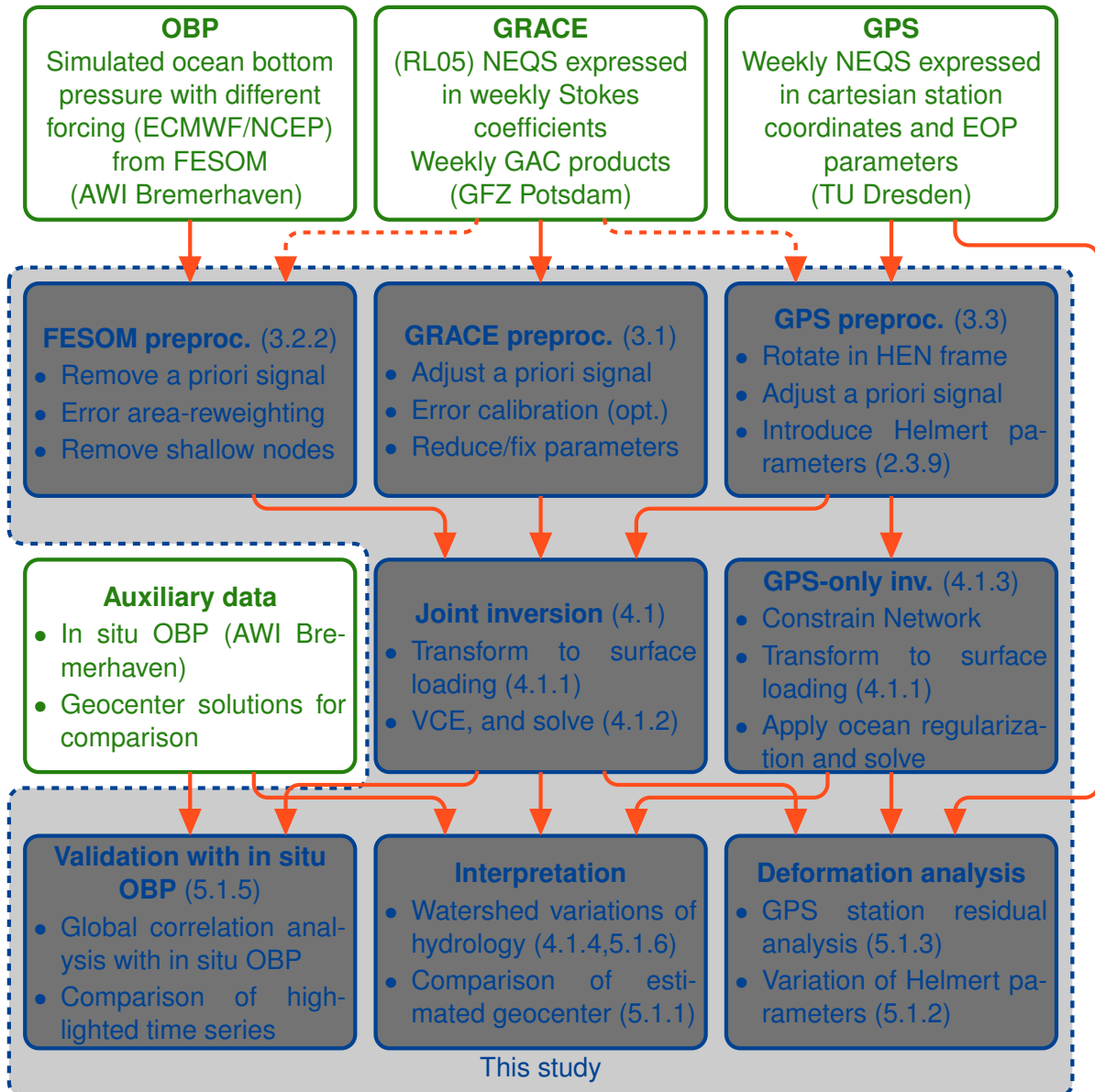
Figure 1.1: Inversion scheme of the weekly global surface loading inversion. The numbers in the brackets denote the relevant section numbers in this thesis. The gray shaded areas delimit the work performed in this thesis. Abbreviations: NEQs (normal equation systems), HEN (Height, East, North), OBP (ocean bottom pressure), FESOM (Finite Element Sea-Ice Model), VCE (Variance Component Estimation), EOP (Earth Orientation Parameters).
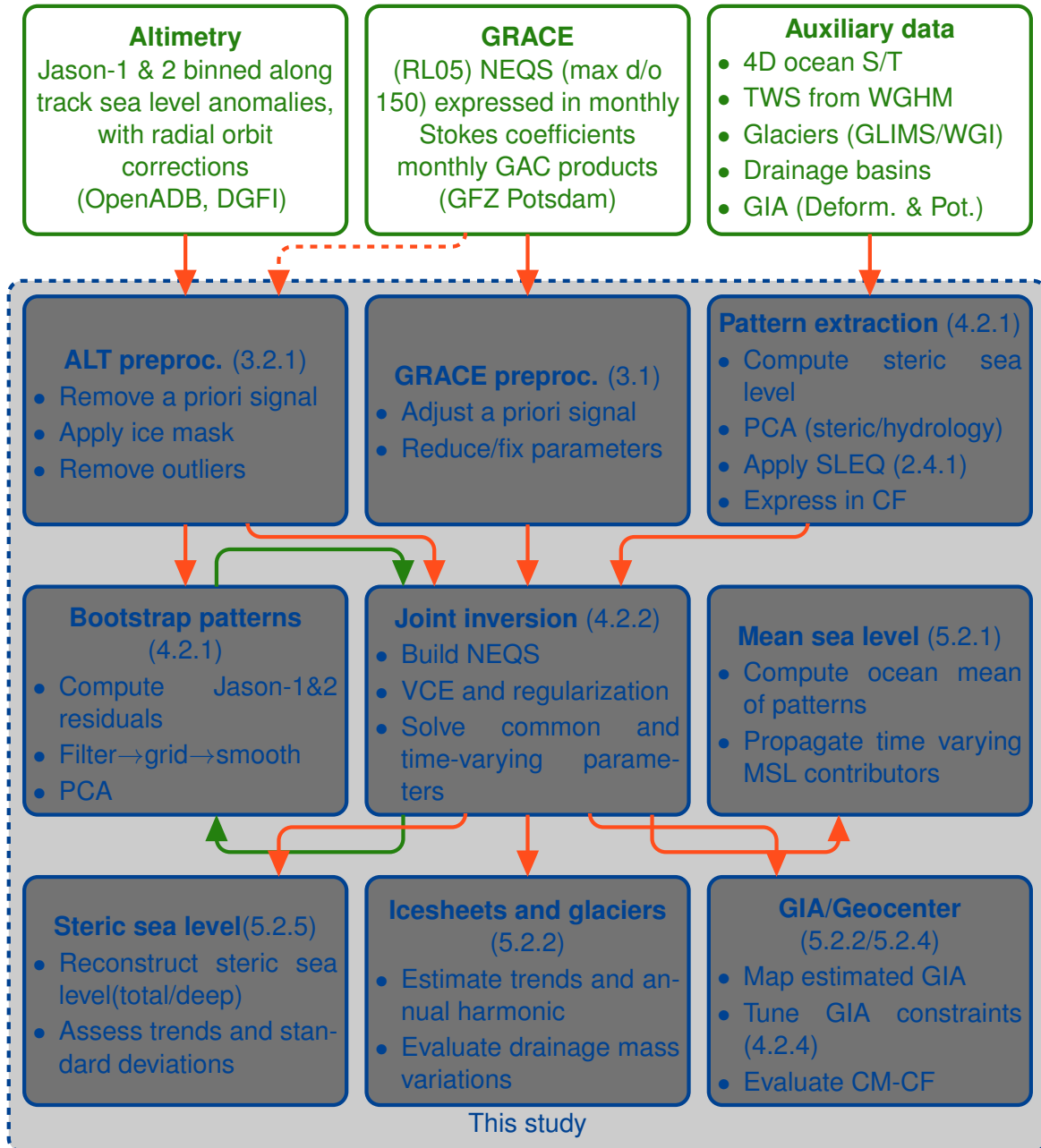
Figure 1.2: As in Fig. 1.1, but now for the 'fingerprint' inversion. Abbreviations: TWS (total water storage), PCA (principal component analysis).

The methodology concerning the alternative joint inversion, using predefined patterns, whose time varying scales are fitted against GRACE and altimetry has been published in Rietbroek et al. (2012a). The corresponding data and software provided the basis for the study of Jensen et al. (2013). Along track Jason-1 and Jason-2 residuals, after removing the signal from a joint GRACE+Jason inversion, have been studied in Rietbroek et al. (2012c).

Besides the already published results, this thesis covers several newly developed methods and algorithms, utilizes updated datasets, offers new interpretations, and provides a more comprehensive review of the techniques used.

For example, the newest GRACE-GFZ data (release 05) are now used in the inversion schemes. Furthermore, to improve the relative weighting of the different observational groups, Variance Component Estimation (VCE) has now been used. Using this technique, observational groups are also weighted based on their posterior fit, in addition to their relative error-covariance. Newly reprocessed GPS network solutions have been fed into the inversions. And ocean model data has now been incorporated which have been computed on a denser and tuned finite element grid. Concerning GPS-only inversions, a new regularization method is described in this thesis, which serves to constrain the solution over the ocean towards an equipotential surface, instead of a zero-valued surface as in Kusche and Schrama (2005).

Also new is, that the patterns, used in the GRACE-altimetry inversion, have been updated. Besides a different realization of the Antarctic drainage divides, five GIA (glacial isostatic adjustment) patterns are now used instead of one. Furthermore, a new method for computing additional steric patterns from the altimetry residuals has been developed. On the altimeter side, parameters were introduced to absorb network errors in the altimeter frames, and an ocean/atmosphere background model has been subtracted a priori. An inter-drainage basin constraint has been designed, which suppresses spurious correlations between small basins, while the common mass changes of the basins are still freely estimable.

The remainder of the introduction highlights the themes which inspired this thesis work. It covers the most relevant previous research, and several methodological milestones which are important. Chapter 2 provides the geophysical framework, linking all relevant observables using surface loading and frame theory. Chapter 3 discusses the characteristics of the relevant observations, and explains the preprocessing steps applied. The two inversion schemes are then elaborated upon in Chapter 4. It covers the used observation equations, nuisance parameters, and discusses the obtainable accuracies and stability of the inversion schemes. Some results from the joint inversions are then discussed and compared in Chapter 5. The chapter serves to illustrate the quality and usefulness of the inversion schemes, but is by no means comprehensive, as the estimated data can be used in a variety of other applications. Finally, main conclusions are drawn on the usefulness of the joint inversion scheme, and recommendations for future schemes are provided.

1.2 Time Variable Gravity from GRACE

Time variable gravity plays a crucial role in this thesis. With the exception of the volumetric sea level changes, all observables discussed in this thesis can be linked to the changes in the gravity field. For that reason, the space-borne Gravity Recovery and Climate Experiment (GRACE), supplies the most important observational constraints in this thesis.

Launched in 2002, the GRACE mission stood at the base of a steady sequence of discoveries. Hydrological variations have already been monitored at an early stage (Tapley et al., 2004), and the 2004 Sumatra-Andaman Earthquake was also seen by the twin mission (Han et al., 2006). Large scale mass variations in the ocean were discovered (Chambers et al., 2004), and validated against in situ bottom pressure recorders (Rietbroek et al., 2006). Furthermore, significant ice mass losses in Greenland and Antarctica were detected (Velicogna and Wahr, 2006a,b). Concerning groundwater changes, Rodell et al. (2009) found that large scale anthropogenic water use in India had been observed by GRACE.

In order to extract useful results from the level 2 GRACE products, a filtering step is commonly applied. Due to the measurement geometry of GRACE, strong correlated errors exist in these products. These errors have been decreasing with the releases, but cannot be completely eliminated. A whole family of filters has been developed over the years, which are either isotropic (e.g. Wahr et al., 1998) or anisotropic and designed specifically for GRACE (e.g. Swenson and Wahr, 2006; Kusche, 2007; Kusche et al., 2009; Wouters and Schrama, 2007).

1.3 Using the Earth's Crust as a Scale

On short timescales, the solid part of the Earth responds elastically to changing surface loads. These deformation responses can be approximated using a spherically symmetric non-rotating elastic isotropic Earth model (Farrell, 1972). As will be shown later in Sec. 2.2.2, 1-dimensional Earth models yield elegant relations between the surface load and the deformation response, which makes geodetic observations of the Earth's crustal movement suitable candidates for the retrieval of time varying surface loading signals.

Using deformations from permanent GPS stations, seasonal loading signals in the Amazon have been detected (Davis et al., 2004). van Dam et al. (2007) concluded that errors in GPS processing were still masking the seasonal hydrological cycle in Europe. Using improved GPS processing, Tregoning et al. (2009) found a better agreement between GRACE derived surface deformation and GPS network changes. Furthermore, Jiang et al. (2010) found that the deformation patterns, associated with the accelerating mass loss in Greenland were confirmed by GPS stations in the North Atlantic.

When formulated as an inverse problem, large scale surface loading have been inferred from GPS data by Wu et al. (2002), Blewitt and Clarke (2003), and Kusche and Schrama (2005). The retrieval of global surface loading from GPS data only is difficult as the distribution of the permanent GPS stations exhibit large uncovered regions in for example the ocean domain. Furthermore, isolated GPS stations with erroneous values may potentially

contaminate the solution in large regions (van Loon, 2008).

Kusche and Schrama (2005) also provided a framework for the joint inversion of surface loading from GRACE data and GPS network deformations. Wu et al. (2006) combined GRACE data with GPS network deformations and also added modelled ocean bottom pressure from the ECCO model to solve for surface loading in a joint inversion. Jansen et al. (2009) provided a sensitivity study for such inversions, investigating the influence of the GPS station distribution, and the used ocean model grid. Joint inversions with real data have been described in Rietbroek et al. (2009, 2012b).

Focusing on secular behavior, Wu et al. (2010), separated GIA induced variations from present day surface loading trends using GPS, GRACE and modelled OBP. Their inverse problem is in particular challenging and requires a variety of constraints which have been imposed to stabilize the solution. Nevertheless, such multi-sensor inversions are expected to play an increasingly important role in the near future.

1.4 Geocenter Motion

The surface loading inversions from this study inherently lead to a discussion of observational reference frames. For that reason, the dynamical theory associated with geocenter motion is extensively elaborated upon in this thesis (see Sec. 2.3).

Applying surface loading theory in combination with the conservation of linear momentum, Trupin et al. (1992) studied the effect of glacier melting on the displacement of the center of mass of the Earth system from the center of mass of the solid Earth. Geocenter motion associated with the atmosphere, ocean and hydrology were quantified by Dong et al. (1997), from geophysical models.

These, mostly seasonal, variations have been detected using GPS network solutions (Blewitt et al., 2001). Other satellite tracking techniques such as Satellite Laser Ranging (SLR) and DORIS have also shown to yield geophysically induced geocenter motion (Eanes et al., 1997; Chen et al., 1999; Bouillé et al., 2000; Crétaux et al., 2002; Feissel-Vernier et al., 2006; Cheng et al., 2010).

The inter-satellite ranging measurements of GRACE are principally insensitive to geocenter motion, as they represent a relative measure between two satellites in the same reference frame. The reference frame origin of the GRACE gravity fields is set to the center of mass of the Earth system. In this frame of reference, only the combined effect of the mass center of the solid part of the Earth, and the mass of the the fluid envelope of the Earth can be detected. Consequently, in this frame of reference, the inversion of surface loading variations from the gravity field is essentially a singular problem (see Sec. 5.1.1), which is still a cause of confusion among many. A possible way out of this caveat is to use auxiliary information from an ocean model, together with GIA-corrected GRACE, to estimate the present day geocenter motion (Swenson et al., 2008).

Many geocenter motion estimates are derived from a geometrical approach. This means that the tracking network is assumed to be rigid, possibly drifting, and the computed geocenter motion is representative for the motion of the center of mass of the Earth relative to the geometrical center of network[1]. Over time however, the network also deforms due to surface loading effects, which can alias into the estimates (Lavallée et al., 2006; Collilieux et al., 2009). Furthermore, technique specific errors (e.g. from pressure radiation modelling) may leak into the computed geocenter motion (Fritsche et al., 2009).

Besides the center of mass of the Earth system, there are other frame origins which are independent of the used network and can be mathematically described as functions of the surface deformations or gravity. Well known, are for example the mass center of the solid Earth (excluding the surface load), and the center of (surface) figure. Blewitt (2003) described methods to transform geodetic observables between these frames.

The frame theory opens up possibilities to solve for surface loading where the rigid network assumption can be abandoned (the deformation approach). For the GPS network, the difference between approaches have been studied by Collilieux et al. (2011b).

For visco-elastic loading problems, which are important for the study of glacial isostatic adjustment, the frame theory can be extended (see also Sec. 2.3.7 and Wu et al., 2012 for a review). Klemann and Martinec (2009) showed for example that the chosen lower mantle viscosity heavily influences the magnitude of the secular geocenter motion, while its orientation is less affected. The trends in the Z direction are important for the mass trends on the Antarctic continent. Wu et al. (2010) estimated this component to be -0.16 mm/yr, which causes an apparent mass trend in Antarctica of 13 Gt/yr, when ignored. Other estimates (e.g. this work, Rietbroek et al., 2012a; Schrama et al., 2014) also indicate significantly larger present day mass components.

1.5 Sea Level Change

Eustatic Sea Level Change
Averaged over the ocean, the current eustatic sea level rise over the last two decades is estimated to be around 3.3 mm/yr (Cazenave and Llovel, 2010). This estimate comprises volume (or steric) changes due to variations in salinity and temperature, but equally important are mass induced changes from melting glaciers, ice sheets and terrestrial water storage (Miller and Douglas, 2004). Furthermore, there are significant contributions in the observed sea level which can be attributed to inter-annual variability (Church and White, 2011). A prime example is the El Niño La Niña cycle, which has profound effect on sea level on inter-annual time scales (Böning et al., 2012). Consequently, different time intervals yield different eustatic sea level rates.

Historically, tide gauges have been used to measure tides in harbors. When long enough time series are available, one can use it to compute local tide tables. After removing the harmonic tides a useful residual is left which also shows long term variations in sea level.

---

[1] or vice versa depending on the used definition of the geocenter motion

Although accurate historical tide gauges are sparsely located over the globe, one can still use these to compute the sea level change over the last century (Church and White, 2006). They found not only that over the last 134 years (1870-2004) sea level rose by $1.7\pm0.3\,\mathrm{mm/yr}$, but that it also displayed an acceleration of about $0.013\pm0.006\,\mathrm{mm/yr^2}$. It must be noted however that these historical sea level reconstructions were only possible since the advent of satellite radar altimetry in the 1990's, which provided important constraints in the spatial domain. These spatial constraints are necessary to correct the tide gauge data for non-eustatic sea level change. Consequently, the lack of sufficient spatial information before the satellite altimetry era, and the heterogeneous spatial coverage of the tide gauges, cause larger errors in the earlier epochs.

Steric variations can be inferred from measured temperature and salinity profiles in the ocean (see section 2.5). Traditionally, those measurements mostly came from shipborne XBT (eXpendable BathyThermograph) and CTD (Conductivity Temperature Depth). Recently, a steadily growing array of freely drifting automated floats (ARGO), additionally samples the ocean. The retrieval of long term trends from these data is not a trivial task, and the sampling is mainly restricted to the upper 1000 m of the ocean.

With the advent of satellite gravimetry and altimetry, a new way to compute steric sea level variations has been possible. Steric variations can be computed by subtracting the mass induced sea level from GRACE from the total sea level from altimetry. Early estimates, in terms of global mean sea level, were studied in Lombard et al. (2007). They compared their steric sea level estimates with those derived from ARGO data and found that the ARGO estimates showed unrealistic cooling from 2003 and onward. Similar cooling events in the ARGO data have been found by (Lyman et al., 2006). The issue has been addressed in the meanwhile, and the exaggerated cooling was found to be caused by biases in the ARGO and XBT data (Willis et al., 2008; Lyman et al., 2010).

The ocean plays a dominant role in the Earth's climate system. From the observed radiation imbalance at the Earth's surface more than 90% of the excess heat is absorbed by the ocean (see Bindoff et al., 2007 and the upcoming fifth assessment report of the Intergovernmental panel on climate change). Although the ocean heat content increase is consistent with the observed radiation imbalance of the Earth, large uncertainties still remain in its estimates (Loeb et al., 2012). To complicate matters further, the deeper part of the ocean is very poorly sampled. Based on a non-Boussinesq model Song and Colberg (2011) suggested that deep ocean warming may contribute up to $1\,\mathrm{mm/yr}$. In fact, as will be shown later by the inversion results in Sec. 5.2.1, such trends are in fact not inconsistent with the results from this work.

In addition to steric variations, mass fluxes in and out of the ocean contribute to sea level changes. The ice sheets on Greenland and Antarctica are melting at alarming rates. Melting estimates, obtained from satellite gravimetry, of the melting in Greenland are in the order of $200\,\mathrm{Gt/yr}$ ($0.5\,\mathrm{mm/yr}$ of eustatic sea level rise, Schrama and Wouters, 2011; Wouters et al., 2008), although this rate is increasing steadily (Velicogna and Wahr, 2006a). In Antarctica, significant melting is ongoing and shows strong inter-annual variations (Velicogna, 2009; Horwath et al., 2012). Most of the melting is occurring in the West Antarctic and on the Antarctic Peninsula. For example, Sasgen et al. (2010) found melting rates varying from

91 $^{Gt}/_{yr}$ to 117 $^{Gt}/_{yr}$ depending on the measurement techniques (GRACE Gravimetry versus InSAR) and time span (0.25-0.31 $^{mm}/_{yr}$ of sea level rise).

Although their total ice volume is smaller than that of the ice sheets, land glaciers also contribute significantly to sea level rise (Meier et al., 2007; Cogley, 2009). Using direct and geodetic measurements Cogley (2009) suggested that land glaciers contribute to sea level rise with 1.1 - 1.4 $^{mm}/_{yr}$. The available measurements are however very sparse in both time and space. Using the GRACE mission a significant smaller contribution of 0.4 $^{mm}/_{yr}$ was estimated by Jacob et al. (2012) for the period 2003-2010.

Continental water storage change also affect sea level. Llovel et al. (2010) estimated a negative contribution to sea level of -0.22±0.05 $^{mm}/_{yr}$. Riva et al. (2010) also found a negative (but not significant) trend of -0.1±0.3 $^{mm}/_{yr}$. A negative trend of -0.20±0.04 $^{mm}/_{yr}$ was also confirmed by Jensen et al. (2013).

When discussing sea level change, one has to appreciate the difference between *geocentric* and *relative* sea level. Relative sea level, is the column of water relative to the Earth's crust, while geocentric sea level is essentially the geoid change augmented with a uniform layer ensuring the conservation of mass globally. While all elastic loading effects cause changes between the relative and geocentric sea level, the largest difference between the relative and the geocentric sea level is caused by glacial isostatic adjustment (GIA). Roughly speaking, this effect causes mantle material to gradually flow back to the regions of the former ice sheets (e.g. Laurentide and Fennoscandia). In the ocean domain, this is consequently accompanied by an overall lowering of the ocean floor. For that reason, a GIA correction of 0.3 $^{mm}/_{yr}$ from Douglas and Peltier (2002) is usually added to the mean sea level changes from altimetry.

Several authors have attempted to close the total sea level budget using satellite altimetry (measuring total sea level), data from ARGO floats (measuring steric sea level) and GRACE gravimetry (measuring mass related sea level). Willis et al. (2008) found strongly diverging curves of the measured and inferred sea level components (steric, mass and total sea level). However, using virtually the same data, Leuliette and Miller (2009) found a much better agreement. The largest disagreement was actually found in the ARGO derived steric sea level, which pointed to differences in the ARGO interpolation schemes used.

Regional Sea Level Change

A closer look at these satellite data reveals that sea level changes are all but uniform over the ocean (see Fig. 1.3). This has several causes. On the one hand, temperature and salinity changes differ greatly depending on the region and climate regimes. Consequently, the associated volumetric (steric) sea level changes display considerable regional variations. On the other hand, the meltwater from ice sheets and glaciers originate from locally concentrated sources. Although counter-intuitive at first glance, the sea level actually tends to drop for locations in the direct vicinity of these melting sources. This effect is caused by the lowering of the regional geoid due to the removal of the local ice masses and is even further enhanced by the elastic rebound of the Earth's crust, which is being relaxed as the ice melts. As mass is conserved on a global scale, this will lead to larger than average sea level rise

Jason−1 Sea level trend
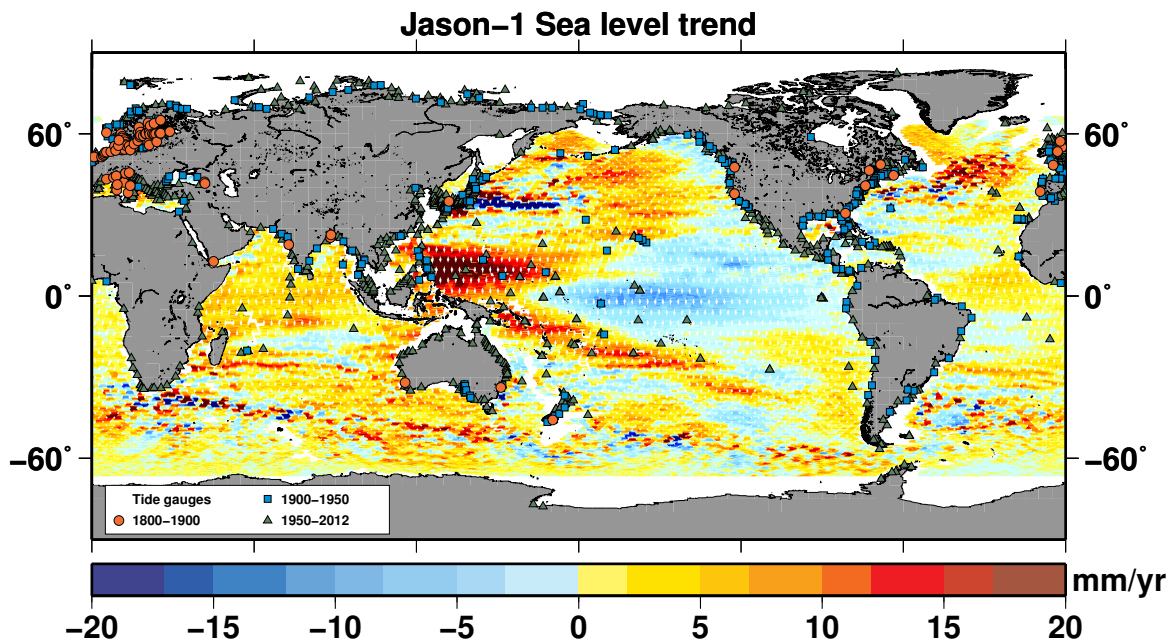
Figure 1.3: Along track sea level trends (period from 2003-2009), as seen by the Jason-1 altimeter. Tide gauge locations from the PSMSL database are superimposed on the map, and grouped per observation epoch.

far away from the melt sources. The physics behind these problems is well understood, and the ocean response due to a spatially predefined load can be computed accordingly (Mitrovica et al., 2001; Riva et al., 2010; Rietbroek et al., 2012a). With regard to future sea level rise projections, this effect has only recently been considered, and was found to cause significant regional variations (Slangen et al., 2012). The theory of the self-consistent sea level response is treated in section 2.4.

The non-uniform responses of the ocean, actually open up opportunities to separate different sea level contributions based on their spatial characteristic or 'fingerprint'. Plag and Jüttner (2001) tried to separate contributions from Greenland and Antarctica by fitting self consistent sea level responses to tide gauge measurements. They found that the inverse problem using tide gauges was highly ill-posed, and no realistic estimates could be obtained. This 'fingerprint' inversion approach is however a very attractive one, as it allows the decomposition of the various contributors to sea level. With a similar approach, data from GRACE has already been successfully decomposed in different mass contributions (Schmeer et al., 2012). For these reasons, such a fingerprint inversion, based on much more extensive GRACE data and altimetry, is pursued in this thesis.

2 Gravity, Surface Loading and Sea Level

The changing gravitational field and surface loading phenomena such as sea level rise are strongly interconnected. The observed gravity at a certain point is caused by the gravitational pull of all mass-compartments together. Consequently, moving mass, let it be ice, water, air, tectonic plates or mantle material, will all cause tiny changes in the gravitational field.

Many of the mass movements will also indirectly cause changes in the geometrical shape of the Earth and the sea surface. On long time scales, tectonic plate movement and mantle upwelling have shaped the topography. On shorter time scales, ranging from decades to weeks, ice and water masses deform the solid part of the Earth. Today, the land surface is still rebounding from the loading of the ice sheets from the last glacial periods. Furthermore, the global terrestrial water cycle causes strong annual and sub-annual mass movements, which are consequently deforming the Earth, through the loads exerted on the surface. On the shortest timescales, mainly ranging from weeks to hours one finds the effect of the moon and other astronomical bodies in the form of solid Earth and ocean tides.

A changing geometrical shape of the Earth or the sea surface can also have causes, which are *not* caused by mass movement. For example, the thermal expansion of sea water due to seasonal and long term warming is associated with the so called steric sea level. Furthermore, the compaction of snow on top of ice sheets can change the thickness of the ice sheet without changing its mass.

This chapter describes the mathematical/physical relationship between several observables, which are used in this work.

2.1 The Earth's Gravity Field

The distribution of masses in the (non-rotating) Earth system will cause a gravitational potential field ϕ

$$\phi(\mathbf{r}) = G \oint_{V_{earth}} \frac{\rho(v')}{|\mathbf{r} - \mathbf{r}'|} dv'. \tag{2.1}$$

In words, each volume element, dv', with local density ρ contributes to the potential at position $\mathbf{r}$.

Exterior of the Earth's mass, the gravitational potential satisfies the Laplace equation:

$$\nabla^2 \phi = 0. \tag{2.2}$$

The analytical solution of the Laplace equation can be conveniently expressed in terms of spherical harmonic base functions:

$$\phi(\lambda, \theta, r) = \frac{GM}{a} \sum_{n=0}^{\infty} \sum_{m=-n}^{n} \left(\frac{a}{r}\right)^{n+1} C_{nm} \bar{Y}_{nm}(\lambda, \theta). \tag{2.3}$$

Here, a denotes the mean radius of the Earth, whereas G is the gravitational constant which is multiplied by the mass of the Earth (M). The dimensionless and normalized Stokes coefficients, C_{nm}, describe the gravitational field of the Earth in terms of the spectral degree and order n and m. The normalized base functions, $\bar{Y}_{nm}$, are evaluated at co-latitude θ, longitude λ and radius r and depend on the associated Legendre function P_{nm}[1]

$$\bar{Y}_{nm}(\lambda, \theta) = \begin{cases} N_{nm} P_{nm}(\cos\theta) \cos m\lambda, & m \geq 0 \\ N_{n|m|} P_{n|m|}(\cos\theta) \sin|m|\lambda, & m < 0 \end{cases}. \tag{2.4}$$

Where a normalization factor N_{nm} is applied:

$$N_{nm} = \sqrt{(2 - \delta_{0m})(2n + 1)\frac{(n-m)!}{(n+m)!}}. \tag{2.5}$$

The applied normalization is that which is commonly used in geodesy, based on the following orthogonality relation:

$$\oint_{\Omega} \bar{Y}_{nm}(\omega)\bar{Y}_{n'm'}(\omega)d\omega = 4\pi\delta_{nn'}\delta_{mm'}. \tag{2.6}$$

The integral is evaluated over the unit sphere, which is denoted by Ω.

The largest component of ϕ is the central degree 0 term, followed by the ellipsoidal flattening manifesting itself in the C_{20} coefficient. In addition, on the Earth, rotating with angular speed Ω_E, a centrifugal potential will arise. When the Z-axis of the chosen reference frame if perfectly aligned with the rotation axis one can describe the centrifugal potential as

$$\Lambda(r, \theta) = \frac{1}{2}\Omega_E^2 (r\sin\theta)^2. \tag{2.7}$$

In the absence of currents and other dynamics, the ocean's shape will have adjusted itself to an equipotential surface. This is commonly referred to as the geoid, N, and its height above an ellipsoid can be approximated by Bruns's formula (e.g. Heiskanen and Moritz, 1967)

$$N = \frac{\phi + \Lambda - \tilde{U}}{\gamma}. \tag{2.8}$$

The potential $\tilde{U}$ is the normal potential of the ellipsoid (e.g. GRS80), including the centrifugal potential, Λ. The associated normal gravity acceleration is denoted by γ

In this thesis, the primary focus lies on time-variable deviations from the steady state situation, so the normal potential $\tilde{U}$ is commonly replaced by a multi year mean gravity field, yielding associated geoid perturbations δN.

---

[1]no Condon-Shortly Phase applied

2.2 Surface Loading

2.2.1 Thin Shell Approximation of a Surface Load

Even when the gravitational potential outside a body is perfectly known, it is still impossible to uniquely determine the mass distribution inside the body (there exist infinitely many mass distributions all yielding the same external gravity field). In the case of the Earth, one may however make assumptions which allow linking potential changes to mass changes.

Most of the changes in the time-variable gravity originate from movements of water and air, which occur close to or on the surface of the Earth. In other words, one may approximate the region where the mass changes are occurring as a thin shell having the Earth's radius. For a spherical thin shell, Eq. 2.1 may be adapted to compute the potential changes as

$$\delta\phi(\mathbf{r}) = G \oint_{|r'|=a} \frac{\sigma(\omega')}{|\mathbf{r} - \mathbf{r}'|} a^2 d\omega'. \tag{2.9}$$
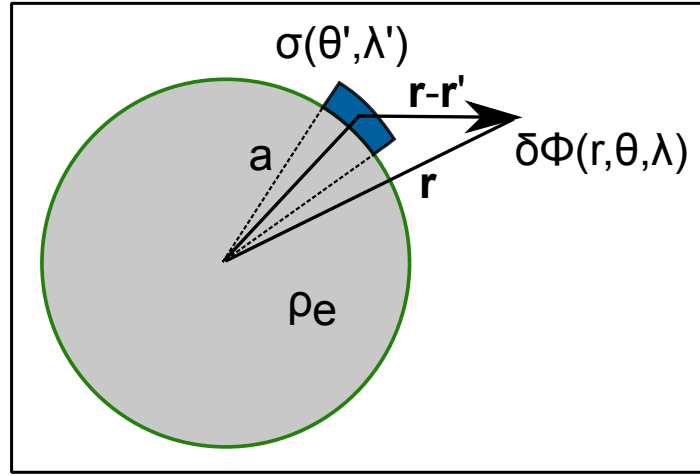
Figure 2.1: Graphical representation of the potential changes as induced by a spherical shell. The thickness of the shell is vanishingly small, compared to the Earth's radius.

Here, the surface density σ is given in kg/m^2. The reciprocal of $|\mathbf{r} - \mathbf{r}'|$ may be written as an infinite series of (unnormalized) Legendre polynomials, P_n, as a function of the relative angle α between $\mathbf{r}$ and $\mathbf{r}'$:

$$\frac{1}{|\mathbf{r} - \mathbf{r}'|} = \sum_{n=0}^{\infty} \frac{|\mathbf{r}'|^n}{|\mathbf{r}|^{n+1}} P_n(\cos\alpha), \quad \text{for} |\mathbf{r}| \geq |\mathbf{r}'|. \tag{2.10}$$

The addition theorem may be used such that the dependency on co-latitude (θ) and longitude (λ) is introduced according to

$$P_n(\cos\alpha) = \frac{1}{2n+1} \sum_{m=-n}^{n} \bar{Y}_{nm}(\lambda, \theta) \bar{Y}_{nm}(\lambda', \theta'). \tag{2.11}$$

It is convenient to expand the surface density variations, σ, in surface spherical harmonics:

$$\sigma(\lambda, \theta) = a\rho_w \sum_{n=0}^{\infty} \sum_{m=-n}^{n} T_{nm} \bar{Y}_{nm}(\lambda, \theta). \tag{2.12}$$

The spherical harmonic coefficients of the surface density, T_{nm}, are dimensionless. The average density of seawater, usually taken as $1025 \, \text{kg/m}^3$, is denoted by ρ_w.

Eqs. 2.10-2.12 can now be substituted in Eq. 2.9. In this case, most of the integrals will be zero-valued as a consequence of the orthogonality relation 2.6. The vector magnitudes $|\mathbf{r'}|$ and $|\mathbf{r}|$ may be simplified to the scalars a and r respectively. The result is a double sum

$$\delta\phi(\mathbf{r}) = 4\pi G \rho_w a^3 \sum_{n=0}^{\infty} \sum_{m=-n}^{n} \frac{1}{2n+1} \frac{a^n}{r^{n+1}} T_{nm} \bar{Y}_{nm}(\lambda, \theta). \tag{2.13}$$

A further simplification can be made by introducing the mean density of the Earth $\rho_e = 3M/(4\pi a^3)$ (adopted value $\rho_e = 5517 \, \text{kg/m}^3$)

$$\delta\phi(\mathbf{r}) = \frac{GM}{a} \sum_{n=0}^{\infty} \sum_{m=-n}^{n} \frac{1}{2n+1} \frac{3\rho_w}{\rho_e} \left(\frac{a}{r}\right)^{n+1} T_{nm} \bar{Y}_{nm}(\lambda, \theta). \tag{2.14}$$

Analogous to Eq. 2.3, Eq. 2.14 can be written in terms of anomalous Stokes coefficients, δC_{nm}^r

$$\delta\phi(\mathbf{r}) = \frac{GM}{a} \sum_{n=0}^{\infty} \sum_{m=-n}^{n} \left(\frac{a}{r}\right)^{n+1} \delta C_{nm}^r \bar{Y}_{nm}(\lambda, \theta), \tag{2.15}$$

where

$$\delta C_{nm}^r = \frac{1}{2n+1} \frac{3\rho_w}{\rho_e} T_{nm}. \tag{2.16}$$

The superscript ^{r}, denotes the potential change for the case when the solid part of the Earth is rigid. In practice, the Earth deforms (elastically) when a surface load is applied to it. The associated potential changes and Earth deformations are described in the next section.

2.2.2 Deformation of the Elastic Earth

Since the Earth is not a rigid sphere, its shape will change in time under past and present loads. At location $\mathbf{r}$, a general deformation can be described with a vector field

$$\mathbf{D}(\mathbf{r}) = \nabla\phi(\mathbf{r}) + \nabla \times \Gamma(\mathbf{r})\mathbf{r} + \nabla \times (\nabla \times \Xi(\mathbf{r})\mathbf{r}) . \tag{2.17}$$

Here, Helmholtz's theorem has been used to decompose the vector field into a curl-free (Spheroidal) component, $\nabla\phi$, and in two divergence-less (incompressible) components. The latter terms are referred to as 'toroidal' and 'poloidal' and are associated with the scalar fields Γ, and Ξ respectively.

Under good approximation, one may assume that the Earth is a SNREI (Spherically-symmetric Non-rotating Elastic Isotropic) body (Pagiatakis, 1990). For tidally induced ocean loading, the neglection of anisotropy typically accounts for a few percent (Pagiatakis, 1990). Love (1909) suggested a solution for the deformation of a radially symmetric Earth, induced by a unit point load. He postulated that the deformation response must also be axially symmetric, which is now commonly known as the Love-Shida hypothesis. Assuming the radial symmetry of the Earth, and the boundary conditions at the (stress-free) surface, the deformation then only contains a radial (U) and a tangential (V) component and the

spheroidal and poloidal modes of $\mathbf{D}$ are coupled. As a result, the Earth's response to an axis-symmetrical surface load (Farrell, 1972) can be described as

$$\hat{\mathbf{D}}(r, \alpha) = \sum_{n=0}^{\infty} \left[U_n(r) P_n(\cos \alpha) \mathbf{e}_r + V_n(r) \frac{d P_n(\cos \alpha)}{d\alpha} \mathbf{e}_\alpha \right], \tag{2.18}$$

where the '$\hat{}$' indicates that the deformation obeys the Love-shida hypothesis. The deformed Earth additionally generates a distorted geoid

$$N(\alpha) = \sum_{n=0}^{\infty} \frac{\phi_n(a)}{g} P_n(\cos \alpha), \tag{2.19}$$

where the mean gravity is denoted by g.

In the remainder of the chapter, the deformation at the Earth's surface is discussed. For ease of reading, the radial dependency $(r = a)$ is subsequently omitted from the notation. At the surface of the Earth[2], the scalars U_n, V_n and ϕ_n are computed using a Love number formalism (Farrell, 1972)

$$\begin{bmatrix} U_n \\ V_n \\ \phi_n \end{bmatrix} = \phi_n' \begin{bmatrix} \frac{h_n'}{g} \\ \frac{l_n'}{g} \\ 1 + k_n' \end{bmatrix}. \tag{2.20}$$

Here, the direct potential change of the load is indicated by ϕ_n'. The mechanical properties of the Earth are reflected in the, degree dependent, dimensionless load 'Love numbers', h_n', l_n', k_n'. Practical values of the load Love numbers are depicted in Fig. 2.2. Generally, the variations at large degrees are mostly determined by the shallow properties of the Earth. What is notable, is that Fig. 2.2 indicates that an incompressible Earth model yields significantly different Love numbers also at low degrees. The difference can be understood in that incompressible models are more resistant to a load than compressible Earth models (or to put differently: more mass needs to be displaced against the force of gravity for a given deformation). The deformation Love numbers are therefore found closer to zero. Consequently, compressibility of the Earth model should not be ignored on elastic time scales. Incompressible models are commonly used to model the viscous response to former glacial loads, for which the effect of compressibility is less important (Tanaka et al., 2011).

As can be seen from Eq. 2.20, all three observables are dependent only on the direct potential contribution of the load, Φ_n'. Green's functions in terms of deformation and geoid height change can be constructed by applying a point load to the Earth model, which is placed at the surface of the Earth. Graphically, the situation is similar to the contribution of the surface element in Fig. 2.1, except that a point load is now chosen instead and the Earth is allowed to deform. The direct potential contribution of a point load of 1 kg can be written as

$$\delta\phi'^p(\mathbf{r} - \mathbf{r}') = \frac{G}{|\mathbf{r} - \mathbf{r}'|} = G \sum_{n=0}^{\infty} \frac{|\mathbf{r}'|^n}{|\mathbf{r}|^{n+1}} P_n(\cos \alpha). \tag{2.21}$$

Where the term on the right-hand side has been obtained by using Eq. 2.10. When evaluated only on the surface of the Earth, one can set $|r| = |r'| = a$, and recognize that $G = \frac{ga^2}{M}$

---

[2]A general depth dependent formulation is also possible

Elastic load Love numbers
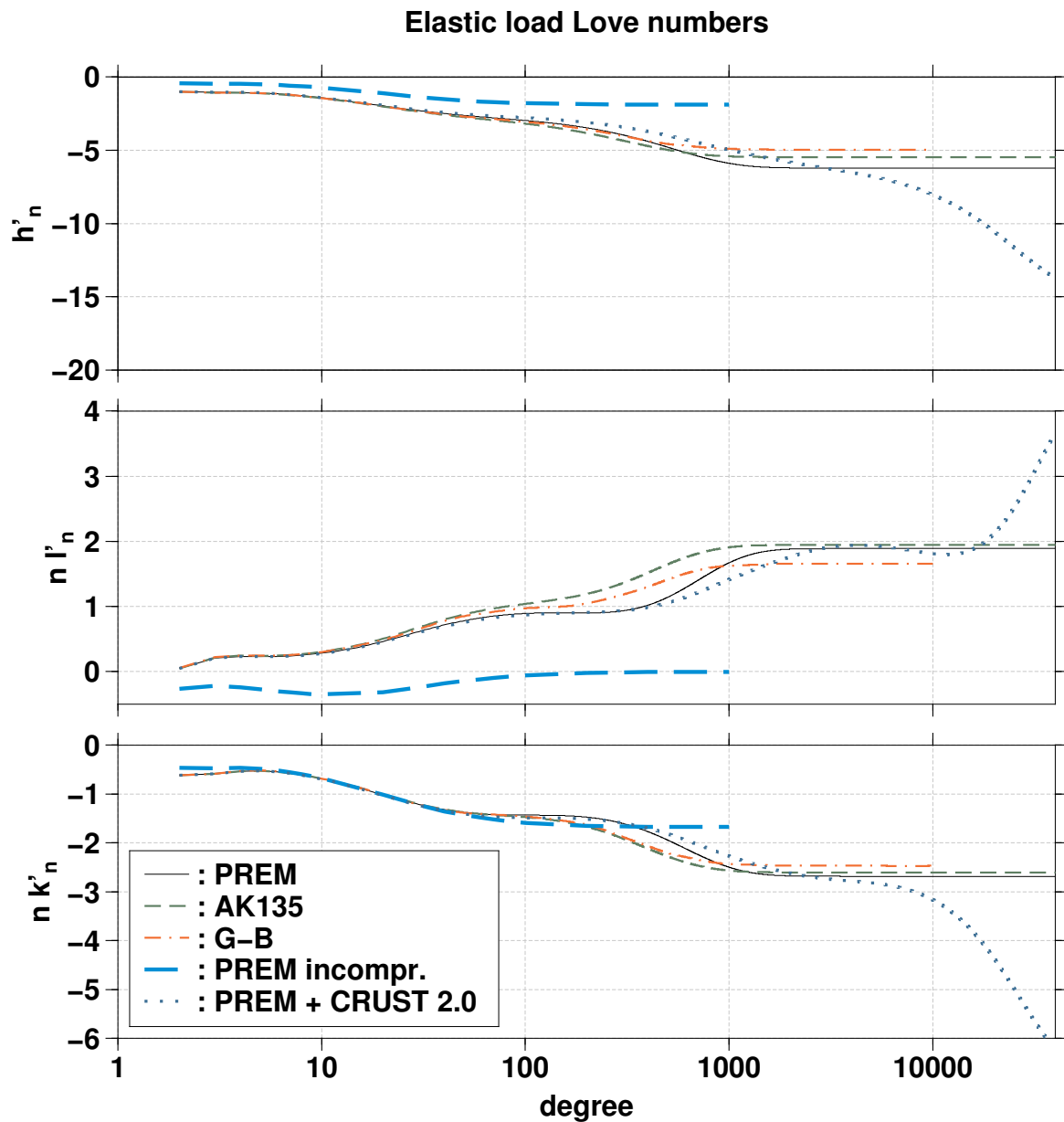
Figure 2.2: Elastic load Love numbers for various Earth models: PREM (Dziewonski, 1981), a modified PREM with crustal properties from CRUST2.0 Wang et al. (2012), AK135 (Kennett et al., 1995), Gutenberg-Bullen (Farrell, 1972), and the elastic limit of a viscous incompressible GIA model (Spada, 2008). The Love numbers for PREM, PREM+CRUST2.0 and AK135 are taken from Wang et al. (2012)(suppl. mat.), the G-B Love numbers from Farrell (1972), and the incompressible Love numbers are computed in-house with the ALMA software from Spada (2008).

to obtain

$$\delta\phi'^p(a,\alpha) = \sum_{n=0}^{\infty} \phi_n'^p P_n(\cos\alpha),$$

$$\text{with } \phi_n'^p = \frac{ag}{M}. \tag{2.22}$$

The coefficients, $\phi_n'^p = \frac{ag}{M}$, can now be used in Eq. 2.20, which can subsequently be substituted in Eqs. 2.18, 2.19. This results in the deformation[3] and geoid height Green's functions, G_X, expressed in terms of load Love numbers:

$$G_U(\alpha) = \frac{a}{M} \sum_{n=0}^{\infty} h_n' P_n(\cos\alpha),$$

$$G_V(\alpha) = \frac{a}{M} \sum_{n=1}^{\infty} l_n' \frac{dP_n(\cos\alpha)}{d\alpha}, \tag{2.23}$$

$$G_N(\alpha) = \frac{a}{M} \sum_{n=0}^{\infty} \left(1 + k_n'\right) P_n(\cos\alpha).$$

In practice, the Love numbers, l_n', h_n' and k_n', are only provided up to a finite degree, so the sum can not be evaluated exactly. However, observing Fig. 2.2 one sees that the load Love numbers exhibit an asymptotic behavior for large degrees

$$\lim_{n\to\infty} h_n' = h_\infty',$$

$$\lim_{n\to\infty} nl_n' = l_\infty', \tag{2.24}$$

$$\lim_{n\to\infty} nk_n' = k_\infty'.$$

The Green's functions can be rewritten using a so-called Kummer's transformation (see for example Farrell, 1972):

$$G_U(\alpha) = \frac{ah_\infty'}{M} \sum_{n=0}^{\infty} P_n(\cos\alpha) + \frac{a}{M} \sum_{n=0}^{\infty} \left(h_n' - h_\infty'\right) P_n(\cos\alpha),$$

$$G_V(\alpha) = \frac{al_\infty'}{M} \sum_{n=1}^{\infty} \frac{1}{n} \frac{dP_n(\cos\alpha)}{d\alpha} + \frac{a}{M} \sum_{n=1}^{\infty} \frac{nl_n' - l_\infty'}{n} \frac{dP_n(\cos\alpha)}{d\alpha}, \tag{2.25}$$

$$G_N(\alpha) = \frac{a}{M} \sum_{n=0}^{\infty} P_n(\cos\alpha) + \frac{ak_\infty'}{M} \sum_{n=0}^{\infty} \frac{1}{n} P_n(\cos\alpha) + \frac{a}{M} \sum_{n=0}^{\infty} \frac{nk_n' - k_\infty'}{n} P_n(\cos\alpha).$$

The summations in the last terms converge quickly enough such that they may be truncated to a maximum degree N. The asymptotic Love numbers may be approximated by $h_\infty' = h_N'$, $l_\infty' = Nl_N'$, and $k_\infty' = Nk_N'$. The first terms can be written in closed forms using

---

[3]The summation for G_V starts at $n = 1$ as $dP_0(\cos\alpha)/d\alpha = 0$

the formulas from Singh and Ben-Menahem (1968), such that

$$G_U(\alpha) = \frac{ah'_\infty}{2M\sin(\alpha/2)} + \frac{a}{M}\sum_{n=0}^{\infty}\left(h'_n - h'_\infty\right)P_n(\cos\alpha),$$

$$G_V(\alpha) = -\frac{al'_\infty}{4M\sin(\alpha/2)} + \frac{a}{M}\sum_{n=1}^{\infty}\frac{nl'_n - l'_\infty}{n}\frac{dP_n(\cos\alpha)}{d\alpha}, \qquad (2.26)$$

$$G_N(\alpha) = \frac{a}{2M\sin(\alpha/2)} - \frac{ak'_\infty}{M}\ln\left(s(s-\sqrt{2})\right) + \frac{a}{M}\sum_{n=0}^{\infty}\frac{nk'_n - k'_\infty}{n}P_n(\cos\alpha),$$

where $s = \sqrt{\cos\alpha}$.

The isotropic Green's functions may also be used to compute the deformation and geoid changes due to a geographically varying surface load. The radial deformation can therefore be written as a convolution of the surface mass elements with mass $\sigma a^2 d\omega$

$$U(\theta,\lambda) = \int_\Omega G_U(\alpha - \alpha')\sigma(\theta',\lambda')a^2 d\omega'. \qquad (2.27)$$

The Green's function from Eq. 2.23 can now be expanded using the addition theorem (Eq. 2.11) and the surface density is expressed in spherical harmonics:

$$U(\theta,\lambda) = \frac{a^4\rho_w}{M}\int_\Omega \sum_{n,m=0}^{\infty}\frac{h'_n}{2n+1}\bar{Y}_{nm}(\theta,\lambda)\bar{Y}_{nm}(\theta',\lambda')$$

$$\sum_{n',m'=0}^{\infty}T_{n'm'}\bar{Y}_{n'm'}(\theta',\lambda')d\omega'. \qquad (2.28)$$

For brevity, the double summation over degree and order is now abbreviated to $\sum_{n,m=0}$. Using the orthogonality relation (Eq. 2.6), and substituting $M = \frac{4}{3}\pi a^3\rho_e$ one can write:

$$U(\theta,\lambda) = \frac{3a\rho_w}{\rho_e}\sum_{n,m=0}^{\infty}\frac{h'_n}{2n+1}T_{nm}\bar{Y}_{nm}(\theta,\lambda). \qquad (2.29)$$

For the horizontal deformation vector field, $\mathbf{V}$, we may use the surface gradient operator $\nabla_\Omega = \mathbf{e}_\theta\partial/\partial\theta + \mathbf{e}_\lambda\partial/\sin\theta\partial\lambda$ to write the convolution as

$$\mathbf{V}(\theta,\lambda) = \frac{a^4\rho_w}{M}\int_\Omega \sum_{n,m=0}^{\infty}\frac{l'_n}{2n+1}\nabla_\Omega\bar{Y}_{nm}(\theta,\lambda)\bar{Y}_{nm}(\theta',\lambda')$$

$$\sum_{n',m'=0}^{\infty}T_{n'm'}\bar{Y}_{n'm'}(\theta',\lambda')d\omega'. \qquad (2.30)$$

Which yields two separate surface components:

$$\mathbf{V}(\theta,\lambda) = \frac{3a\rho_w}{\rho_e}\sum_{n,m=0}^{\infty}\frac{l'_n}{2n+1}T_{nm}\left[\frac{\partial\bar{Y}_{nm}(\theta,\lambda)}{\partial\theta}\mathbf{e}_\theta + \frac{\partial\bar{Y}_{nm}(\theta,\lambda)}{\sin\theta\partial\lambda}\mathbf{e}_\lambda\right]. \qquad (2.31)$$

In analogy with Eq. 2.18, a spatially-varying surface deformation on a Love-Shida Earth (relative to a hydrostatically pre-stressed state) can be expressed by a set of degree and order dependent deformation coefficients U_{nm} and V_{nm}:

$$\hat{\mathbf{D}}(a,\lambda,\theta) = \sum_{n,m=0}^{\infty}\left[U_{nm}\bar{Y}_{nm}(\lambda,\theta)\mathbf{e}_r + V_{nm}\nabla_\Omega\bar{Y}_{nm}(\lambda,\theta)\right]. \qquad (2.32)$$
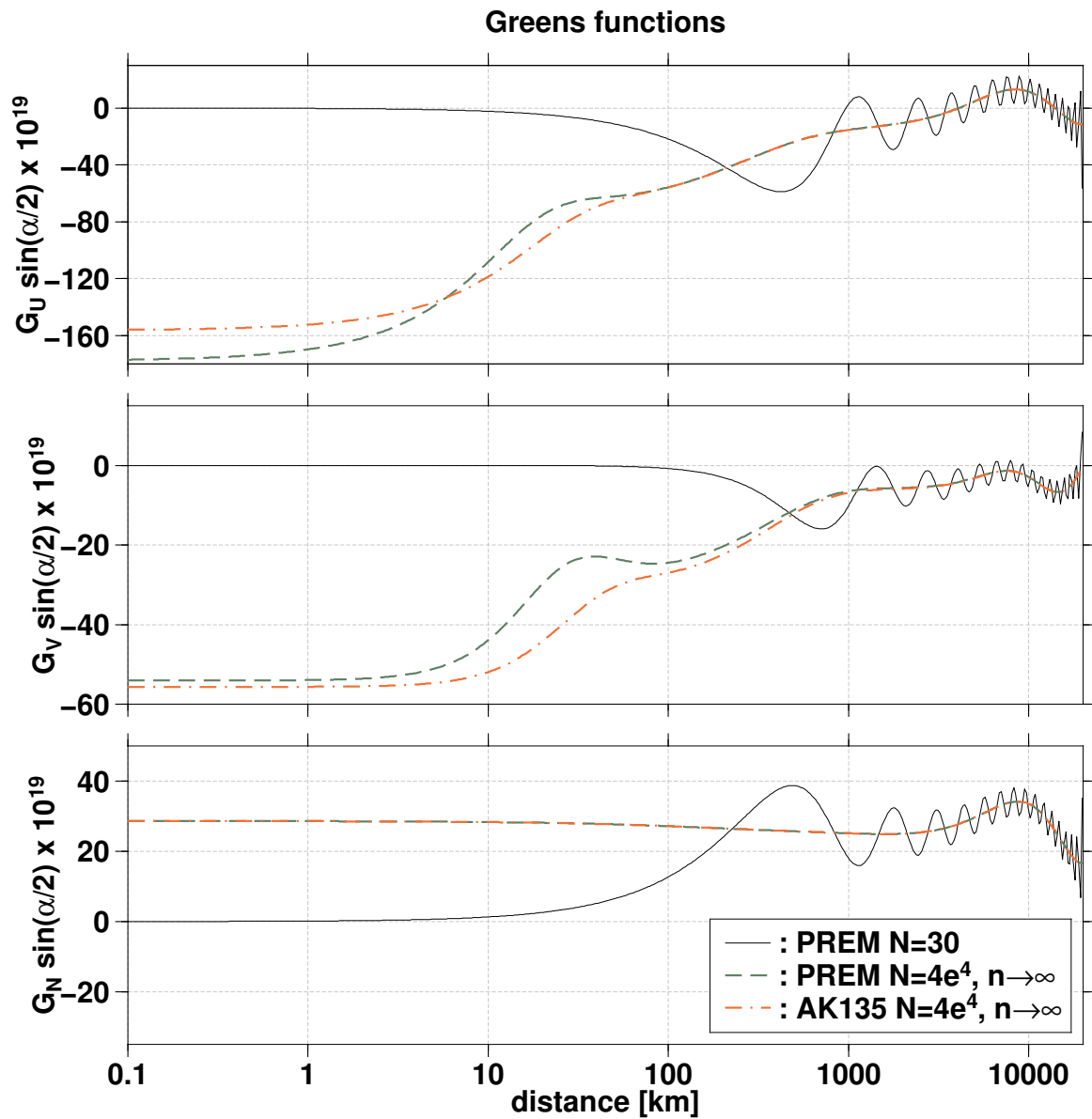
Greens functions

Figure 2.3: Truncated and asymptotic Green's functions for an unit point load of 1 kg. The Green's functions are scaled by $\sin \alpha/2$ to prevent the singularity at $\alpha = 0$. The difference between the truncated and asymptotic series is most pronounced in the direct vicinity of the load, where the asymptotic part dominates, whereas the series agree at the longer wave lengths. The oscillations are caused due to the Gibbs effect arising from representing a point load by a truncated series.

By comparing Eq. 2.32 with Eqs. 2.31 and 2.29 one can readily see that for a surface load

$$U_{nm} = \frac{3a\rho_w}{\rho_e} \frac{h'_n}{2n+1} T_{nm},$$

(2.33)

$$V_{nm} = \frac{3a\rho_w}{\rho_e} \frac{l'_n}{2n+1} T_{nm}.$$

(2.34)

The derivation of the potential change due to the surface load is similar to the radial deformation change,

$$\delta\phi(\theta,\lambda) = \frac{3ag\rho_w}{\rho_e} \sum_{n,m=0}^{\infty} \frac{1+k'_n}{2n+1} T_{nm} \bar{Y}_{nm}(\theta,\lambda).$$

(2.35)

Just as for a rigid Earth (see Eq. 2.16), the residual Stokes coefficients of the deformed Earth and its load, are one to one related to the surface loading coefficients

$$\delta C_{nm} = \frac{1+k'_n}{2n+1} \frac{3\rho_w}{\rho_e} T_{nm}.$$

(2.36)

2.3 Reference System Theory

The degree one terms of Eqs. 2.29-2.35 are a special case as they depend on the chosen reference frame. Blewitt (2003) showed that for a certain family of reference frames, so called isomorphic frames, the elastic deformation on a SNREI Earth model can be transferred to a different frame by simply changing the degree 1 Love numbers. Furthermore, for deformations arising from glacial isostatic adjustment, Klemann and Martinec (2009) provide relations to translate the deformations in various reference frames. A necessary condition is that, in addition to geoid changes, both vertical and horizontal degree 1 deformations are available from the GIA model in a well defined reference frame. Unfortunately, this is information is often not available, or it is unclear whether the reference frame is applied consistently for all observables.

The imbalance of the surface load and the associated deformation of the Earth induces a shift of the center of figure (CF) of the solid Earth relative to the center of mass of the Earth system (CM). This movement is commonly referred to as 'geocenter motion'. It is an important quantity to consider when comparing space based observations with crust-fixed observations (e.g. tide gauges, bottom pressure recorders, etc.). This section describes the most important formulas used in this thesis, and provides the physical basis for them.

2.3.1 Center of Surface Figure

The position of the Center of surface Figure (CF) of the Earth in the loaded state can be computed by integrating the surface deformation over the entire globe (e.g. Blewitt (2003)):

$$\mathbf{x}_{CF} = \frac{1}{4\pi} \int_{\Omega} \mathbf{D}(a,\omega') d\omega'.$$

(2.37)

For a Love-Shida Earth, the deformation $\hat{\mathbf{D}}$ from Eq. 2.32 can be substituted. Furthermore, upon recognizing that

$$
\mathbf{e}_r = \begin{bmatrix} \sin\theta\cos\lambda \\ \sin\theta\sin\lambda \\ \cos\theta \end{bmatrix} = \frac{1}{\sqrt{3}} \begin{bmatrix} \bar{Y}_{11} \\ \bar{Y}_{1-1} \\ \bar{Y}_{10} \end{bmatrix},
\tag{2.38}
$$

one may describe, after some manipulation, the integral in terms of Cartesian components:

$$
\mathbf{x}_{CF} = \frac{1}{4\pi\sqrt{3}} \int_\Omega \sum_{n,m=0}^\infty U_{nm}\bar{Y}_{nm} \begin{bmatrix} \bar{Y}_{11} \\ \bar{Y}_{1-1} \\ \bar{Y}_{10} \end{bmatrix} + V_{nm} \begin{bmatrix} \nabla_\Omega\bar{Y}_{nm}\cdot\nabla_\Omega\bar{Y}_{11} \\ \nabla_\Omega\bar{Y}_{nm}\cdot\nabla_\Omega\bar{Y}_{1-1} \\ \nabla_\Omega\bar{Y}_{nm}\cdot\nabla_\Omega\bar{Y}_{10} \end{bmatrix} d\omega'.
\tag{2.39}
$$

Most of the terms from the summation will drop out because of the orthogonality relations from Eq. 2.6 and the identity

$$
\oint_\Omega \nabla_\Omega\bar{Y}_{nm}(\omega)\cdot\nabla_\Omega\bar{Y}_{n'm'}(\omega)d\omega = 4\pi n(n+1)\delta_{nn'}\delta_{mm'}.
\tag{2.40}
$$

This implies that the X, Y and Z -component of $\mathbf{x}_{CF}$ are directly linked to the coefficients U/V_{11}, U/V_{1-1}, and U/V_{10}, respectively:

$$
\mathbf{x}_{CF} = \frac{1}{\sqrt{3}} \begin{bmatrix} U_{11} + 2V_{11} \\ U_{1-1} + 2V_{1-1} \\ U_{10} + 2V_{10} \end{bmatrix}.
\tag{2.41}
$$

In practice, the center of figure is often approximated. A network of GPS stations, at location $\mathbf{r}_i$, may yield a (geometrical) center of network $\mathbf{x}_{CN}$,

$$
\mathbf{x}_{CN} = \frac{1}{N} \sum_i^N \mathbf{r}_i,
\tag{2.42}
$$

which differs from $\mathbf{x}_{CF}$ as the network covers only part of the Earth surface and errors of isolated stations and orbit errors (.e.g. from inaccurate solar radiation pressure modelling) may creep into the estimate (Wu et al., 2002). Reference frames, having this origin are commonly denoted as center of network frames (CN).

2.3.2 Center of Mass of the Earth System

For satellites orbiting the Earth, a natural choice for their reference system origin is the 'center of mass of the Earth system' (CM). Satellites sense both the solid Earth and the surface load and will therefore revolve around this common center of mass. Considering the combined masses of both the solid Earth and the surface load, this is the point where a translated potential field would yield zero valued degree 1 coefficients. Its location is directly related to the degree 1 Stokes coefficients of the gravity field (see App. A.1 for a proof):

$$
\mathbf{x}_{CM} = \sqrt{3}a \begin{bmatrix} C_{11} \\ C_{1-1} \\ C_{10} \end{bmatrix}.
\tag{2.43}
$$

2.3.3 Center of Earth

For surface loading problems, the center of mass of the Earth system is a weighted sum of the barycenter of the solid Earth (denoted by CE) and that of the barycenter of the surface load (denoted by L). Although the center of mass of the Earth system remains stationary, the CE will alter its position whenever the barycenter of the surface load changes (Trupin et al., 1992; Dong et al., 1997):

$$\mathbf{x}_{CM} = \frac{1}{M_L + M_S}(M_L\mathbf{x}_L + M_S\mathbf{x}_{CE}) = \frac{1}{M}(\mathbf{m}_L + \mathbf{m}_{CE}). \tag{2.44}$$

Here, M_L and M_S are the masses of the surface load and the solid Earth respectively. The more compact vectors $\mathbf{m}_L$ and $\mathbf{m}_{CE}$ are sometimes called moment vectors[4] (e.g. Blewitt, 2003).

The moment vector, $\mathbf{m}_{CE}$, may be computed from integrating the density and deformation over the entire solid Earth (e.g. Klemann and Martinec (2009)):

$$\mathbf{m}_{CE} = \int_{V_S} \rho(\theta', \lambda', r')\mathbf{D}(r', \theta', \lambda')dv'. \tag{2.45}$$

In most Earth deformation (both viscous and elastic) models, the barycenter of the solid Earth (CE) is often used as the origin of the model reference frame (implying $\mathbf{m}_{CE} = 0$). This is because, for a given surface load, the position of the CE is invariant w.r.t. the used Earth parameters and the response of different Earth models may be conveniently compared.

Using Eq. 2.45 to estimate $\mathbf{x}_{CE}$ requires the depth dependent density and deformation from a mechanical Earth model, which is often not available. However, when the surface load is known Eq. 2.44 may be used to find a simpler expression. This method will be described below.

The load moment vector, $\mathbf{m}_L$, may be computed from integrating the surface load over a thin shell (Blewitt, 2003):

$$\mathbf{m}_L = \int_{\Omega} a\mathbf{e}_r\sigma(\omega')a^2d\omega'. \tag{2.46}$$

Using Eqs. 2.38, 2.6 and substituting Eq. 2.12, one obtains

$$\mathbf{m}_L = \frac{4\pi a^4 \rho_w}{\sqrt{3}} \begin{bmatrix} T_{11} \\ T_{1-1} \\ T_{10} \end{bmatrix} = \frac{\sqrt{3}a\rho_w M}{\rho_e} \begin{bmatrix} T_{11} \\ T_{1-1} \\ T_{10} \end{bmatrix}. \tag{2.47}$$

Since the mass elements, $\sigma(\omega')a^2d\omega'$, in Eq. 2.46 are far away from the Earth's center, $\mathbf{m}_L$ will be virtually independent on the used reference frame, as long as it is approximately geocentric (Blewitt, 2003). Conversely, the degree 1 coefficients of the surface load will be insensitive to reference system changes.

---

[4]after the first mass moment of inertia

As an alternative to Eq. 2.45, $\mathbf{x}_{CE}$, may be derived from Eq. 2.44

$$\mathbf{x}_{CE} = \frac{1}{M_S} \left(M\mathbf{x}_{CM} - \mathbf{m}_L \right). \tag{2.48}$$

Substituting the expression for the center of mass and the load moment vector (Eqs. 2.43 and 2.47) one finds:

$$
\begin{aligned}
\mathbf{x}_{CE} &= \sqrt{3}a \frac{M}{M_S} \begin{bmatrix} C_{11} \\ C_{1-1} \\ C_{10} \end{bmatrix} - \frac{\sqrt{3}a\rho_w}{\rho_e} \frac{M}{M_S} \begin{bmatrix} T_{11} \\ T_{1-1} \\ T_{10} \end{bmatrix} \\
&\approx \sqrt{3}a \begin{bmatrix} C_{11} \\ C_{1-1} \\ C_{10} \end{bmatrix} - \frac{\sqrt{3}a\rho_w}{\rho_e} \begin{bmatrix} T_{11} \\ T_{1-1} \\ T_{10} \end{bmatrix},
\end{aligned}
\tag{2.49}
$$

where in the approximation it is assumed that $M \approx M_S$.

2.3.4 Shifting the Reference Frame

The deformation vector field, $\hat{\mathbf{D}}^A$, as observed from reference system A, may be observed from a translated reference frame, B as

$$\hat{\mathbf{D}}^B(\lambda, \theta) = \hat{\mathbf{D}}^A(\lambda, \theta) - \mathbf{t}^{A \to B}. \tag{2.50}$$

The translation vector from the origin of A to the origin of B is denoted by $\mathbf{t}^{A \to B}$ (with Cartesian components $t_{x,y,z}$). In the local spherical frame, $\mathbf{t}^{A \to B}$, may be written as a spherical harmonic expansion of degree 1:

$$\mathbf{t}^{A \to B} = \frac{1}{\sqrt{3}} \sum_{m=-1}^{1} t_{1m} \left[\bar{Y}_{1m}\mathbf{e}_r + \nabla_\Omega \bar{Y}_{1m} \right] \tag{2.51}$$

$$with \quad t_{11} = t_x, \quad t_{1-1} = t_y, \quad t_{10} = t_z.$$

The transformed deformation, $\hat{\mathbf{D}}^B$, may therefore be constructed by changing the degree 1 deformation coefficients:

$$\begin{bmatrix} U/V_{11} \\ U/V_{1-1} \\ U/V_{10} \end{bmatrix}^B = \begin{bmatrix} U/V_{11} \\ U/V_{1-1} \\ U/V_{10} \end{bmatrix}^A - \frac{1}{\sqrt{3}} \begin{bmatrix} t_x \\ t_y \\ t_z \end{bmatrix}^{A \to B}. \tag{2.52}$$

When changing the reference frame of a potential field, one generally has to replace all Stokes coefficients. However , for small translations, such as those involved in geocenter motion, it is safe to modify only the degree one Stokes coefficients (see App. A.2):

$$\begin{bmatrix} C_{11} \\ C_{1-1} \\ C_{10} \end{bmatrix}^B = \begin{bmatrix} C_{11} \\ C_{1-1} \\ C_{10} \end{bmatrix}^A - \frac{1}{\sqrt{3}a} \begin{bmatrix} t_x \\ t_y \\ t_z \end{bmatrix}^{A \to B}. \tag{2.53}$$

2.3.5 Center of Surface Height and Lateral Figure

There are two more frame origins which may be of interest. The first one is the so called Center of surface Height (CH). A deformation expressed in this frame will yield a zero valued integral when integrating over the vertical deformation field. Thus by inserting a deformation field shifted by $\mathbf{CH}$, and projecting it on the radial component, one may construct the following condition:

$$\mathbf{0} = \frac{1}{4\pi} \int_\Omega \mathbf{e}_r \left[\mathbf{e}_r \cdot \left(\mathbf{D}(\omega') - \mathbf{x}_{CH} \right) \right] d\omega'. \tag{2.54}$$

Only the degree 1 uplift components will yield a non-zero contribution to the integral, due to the orthogonality properties of the spherical harmonics. Furthermore, for a Love-Shida Earth, one may use Eq. 2.52 to separate $\mathbf{x}_{CH}$:

$$\mathbf{x}_{CH} = \sqrt{3} \begin{bmatrix} U_{11} \\ U_{1-1} \\ U_{10} \end{bmatrix}. \tag{2.55}$$

Similarly, the Center of Lateral surface figure (CL) is the frame origin where the integral over the horizontal deformation field vanishes. The deformation is now shifted and projected onto the horizontal components

$$\begin{aligned} \mathbf{0} = \frac{1}{4\pi} \int_\Omega \Big\{ & \mathbf{e}_\theta \left[\mathbf{e}_\theta \cdot \left(\mathbf{D}(\omega') - \mathbf{x}_{CL} \right) \right] \\ + & \mathbf{e}_\lambda \left[\mathbf{e}_\lambda \cdot \left(\mathbf{D}(\omega') - \mathbf{x}_{CL} \right) \right] \Big\} d\omega'. \end{aligned}$$

Again, for a Love-Shida Earth, only the degree 1 components are relevant and one may then write

$$\mathbf{x}_{CL} = \sqrt{3} \begin{bmatrix} V_{11} \\ V_{1-1} \\ V_{10} \end{bmatrix}. \tag{2.56}$$

2.3.6 Degree 1 Considerations for a Radially Symmetric Elastic Earth

In Sec. 2.2.2, the reference frame has not been clearly defined yet. In fact, a whole family of reference frames exists, in which the degree 1 deformation and potential changes can be described in the forms of Eqs. 2.29, 2.31, and 2.35 (i.e. they can be described with a Load Love number formalism). Blewitt (2003) coined these reference systems 'isomorphic frames'.

To translate one isomorphic frame into another, one requires a translation vector which is a scaled version of the load moment vector $\mathbf{m}_L$ (Blewitt, 2003). For surface loading on a SNREI Earth, *any* linear combination of the degree 1 components of deformation and

gravity change, will obey the property

$$
\mathbf{t}^{A \to B} = \beta \begin{bmatrix} C_{11} \\ C_{1-1} \\ C_{10} \end{bmatrix}^A + \eta \begin{bmatrix} U_{11} \\ U_{1-1} \\ U_{10} \end{bmatrix}^A + \epsilon \begin{bmatrix} V_{11} \\ V_{1-1} \\ V_{10} \end{bmatrix}^A
$$

$$
= \alpha^{A \to B} \frac{\mathbf{m}_L}{M} = \alpha^{A \to B} \frac{\sqrt{3} a \rho_w}{\rho_e} \begin{bmatrix} T_{11} \\ T_{1-1} \\ T_{10} \end{bmatrix}.
$$

(2.57)

With the exception of the Center of Network (CN) frame, all frame origins described so far obey this form (CF, CM, CH, CL, CE). The parameter $\alpha^{A \to B}$ is denoted as the "isomorphic parameter" (Blewitt, 2003). As will be shown below, the transformation from one isomorphic frame into another is represented by this single parameter, which implies that all of these isomorphic frame origins lie on a straight line.

The degree 1 coefficients of the potential and deformation in reference frame A are expressed as

$$
\delta C_{1m}^A = (1 + k_1'^A) \frac{\rho_w}{\rho_e} T_{1m},
$$

$$
U_{1m}^A = h_1'^A \frac{a \rho_w}{\rho_e} T_{1m},
$$

(2.58)

$$
V_{1m}^A = l_1'^A \frac{a \rho_w}{\rho_e} T_{1m}.
$$

Using Eqs. 2.52 and 2.53, the reference frame of these observables may be shifted by a vector of the form of Eq. 2.57, to another (isomorphic) frame B:

$$
\delta C_{1m}^B = (1 + k_1'^A - \alpha^{A \to B}) \frac{\rho_w}{\rho_e} T_{1m} = (1 + k_1'^B) \frac{\rho_w}{\rho_e} T_{1m},
$$

$$
U_{1m}^B = (h_1'^A - \alpha^{A \to B}) \frac{a \rho_w}{\rho_e} T_{1m} = h_1'^B \frac{a \rho_w}{\rho_e},
$$

(2.59)

$$
V_{1m}^B = (l_1'^A - \alpha^{A \to B}) \frac{a \rho_w}{\rho_e} T_{1m} = l_1'^B \frac{a \rho_w}{\rho_e}.
$$

The equations above demonstrate that the load Love numbers may be interpreted as 'frame specific'. As shown above, if the Love numbers are provided in one particular frame, the load Love numbers in another frame may be derived by computing $\alpha^{A \to B}$, and applying the transformation

$$
1 + k_1'^B = 1 + k_1'^A - \alpha^{A \to B},
$$

$$
h_1'^B = h_1'^A - \alpha^{A \to B},
$$

(2.60)

$$
l_1'^B = l_1'^A - \alpha^{A \to B}.
$$

Using Eqs. 2.41, 2.55, 2.56, 2.43, 2.49 in combination with Eq. 2.59 the following parame-

ters are obtained:

$$\alpha^{A \to CM} = 1 + k_1'^{A},$$
$$\alpha^{A \to CF} = \left(h_1'^{A} + 2l_1'^{A} \right) / 3,$$
$$\alpha^{A \to CE} = k_1'^{A}, \tag{2.61}$$
$$\alpha^{A \to CH} = h_1'^{A},$$
$$\alpha^{A \to CL} = l_1'^{A}.$$

Blewitt (2003) derived these parameters for the example $A = CE$. However, in the expressions above, one may substitute any of the isomorphic frames for system A.

In the elastic loading case, it is interesting to consider the distance of the CM from the CE and the CF:

$$\mathbf{x}_{CM} - \mathbf{x}_{CE} = \sqrt{3}a \frac{(1+k_1'^{CE})\rho_w}{\rho_e} \begin{bmatrix} T_{11} \\ T_{1-1} \\ T_{10} \end{bmatrix} = \sqrt{3}a \frac{\rho_w}{\rho_e} \begin{bmatrix} T_{11} \\ T_{1-1} \\ T_{10} \end{bmatrix}, \tag{2.62}$$

$$\mathbf{x}_{CM} - \mathbf{x}_{CF} = \sqrt{3}a \frac{(1+k_1'^{CF})\rho_w}{\rho_e} \begin{bmatrix} T_{11} \\ T_{1-1} \\ T_{10} \end{bmatrix}. \tag{2.63}$$

From the above, it is clear that the displacement, $\mathbf{x}_{CM} - \mathbf{x}_{CE}$, is independent of the Earth model used. Although, $\mathbf{x}_{CM} - \mathbf{x}_{CF}$, does depend on $k_1'^{CF}$ its value is very small ($k_1'^{CF} = 0.026$) for the preliminary Reference Earth model from Dziewonski (1981)). Consequently, the CE and the CF coincide to within 3%, for realistic elastic loading problems, whereas the center of mass of the Earth (CM) is located farther away. This is schematically shown in Fig. 2.4.

2.3.7 Degree 1 Considerations for a Radially Symmetric Visco-elastic Earth

A formulation of deformation and gravity change in terms of time dependent load Love numbers (see for example Spada (2008)), is possible when certain conditions are satisfied. This occurs when the variations of the Earth's density, rigidity and viscosity are radially symmetric, and when the rheology of the Earth is assumed to be linear. Furthermore, the time dependency of the load is decoupled from the spatial variation and must follow an analytical function which is easily expressed in the Laplace domain. This can be for example a Dirac delta function, an Heaviside (step) function or a ramp function.

For a Heaviside loading, the time dependent variation of the deformation and gravity change for a load on a visco-elastic Earth can be described as follows:

$$\Delta U^*(\theta, \lambda, t) = \frac{3a\rho_w}{\rho_e} \sum_{n,m=0}^{\infty} \frac{h_n'(t-t_\delta)}{2n+1} H_{t_\delta}(t) \Delta T_{nm} \bar{Y}_{nm}(\theta, \lambda),$$

$$\Delta \mathbf{V}^*(\theta, \lambda, t) = \frac{3a\rho_w}{\rho_e} \sum_{n,m=0}^{\infty} \frac{l_n'(t-t_\delta)}{2n+1} H_{t_\delta}(t) \Delta T_{nm} \left[\frac{\partial \bar{Y}_{nm}(\theta, \lambda)}{\partial \theta} \mathbf{e}_\theta + \frac{\partial \bar{Y}_{nm}(\theta, \lambda)}{\sin \theta \partial \lambda} \mathbf{e}_\lambda \right], \quad (2.64)$$

$$\Delta \delta \phi^*(\theta, \lambda, t) = \frac{3ag\rho_w}{\rho_e} \sum_{n,m=0}^{\infty} \frac{1+k_n'(t-t_\delta)}{2n+1} H_{t_\delta}(t) \Delta T_{nm} \bar{Y}_{nm}(\theta, \lambda).$$
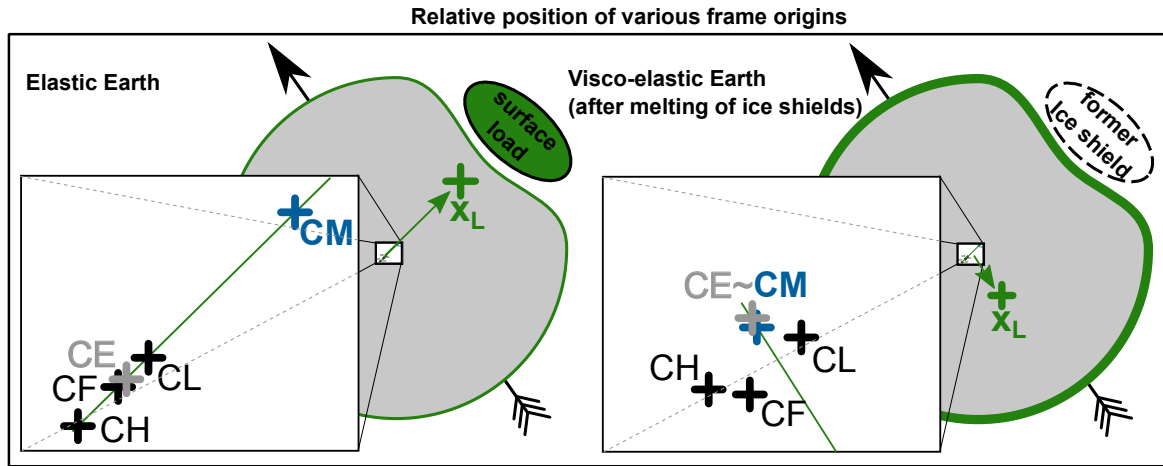
Figure 2.4: Schematic drawing of the relative locations of various frame origins. For the elastic loading problem (left), all points lie on the same line (in line with the (load) vector, $\mathbf{x}_L$). The drawing on the right-hand side shows the situation where a visco-elastic Earth is loaded with an ice-history (after melting). In contrast to the elastic case, the frame origins generally do not lie on the same line (except CE, CM and $\mathbf{x}_L$).

As mentioned before, the surface load increment is factorized in a spatial component (contained in the coefficients ΔT_{nm}) and the Heaviside (step) function $H_{t_\delta}(t)$. Therefore, the total surface load will be 0 when $t < t_\delta$ and will increment discontinuously at time t_δ. The time dependent load Love numbers must be specifically computed for a Heaviside load.

The formulation is very similar to the elastic case. Therefore, in the same line of reasoning, one may introduce a time dependent isomorphic frame parameter, $\alpha^{A\to B}(t - t_\delta)$, which is coupled to the degree 1 load Love numbers,

$$
\begin{aligned}
1 + k_1'^{B}(t - t_\delta) &= 1 + k_1'^{A}(t - t_\delta) - \alpha^{A\to B}(t - t_\delta), \\
h_1'^{B}(t - t_\delta) &= h_1'^{A}(t - t_\delta) - \alpha^{A\to B}(t - t_\delta), \\
l_1'^{B}(t - t_\delta) &= l_1'^{A}(t - t_\delta) - \alpha^{A\to B}(t - t_\delta).
\end{aligned}
\tag{2.65}
$$

In analogy with Eq. 2.61, one can see that the isomorphic frame parameter only depends on the Love numbers at the same epoch. Shifting the time axis for clarity, it becomes clear that

$$
\begin{aligned}
\alpha^{A\to CM}(t) &= 1 + k_1'^{A}(t), \\
\alpha^{A\to CF}(t) &= \left(h_1'^{A}(t) + 2l_1'^{A}(t) \right)/3, \\
\alpha^{A\to CE}(t) &= k_1'^{A}(t), \\
\alpha^{A\to CH}(t) &= h_1'^{A}(t), \\
\alpha^{A\to CL}(t) &= l_1'^{A}(t).
\end{aligned}
\tag{2.66}
$$

Consequently, when using a load Love number formalism, a visco-elastic loading problem can be computed in a reference frame of choice by simply transforming the degree 1 Love

numbers at every time step.

The spatial distribution of the load increment does not change in time. In order to accommodate for loads, varying in space and time such as caused by former ice sheets, one can discretize a generic loading history, $T(\theta, \lambda, t)$, by summing over various increments ΔT^i:

$$T(\theta, \lambda, t) \approx \sum_{i=0}^{K} \left(T(\theta, \lambda, t_i) - T(\theta, \lambda, t_{i-1}) \right) H_{t_i}(t) = \sum_{i=0}^{K} \Delta T^i(\theta, \lambda) H_{t_i}(t). \quad (2.67)$$

The discretized load can now be introduced in Eq. 2.64. Since the relations are linear, the superposition principle yields the total deformation and gravity change for a given load history:

$$
\begin{aligned}
U^*(\theta, \lambda, t) &= \frac{3a\rho_w}{\rho_e} \sum_{i=0}^{K} \sum_{n,m=0}^{\infty} \frac{h'_n(t - t_i)}{2n+1} H_{t_i}(t) \Delta T^i_{nm} \bar{Y}_{nm}(\theta, \lambda), \\
\mathbf{V}^*(\theta, \lambda, t) &= \frac{3a\rho_w}{\rho_e} \sum_{i=0}^{K} \sum_{n,m=0}^{\infty} \frac{l'_n(t - t_i)}{2n+1} H_{t_i}(t) \Delta T^i_{nm} \left[\frac{\partial \bar{Y}_{nm}(\theta, \lambda)}{\partial \theta} \mathbf{e}_\theta + \frac{\partial \bar{Y}_{nm}(\theta, \lambda)}{\sin\theta \partial \lambda} \mathbf{e}_\lambda \right], \quad (2.68) \\
\delta\phi^*(\theta, \lambda, t) &= \frac{3ag\rho_w}{\rho_e} \sum_{i=0}^{K} \sum_{n,m=0}^{\infty} \frac{1 + k'_n(t - t_i)}{2n+1} H_{t_i}(t) \Delta T^i_{nm} \bar{Y}_{nm}(\theta, \lambda).
\end{aligned}
$$

Equally valid in this case, the deformation and gravity change can be provided in a reference frame of choice by modifying the degree 1 Love numbers for all time steps. However in this case, the time convolution causes that the reference frame origins stray away from a straight line, as is the case of a purely elastic Earth. This effect is schematically illustrated in Fig. 2.4).

Often however, GIA models provide only the result of the convolutions. When the 3D deformation as well as the gravity change are computed in a consistent reference frame, one can still transform the results from one frame into another. The necessary translations can be computed from Eqs. 2.41, 2.55, 2.56, 2.43, 2.49. Which can consequently be used in Eqs. 2.53, 2.52 to compute the degree 1 coefficients in the new frame.

For present day changes of GIA, one finds that CM lies close to the CE. This is because, in ice history models (e.g. ICE5-G,Peltier, 2004), the present day distribution of the ice/meltwater is rather smooth (almost all the glacial mass is smoothly distributed as melt water over the globe). Consequently, the degree 1 components of the present day load are relatively small, and CE is only marginally shifted from the CM. However, during the last glacial maximum, this offset was considerable (several tens of meters Klemann and Martinec, 2009).

2.3.8 Geocenter Motion

The term 'geocenter motion' is used ambiguously in literature (Blewitt, 2003). Loosely speaking, it refers to the time varying displacement between the different reference frame origins (CM, CE, CH, CL, CF). For example, some authors define the geocenter as the CF: (Dong et al., 1997; Blewitt, 2003; Klemann and Martinec, 2009; Wu et al., 2012). Others

use the CM as the definition of the geocenter (e.g. Heiskanen and Moritz, 1967; Chen et al., 1999; Crétaux et al., 2002; Bouillé et al., 2000; Rietbroek et al., 2012b). Consequently, whenever the term 'geocenter motion' is coined one should invest some time in figuring out which definition the author uses. To be consistent with the published geocenter motion time series (Rietbroek et al., 2009, 2012b), the geocenter motion is defined in this thesis as

$$\mathbf{x}_{GC} \equiv \mathbf{x}_{CM} - \mathbf{x}_{CF}. \tag{2.69}$$

Most of the time however, the offset is defined explicitly, to avoid confusion.

2.3.9 Helmert Transformation

The procedures described in the previous sections allow a transformation of potential and deformation between different isomorphic frames. The dynamic theory involved, allows a deformation of the surface, induced by surface loading or GIA related processes. In addition to these dynamic transformations, purely *rigid* transformation techniques are often used on sets of station coordinates. These implicitly postulate that the relative distance between stations does not change. On the other hand, the dynamic transformations, implicitly assume a non-rotating Earth, and a possible coupling with the Earth's rotation vector is therefore neglected (i.e. the orientation of the axes before and after an isomorphic transformation remain parallel).

In order to augment the deformation theory of this work, it is of interest to have available a tool with which rigid network transformations can be applied. For this means I discuss the 7-parameter Helmert transform, commonly applied in geodesy, which can be used to transform a set of coordinates of a rigid network into a different reference system (see for example Heiskanen and Moritz, 1967)

$$\mathbf{x}^B = \begin{bmatrix} t_x \\ t_y \\ t_z \end{bmatrix} + (1+s) \begin{bmatrix} 1 & -r_z & r_y \\ r_z & 1 & -r_x \\ -r_y & r_x & 1 \end{bmatrix} \mathbf{x}^A. \tag{2.70}$$

The transformation is defined by the 7 Helmert parameters, representing a translation (t_x, t_y, t_z), a rotation (r_x, r_y, r_z), and a (radial) scaling of the network by $(1+s)$. Inversely, when a set of (noisy) station coordinates is known in the frames A and B, the Helmert transformation may be approximately rewritten as (Heiskanen and Moritz, 1967):

$$\begin{bmatrix} 1 & 0 & 0 & x^A & 0 & z^A & -y^A \\ 0 & 1 & 0 & y^A & -z^A & 0 & x^A \\ 0 & 0 & 1 & z^A & y^A & -x^A & 0 \end{bmatrix} \begin{bmatrix} t_x \\ t_y \\ t_z \\ s \\ r_x \\ r_y \\ r_z \end{bmatrix} = \mathbf{H}\mathbf{t}_H = \mathbf{x}^B - \mathbf{x}^A + \boldsymbol{\epsilon}. \tag{2.71}$$

The linearity of Eq. 2.71 above is exploited throughout the thesis. The non-linear terms which contain multiplications of, sr_i, may be safely neglected for the small changes considered. Eq. 2.71 is usually solved in a least squares sense to estimate unknown Helmert parameters from a set of noisy station coordinate pairs. The Helmert parameters, and the station residuals, $\mathbf{x}^B - \mathbf{x}^A$, are typically very small such that it suffices to use approximate station positions in the matrix on the left-hand side.

2.3.10 Plate Motion

When one considers the tectonic plates to be rigid segments of spherical shells, one may describe the movement of a station attached to it by means of a so called Euler (plate) vector, $\dot{\omega}^i$. The formulation is very similar to a Helmert transform, except that the relevant Euler plate vector depends on the station location (see for example Altamimi et al., 2012)

$$\dot{\mathbf{x}} = \dot{\omega}^i \times \mathbf{x} = \begin{bmatrix} 0 & z & -y \\ -z & 0 & x \\ y & -x & 0 \end{bmatrix} \begin{bmatrix} \dot{\omega}^i_x \\ \dot{\omega}^i_y \\ \dot{\omega}^i_z \end{bmatrix}. \tag{2.72}$$

From the cross product it is obvious, that the associated plate motion results in a purely horizontal motion in the local station frame.

The Euler plate vectors may be given in various reference frames. For global studies they are commonly provided in a frame which is fixed with a Tisserand or no-net-rotation condition (Argus et al., 2011; Altamimi et al., 2012). This is the frame where the total angular momentum of the Euler plates is zero:

$$\mathbf{0} = \mathbf{L} = \int_\Omega \mathbf{x} \times (\dot{\omega} \times \mathbf{x}) d\omega = \sum_{i=1}^{K} \mathbf{Q}^i \dot{\omega}^i. \tag{2.73}$$

The inertia tensor of each plate, $\mathbf{Q}^i$, may be computed when its boundary is available in digital form. Under the assumption that the lithospheric thickness is constant, the tensor may be computed by discretizing the following integral (Schettino, 1999; Jin and Zhu, 2004):

$$\mathbf{Q}^i = \int_{plate^i} \begin{bmatrix} y^2 + z^2 & -xy & -xz \\ -xy & x^2 + z^2 & -yz \\ -xz & -yz & x^2 + y^2 \end{bmatrix} \sin\theta d\theta d\lambda. \tag{2.74}$$

2.4 Self-consistent Sea Level Theory

The distribution of water and ice on land has a heterogeneous spatial nature, since sources may be localized and constrained by topographic features. In contrast, the ocean generally adapts itself quickly to an equipotential surface, which results in a much smoother spatial surface load.

In first approximation, the ocean is at rest and adapts itself to the geoid. This is commonly denoted as the passive response of sea level. Whenever the surface load changes, the geoid will change as a result and the ocean will adapt itself to the new geoid. The ocean responds quickly to such changes, typically in the order of 4 days (Kuhlmann et al., 2011), such that the transient behavior can be ignored for this work.

In the following sections, methods are described to compute the passive response of the ocean while ensuring mass conservation on a global scale. The key to this computation lies in solving the so-called "sea level equation" (SLE).

The physical principle has been described as early as 1888 (Woodward, 1888). Farrell and Clark (1976) applied an iterative approach to solve the SLE, in the framework of (visco-)

elastic loading of the Earth by glacial masses (see also a more recent discussion in Sabadini and Vermeersen, 2004). A spherical harmonic spectral approach to solve the sea level equation was proposed by Dahlen (1976) who used the theory to compute the ocean's response to the pole tide.

2.4.1 The Sea Level Equation

The "Sea Level Equation" describes the physical relationship between the sought-for passive sea level, S, and the prescribed (continental) surface load, H. Since mass is conserved on a global scale, the change in mass of S must be compensated by that of H. The total surface load, T, expressed in equivalent water height, therefore constitutes of both components:

$$T(\lambda, \theta, t) = S(\lambda, \theta, t) + H(\lambda, \theta, t). \tag{2.75}$$

Fig. 2.5 schematically depicts the phenomena associated with a self-consistent sea level response to a continental ice load. Relative sea level change, S, is measured with respect to the Earth's crust. This observable may be measured by instruments such as tide gauges and bottom pressure recorders. Changes in relative sea level are therefore important for coastal regions. On the other hand, an altimeter would observe geocentric sea level changes, which essentially follow changes in the geoid height. However, two effects may induce a shift of the geocentric sea level away from the geoid. Firstly, a mass flux into the ocean will cause an uniform upward shift, also known as the eustatic sea level rise. Secondly, a change in the overall ocean basin volume, due to deformations of the ocean floor, will additionally cause an offset. These shifts are relatively small, such that the sea level surface can still be considered an equipotential surface. Compared to the geoid, its potential value has now changed by $\Delta\phi$. The above effects can be put together in the form of the "Sea level equation":

$$\begin{aligned} S(\lambda, \theta, t) &= O(\lambda, \theta) \int_\Omega G_{N-U}(\alpha - \alpha') \left[S(\lambda', \theta', t) + H(\lambda', \theta', t) \right] d\omega' \\ &+ \frac{\Lambda_{N-U}(S, H, \lambda, \theta)}{g} + \frac{\Delta\phi}{g}. \end{aligned} \tag{2.76}$$

Here the total surface load is convolved with the Green's function adapted from Eq. 2.23:

$$G_{N-U}(\alpha) = \frac{a}{M} \sum_{n=0}^{\infty} \left(1 + k'_n - h'_n\right) P_n(\cos\alpha). \tag{2.77}$$

The reference system associated with the degree 1 load Love numbers can be chosen freely here, since the combination $(1 + k'_n - h'_n)$ is frame independent (i.e. the isomorphic frame parameter from Sec. 2.3.6 cancels out).

The ocean function,

$$O(\theta, \lambda) = \begin{cases} 1, & ocean \\ 0, & elsewhere \end{cases}, \tag{2.78}$$

projects a function onto the ocean region.

The final term $\Delta\phi/g$, has already been explained above, and ensures mass conservation globally. The second term, containing Λ_{N-U}, represents the effect of the rotational feedback (see Sec. 2.4.3 for the computation of this term).

Principle of self consistent sea level

Surface loaded with ice shield

After unloading
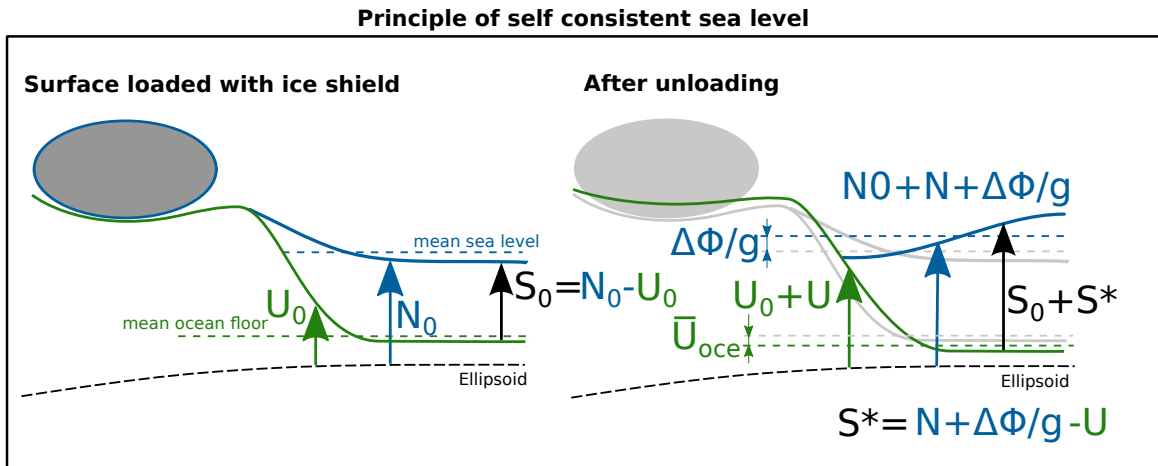
Figure 2.5: Schematic representation of the self consistent sea level. After the disappearance of a continental surface load, several effects can be seen. (1) The changed surface load changes the deformation of the solid Earth. (2) The mean sea surface adapts to a new equipotential surface. (3) The potential value of this surface differs from that of the geoid by $\Delta\phi$, since melt water changes the overall ocean mass. (4) The volumetric change of the ocean basin $\bar{U}_{oce}$ corresponds to the offset between the geocentric (relative to an ellipsoid) global mean sea level, and the relative (to the crust) global mean sea level.
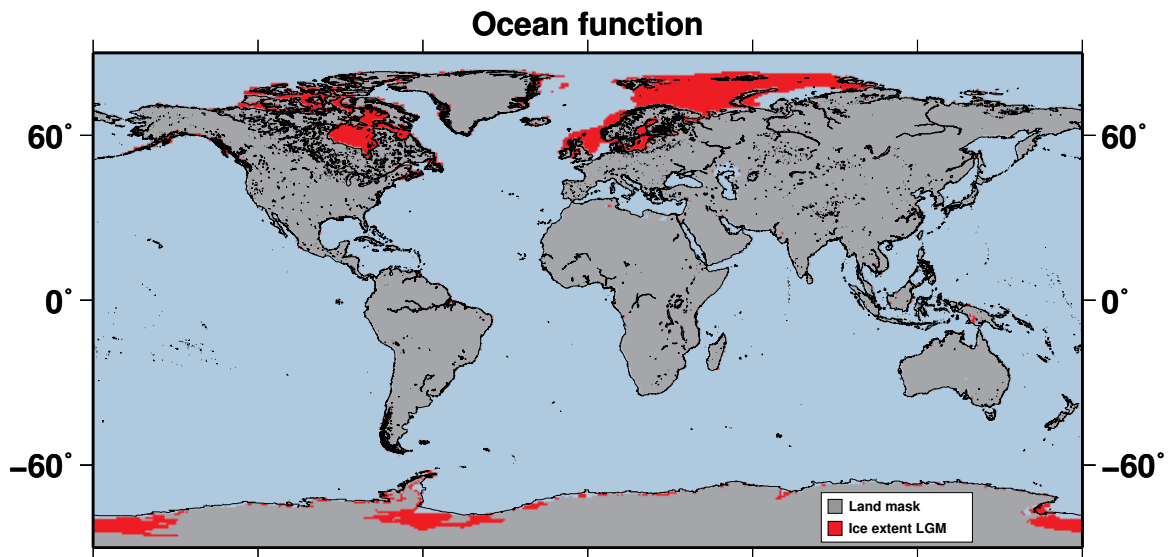
Ocean function

Figure 2.6: The present day ocean function is determined by the coastline and the grounding line of marine terminating glaciers. In particular in Antarctica there is an appreciable difference between the grounding line and the sea shelf extent (black line). Furthermore, during the last glacial maximum (LGM), significant differences can be noted in the former glaciated regions. (Ocean functions courtesy of Wouter vd. Wal.)

As can be noted, S, occurs at both sides of the equality sign. In practice, this implies that one either solves the equation for S, or one uses an iterative procedure to converge to the correct S. In the next section, the sea level is solved explicitly.

2.4.2 Spectral Solution of the SLE without Rotational Feedback

The variables of the SLE can be approximated by a (truncated) spherical harmonic expansion:

$$S(\theta, \lambda) = \sum_{n=0}^{N_{max}} \sum_{m=-n}^{n} S_{nm} \bar{Y}_{nm}(\theta, \lambda),$$

$$H(\theta, \lambda) = \sum_{n=0}^{N_{max}} \sum_{m=-n}^{n} H_{nm} \bar{Y}_{nm}(\theta, \lambda),$$

$$aT_{nm} = H_{nm} + S_{nm}. \tag{2.79}$$

H_{nm}, S_{nm} are given in meter of equivalent water height, whereas the T_{nm} is dimensionless and multiplied by the Earth's radius, a, in order to be consistent with the previous sections.

To simplify the formulation of the SLE, the so-called quasi-spectral Sea level, $\tilde{S}$, is introduced (Blewitt and Clarke, 2003). The quasi-spectral sea level is a band-limited quantity which is related to S according to

$$S(\theta, \lambda) = O(\theta, \lambda)\tilde{S}(\theta, \lambda), \tag{2.80}$$

$$\tilde{S}(\theta, \lambda) = \sum_{n=0}^{N_{max}} \sum_{m=-n}^{n} \tilde{S}_{nm} \bar{Y}_{nm}(\theta, \lambda).$$

When expressed as a truncated spherical harmonic series, $\tilde{S}$ is significantly smoother than S, which suffers from truncation effects at the discontinuous change at the coastline. $\tilde{S}$ is therefore much more suitable to represent an *equipotential surface*. However, since its value over land is far from zero, $\tilde{S}$, cannot be used to represent the actual *surface load*, for which S should be used. Only in the limit, $N_{max} \to \infty$, the two will coincide with each other over the ocean.

In appendix B, it is shown that Eq. 2.80 can be written as a matrix-vector multiplication in the spectral domain, when $\tilde{S}$ is truncated at N_{max}. The spherical harmonic coefficients of the ocean function, O_{nm}, will be used as input for the 'product to sum' matrix **O** (see App. B for the computation of this matrix). This allows the following matrix notation for the relation of the Quasi-spectral sea level:

$$\mathbf{s} = \mathbf{O}\tilde{\mathbf{s}}. \tag{2.81}$$

Above and in the following discussion, the spherical harmonic coefficients are stacked in vectors of the form,

$$\mathbf{s}^T = \begin{bmatrix} S_{00} & \cdots & S_{nm} \end{bmatrix},$$
$$\tilde{\mathbf{s}}^T = \begin{bmatrix} \tilde{S}_{00} & \cdots & \tilde{S}_{nm} \end{bmatrix}, \tag{2.82}$$
$$\mathbf{o}^T = \begin{bmatrix} O_{00} & \cdots & O_{nm} \end{bmatrix}.$$

The sea level equation can now be written in matrix form

$$\mathbf{P}\tilde{\mathbf{s}} = \mathbf{G}_{N-U}(\mathbf{s} + \mathbf{h}) = \mathbf{G}_{N-U}(\mathbf{O}\tilde{\mathbf{s}} + \mathbf{h}), \quad n > 0. \tag{2.83}$$

Where the projection matrix $\mathbf{P}$ sets the degree 0 coefficients to zero,

$$\mathbf{P} = \left[\begin{array}{c|cccc} 0 & 0 & \cdots & 0 \\ \hline 0 & 1 & \cdots & 0 \\ \vdots & \vdots & \ddots & \vdots \\ 0 & 0 & \cdots & 1 \end{array} \right]. \tag{2.84}$$

Furthermore, the diagonal matrix $\mathbf{G}_{N-U}$ contains the entries from the Green's functions in the spectral domain:

$$\mathbf{G}_{N-U} = \left[\begin{array}{c|cccc} 1 & 0 & \cdots & 0 \\ \hline 0 & \frac{\rho_w}{\rho_e}(1 + k_1' - h_1') & \cdots & 0 \\ \vdots & \vdots & \ddots & \vdots \\ 0 & 0 & \cdots & \frac{3\rho_w}{\rho_e}\frac{1+k_N'-h_N'}{2N+1} \end{array} \right]. \tag{2.85}$$

The entry for degree 0, initially undefined, has been set to 1 here, which will turn out to be convenient for enforcing mass conservation.

The conservation of mass of the system namely requires that

$$0 = S_{00} + H_{00} = \int_\Omega O(\theta, \lambda)\tilde{S}(\theta, \lambda)d\omega + H_{00}. \tag{2.86}$$

In the spectral domain, the integral may be solved using the orthogonality property from Eq. 2.6, resulting in the inner product of the coefficient vector $\tilde{\mathbf{s}}$ and the equivalent vector $\mathbf{o}$

$$\int_\Omega O(\theta, \lambda)\tilde{S}(\theta, \lambda)d\omega = \mathbf{o}^T\tilde{\mathbf{s}}. \tag{2.87}$$

The quasi-spectral sea level in Eq. 2.83 is now taken to the left hand side of the equation

$$[\mathbf{P} - \mathbf{G}_{N-U}\mathbf{O}]\tilde{\mathbf{s}} = \mathbf{G}_{N-U}\mathbf{h}. \tag{2.88}$$

It can be seen that the mass conservation requirement is fulfilled, by writing the first row of the equation explicitly as:

$$\begin{aligned} -[\mathbf{O}]_{1^{st}row}\tilde{\mathbf{s}} &= H_{00} \\ -\mathbf{o}^T\tilde{\mathbf{s}} &= -S_{00} = H_{00}. \end{aligned} \tag{2.89}$$

The conservation of mass is now automatically fulfilled since the first row of the matrix $\mathbf{O}$ is nothing more than the transposed vector of the ocean basin coefficients, $\mathbf{o}^T$.

The quasi-spectral sea level may now be obtained by inversion:

$$\tilde{\mathbf{s}} = \mathbf{G}_{\tilde{S}}\mathbf{G}_{N-U}\mathbf{h}, \tag{2.90}$$

where,

$$\mathbf{G}_{\tilde{S}} = [\mathbf{P} - \mathbf{G}_{N-U}\mathbf{O}]^{-1}. \tag{2.91}$$

The inversion to obtain matrix $\mathbf{G}_{\bar{s}}$ is very stable, associated with typical condition numbers of around 4 (for inversions up to degree and order 180). Alternatively, as is commonly found in literature (see Spada and Stocchi, 2007 for a detailed review), the sea level equation is solved iteratively within just a few iterations in a pseudo-spectral sense, which also hints at the stability of the SLE . The term pseudo-spectral means that the product to sum operation of matrix $\mathbf{O}$ is replaced by a spherical harmonic synthesis on a suitable grid [5], followed by a projection on the ocean nodes, which is then followed by a spherical harmonic analysis to obtain the coefficients of the relative sea level $\mathbf{s}$.

2.4.3 Solution of the SLE with Rotational Feedback

Eq. 2.76 also contains a term representing the rotational feedback mechanism. A changing surface load will generally induce a change in the Earth's moment of inertia tensor. Consequently, the rotational axis of the Earth will move away from its initial position. The rotational axis of the Earth is now misaligned with the z-axis of the reference system, which will induce a small anomalous rotational potential. This potential can be considered as a tidal load acting on the Earth, deforming it and inducing a change in the geoid. The mechanism above may be linearized w.r.t. the surface load for small changes, such as considered in this work. The linearization allows a spectral inversion which is very similar to that found in the previous section.

The Euler-Liouville equations may be linearized by assuming that the Earth's rotational axis, ω, is perturbed by a small disturbance m_1, m_2, m_3 and that the Earth's inertial tensor, $\mathbf{J}$, deviates only slightly from a perfectly aligned ellipsoid (Munk and MacDonald, 1960)

$$\omega = \Omega_E \begin{bmatrix} m_1 \\ m_2 \\ 1 + m_3 \end{bmatrix}, \tag{2.92}$$

$$\mathbf{J} = \begin{bmatrix} A & 0 & 0 \\ 0 & A & 0 \\ 0 & 0 & C \end{bmatrix} + \begin{bmatrix} \delta J_{11} & \delta J_{12} & \delta J_{13} \\ \delta J_{12} & \delta J_{22} & \delta J_{23} \\ \delta J_{13} & \delta J_{23} & \delta J_{33} \end{bmatrix}. \tag{2.93}$$

Here, Ω is the mean rotational speed of the Earth, and A and C are the Earth's principal moments of inertia.

In fact, only the components δJ_{13}, δJ_{23} and δJ_{33}, will occur in the first order terms of the linearized Euler-Liouville equations. These changes in moment of inertia may be induced by a change in surface density. For a spherical layer with density $\sigma(\theta, \lambda)$ one can write for δJ_{i3}:

$$\delta J_{13} = \int_\Omega -xz\sigma(\theta, \lambda)a^2 d\omega,$$

$$\delta J_{23} = \int_\Omega -yz\sigma(\theta, \lambda)a^2 d\omega, \tag{2.94}$$

$$\delta J_{33} = \int_\Omega \left(x^2 + y^2\right)\sigma(\theta, \lambda)a^2 d\omega.$$

---

[5]A certain arbitrariness remains in the choice of a suitable grid. There is no unique choice of resolution and geometry of the grid, such that the procedure might result in slightly different results.

Substituting Eq. 2.12 and observing that:

$$xz = a^2 \cos\lambda \sin\theta \cos\theta = a^2 \frac{\bar{Y}_{21}(\theta,\lambda)}{\sqrt{15}},$$

$$yz = a^2 \sin\lambda \sin\theta \cos\theta = a^2 \frac{\bar{Y}_{2-1}(\theta,\lambda)}{\sqrt{15}}, \tag{2.95}$$

$$x^2 + y^2 = a^2 \sin^2\theta = a^2 \frac{2}{3}\left(\bar{Y}_{00}(\theta,\lambda) - \frac{\bar{Y}_{20}(\theta,\lambda)}{\sqrt{5}}\right).$$

One can use the orthogonality relation 2.6 together with Eq. 2.79 to write the relevant terms as a matrix vector multiplication:

$$
\begin{bmatrix} \delta J_{13} \\ \delta J_{23} \\ \delta J_{33} \end{bmatrix} = \pi a^4 \rho_w
\begin{bmatrix} 0 & 0 & -\frac{4}{\sqrt{15}} & 0 \\ 0 & 0 & 0 & -\frac{4}{\sqrt{15}} \\ \frac{8}{3} & -\frac{8}{3\sqrt{5}} & 0 & 0 \end{bmatrix}
\begin{bmatrix} aT_{00} \\ aT_{20} \\ aT_{21} \\ aT_{2-1} \end{bmatrix}
$$

$$
= \Psi_{J\leftarrow T}
\begin{bmatrix} H_{00} + S_{00} \\ H_{20} + S_{20} \\ H_{21} + S_{21} \\ H_{2-1} + S_{2-1} \end{bmatrix}. \tag{2.96}
$$

Considering the normalizations used, this is consistent with the results obtained in Wu and Peltier (1984) and Milne and Mitrovica (1998), except that the latter would require the application of the Condon-Shortley phase, $(-1)^m$, to fix the signs for the order 1 coefficients.

For an elastic Earth, the linearized Euler-Liouville equations relate the changes in polar motion to the changed inertial tensor (Peltier and Luthcke, 2009; Nakada and Okuno, 2003; Mitrovica et al., 2005):

$$
\begin{bmatrix} m_1 \\ m_2 \\ m_3 \end{bmatrix} =
\begin{bmatrix} \Omega_E \frac{1+k_2'}{A\sigma_0} & 0 & 0 \\ 0 & \Omega_E \frac{1+k_2'}{A\sigma_0} & 0 \\ 0 & 0 & -\frac{1+k_2'}{C} \end{bmatrix}
\begin{bmatrix} \delta J_{13} \\ \delta J_{23} \\ \delta J_{33} \end{bmatrix}
= \Gamma_{m\leftarrow J}
\begin{bmatrix} \delta J_{13} \\ \delta J_{23} \\ \delta J_{33} \end{bmatrix}. \tag{2.97}
$$

Where, σ_0 is the Chandler frequency. It must be noted however, that the expression holds only for slowly varying phenomena (e.g. secular changes and phenomena which have periods longer than the Chandler wobble). To account for quicker phenomena, one would need to either apply the non-linear theory, or to correct the results using observed Earth orientation parameters.

As mentioned before, the motion of the pole will induce a change in the centrifugal potential. In the initial state, the rotation axis is perfectly aligned with the z axis such that one may use Eq. 2.7 and write it as:

$$\Lambda(\theta) = \frac{\Omega_E^2 a^2}{2} \sin^2\theta = \frac{\Omega_E^2 a^2}{3}\left(1 - P_2(\cos\theta)\right). \tag{2.98}$$

In the new situation, this potential, $\Lambda'(\theta, \lambda)$, has now a new rotation axis, $\boldsymbol{\omega}$, while the reference system remains fixed. Substituting Eq. 2.92 and applying the addition theorem we may write for the potential difference:

$$
\begin{aligned}
\delta\Lambda(\theta, \lambda) &= \Lambda(\theta) - \Lambda'(\theta, \lambda) \\
&= \frac{\Omega_E^2 a^2}{3}\left(1 - P_2(\cos\theta)\right) - \frac{|\boldsymbol{\omega}^2|a^2}{3}\left(1 - \frac{1}{5}\sum_{m=-2}^{2}\bar{Y}_{2m}(\theta, \lambda)\bar{Y}_{2m}(\theta', \lambda')\right).
\end{aligned}
\tag{2.99}
$$

Where,

$$
\lambda' = \arctan\left(\frac{m_2}{m_1}\right), \quad \theta' = \arctan\left(\frac{\sqrt{m_1^2 + m_2^2}}{m_3}\right),
\tag{2.100}
$$

indicate the position of the new rotation axis. For small perturbations of m_i only the first order terms need to be accounted for, such that:

$$
\begin{bmatrix} \delta\Lambda_{00} \\ \delta\Lambda_{20} \\ \delta\Lambda_{21} \\ \delta\Lambda_{2-1} \end{bmatrix} \approx (a\Omega_E)^2 \begin{bmatrix} 0 & 0 & \frac{2}{3} \\ 0 & 0 & -\frac{2}{3\sqrt{5}} \\ -\frac{1}{\sqrt{15}} & 0 & 0 \\ 0 & -\frac{1}{\sqrt{15}} & 0 \end{bmatrix} \begin{bmatrix} m_1 \\ m_2 \\ m_3 \end{bmatrix} = \Phi_{\Lambda\leftarrow m}\begin{bmatrix} m_1 \\ m_2 \\ m_3 \end{bmatrix}.
\tag{2.101}
$$

The change in potential acts on the Earth as a tidal load, which will deform the Earth and induces geoid changes. The associated geoid height changes minus the vertical deformation can also be computed using a Love number formalism. So the contribution of the rotational feedback to the Quasi-spectral sea level is limited to a subset of coefficients and may be written as:

$$
\begin{bmatrix} \tilde{S}_{20} \\ \tilde{S}_{21} \\ \tilde{S}_{2-1} \end{bmatrix}_{rot} = \frac{1 + k_2 - h_2}{g}\begin{bmatrix} 0 & 1 & 0 & 0 \\ 0 & 0 & 1 & 0 \\ 0 & 0 & 0 & 1 \end{bmatrix}\begin{bmatrix} \delta\Lambda_{00} \\ \delta\Lambda_{20} \\ \delta\Lambda_{21} \\ \delta\Lambda_{2-1} \end{bmatrix} = \mathbf{T}_{\tilde{S}\leftarrow\Lambda}\begin{bmatrix} \delta\Lambda_{00} \\ \delta\Lambda_{20} \\ \delta\Lambda_{21} \\ \delta\Lambda_{2-1} \end{bmatrix}.
\tag{2.102}
$$

In contrast to the load Love numbers, k_2 and h_2 are denoted as 'body Love numbers' and are computed by applying a unit load on an Earth model, which does not exert surface pressure on the Earth. The degree 0 component is small and has been removed in order to ensure mass conservation in the system. From the three coefficients affected, $\tilde{S}_{21}$ and $\tilde{S}_{2-1}$ are the most dominant, as variations in m_1 and m_2 are relatively large.

The extra term may now be added to the Sea Level Equation (Eq. 2.90):

$$
\mathbf{P}\tilde{\mathbf{s}} = \left(\mathbf{G}_{N-U} + \Xi_{N-U}\right)\left(\mathbf{O}\tilde{\mathbf{s}} + \mathbf{h}\right).
\tag{2.103}
$$

Where the (3 x 4) matrix Ξ_{N-U} contains the rotational feedback mechanism as described above:

$$
\Xi_{N-U} = \left[T_{S\leftarrow\Lambda}\Phi_{\Lambda\leftarrow m}\Gamma_{m\leftarrow J}\Psi_{J\leftarrow T}\right].
\tag{2.104}
$$

The quasi-spectral sea level can be solved similarly as in the previous section:

$$
\tilde{\mathbf{s}} = \mathbf{G}_{\tilde{S}}^{\dagger}\left(\mathbf{G}_{N-U} + \Xi_{N-U}\right)\mathbf{h},
\tag{2.105}
$$

where one can explicitly solve the matrix

$$
\mathbf{G}_{\tilde{S}}^{\dagger} = \left[\mathbf{P} - \left(\mathbf{G}_{N-U} + \Xi_{N-U}\right)\mathbf{O}\right]^{-1}.
\tag{2.106}
$$

2.4.4 Sea Level Equation on a Visco-elastic Earth

The theory of the sea level equation has a long history in the study of Glacial Isostatic Adjustment (GIA) problems where a visco-elastic Earth model is subjected to a loading history of glacial ice masses. At each time step, the ocean response to the present and past ice loading is computed using the sea level equation. In this section I show that the solution of the SLE for visco-elastic problems is very similar to the elastic case, except that an additional forcing vector, depending on the variations in the past, is added. The theory on post-glacial sea level with moving shorelines has been extensively described in for example Mitrovica and Milne (2003); Kendall et al. (2005). Here, the aim is to provide a description in the spectral domain following matrix notation, for the case of a Heaviside loading history, using time dependent Love numbers.

As introduced in Sec. 2.3.7, the time history of the load and the sea level may be discretized with Heaviside increments. In matrix notation this can be written as:

$$\mathbf{I}^*(t_j) = \mathbf{I}_j^* = \sum_{i=0}^{j} \mathbf{I}_i^* - \mathbf{I}_{i-1}^* = \sum_{i=0}^{j} \Delta \mathbf{I}_i^*, \tag{2.107}$$

$$\mathbf{h}^*(t_j) = \mathbf{h}_j^* = \sum_{i=0}^{j} \mathbf{h}_i^* - \mathbf{h}_{i-1}^* = \sum_{i=0}^{j} \Delta \mathbf{h}_i^* = \frac{\rho_{ice}}{\rho_w} \mathbf{I}_j^*, \tag{2.108}$$

$$\mathbf{s}^*(t_j) = \mathbf{s}_j^* = \sum_{i=0}^{j} \mathbf{s}_i^* - \mathbf{s}_{i-1}^* = \sum_{i=0}^{j} \Delta \mathbf{s}_i^*, \tag{2.109}$$

$$\widetilde{\mathbf{s}}^*(t_j) = \widetilde{\mathbf{s}}_j^* = \sum_{i=0}^{j} \widetilde{\mathbf{s}}_i^* - \widetilde{\mathbf{s}}_{i-1}^* = \sum_{i=0}^{j} \Delta \widetilde{\mathbf{s}}_i^*. \tag{2.110}$$

Similar to the previous section, the vectors contain the stacked spherical harmonic coefficients of sea level($\mathbf{s}^*$,$\widetilde{\mathbf{s}}^*$), uplift($\mathbf{h}^*$) and additionally the metric ice thickness of the glacial ice sheet, $\mathbf{I}^*$.

To convolve a load in the time domain, the time offset between the loading epoch,t', and the present time, t is now introduced into the loading Green's functions:

$$\mathbf{G}_{N-U}^*(t - t') = \begin{bmatrix} 1 & 0 & \cdots & 0 \\ \hline 0 & \frac{\rho_w}{\rho_e}\left(1 + k_1'(t-t') - h_1'(t-t')\right) & \cdots & 0 \\ \vdots & \vdots & \ddots & \vdots \\ 0 & 0 & \cdots & \frac{3\rho_w}{\rho_e} \frac{1 + k_N'(t-t') - h_N'(t-t')}{2N+1} \end{bmatrix}. \tag{2.111}$$

In the elastic limit, when $t \to t'$, the matrix converges to $\mathbf{G}_{N-U}$.

Using the time dependent Green's functions, the sea level equation can be written as:

$$\mathbf{P}\widetilde{\mathbf{s}}_j = \sum_{i=0}^{j} \mathbf{G}_{N-U}^*(t_j - t_i) \left(\frac{\rho_{ice}}{\rho_w} \Delta \mathbf{I}_i + \Delta \mathbf{s}_i \right). \tag{2.112}$$

Where the Heaviside loading history is accounted for by the cumulative sum up to index

j. The increment $\Delta\tilde{\mathbf{s}}_j = \tilde{\mathbf{s}}_j - \tilde{\mathbf{s}}_{j-1}$ can now be written as:

$$
\begin{aligned}
\mathbf{P}\Delta\tilde{\mathbf{s}}_j =& \mathbf{G}^*_{N-U}(0)\left(\frac{\rho_{ice}}{\rho_w}\Delta\mathbf{I}_j + \Delta\mathbf{s}_j\right) \\
&+ \sum_{i=0}^{j-1}\left(\mathbf{G}^*_{N-U}(t_j - t_i) - \mathbf{G}^*_{N-U}(t_{j-1} - t_i)\right)\left(\frac{\rho_{ice}}{\rho_w}\Delta\mathbf{I}_i + \Delta\mathbf{s}_i\right).
\end{aligned}
\tag{2.113}
$$

Furthermore, when considering that

$$
\mathbf{s}_j = \mathbf{O}_j\tilde{\mathbf{s}}_j,
\tag{2.114}
$$

the increment of the relative sea level can be written as:

$$
\begin{aligned}
\Delta\mathbf{s}_j =& \mathbf{O}_j\sum_{i=0}^{j}\Delta\tilde{\mathbf{s}}_i - \mathbf{O}_{j-1}\sum_{i=0}^{j-1}\Delta\tilde{\mathbf{s}}_i \\
& \mathbf{O}_j\Delta\tilde{\mathbf{s}}_j + \left(\mathbf{O}_j - \mathbf{O}_{j-1}\right)\tilde{\mathbf{s}}_{j-1}.
\end{aligned}
\tag{2.115}
$$

The last term represents the phenomena that a moving shoreline alone will also induce a sea level change by displacing the ocean mass (see Mitrovica and Milne (2003); Kendall et al. (2005)). Substituting the $\Delta\mathbf{s}_j$ in the first term of the sea level equation yields:

$$
\mathbf{P}\Delta\tilde{\mathbf{s}}_j = \mathbf{G}_{N-U}\left(\frac{\rho_{ice}}{\rho_w}\Delta\mathbf{I}_j + \mathbf{O}_j\Delta\tilde{\mathbf{s}}_j\right) + \mathcal{F}.
\tag{2.116}
$$

Where the vector $\mathcal{F}$ is dependent on the load from the previous steps only:

$$
\mathcal{F} = \left(\mathbf{O}_j - \mathbf{O}_{j-1}\right)\tilde{\mathbf{s}}_{j-1} + \sum_{i=0}^{j-1}\left(\mathbf{G}^*_{N-U}(t_j - t_i) - \mathbf{G}^*_{N-U}(t_{j-1} - t_i)\right)\left(\frac{\rho_{ice}}{\rho_w}\Delta\mathbf{I}_i + \Delta\mathbf{s}_i\right).
\tag{2.117}
$$

Separating the quasi spectral sea level yields

$$
\Delta\tilde{\mathbf{s}}_j = \mathbf{G}_{\tilde{s}j}\left(\mathbf{G}_{N-U}\frac{\rho_{ice}}{\rho_w}\Delta\mathbf{I}_j + \mathcal{F}\right),
\tag{2.118}
$$

with the matrix

$$
\mathbf{G}_{\tilde{s}j} = \left[\mathbf{P} - \mathbf{G}_{N-U}\mathbf{O}_j\right]^{-1}.
\tag{2.119}
$$

The ocean function above, has actually varied significantly over the time from the last glacial maximum until now (see Fig. 2.6). More specifically, the shorelines migrate due to changes in the relative sea level themselves. This issue manifests itself as a feedback in Eq. 2.118, prohibiting a direct solution. A way out of this caveat is to use an iterative approach, where an initial ocean function is updated after each loading cycle, until the negated total present day sea level agrees with a given present day topography: $-\tilde{\mathbf{s}}(t_p) = T(t_p)$ (see Kendall et al., 2005 for an elaborate discussion).

The effect of rotational feedback has been left out of the discussion. In the time domain, a linear relation between the inertia perturbations and the polar motion exist when the Love numbers are described by a finite set of normal modes, and the linearized Euler-Liouville equations are applied (see for example Wu and Peltier (1984)). However, for continuous

viscosity/rigidity profiles and/or a compressible Earth one generally needs to convolve the loading history with the Love numbers in the Laplace domain, and consequently apply an inverse Laplace transform (see Cambiotti et al., 2010 for a thorough discussion on this topic). Although this is an interesting and ongoing topic in science, a proper treatment with the time dependent Love number formalism would be laborious and out of the current scope as it would introduce non-linearities in the sea level equation.

2.4.5 Sea Level Equation with other Forcings

For completeness it is mentioned here that the elastic solutions for the sea level equation may be slightly adapted to incorporate other forcings. For example, the computation of the equilibrium ocean pole tide (Desai, 2002) may be constructed by fixing the polar motion, m_i to prescribed (i.e. measured Earth Orientation Parameters) values, while fixing $\mathbf{h} = 0$. Resulting in

$$\tilde{\mathbf{s}} = [\mathbf{G}_{\tilde{S}}] \, T_{\tilde{S} \leftarrow \Lambda} \Phi_{\Lambda \leftarrow m} \begin{bmatrix} m_1 \\ m_2 \\ m_3 \end{bmatrix} \tag{2.120}$$

In a different problem, the self consistent sea level response may be computed when geoid and uplift changes induced by Earthquakes are used as a forcing (Melini et al., 2010).

2.5 Steric Sea Level

Apart from the mass related sea level, changes in temperature and salinity do also effect the change the column height without changing the net mass. These so-called steric effects have the same order of magnitude as the mass induced changes and play a vital role in understanding ocean circulation and global changes. In particular, steric sea level change is related to changes in the ocean heat content, linking the Earth's radiation imbalance directly to sea level change. It is therefore not surprising that the separation of the steric part from the mass induced part is an important goal of this thesis. In a nutshell, separation of those components may be achieved when gravity (mass) related measurements, such as those from GRACE, are combined with geometrical measurements of the sea level, such as those from altimetry and tide gauges.

Consider a column of sea water. Measured from the ocean floor, its height depends on the net mass flux into the column. Additionally, the warming of the water column, will cause an expansion or equivalently a density decrease. Another effect is caused by changes in salinity. The removal of salt from the column will cause a density decrease and is therefore associated with a volumetric expansion.

The steric height change, h_{steric}, relative to a reference sea water column, can be obtained from integrating the density anomalies, ρ, from the bottom, H up to the sea surface:

$$h_{steric}(t) = \int_{-H}^{0} \frac{\rho_0(T_0, S_0, p(z)) - \rho(T, S, p(z), t)}{\rho_0(T_0, S_0, p(z))} dz. \tag{2.121}$$

The nonlinear relation between the density, ρ, temperature, T, salinity, S, and pressure, $p(z)$, is called the equation of state for sea water (Gill, 1982), and is determined empirically. The subscript '0', denotes the reference density for 'standard sea water'. Under good approximation, one may separate the steric sea level in a thermo-steric and a halo-steric component (Landerer et al., 2007):

$$
\begin{aligned}
h_{steric}(t) \approx & \int_{-H}^{0} \frac{\rho_0(T_0, S_0, p(z)) - \rho(T, S_0, p(z), t)}{\rho_0(T_0, S_0, p(z))} dz + \\
& \int_{-H}^{0} \frac{\rho_0(T_0, S_0, p(z)) - \rho(T_0, S, p(z), t)}{\rho_0(T_0, S_0, p(z))} dz.
\end{aligned}
\tag{2.122}
$$

3 Observations

Within this work, observations from several geodetic measurement techniques are used. This chapter describes the relevant observations and its characteristics. In combination with chapter 2, the following sections provide the implementation basis of the thesis work.

3.1 GRACE Gravimetry

With the launch of the satellite twin mission GRACE in March 2002, unprecedented global gravity field solutions became available every month. Several processing centers, GFZ, CSR, JPL, and GRGS publish new Stokes coefficients on a regular basis. Furthermore, alternative GRACE solutions have been published based on different processing techniques, e.g. using shorter processing arcs (Mayer-Gürr et al., 2006) and Kalman filtering techniques to obtain daily solutions (Kurtenbach et al., 2009).

GRACE measurement principle
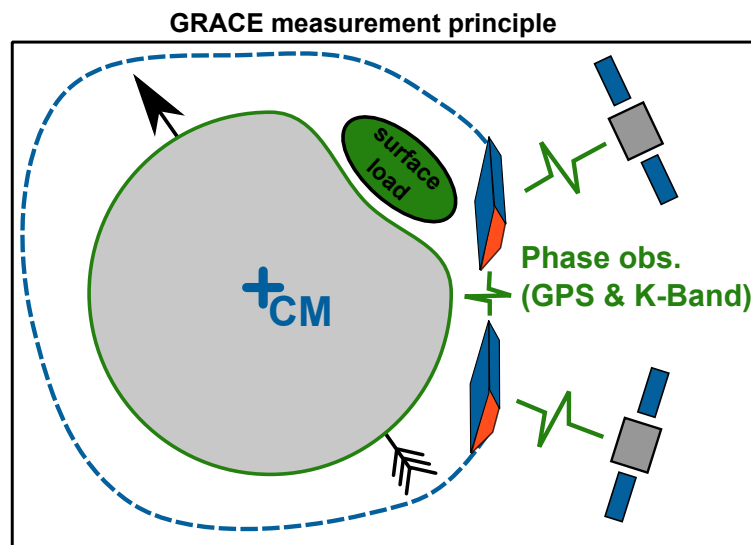
Figure 3.1: GRACE measurement principle. Changes in the gravity field induce minute orbit perturbations of the GRACE twin satellites. The inter-satellite distance is accurately measured with the K-band instrument. At the same time the orbit is tracked using GPS observations.

The primary observation of GRACE is a highly accurate measurement of the inter-satellite range (rate). This is obtained from the K-band ranging instrument, with an accuracy in the order of $1\,\mu\mathrm{m/s}$. Furthermore, the GRACE satellites are positioned using GPS measurements from the on-board receivers. (see Fig. 3.1). On a regular basis, direct laser tracking observations to the satellites retro-reflector are obtained, although these are mainly used as a validation dataset (Schmidt et al., 2008).

Since the earliest solutions, many improvements have been made to the processing standards, which are reflected in the consequent releases. As of 2013, the fifth release is the most up to date. The largest reduction in errors over the previous release is achieved by

the use of better background models (see Tab. 3.1).

Background model	Release 04	Release 05
Ocean	OMCT (Dobslaw and Thomas, 2007a)	OMCT2011 (Dobslaw et al., 2013)
Atmosphere	ECMWF	ECMWF
Static gravity field	EIGEN-GL04C	EIGEN-6C
Time variable gravity	-	EIGEN-6C (trend, seas. harm.)
solid Earth Tides	IERS2003	IERS2010
Pole tide	IERS2003	IERS2010
Ocean pole tide	Desai (2002)	Desai (2002)
Ocean tides	FES2004(Lyard et al., 2006)	EOT11a (Savcenko and Bosch, 2012)
Atmospheric tides	Biancale and Bode (2006)	Biancale and Bode (2006)

Table 3.1: Background models used in the GRACE processing of the GFZ release 4 and 5.

The use of the atmospheric and ocean background models, remove a significant amount of high-frequency signal from the measurements. Nevertheless, the models are not perfect, and the discrepancies induce still spurious errors in the solutions, known as temporal aliasing. These effects can be mitigated by applying a filtering step to the solutions (e.g. Kusche et al. (2009)). An unavoidable side-effect is that the filters also reduce the signal contents. For studies of ocean mass variations and atmospheric effects, one needs to restore the modeled signal content which has been removed during the processing. For this means, GFZ also provides monthly (and weekly) averages of the (de-aliasing) models, which may be added back by the user.

In this thesis, weekly and monthly GRACE-derived Stokes coefficients and their full error-covariance are used from the GFZ release 04 and 05. To be more specific, GFZ has made these data available in binary form as (unsolved/unfiltered) normal equation systems, which are then further processed in the framework of this thesis. GRACE specific nuisance parameters (e.g. accelerometer biases), are implicitly solved for using the method from App. C.2.

The GFZ processing center also provides a calibrated diagonal error-covariance matrix computed according to Schmidt et al. (2007b). It is derived from applying degree-wise rescaling factors to the formal GRACE errors. This procedure allows a correction of the formal errors which are likely too optimistic at low degrees. In an earlier stage of the thesis work, I used calibrated normal equation systems in the joint inversions computed according to Rietbroek et al. (2009):

$$\mathbf{N}_{cal} = \mathbf{D}^{-1}\mathbf{N}\mathbf{D}^{-1},$$
$$\mathbf{b}_{cal} = \mathbf{D}^{-1}\mathbf{N}\mathbf{D}^{-1}\hat{\mathbf{x}},$$
$$[\mathbf{l}_0^T\mathbf{P}\mathbf{l}_0]_{cal} = \hat{\mathbf{x}}^T\mathbf{D}^{-1}\mathbf{N}\mathbf{D}^{-1}\hat{\mathbf{x}},$$
$$\hat{\mathbf{x}} = \mathbf{N}^{-1}\mathbf{b}.$$

(3.1)

Where the calibrated normal matrix and right hand side vector is denoted by $\mathbf{N}_{cal}$ and $\mathbf{b}_{cal}$. The diagonal matrix, $\mathbf{D}$, contains the calibration scales. Furthermore, the new a priori cost functional is denoted by $[\mathbf{l}_0^T \mathbf{P} \mathbf{l}_0]_{cal}$ (see also App. C). A disadvantage of the above calibration procedure is that it requires an intermediate solving step to obtain $\hat{\mathbf{x}}$. Consequently, this calibration procedure cannot be applied when the uncalibrated system has (near) rank defects.

Unfortunately, the GRACE measurement system is insensitive to degree 1 variations. A common application of the GRACE Stokes coefficients is to compute surface loading variations using the inverse of Eq. 2.36. The degree 1 surface loading coefficients are thus described by:

$$T_{1m} = \frac{1}{1 + k_1'^{CM}} \frac{\rho_e}{\rho_w} \delta C_{1m} = \frac{1}{0} \frac{\rho_e}{\rho_w} \delta C_{1m}. \tag{3.2}$$

In the CM reference frame, the degree 1 load Love number $k_1'^{CM} = -1$, making the equation singular, and the value of T_{1m} can obtain *any* value. The degree 1 surface loading must therefore be constrained by the addition of external data, such as is performed in this thesis.

3.2 Sea Surface Height and Ocean Bottom Pressure

3.2.1 Radar Altimetry

A radar altimeter essentially measures the round trip time of a radar pulse emitted from the satellite which is then reflected by the sea surface. Additionally, tracking techniques such as DORIS and GPS , are used in determining a precise orbit of the satellite. The principle product are sea surface heights (h_{ssh}), which represent the height of the sea surface relative to a chosen ellipsoid. h_{ssh} is derived from the measured range, the orbit and from a suite of instrumental and geophysical corrections (See Fig 3.2 and Table 3.2)

$$h_{ssh} = h_{orbit} - h_{range} + \sum_i h_{corr,i}. \tag{3.3}$$

In this work, along track Jason-1 and Jason-2 data from the Open Altimeter Database are used (Schwatke et al., 2010). The along track data have been gathered in mean along-track bins, with a length of about 5.8 km. Since the locations of these bins do not change over time, an advantage exists when setting up normal equations. The data have been corrected with the usual instrument errors and the EOT11a tidal model (Savcenko and Bosch, 2012). Furthermore, radial orbit errors have been estimated and corrected for by applying a multi-mission crossover analysis (Bosch and Savcenko, 2007). The dynamic atmosphere correction comes from the MOG2D model (Carrère and Lyard, 2003). A mean sea surface height model (Rio and Hernandez, 2004) is also subtracted and provided at the locations of the bins.

In this thesis, the time variable effects of sea level and gravity are jointly investigated. Therefore, the sea level anomalies (sea surface height relative to the mean sea surface, h_{mssh}) are decomposed as follows:

$$h_{ssh} - h_{mssh} = h_{IB} + h_{steric} + [\tilde{S} + U]_{elas} + [\tilde{S} + U]_{GIA} + h_{dyn}. \tag{3.4}$$

Figure 3.2: Radar altimetry measurement principle. The return trip of the radar pulse from the microwave altimeter, is a measure of the difference between the satellite and the sea surface. Additionally, to aid in the precise orbit determination, the satellites measures the signal emitted from the crust-fixed DORIS beacons (Doppler Orbitography and Radio-positioning Integrated by Satellite).
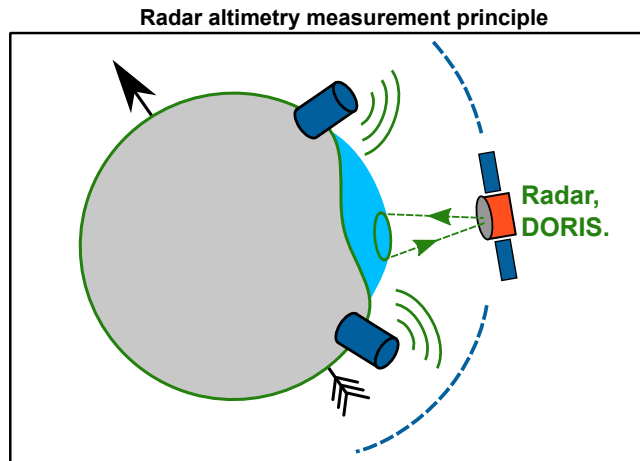
It should be stressed that the sea level anomaly, instead of the commonly used dynamic topography (sea surface height relative to a mean geoid) is decomposed here. The terms above will be elaborated upon in the following paragraphs.

Table 3.2: Altimetry corrections and associated order of magnitude. Values taken from (Rosmorduc et al., 2009; Fu and Cazenave, 2001)

Name	Magnitude
Instrument corrections	
Ultra-stable oscillator drift	1cm
Satellite center of gravity	sat. dep.
(Radial) orbit correction	few cm
Geophysical corrections	
Ocean tides	1-20 m
Solid Earth tides	50 cm
Ocean Pole tide	2 cm
Tidal loading	30 cm
Ionosphere	50 cm
Wet troposphere	50 cm
Dry troposphere	2.3 m
Surface corrections	
Dynamic Atmosphere correction	15 cm
Sea state bias	50 cm

Sea level response to atmospheric pressure

In Eq. 3.3, a high frequency dynamic atmosphere correction is included, to account for the quick ocean response to atmospheric forcing. On the time scales longer then 10 days, which are the representative scales of this work, the correction can be assumed to be a steady-state response which is commonly denoted as the Inverted Barometer (IB) response to atmospheric pressure, h_{IB}. Correcting the sea level anomalies with the IB response essentially adds the local atmospheric surface pressure as a column of sea water to the ocean surface:

$$h_{IB} = \frac{P_{atm} - P_{ref}}{g\rho_w}. \tag{3.5}$$

In the *modified* IB response, the reference pressure, P_{ref}, is taken to be the oceanic mean of the atmospheric pressure

$$P_{ref} = \frac{1}{A_{oce}} \int_{Oce} P_{atm} d\omega. \qquad (3.6)$$

The integral arises from the assumption that the ocean can be treated as incompressible w.r.t. atmospheric pressure variations, implying that only variations relative to the oceanic mean of the pressure field are relevant. The corrected sea level anomalies are less noisy, but now contain an atmospheric component. In contrast, GRACE data generally has its atmospheric component removed, such that care must be taken when combining altimetry with GRACE. This will be further discussed below.

Mass versus Steric Induced Variations

The volumetric sea level variations, h_{ster}, are induced by changes in temperature and salinity (see Sec. 2.5). These volume changes are visible in the sea level anomalies, but are not (directly) related to the mass changes. Since these changes do not induce ocean bottom pressure variations, they cannot be detected by GRACE. As such, the altimetric sea level anomalies are highly complementary to GRACE data.

Besides these volumetric effects, there are mass related changes in sea level (see Sec. 2.4), which originate from a changing continental surface load. Both the change in the loading distribution as well as the addition or removal of water from the ocean play a significant role here.

The orbit of a satellite altimeter is provided relative to a time-fixed reference frame (for example the TOPEX ellipsoid), such that deformations of the ocean floor will also be sensed by the altimeter. The observed sea surface change is commonly denoted as geocentric sea level change. This is essentially the variation of the geoid, with additional uniform layer changes in order to impose the conservation of mass. The term $[\tilde{S} + U]_{elas}$, thus represents the geocentric sea surface change due to elastic surface loading effects. In this thesis, these geocentric sea level variations are computed using the sea level equation as described in Sec. 2.4.1 to ensure a gravitationally consistent sea level response, conversing mass on a global scale.

A similar term, $[\tilde{S} + U]_{GIA}$, corresponds to the GIA induced geocentric sea level change. On the timescales considered, this will be treated as a secular variation. Two effects play a role here. Firstly, the slow adjustment of the solid Earth, induce a non-uniform trend in the geoid. Secondly, as the mantle material is flowing back to the former glaciation areas (Laurentide and Fennoscandia), the ocean floor is sinking on average. The latter effect accounts for the slight offset between the GIA induced geoid surface and the geocentric sea level (i.e. the two equipotential surfaces do not share the same potential value).

Dynamic Sea Level Variations

Finally, there are dynamic variations of the sea level, h_{dyn}, which do not cancel out on the time scales considered. This term contains the (net) effects of the wind and pressure driven sea level variations and its associated (time-varying) currents. The dynamic sea surface height as stated here can therefore not be simply thought of as the dynamic topography, since the steric height, which is not included in h_{dyn}, would also contribute to the dynamic topography. In fact, the sum of $h_{IB} + h_{dyn}$ introduce variations in ocean bottom pressure.

In this thesis, $h_{IB} + h_{dyn}$ is not the signal of interest, but it is reduced by subtracting the (monthly) ocean bottom pressure variations from the GRACE de-aliasing model (GAC). However, before correcting, the GAC product is modified by subtracting the oceanic mean of the GAC product itself. This step prevents the introduction of artificial mean sea level changes in the altimeter residuals. After correcting, the remainder of $h_{dyn} + h_{IB}$ is simply treated as measurement residual. After the correction, the altimetry data still contain the signal of interest, namely the steric variations and the time-varying passive sea level response to terrestrial surface loading.

In summary, the along-track corrected altimeter measurements, flow as observations in the fingerprint inversion as

$$\Delta h(\theta, \lambda) = h_{ssh}(\theta, \lambda) - h_{mssh}(\theta, \lambda) - \left(T_{GAC}(\theta, \lambda) - \frac{1}{A_{oce}} \int_{Oce} T_{GAC}(\theta', \lambda') d\omega' \right). \quad (3.7)$$

3.2.2 Ocean Models

In this thesis, simulated ocean bottom pressure from FESOM (Finite Element Sea Ice Model, Brunnabend (2011); Timmermann et al. (2009)) are used as pseudo-observations. Strictly speaking, the output from an ocean model is not a measurement, since it is also based on physical relationships. However, to some extent, the propagated observational noise from the forcing fields and the model errors itself, can be considered as (Gaussian) measurement noise. In that line of reasoning, it is justifiable to consider the model output as a set of pseudo-observations. The information contained in the model serves as a useful constraint keeping the oceanic variations within reasonable limits.

The model is forced by both wind stress and pressure from ECMWF data, which ensures that the derived ocean bottom pressure plus the ECMWF atmospheric surface pressure adds up to the total bottom pressure.

The model applies a Greatbatch correction (Greatbatch, 1994), which essentially makes the model mass consistent with the river flux from the hydrological model LSDM (Dill, 2008). Nevertheless, the river fluxes are to a large extent unknown such that the mass content of the entire ocean is associated with a large error as well. In the joint inversion, this problem will be mitigated by co-estimating a mass-correction term for the ocean model, which is constrained by the other data (GPS and GRACE).

Due to the complexity and non-linearity of an ocean model, its errors are difficult to quantify. In order to estimate an error, FESOM has been forced by two atmospheric models, ECMWF and NCEP, separately (Brunnabend et al., 2011). The time variable difference between the model runs may be used to assess the model error. The median of the absolute value of the difference is plotted in Fig. 3.3.

The development, and tedious task of tuning and running the model has been performed at the Alfred Wegener Institute and falls outside the scope of this thesis (a detailed assessment can be found in the Ph.D. thesis of S.-E. Brunnabend (Brunnabend, 2011)). The input for this work consists of the derived ocean bottom pressure variations and its time varying
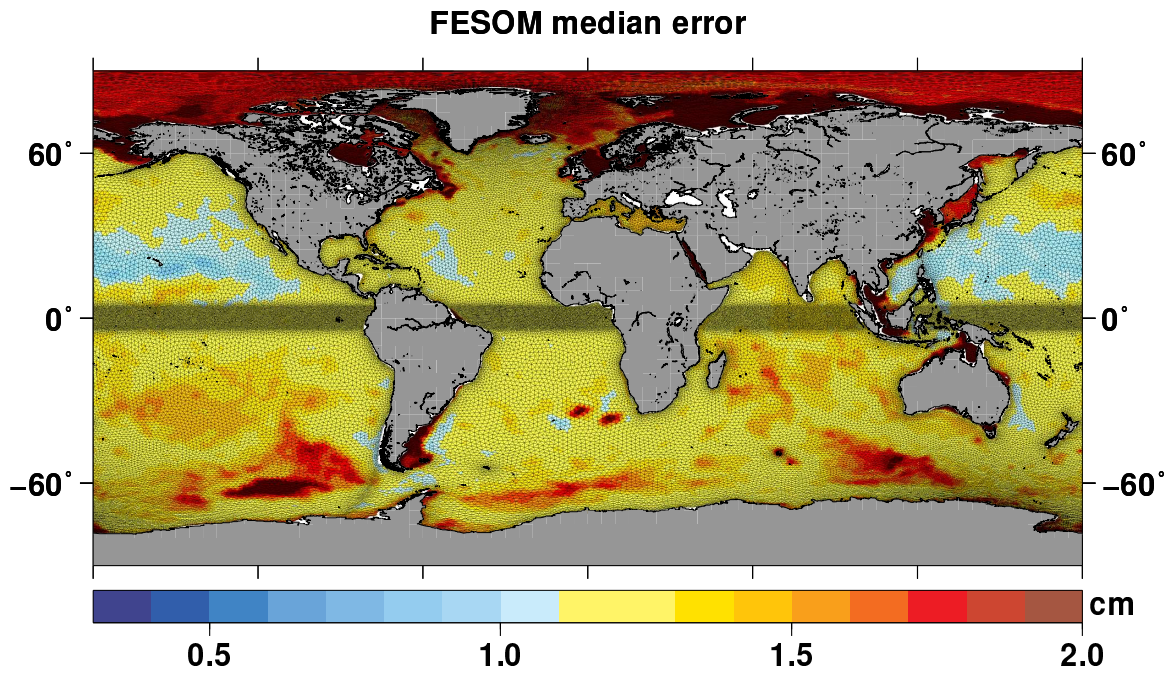
FESOM median error

Figure 3.3: Median error of the FESOM model. The error has been estimated from the difference between two model runs, each forced by distinct atmospheric forcings.

FESOM median error (area weighted)
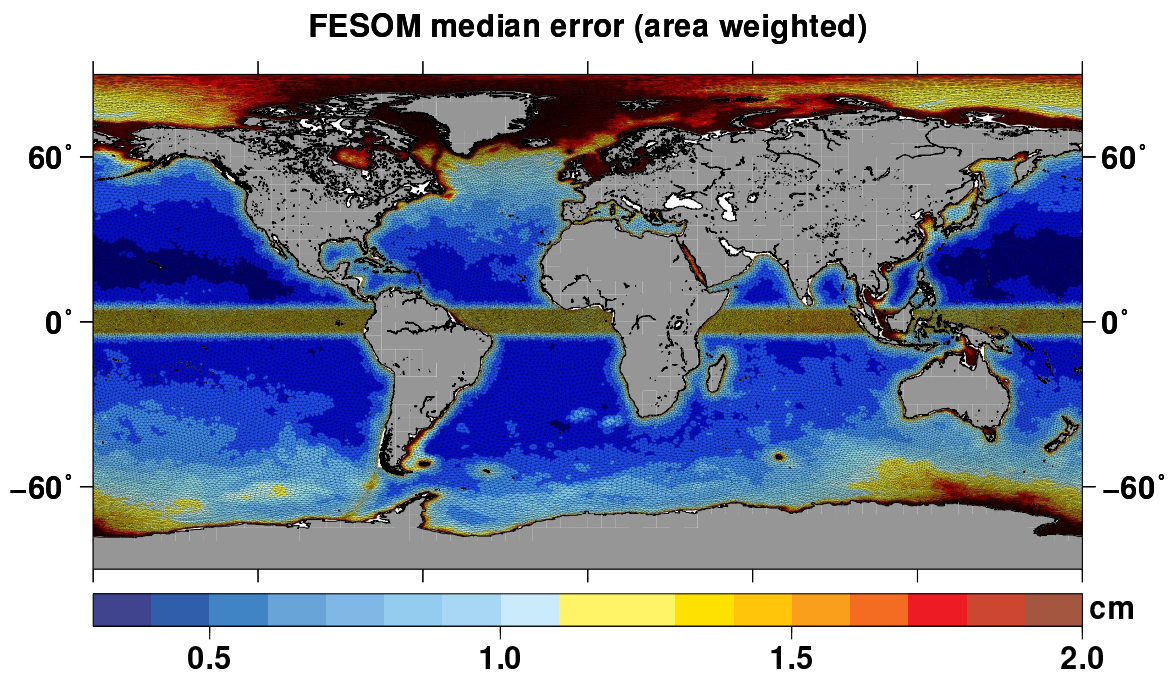
Figure 3.4: Area weighted (median) error of the FESOM model. The area weighting ensures that regions with a high density of vertices will not be overweighted in the inversion. The error displayed is therefore representative for an area of 1990 km^2 (the median nodal area of the model)

uncertainties.

Two different spatial discretizations of the model are available. The first discretization is relatively uniform with a resolution of about 1.5 degrees. These model realizations have been used in Rietbroek et al. (2009, 2012b). More recently, the model resolution has been refined such that the finite element vertices have separations between ~20 km in shallow coastal areas to about 150 km in the open ocean (see Fig. 3.4). In this study, nodes in the shallow part of the ocean (up to 600 m deep) have been removed from the joint inversions.

When the FESOM data is used in a least squares weighting scheme with other data, the adopted errors determine the relative weight of the ocean model. In order to develop a realistic weighting scheme, an ocean model error must be adopted, which takes into account the model errors themselves and at the same time prevents overweighting the model data in regions with a dense concentration of nodes. Therefore the following error (σP_i) has been adopted for the pressure at each node:

$$\sigma P_i = \sqrt{\frac{A_{med}}{A_i}} \, \text{med} \left(|\Delta P_i(t_0 \cdots t_n)| \right). \tag{3.8}$$

Here, A_i, denotes the cluster area[1] of the node in question. The median cluster area of all model nodes is denoted by A_{med} and amounts to 1990 km^2. The time varying approximate error at the node i, is given by $\Delta P_i(t_0 \cdots t_n)$, and is obtained from the difference of the model runs. The median of this series, plotted in Fig. 3.3 is taken to be representative for the model, and is consequently independent of time. Alternatively, it has been investigated whether the root mean square or the the standard deviation of $\Delta P_i(t_0 \cdots t_n)$ could be used as a measure of the error. However, when considering the non-Gaussianity of the modeled OBP differences and the non-zero time mean over most of the grid points, the median is the most useful candidate.

The area weighted errors, in terms of equivalent water height, are plotted in Fig. 3.4. Up to date, the error-covariance between different nodes have not yet been estimated and/or accounted for, such that the adopted error-covariance matrix is assumed to be diagonal.

3.2.3 Ocean Bottom Pressure Recorders

At a selected set of oceanic locations, Bottom Pressure Recorders (BPRs) have been deployed by various institutes (e.g. AWI, POL) to measure high frequency variations of the local bottom pressure. A BPR is typically deployed in the deeper waters (> 1000 m), and primarily consists of a pressure sensor. Auxiliary instruments, such as inverted echo sounders are sometimes also added to the mooring.

The BPRs are commonly used as research instruments, where they are typically installed and recovered after a certain amount of time (1-2 years). Scientific studies have interpreted the signal and compared the time series with GRACE data in various regions (Kanzow

---

[1] amounting to one-third of the surrounding triangular surfaces

et al., 2005; Rietbroek et al., 2006; Morison et al., 2007; Hughes et al., 2007; Macrander et al., 2010; Rietbroek et al., 2012b). Additionally, in the framework of the DART project (Deep-ocean Assessment and Reporting of Tsunamis, e.g. Bouchard et al. (2007)), BPRs are used which send in near real time their data to telemetry buoys over an acoustic link.

Even at depths of 4000 m, the bottom pressure recorder can measure pressure changes corresponding to a mm of water. The sustained extreme pressure may however cause metal creep and long term volume changes in the instrument vacuum chamber. Furthermore, the transient settling of the mooring in the ocean sediment is also suspected to introduce (non-linear) drifts. Drifts and transient effects are often visible in the time series and their removal is problematic, as the correction may also remove signal of interest.

The time series of various bottom pressure recorders are used as a validation dataset in this work, and are therefore not part of the inversion themselves (for a sensitivity study one is referred to Gebler, 2013). The time series are taken from the ocean bottom pressure database of AWI (Macrander et al., 2010) who have assembled the publicly available time series. The tides were corrected for using the EOT11a model (Savcenko and Bosch, 2012). The deployment locations are visible in Fig. 5.8 of the results chapter.

3.3 GPS-derived Crustal Deformations

The global network of permanent GPS stations provide valuable data for the study of surface loading. As described in Chap. 2.2, the changing surface load induces crustal deformations, which provides the basis of the inverse problem of Sec. 4.1.
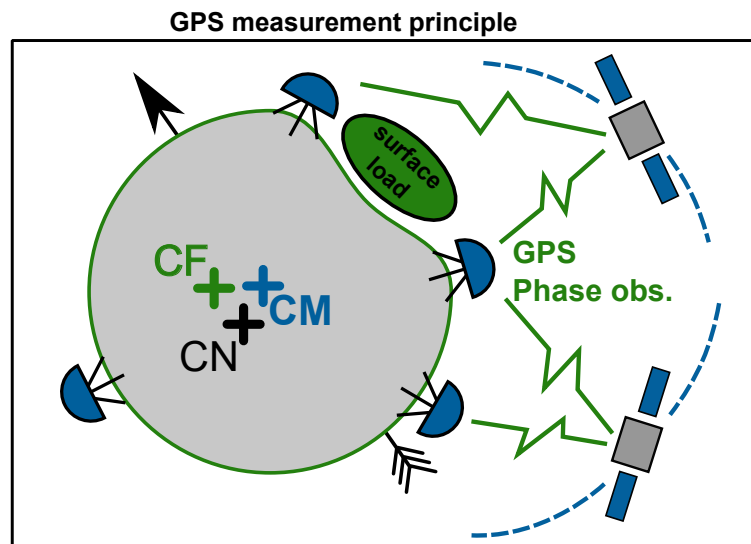
Figure 3.5: The GPS phase measurements provide range information between the satellites and the stations. The measurement principle allows the detection of geocenter motion, since the GPS satellites orbit the center of mass of the Earth system, whereas the station network is sample of the Earth's surface.

However, many GPS station monuments are also sensitive to local effects such as for example local subsidence due to ground water extraction. Furthermore, plastic deformations in the plate collision zones do not obey the rigid plate model from Sec. 2.3.10. Consequently, the screened subset of stations, which are suitable for the study of surface loading

phenomena, should not be influenced too much by local phenomena and, maybe more importantly, the network geometry should cover the Earth as homogeneously as possible. Fig. 3.5, shows the GPS network as used in this thesis.

RMS (Height comp.) of GPS stations
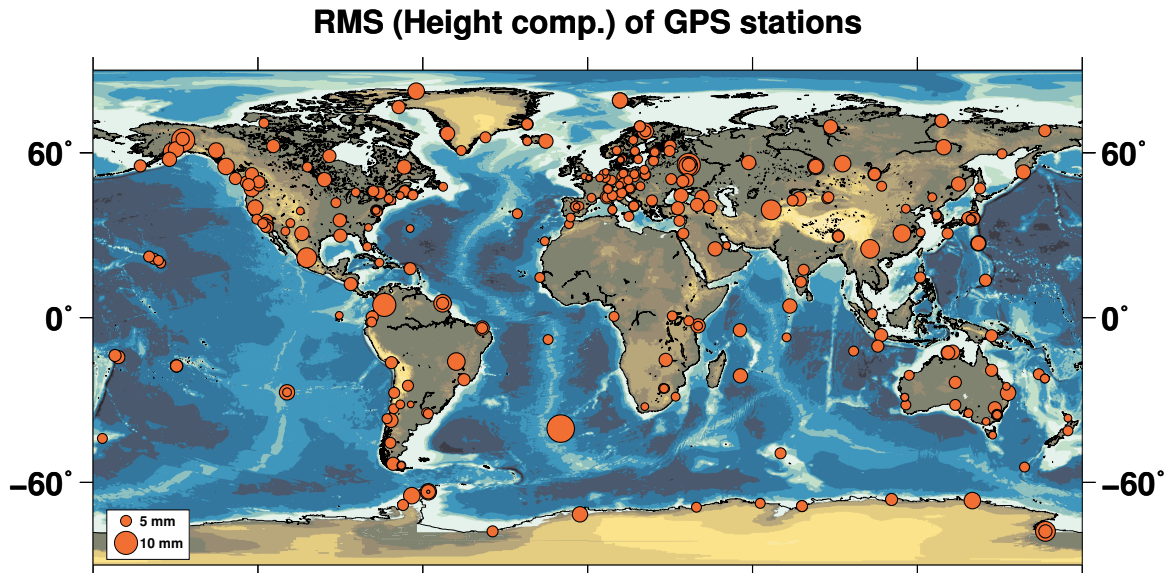
Figure 3.6: Positions of the 316 GPS stations contained in the reprocessing data. The size of the symbols indicate the RMS of the height component over an eight year period 2003-2010 (without trend).

To be as consistent as possible, the station positions and the orbits of the GPS satellites should be estimated simultaneously. In this way, the network may be expressed in the CM frame. With GPS measurements only, the absolute orientation of the network and orbit constellation, is not uniquely defined. This manifests itself as a rank defect in the GPS normal equation systems, which can only be solved by adding new constraints. Most notably, VLBI (Very Long Baseline Interferometry) is needed to constrain the Universal time (UT1) (Rothacher et al., 1999).

During the GPS data processing, dry and wet tropospheric delays are corrected for. In addition, a higher order ionospheric correction has been applied (Fritsche et al., 2005). Furthermore, the station positions have been corrected for the Solid Earth tides (IERS 2003, McCarthy and Petit, 2004), and ocean tidal loading. In some of the used versions a loading correction, derived from the GRACE de-aliasing product (AOD1B RL04), has been additionally applied. The radiation pressure acting on the GPS satellites, has been accounted for by the CODE model (and the older ROCK model for comparison, see Fritsche et al., 2009).

The mean station positions and velocities, estimated from the reprocessed data, have been removed, to obtain residual deformations. Furthermore, during the estimation of the secular reference frame discontinuities in the GPS station time series have been estimated and removed.

The (re)processing of the raw GPS data, takes significant amounts of time, and is not

part of this thesis. In this work, I use the data from the reprocessing efforts of the TU Dresden/TU Munich/GFZ (Rülke et al., 2008; Fritsche et al., 2009; Steigenberger et al., 2006). Cartesian GPS station positions augmented with the Earth Orientation Parameters (EOP) are provided as SINEX files with their full error-covariance information in the form of weekly normal equation systems. The parameters of the GPS satellite orbits are reduced (implicitly solved, see App. C.2). In earlier work, GPS network deformation and its full error-covariance from the international GNSS service (IGS) have been used as input for the joint inversion Rietbroek et al. (2009). The advantage of using the reprocessed data , is that the unsolved normal equation systems are available without any constraints applied. This allows a more consistent combination compared to the standard IGS products. Similar to the GRACE data, the inversion of the data is postponed until after the combination.

3.3.1 Pre-processing of GPS Normal Equation Systems

In a preprocessing step, the deformation associated with the ocean pole tide (Desai, 2002) has been removed from the data by changing the a priori vector of the normal equation system (see App. C.3). Although this effect is small (maximum deformations in the order of 0.5 mm), it makes the systems consistent with the GRACE data. For the same reason, the loading effect from non-tidal mass variations of the ocean and atmosphere are removed from the station deformations. These corrections are derived from the GRACE de-aliasing model, up to degree and order 100.

The Earth orientation parameters, still present as unknown parameters, are fixed to the values which are used in the GRACE processing (See App C.3,C.4). This procedure then also removes the rank defect caused by UT1, as discussed earlier.

When used in the joint inversion, the parameter space of the normal equations needs to be converted from station positions to spherical harmonic surface loading coefficients (see Sec. 4.1). After that step, it will be difficult to apply (or estimate) residual Helmert transforms, as the station positions are removed from the parameter space. These Helmert transformation are useful as they allow the absorption of erroneous network effects, which are linked to GPS-specific processing errors (see Sec. 5.1.2 for a discussion of the estimated Helmert parameters). It should be reemphasized that these *rigid* transformations may be estimated simultaneously with the degree 1 surface loading components, which linked to the *deformation* of the network. To accommodate network transformation at the joint inversion stage, 7 Helmert parameters are introduced in the original normal equation systems. This corresponds to applying the following transformation to the station coordinates:

$$\mathbf{x}_i^{\dagger} = \begin{bmatrix} \mathbf{H}_i & \mathbf{I} \end{bmatrix} \begin{bmatrix} \mathbf{t}_H \\ \mathbf{x}_i \end{bmatrix}. \tag{3.9}$$

Obviously, the transformation introduces 7 rank defects in the system. In a joint inversion, these rank defects may be constrained by the GRACE and OBP data. However, in a GPS-only inversion these rank defects prohibit the inversion of the normal equation system. One way to mitigate this, is to apply an additional network constraint on the remaining station positions. In that case, the transformation and optional regularization of

the normal equation system may be written as:

$$\tilde{\mathbf{N}} = \begin{bmatrix} \mathbf{H}^T\mathbf{NH} & \mathbf{H}^T\mathbf{N} \\ \mathbf{NH} & \mathbf{N} + \alpha\mathbf{\Theta}_c \end{bmatrix},$$

$$\tilde{\mathbf{b}} = \begin{bmatrix} \mathbf{H}^T\mathbf{b} \\ \mathbf{b} \end{bmatrix}. \tag{3.10}$$

Here,

$$\mathbf{H} = \begin{bmatrix} \mathbf{H}_1 \\ \vdots \\ \mathbf{H}_k \end{bmatrix}, \tag{3.11}$$

is a composite block matrix incorporating all station positions.

The regularization matrix $\mathbf{\Theta}_c$, constrains the position of the barycenter, orientation and scale of a network of core stations as indicated by the subscript $'_c'$. $\mathbf{\Theta}_c$ can be constructed using a generalized inverse:

$$\mathbf{\Theta}_c = \mathbf{H}_c(\mathbf{H}_c^T\mathbf{H}_c)^{-1}\mathbf{D}_H^{-1}(\mathbf{H}_c^T\mathbf{H}_c)^{-1}\mathbf{H}_c^T. \tag{3.12}$$

The diagonal matrix $\mathbf{D}_H$ determines the strength of the constraint:

$$\mathbf{D}_H = \text{diag} \begin{bmatrix} \sigma_{t_x}^2 & \sigma_{t_y}^2 & \sigma_{t_z}^2 & \sigma_s^2 & \sigma_{r_x}^2 & \sigma_{r_y}^2 & \sigma_{t_z}^2 \end{bmatrix}. \tag{3.13}$$

In Rietbroek et al. (2012b), the weighting was chosen according to: $\sigma_{t_{xyz}} = 0.1$mm, $\sigma_{r_{xyz}} = 3\mu$arcsec and $\sigma_s = 0.01$ppb.

When $\alpha > 0$, the station positions of the normal equation systems are now associated with the center of network, and the offset of the CM from CN is given by the three translational Helmert parameters. Unfortunately, the above method also introduces a certain stiffness in the core network. As α is increasing, the core network stations are pushed towards a configuration whose degrees of freedom are restricted to the 7 Helmert parameters. For the *joint* inversions of this thesis, these constraints are not necessarily needed, and are therefore not applied (i.e. $\alpha = 0$).

In order to link the station deformations to surface loading coefficients, the Cartesian station coordinates of the normal equation systems are rotated in the local station frame (up, north, east), by a matrix $\mathbf{R}_{3\times 3}^i$. This is a more natural choice for surface loading effects. The normal equation system are rotated by the following operation:

$$\check{\mathbf{N}} = \mathbf{R}\tilde{\mathbf{N}}\mathbf{R}^T,$$

$$\check{\mathbf{b}} = \mathbf{R}\tilde{\mathbf{b}}. \tag{3.14}$$

Where the block-diagonal rotation matrix is build up from the station specific rotation matrices

$$\mathbf{R} = \begin{bmatrix} \mathbf{I}_{7\times 7} & 0 & \cdots & 0 \\ 0 & \mathbf{R}_{3\times 3}^1 & \cdots & 0 \\ \vdots & \vdots & \ddots & \vdots \\ 0 & 0 & \cdots & \mathbf{R}_{3\times 3}^k \end{bmatrix}. \tag{3.15}$$

4 Joint Inversion Schemes

This chapter covers the inversion schemes used in this thesis. The relation of the data to the estimated parameters is described, and linked to the theory of Chap. 2.

Essentially, two types of inversion are elaborated upon. The first one aims at the estimation of weekly variations of surface loading. These are expressed in spherical harmonic coefficients up to degree and order 30. These low resolution fields aim to describe large scale mass variations from terrestrial hydrology, the ocean and the atmosphere. The data which flows in the inversion are GRACE, GPS and simulated OBP in the form of pseudo-observations. This approach differs from a formal assimilation scheme, where the ocean model is improved by the data. In the joint inversion scheme proposed here, the simulated OBP merely serves as a priori information used to improve and stabilize the solution. In contrast, an assimilation scheme would use the data to stabilize the models state vector, which contains a broad array of model parameters besides surface loading. Thus, in the joint inversion, the parameter vector of interest is not the state vector of the ocean model but the ocean bottom pressure (or surface loading variations). Furthermore, the solution domain also covers the continents, which is outside the realm of the model. In addition, the proposed inversion also allows for the estimation of a mass correction for the model.

The second inversion scheme aims at estimating slowly varying changes of sea level, induced by the melting of the major ice sheets, land glaciers and continental hydrology. Furthermore, the use the combination of GRACE and altimetry in this inversion allows the separation of the mass component from the steric component. In contrast to the first inversion scheme, the unknown parameters are time varying scales associated with predefined patterns of cryospheric melting, hydrology, steric changes, etc. This setup is referred to as a 'fingerprint' inversion (Plag and Jüttner, 2001), as each phenomenon is linked to its unique pattern (see Fig. 4.9).

Both types of joint inversion have their justification. In the first scheme, generic surface loading is solved for with high temporal resolution. The parameters of the second 'fingerprint' inversion form a much more restricted set of parameters, but allow for a meaningful geophysical separation of the different surface loading contributions on longer time scales.

4.1 Estimation of Global Surface Loading

A joint inversion provides the opportunity to estimate parameters from ill-posed problems, which would have been impossible to estimate from a single data set only. Fig. 4.1 visualizes this principle for the current inversion scheme, where weekly surface loading coefficients are estimated up to degree 30. The relatively low truncation degree evolved from the sparser ground track of GRACE associated with the higher (weekly) temporal

resolution.

Figure 4.1: The joint inversion scheme allows resolving parts of the solution space, which could not have been resolved by single techniques alone (the null-space). For example, geocenter motion, unresolved by GRACE is constrained by GPS and the simulated OBP. On the other hand, regions not covered by GPS may be effectively constrained by GRACE and OBP. In addition, mass corrections for the model are resolved by GPS and GRACE.
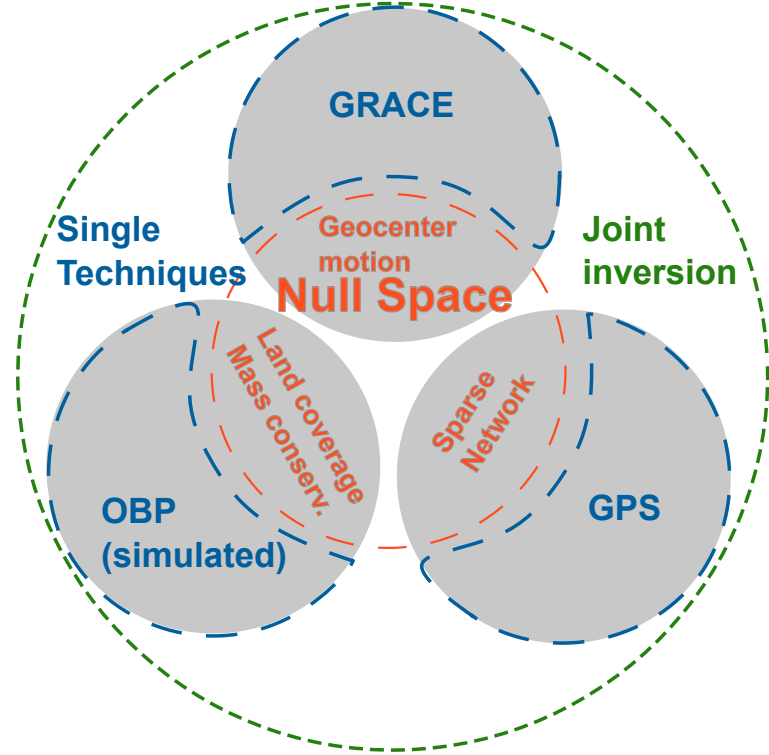
As can be seen, the 'null-space' of the single techniques, would cause problems when estimating, (1) the geocenter motion (GRACE), (2) surface loading in poorly sampled regions (GPS), and (3) the total mass of the ocean model. In the joint inversion, these phenomena can be estimated simultaneously.

4.1.1 Observation Equations

GRACE

In this work, weekly surface loading coefficients up to degree and order 30 are the unknown parameters to be estimated. They can be related to the Stokes coefficients as measured by GRACE (see Eq. 2.36)

$$\delta C_{nm} = \frac{1 + k'_n}{2n + 1} \frac{3\rho_w}{\rho_e} T_{nm}, \quad n > 1,$$ (4.1)

where it must be noted that, since the potential field from GRACE is provided in the CM frame, the relation does not include the effect of degree 1. It is obvious that the observation equation above is linear, and the GRACE normal equation systems can consequently be transformed in terms of the parameters T_{nm} (see App. C.5):

$$\mathbf{N}_{GRC} = \mathbf{DND},$$
$$\mathbf{b}_{GRC} = \mathbf{Db}.$$ (4.2)

Here, the diagonal matrix $\mathbf{D}$ contains the entries from Eq. 4.1.

GPS

Furthermore, using loading theory, the surface deformation may also be written as a (linear) function of the surface loading coefficients (Eqs. 2.29, 2.31):

$$
\begin{bmatrix} \delta h \\ \delta e \\ \delta n \end{bmatrix}_i = \frac{3ag\rho_w}{\rho_e} \sum_{n=1}^{N_{max}} \sum_{m=-n}^{n} \frac{1}{2n+1} \begin{bmatrix} h'_n \bar{Y}_{nm}(\theta_i, \lambda_i) \\ \frac{l'_n \partial \bar{Y}_{nm}(\theta_i,\lambda_i)}{\sin\theta \partial \lambda} \\ \frac{-l'_n \partial \bar{Y}_{nm}(\theta_i,\lambda_i)}{\partial \theta} \end{bmatrix} T_{nm} + \epsilon.
\tag{4.3}
$$

As is the case for GRACE, the maximum degree, N_{max}, is set to 30. The entries of the double summation can be written in the form of a matrix $\mathbf{B}$ such that the pre-processed GPS normal equation systems (Eq. 3.14) are transformed as follows:

$$
\mathbf{N}_{GPS} = \begin{bmatrix} \mathbf{I}_{7\times7} & 0 \\ 0 & \mathbf{B}^T \end{bmatrix} \check{\mathbf{N}} \begin{bmatrix} \mathbf{I}_{7\times7} & 0 \\ 0 & \mathbf{B} \end{bmatrix}
$$

$$
\mathbf{b}_{GPS} = \begin{bmatrix} \mathbf{I}_{7\times7} & 0 \\ 0 & \mathbf{B}^T \end{bmatrix} \check{\mathbf{b}}
\tag{4.4}
$$

In this way, 7 weekly Helmert parameters are also inherited from the GPS normal equation systems.

As illustrated in Sec. 2.3.6, the degree 1 load Love numbers are frame specific. For the joint inversions, no network constraints ($\alpha = 0$ in Eq. 2.3.6), have been applied, and the local station residuals are described in the CM frame. In line with this, the CM degree 1 load Love numbers have been used above. Otherwise, with constraints applied, it makes more sense to use the degree 1 load Love numbers associated with the CF, as the station residuals are described in the CN system. Since the center of network approximates the CF, the Helmert parameters then describe small discrepancies between CF and CN.

Many stations with relatively short time series, also produce time series with spurious signals. For this reason, stations which contain less than 52 weeks (i.e. spanning on average less than a year), are rejected from the solution. In earlier research (Rietbroek et al., 2009) a weekly outlier method (based on a 3σ rule) was additionally implemented, which removed GPS stations which showed anomalous displacements relative to a low degree (7) unconstrained GPS-only inversion. Further techniques to remove or reduce the impact of outliers have been extensively described by van Loon (2008). However, the reprocessed GPS data is much more homogenous, so that virtually no stations exhibit anomalous behavior. Furthermore, the outlier detection method has the tendency to skim off some good quality stations when their surface loading reaches its annual peak. For this reason, I refrain from rejecting weekly outliers in the current study.

Simulated OBP

The ocean bottom pressure variations from the model do not account for the time-variable geoid. The geoid will move over time, due the changing surface load, while the models assumes a static geoid. The modeled OBP therefore represents the surface loading compo-

nent, expressed in equivalent water height, relative to the instantaneous geoid:

$$\frac{\delta P_i}{g\rho_w} = \Delta M_0 + a \sum_{n=1}^{N_{max}=30} \sum_{m=-n}^{n} \left(1 - \frac{1+k'_n}{2n+1}\frac{3\rho_w}{\rho_e}\right)\bar{Y}_{nm}(\theta_i, \lambda_i)T_{nm} + \epsilon. \tag{4.5}$$

The left hand side denotes the modelled pressure expressed in equivalent water height. The observation equation is augmented with a uniform mass correction, ΔM_0. Although a uniform Greatbatch correction is applied in the model, the variations of the simulated ocean mass depend entirely on the external data, and may contain errors. For this reason, the uniform correction is introduced as an unknown parameter, such that it can be constrained by the GRACE and GPS data. Again, the above observation equation is linear, allowing it to be written in a diagonal matrix form, $\mathbf{D}$

Using the pressure variations at the model nodes, and incorporating the approximate diagonal model error-covariance, $\mathbf{C}_{OBP}$ from Fig. 3.4, a normal equation system can be built:

$$\mathbf{N}_{OBP} = \mathbf{D}^T\mathbf{C}_{OBP}^{-1}\mathbf{D},$$

$$\mathbf{b}_{OBP} = \mathbf{D}^T\mathbf{C}_{OBP}^{-1}\frac{\delta\mathbf{P}-\delta\mathbf{P}_0}{g\rho_w},$$

$$\left[\mathbf{1}^T\mathbf{P}\mathbf{1}\right]_{OBP} = (\frac{\delta\mathbf{P}-\delta\mathbf{P}_0}{g\rho_w})\mathbf{C}_{OBP}^{-1}(\frac{\delta\mathbf{P}-\delta\mathbf{P}_0}{g\rho_w}). \tag{4.6}$$

To make the system consistent with their GRACE counterparts, the reference vector, $\delta\mathbf{P}_0$, contains the ocean and atmospheric components from the de-aliasing model as used in the GRACE processing.

4.1.2 Combination and Weighting of GRACE, GPS and OBP

After preparing the data, the information from GRACE, GPS and OBP may be merged in a combined normal equations system, $\mathbf{N}_{comb}$, $\mathbf{b}_{comb}$ (see App. C.6). In addition to the surface loading coefficients, 7 Helmert parameters and the mass correction parameter are included in the unknown vector $\mathbf{x}_{comb}$. The individual normal equation systems are padded with zeros to accommodate these parameters before combining them according to

$$\mathbf{N}_{comb} = \frac{1}{\sigma_{GRC}^2}\mathbf{N}_{GRC} + \frac{1}{\sigma_{GPS}^2}\mathbf{N}_{GPS} + \frac{1}{\sigma_{OBP}^2}\mathbf{N}_{OBP},$$

$$\mathbf{b}_{comb} = \frac{1}{\sigma_{GRC}^2}\mathbf{b}_{GRC} + \frac{1}{\sigma_{GPS}^2}\mathbf{b}_{GPS} + \frac{1}{\sigma_{OBP}^2}\mathbf{b}_{OBP},$$

$$[\mathbf{l}_0^T\mathbf{P}\mathbf{l}_0]_{comb} = \frac{1}{\sigma_{GRC}^2}[\mathbf{l}_0^T\mathbf{P}\mathbf{l}_0]_{GRC} + \frac{1}{\sigma_{GPS}^2}[\mathbf{l}_0^T\mathbf{P}\mathbf{l}_0]_{GPS} + \frac{1}{\sigma_{OBP}^2}[\mathbf{l}_0^T\mathbf{P}\mathbf{l}_0]_{OBP}. \tag{4.7}$$

The observation groups are scaled by the corresponding a priori σ's. For the joint inversion schemes used here, these are estimated by means of VCE (Variance Component Estimation, see App. C.6). The resulting time variation of σ_{OBP}, σ_{GRC}, and σ_{GPS}, is plotted in Fig. 4.2. Clearly, σ_{GPS} remains more or less constant in time, indicating a posteriori error of about 1.4 times the formal error. The variance component of the FESOM derived bottom

pressure fluctuates most strongly, and displays a seasonal signal. A possible explanation can be that seasonal signal may be slightly underestimated in the model.

The error model of the FESOM data contains only diagonal elements, which consequently means that correlations among the model nodes are unaccounted for. To mitigate this effect, an empirically derived factor of five is additionally used to downweight the model error-covariance, after the VCE weights are computed. This reduces the weight the model has in the inversion and also increases the correlations of the joint inversion with in situ bottom pressure recorders slightly (see Sec. 5.1.5). It is expected that this downweighting can be avoided when appropriate error-covariance functions become available for the model error.
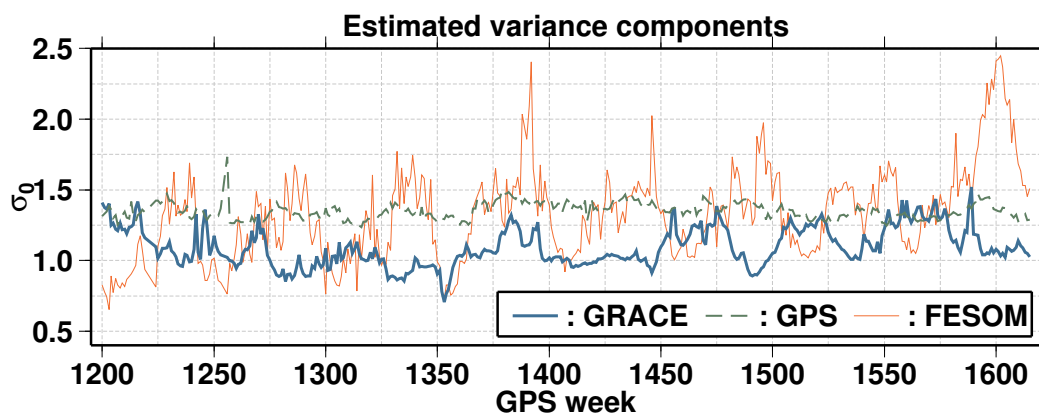
Figure 4.2: Estimated variance components, σ_0, of the joint inversion of GRACE (RL05), GPS and FESOM data.
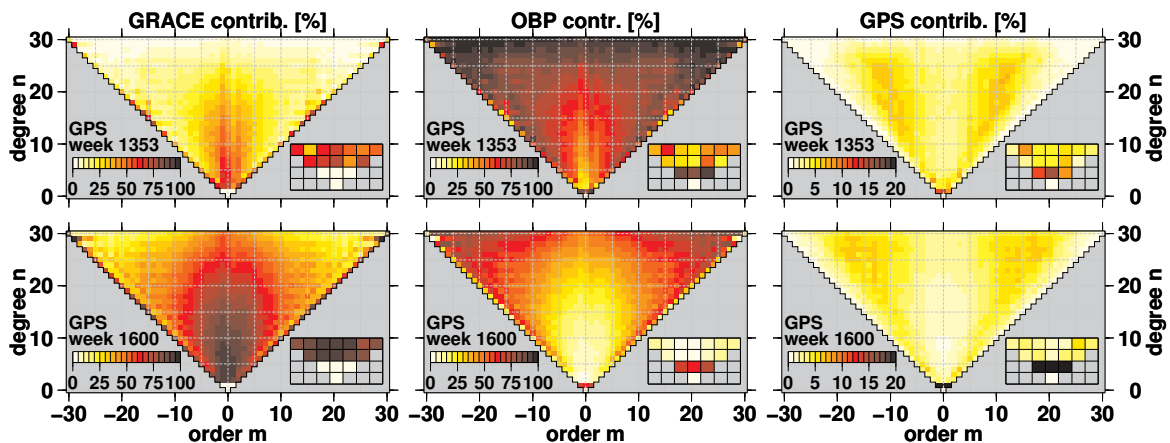
Figure 4.3: Diagonal data contributions at the level of surface loading coefficients for GRACE, GPS and OBP in the joint inversion. σ_{OBP}^2 is additionally downweighted by a factor 5. Note the scale difference for GPS.

To get an impression on how much each data type contributes to the inversion, the diagonal of the redundancy matrix (App. C.6) is plotted in Fig. 4.3. Since the weights also

change over time, two weeks have been considered with strongly differing FESOM weights (see Fig. 4.2). The formal contributions of the datasets to the lowest degree coefficients have been zoomed in for clarity.

From the triangle plots it becomes clear that the FESOM data contributes mostly to the inversion at the higher degrees. Where most of the geophysical signal is occuring, the lower and mid degrees, GRACE is the major contributor. At first sight, the GPS data appear to have only a minor contribution to the joint inversion. It plays however an important role for the degree 1 coefficients, as it is the only data source which provides coverage over the continents. Furthermore, all surface loading coefficients are global parameters. Therefore, by eye-balling Fig. 4.3 it is hard, if not impossible, to see that some data types contribute more strongly in different regions (e.g. the GPS contribution will be larger in Europe because of the denser GPS network there).
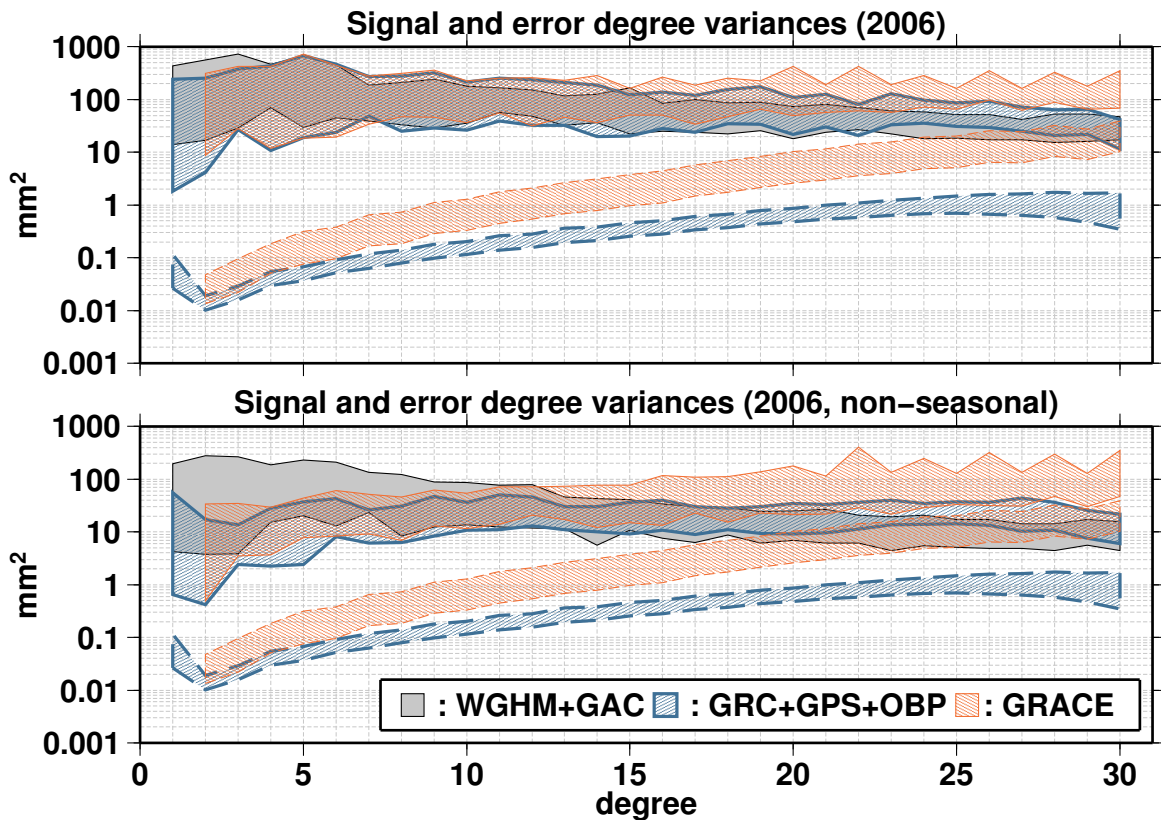
Figure 4.4: Degree variances of the signal and error of the combination solution, a GRACE-only solution, and a background model containing hydrology and the GAC product. The shaded regions span the variations of the weekly solutions over the year 2006. A solid and dashed boundary indicate the signal and noise respectively. The combination solution and GRACE have no background models restored.

A peculiar feature is seen in the sectorial bands ($n = m$) implying a relatively strong contribution of GRACE accompanied by a weak contribution of OBP. At first sight, one might suspect that the area weighting of the FESOM data may have been too strong, and that the

equatorial band, which can be represented by a linear combination of sectorial harmonics, is now under-weighted with respect to the other nodes. However, a closer inspection of the normal matrices indicates that the cause lies in the covariance information of GRACE. From the formal error of the weekly GRACE-only solutions, one can see that that sectorials are more accurate than their immediate neighbors (not shown here). A secondary line, essentially the sectorial shifted by three orders, is also visible in GPS week 1600. This feature is also related to the GRACE covariance information. The exact cause of these features remains unclear, but it is probably related to the weekly ground track patterns of GRACE.

Since OBP and GPS data are combined, the formal errors of the joint inversion are expected to be smaller than those of a single inversion. Additionally, the GRACE errors, increasing for higher degrees, are likely to be dampened. This can can be seen from Fig. 4.4, where degree variances of both the signal and error are plotted. Since different weeks are not behaving in the same way, the spread of the weekly solutions in the entire year 2006 are plotted as regions. A secondary plot shows the non-seasonal signal, where a seasonal fit, performed at the coefficient level, was removed first. Clearly, the signal of the combination solution is smaller than that of the GRACE signal at the higher degrees. This is the consequence of the information from FESOM, which effectively constrains the noisier GRACE data at the higher degree part of the spectrum, as can be expected from Fig. 4.3. This behavior is also reflected in the formal errors of the combination solution, which lie below the errors from GRACE. The removal of the seasonal signal, decreases the signal mostly in the lower degrees.
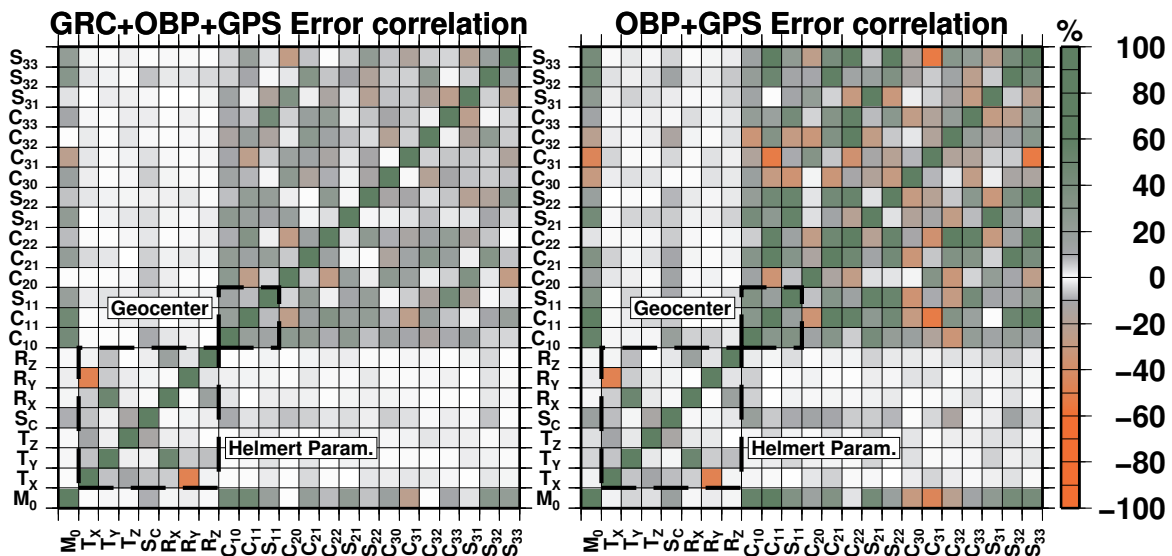
Figure 4.5: Correlations of the error-covariance matrix of a joint inversion from GRACE, GPS and modeled OBP data versus the correlation obtained from a GPS and OBP combination. The week considered is GPS week 1353 (centered at the 14th Jan 2004).

Up to now, only the diagonal part of error-covariance matrix has been discussed. However, the full error-covariance information from the inversion may also provide interesting insights. Fig. 4.5 shows a subsection of the formal error-correlation matrix of two types

of the joint inversion. On the left hand side, all data types are used, whereas at the right hand side the GRACE data is removed. Clearly, the correlation between the surface loading coefficients is lower when GRACE data is used. This illustrates that the GRACE data allows a better separation of the coefficients, at least on the formal side. Since GRACE performs well at the low degrees coefficients this is something which can be expected. A more surprising feature hides in the decreased correlations of the degree 1 coefficients. Although GRACE cannot measure the degree 1 surface loading coefficients directly, its addition in the joint inversion does improve the separability of the degree 1 coefficients from themselves as well as from other parameters (e.g. model bias and other surface loading coefficients). This feature is important but will be hardly visible in the formal (diagonal) errors of the solution.

4.1.3 GPS-only Inversion

It is possible to invert for surface loading using only GPS data (Blewitt and Clarke, 2003; Kusche and Schrama, 2005; Fritsche et al., 2009). However, only a relatively low resolution is possible, roughly speaking up to degree and order 10. The technique is promising as GPS data may be used to fill the gap between GRACE and a follow-on mission. Furthermore, the method may be used to extent the series back in time. This may be particularly interesting for the improved orbit determination of altimeters, in the periods before and after GRACE.

A complication with GPS-only inversions is the heterogenous network, which exhibits large gaps over the ocean and the southern Hemisphere. This problem will manifest itself as noise in the form of a strongly fluctuating solution over the ocean. Blewitt and Clarke (2003) solved this problem by forcing the solution over the ocean to the self-consistent sea level surface (See Sec. 2.4.1). This method works as a strong constraint over the ocean, but this does not allow any other signal to be fitted which deviates from the self-consistent sea level. Kusche and Schrama (2005) applied a more flexible regularization technique, which constrained the ocean part of the solution towards zero. However, the regularization also biases the ocean mass towards zero, affecting the expected seasonal behavior (annual amplitude of ~9 mm Rietbroek et al., 2009).

Here, an alternative approach is proposed, which smoothly regularizes the solution over the ocean towards the self-consistent sea level. The method integrates the approaches of Kusche and Schrama (2005) and Blewitt and Clarke (2003). Over the ocean, the difference between the surface load and the self-consistent sea level (Quasi-spectral), as induced by the land load, can be written as:

$$\Delta T_{oce} = O(\lambda, \theta) \left(T(\lambda, \theta) - \tilde{S}(\lambda, \theta) \right). \tag{4.8}$$

The linearity of the Sea Level Equation (Eq. 2.83) allows a matrix notation in terms of coefficients:

$$a\Delta \mathbf{t}_{oce} = \mathbf{O} \left(a\mathbf{t} - \mathbf{G}_{\tilde{S}} \mathbf{G}_{N-U} \mathbf{h} \right). \tag{4.9}$$

The vector, $\mathbf{t}$, contains the stacked coefficients of the surface loading coefficients. The land load, $\mathbf{h}$, can also be written in terms of the surface load (see App. B.2), such that the differ-

ence vector $\Delta \mathbf{t}_{oce}$ becomes:

$$\Delta \mathbf{t}_{oce} = \mathbf{O}\,(\mathbf{I} - \mathbf{G}_{\tilde{S}}\mathbf{G}_{N-U}(\mathbf{I} - \mathbf{O}))\,\mathbf{t} = \mathbf{F}\mathbf{t}. \qquad (4.10)$$

Loosely speaking, the equation above can be thought of as an observation equation. When the expected value is zero, $\mathrm{E}\{\Delta \mathbf{t}_{oce}\} = \mathbf{0}$, a regularization matrix can be constructed as

$$\Psi_{oce} = \mathbf{F}^{T}\mathbf{C}_{\Delta \mathbf{t}}^{-1}\mathbf{F}. \qquad (4.11)$$
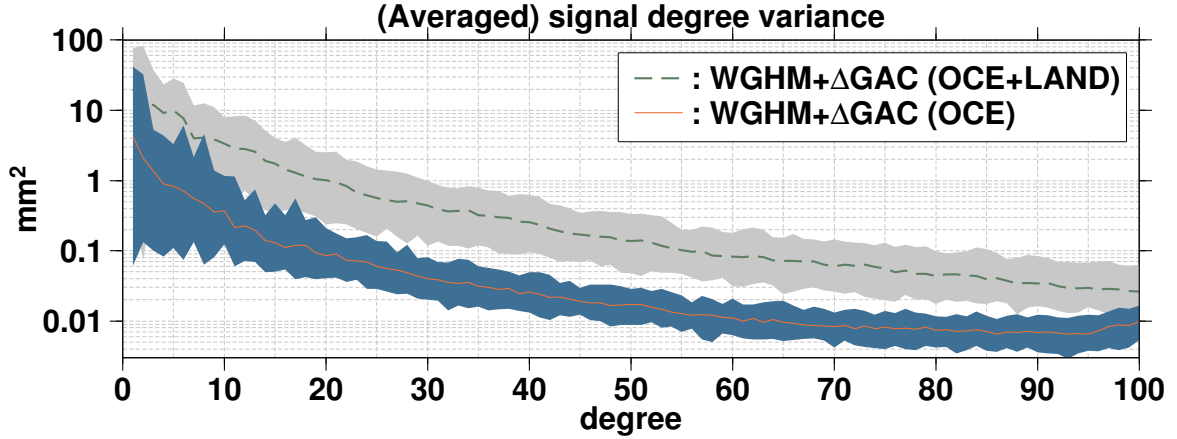
Figure 4.6: Averaged signal degree variances of weekly variations of residual surface loading from continental hydrology, and the difference between the release 05 and release 04 background model (GAC). The data span the years 2002-2007. The centered line in the ensembles represents its RMS.

Since the surface loading signal has a red spectrum, it can be expected that the error-covariance, $\mathbf{C}_{\Delta \mathbf{t}}$, shows a similar behavior. To approximate $\mathbf{C}_{\Delta \mathbf{t}}$, firstly a realistic residual signal has been constructed by augmenting the total water storage output of the hydrological WaterGAP model (Döll et al., 2003) with the *difference* of the ocean/atmosphere (GAC) product from RL05 and RL04. The averaged degree variance of this signal is plotted in Fig. 4.6. In analogy with Eq. 4.9, this signal is then multiplied by the ocean function (see App. B), to obtain realistic variations of $\Delta \mathbf{t}_{oce}$. The ocean function removes most of the terrestrial land signal, which can be seen from the lowering of the curves in Fig. 4.6. Over the considered years 2002-2007, a diagonal covariance, $\mathbf{C}_{\Delta \mathbf{t}}$ is contructed from the square of the RMS of the simulated $\Delta \mathbf{t}_{oce}$. This diagonal covariance is then used in Eq. 4.11 to compute the regularization matrix Ψ_{oce}.

The impact of the constraints on the solution is very strong. Fig. 4.7 shows for the GPS week 1400 a GPS-only solution solved up to degree and order 10. Both a regularized and unregularized solution is plotted. By inspecting the figure it becomes clear that an unconstrained GPS solution yields unacceptably large variations over the ocean as this part of the solution is virtually not constrained by data. The caveat is that, such ocean-based oscillations are not directly obvious from unconstrained surface loading coefficients or their errors, as they represent globally averaged values.
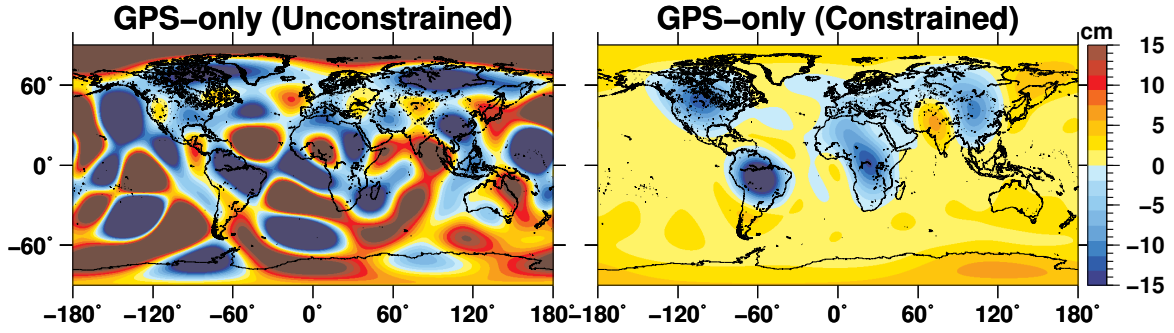
Figure 4.7: GPS-only surface loading solution up to degree and order 10, for GPS week 1400 (centered on 8th Nov. 2006). Left: solution without regularization, right: solution with constraints over the ocean.

Potentially, the maximum spherical harmonic degree can be further increased. van Loon (2008) computed solutions up to degree and order 14. In regions with a dense GPS network, such as Europe, GPS only inversions, up to degree 15 (not shown here) perform well. The downside of increasing the resolution is that the solution in the regions with bad GPS coverage will oscillate spuriously. To mitigate this to some extent van Loon (2008) added more constraints over land where the signal is expected to be small. Alternatively, cleverly placed radial basis functions (see Eicker et al. (2013) for a discussion) may be used to cope with the heterogenous GPS distribution, but this has not been applied to GPS up to now. In this study, the degree 10 solution is used since it represents a good overall compromise between resolution and amplification of noise at higher degrees.

4.1.4 Basin Averaging and Filtering

For many studies it is of interest to compute the average surface load in a certain (large) region. This averaging operation can be performed both in the spatial domain or in the spectral domain. The latter method is explained in more detail here. A basin average can be computed by integrating over the basin function $\vartheta(\lambda, \theta)$ and dividing by its surface area,

$$\bar{T}_\vartheta = \frac{\int_\Omega \vartheta(\lambda,\theta) T(\lambda,\theta) d\omega}{\int_\Omega \vartheta(\lambda,\theta) d\omega}. \tag{4.12}$$

A spectral representation of T and ϑ can now be substituted. Using the orthogonality relation (Eq. 2.6) one then finds

$$\bar{T}_\vartheta = \frac{1}{\vartheta_{00}} \sum_{n=0}^{\infty} \sum_{m=-n}^{n} \vartheta_{nm} T_{nm}. \tag{4.13}$$

In practice, one always needs to truncate the series at some maximum degree N_{max}. Furthermore, since the data is often noisy, it is desirable to apply a filter to the surface load. Unfortunately, whereas the noise in the data is decreased by the filter and truncation, an attenuation of the signal may result, which is known as leakage-out. Likewise, a leakage-in effect may occur as the filter causes signal from the surrounding region to contaminate the basin average estimate. These leakage effects may be compensated to some extent by

applying a rescaling factor, denoted by f_ϑ, to the basin average. In matrix notation the approximated basin average reads:

$$\bar{T}_\vartheta \approx \tilde{T}_\vartheta = \frac{f_\vartheta}{\vartheta_{00}} \boldsymbol{\vartheta}^T \mathbf{W} \mathbf{t}. \tag{4.14}$$

Here, the filter operation is restricted to a linear matrix multiplication by a filter matrix $\mathbf{W}$. This type of filter includes a whole family of filters commonly applied in geodesy (e.g. an isotropic Gaussian filter Jekeli (1981); Wahr et al. (1998) or various anisotropic filters Swenson and Wahr (2006); Kusche (2007); Kusche et al. (2009); Klees et al. (2008)).

The averaging operation of Eq. 4.14 can also be seen as convolving the surface load by a smoothed basin function (Fenoglio-Marc et al., 2012):

$$\tilde{\boldsymbol{\vartheta}} = \mathbf{W}^T \boldsymbol{\vartheta}. \tag{4.15}$$

Since the filter matrix is not necessarily symmetric one must ensure that the transpose of $\mathbf{W}$ is applied to the basin coefficients. Fig. 4.8 shows examples for the case of the Mediterranean and Black Sea, which have been used in Fenoglio-Marc et al. (2012).
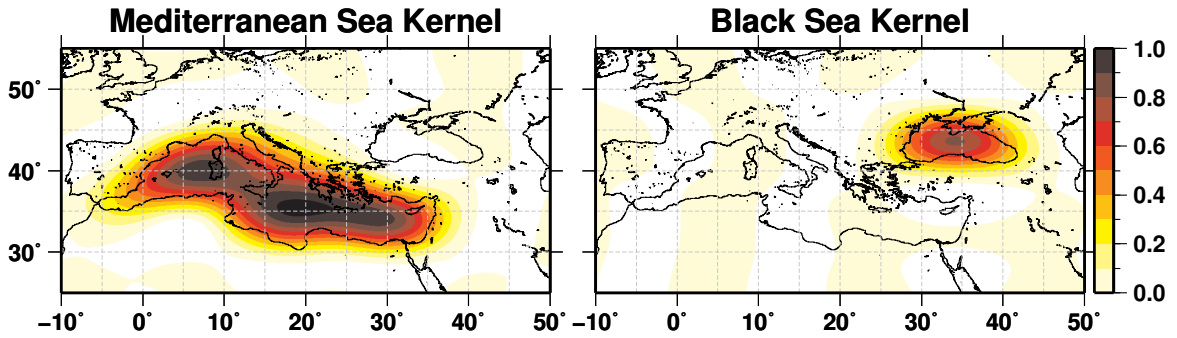
Figure 4.8: Smoothed basin kernels of the Mediterranean and Black Sea. The anisotropic filter (DDK3) comes from Kusche et al. (2009).

The scaling factor, f_ϑ, may be derived empirically through various methods. Principally, it depends on the signal of interest, the truncation degree and the geometry of the basin (Velicogna and Wahr, 2006a; Fenoglio-Marc et al., 2006, 2012; Baur et al., 2009). Further on in Sec. 5.1.6, averages over a variety of basins are computed. For each of these basin averages, a scaling factor, f_ϑ, is computed using the new method described below and in Rietbroek et al. (2014). Since the dominant component of the hydrological cycle, is annual, the first objective is to see how this seasonal signal is attenuated, for different truncations and filters. Firstly, a hydrological reference signal is obtained from the WGHM model (Döll et al., 2003). The simulated data, with daily resolution, were first expressed in terms of surface loading coefficients up to degree and order 120, and averaged over the GPS weeks, for the period 2002-2007. Subsequently, seasonal cosine and sine amplitudes[1] were estimated coefficient-wise.

---

[1]the intersect and a trend relative to 2005 were fitted simultaneously.

The linear representation allows the annual cosine and sine coefficient to be filtered separately such that the annual harmonic of the filtered and truncated basin average looks like:

$$\bar{T}_\vartheta^c \cos(\Omega(t - t_0)) + \bar{T}_\vartheta^s \sin(\Omega(t - t_0)) = \tilde{\boldsymbol{\vartheta}}^T \mathbf{t}^c \cos(\Omega(t - t_0)) + \tilde{\boldsymbol{\vartheta}}^T \mathbf{t}^s \sin(\Omega(t - t_0)) \quad (4.16)$$

Here, the cosine and sine annual amplitude of the vectorized surface load are denoted by $\mathbf{t}^{c/s}$. The annual frequency is denoted by Ω, and the cosine and sine amplitude of the basin average of the hydrology model are contained in $\bar{T}_\vartheta^{c/s}$. From the equation above it is trivial to see that the cosine and sine amplitudes are related as follows:

$$\bar{T}_\vartheta^c = \tilde{\boldsymbol{\vartheta}}^T \mathbf{t}^c \tag{4.17}$$

$$\bar{T}_\vartheta^s = \tilde{\boldsymbol{\vartheta}}^T \mathbf{t}^s \tag{4.18}$$

$$\tag{4.19}$$

The rescaling factor now follows from the damped annual amplitude of the filtered versus unfiltered WGHM data.

$$f_\vartheta = \sqrt{\frac{T_\vartheta^{c2} + T_\vartheta^{s2}}{\bar{T}_\vartheta^{c2} + \bar{T}_\vartheta^{s2}}} \tag{4.20}$$

Similarly, one can compute the expected phase shift, δt_a, for the annual signal:

$$\delta t_a = \frac{1}{\Omega} \left[\arctan\left(\frac{\bar{T}_\vartheta^s}{\bar{T}_\vartheta^c} \right) - \arctan\left(\frac{T_\vartheta^s}{T_\vartheta^c} \right) \right] \tag{4.21}$$

Values for the scale factor and the phase shift are tabulated for the considered basins in Tab 5.3.

4.2 Estimation of Fingerprint Magnitudes

The spherical harmonic representation used in Sec. 4.1, provides a complete and generic basis for solving surface loading. In this section, a different approach is pursued where each signal of interest is assigned a spatial 'fingerprint' from auxiliary data. In doing so, a dedicated set of basis functions together with their associated (time-dependent) coefficients may be superimposed and fitted to GRACE and altimetry data. This is graphically depicted in Fig. 4.9.

A major advantage of these 'fingerprints' over a spherical harmonic basis is that superimposed signals of different geophysical origin may be separated from each other based on their spatial signatures. Similar to the null-space plot of the previous section (Fig. 4.1), Fig. 4.10 shows this schematically for the joint inversion of GRACE and altimetry data. The combination of GRACE and altimetry principally allows the separation of the steric induced changes from the mass induced changes of sea level. With a 'fingerprint' basis these contributions can be further separated into their respective components (e.g. terrestrial water changes, individual ice sheets, steric modes, ..), as will be shown in the results 5.2.
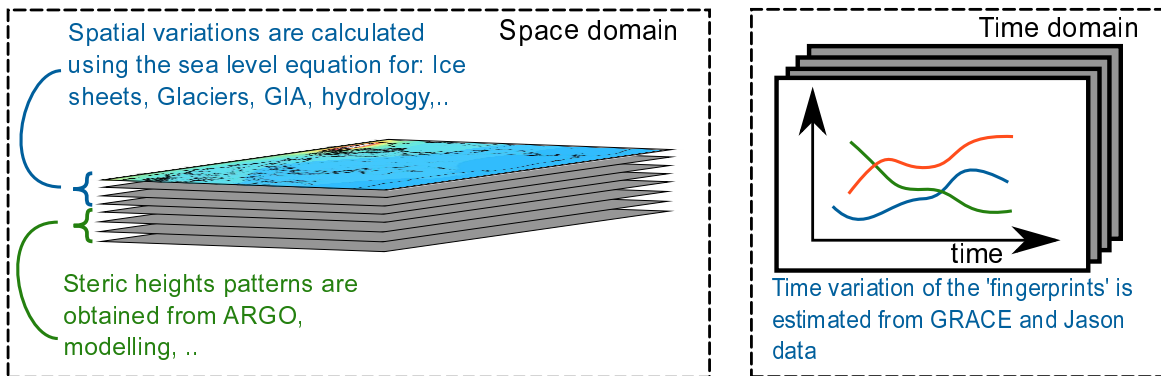
Figure 4.9: Principle of the fingerprint inversion. In the inversion, the spatial patterns are used as base functions. The associated time varying scales are fitted to the data.

The inversion considered here, focuses specifically on slowly changing phenomena but does not restrict itself to pure linear trends. This is important, as sea level changes contain a significant amount of inter-annual behavior which potentially renders a linear fit insignificant on the time scales considered.
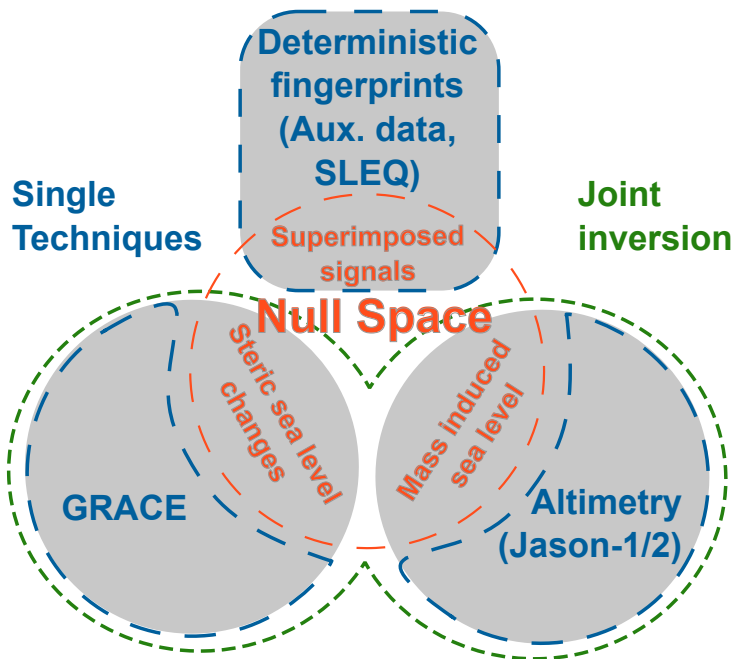
Figure 4.10: The combination of GRACE and altimetry, principally allows the separation of the steric sea level from the mass induced sea level. A further separation of the superimposed signals into its individual (melting) sources, and steric modes can be achieved by using predefined fingerprints from auxiliary data and the implementation of the sea level equation. the fingerprints effectively aid in this separation, although they are not used as a stochastic input.

4.2.1 Selected Fingerprints

The mass loading patterns and steric patterns used in the 'fingerprint' inversion, come from a variety of sources and are associated with different observables (e.g. Geoid change, uplift, steric changes). Table 4.1 summarizes the amount and types of patterns which are available

to the inversions discussed in this thesis. There are several changes which I made with respect to the patterns used in (Rietbroek et al., 2012a). (1) I used a different discretization for Antarctica, which allows a direct comparison with the results from Sasgen et al. (2012b). (2) The number of steric EOFs is strongly increased and is based on updated temperature and salinity from Ishii and Kimoto (2009). (3) The amount of GIA patterns derived from geophysical models is increased from 1 to 5. (4) The amount of hydrological EOFs is increased to 60. The overall increase in the number of parameters allows a better representation of the measurements.

The GRACE and Jason normal equation systems which are to be build contain the time-varying magnitudes of all of these patterns as unknown parameters. These parameters span a large enough solution space such that a variety of inversion setups can be obtained from the same set of normal equation systems. This is done by solving, fixing and/or merging the parameters of choice, at the normal equation level (see App. C).

Contribution	Dimension	Data/Ref.	Observable
Greenland	16(Basins)	Wouters et al. (2008)	N, U, S
Antarctica	27(Basins)	Zwally and Giovinetto (2011)	N, U, S
Glaciers	16(Clusters)	WGI(NSIDC, 1999) GLIMS(Raup et al., 2007)	N, U, S
Hydrology	60(EOFs)	WGHM(Döll et al., 2003)	N, U, S
GIA	1 total + 5 decompos.	ICE-5G, VM2-2 Klemann and Martinec (2009)	$\dot{N}, \dot{U}, \dot{S}$
Steric	100(EOFs)	Ishii and Kimoto (2009)	h_{steric}
Compl. steric (Bootstrap)	100(EOFs)	This section	$h_{steric} + \delta h_{dyn}$

Table 4.1: Description of the patterns available to the inversion.

Ice Sheets

To parameterize the surface mass loading on the major ice sheets of Greenland and Antarctica, the drainage divides from Wouters et al. (2008) and Zwally and Giovinetto (2011) were used. As depicted in Fig. 4.11, Greenland is divided in 8 sectors, of which each sector is subdivided in a section above and below 2000 meter elevation. The delineation of Antarctica in 27 sectors is shown in the right of Fig. 4.11.

For each drainage basin, a self consistent sea level was computed using the SLE from Sec. 2.4.1. Each drainage basin therefore results in a global surface load (ice+sea) which conserves mass globally and which is associated with an equipotential ocean response. From this surface load, (linearly related) observables such as geoid height changes, uplift and relative sea level may be computed and linked to observations.

Land Glaciers

Most of the land glaciers are grouped in mountainous areas. Due to the sheer amount of glaciers and their proximity to each other, it is not possible to estimate their contributions individually. For that reason, the contribution of the glaciers are considered for clusters.
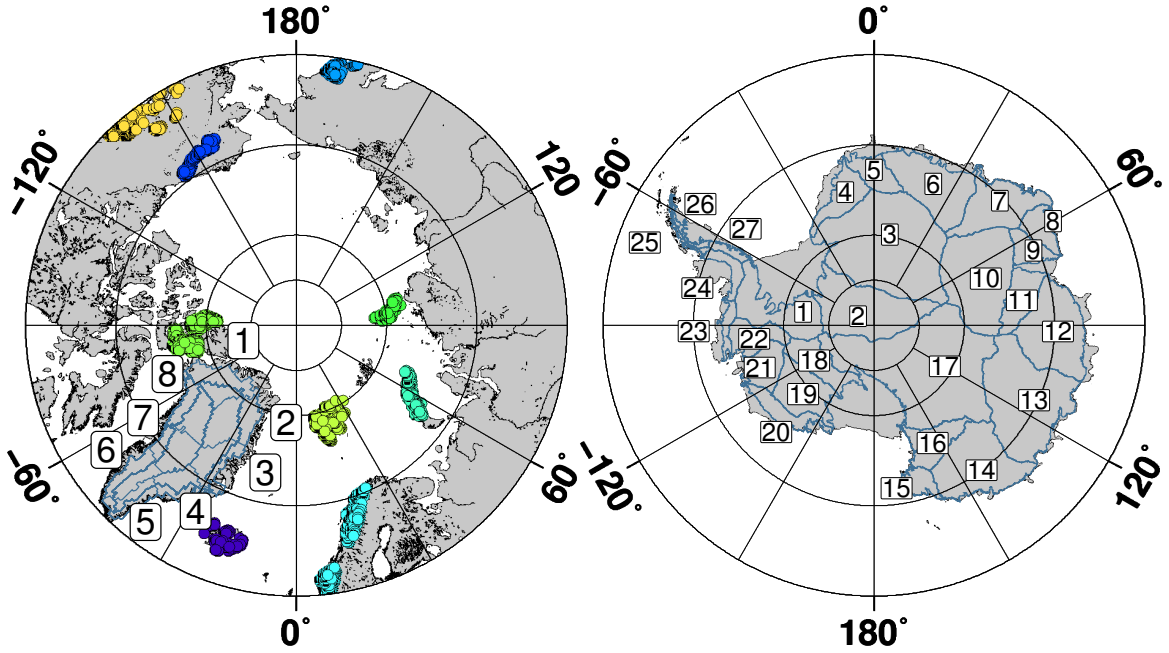
Figure 4.11: Drainage basins in Greenland and Antarctica and the northernmost land-glacier clusters. The drainage basins in Greenland, Antarctica are obtained from Wouters et al. (2008) and Zwally and Giovinetto (2011) respectively. The locations of the land glaciers are taken from WGI/GLIMS.

The glacier positions can be obtained from the GLIMS (Raup et al., 2007) and/or WGI (NSIDC, 1999) databases. Since none of the two databases contains all glaciers[2], I merged them using the GRASS GIS software (GRASS Development Team, 2008). It should be noted that many larger glaciers are represented by multiple points in the database (hence the large amount of glacier sources in Fig. 4.12).

Each glacier cluster, indicated in Fig. 4.12, is constructed by extracting the position of all the individual glaciers in the region of interest (for example the Himalayas) and adding them as unit loads:

$$T^{Himalaya}(\theta, \lambda) = \sum_{n,m}^{\infty} T_{nm}^{Himalaya} \bar{Y}_{nm}(\theta, \lambda), \tag{4.22}$$

$$\text{with} \quad T_{nm}^{Himalaya} = \frac{1}{N_{1Gt}} \sum_{i \in Himalaya}^{N} \bar{Y}_{nm}(\theta_i, \lambda_i) \tag{4.23}$$

The combined cluster surface load, represented by the spherical harmonic coefficient, $T_{nm}^{Himalaya}$, is normalized with the factor N_{1Gt} such that the resulting surface load per cluster amounts to 1 Gton. The above approach produces glacier cluster loads which are larger in regions with a higher glacier density. The use of such clusters to represent land glacier loads, are

---

[2]at the time of writing efforts are underway to harmonize the two databases
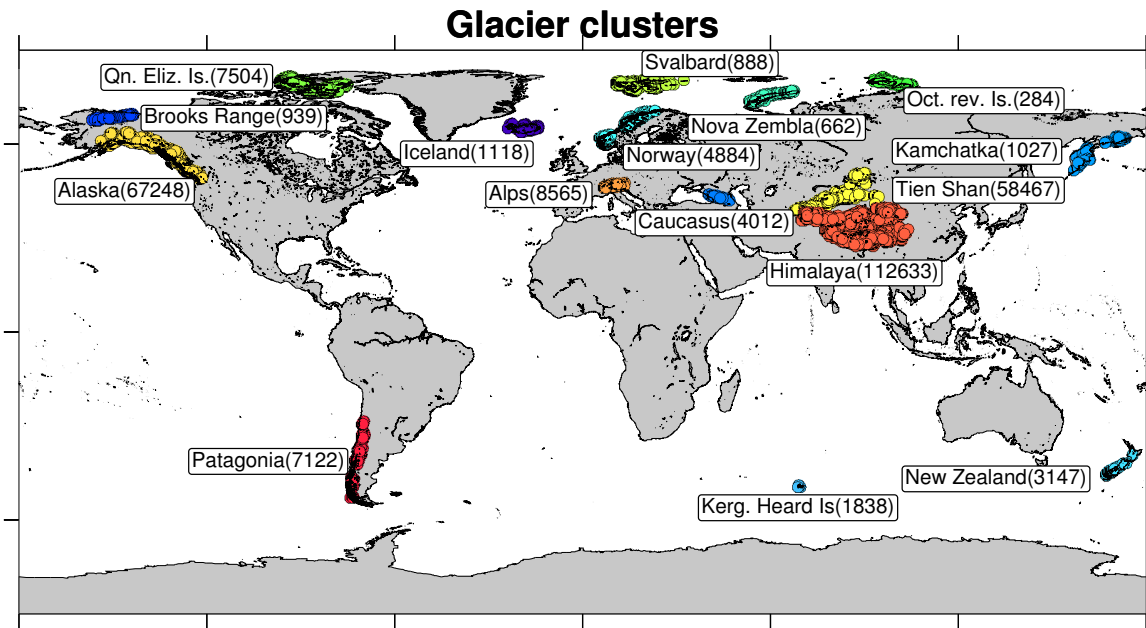
Glacier clusters

Figure 4.12: Geographical distribution of glacier clusters tagged with the corresponding amount of sources as used in the inversion. Larger glaciers may consist of multiple sources(taken from the WGI and GLIMS databases).

based on the following underlying assumptions: (1) all glaciers in the database are approximately the same size, and (2) the time behavior of the glaciers in one cluster is synchronous. It is possible to reduce the effect of assumption (1) by using area dependent disk-loads in Eq. 4.23. But since not all glacier areas are present in the database this poses a problem. Furthermore, it is not necessarily true that the melting of glaciers is proportional to its size. As is illustrated by simplified linear glacier ablation models (Huybers and Roe, 2009), the change in glacier length mainly depends on the precipitation, the melt-season temperature and the length (size) of the glacier itself. Its sensitivity to these forcings is however determined by glacier specific parameters, such as its basal slope. For the present study however, this added complexity is assumed to average out over the entire cluster, and consequently each glacier source is assumed to change according to a unit load. In addition, I implicitly assume for now that the climatic characteristics (e.g. changes in melt-season temperature and precipitation) are highly correlated within the clusters.

Steric Sea Level

There are several gridded datasets which contain observed temperature and salinity variations in the upper part of the ocean (Hosoda et al., 2008; Ishii et al., 2006; Ishii and Kimoto, 2009). In this thesis, monthly temperature and salinity data from Ishii and Kimoto (2009) are used. These are derived from an objective analysis (also known as optimal interpolation) of data from ARGO floats and XBTs (eXpandable Bathythermograph). Regions which are poorly sampled are constrained to monthly climatological values. This holds in particular for the deeper section of the data (700-1500 m). Changes below 1500 m are not provided.

From the depth dependent data, steric sea level changes have been computed using Eqs.

2.121, in the upper 700 m of the ocean. The Gibbs Seawater Oceanographic Toolbox (Mc-Dougall and Barker, 2011) is used to implement the equation of state of sea water.

A limited amount of patterns is needed to parameterize the steric variations of sea level for the fingerprint inversion. These are obtained by a Principal Component Analysis (PCA[3], Preisendorfer and Mobley, 1988) of the steric heights. For completeness, a quick review of the applied PCA method is provided in Appendix D. Steric heights from the period 1990 until 2012 are used in the analysis, such that the exceptionally strong El Niño event of 1997-1998 was included.
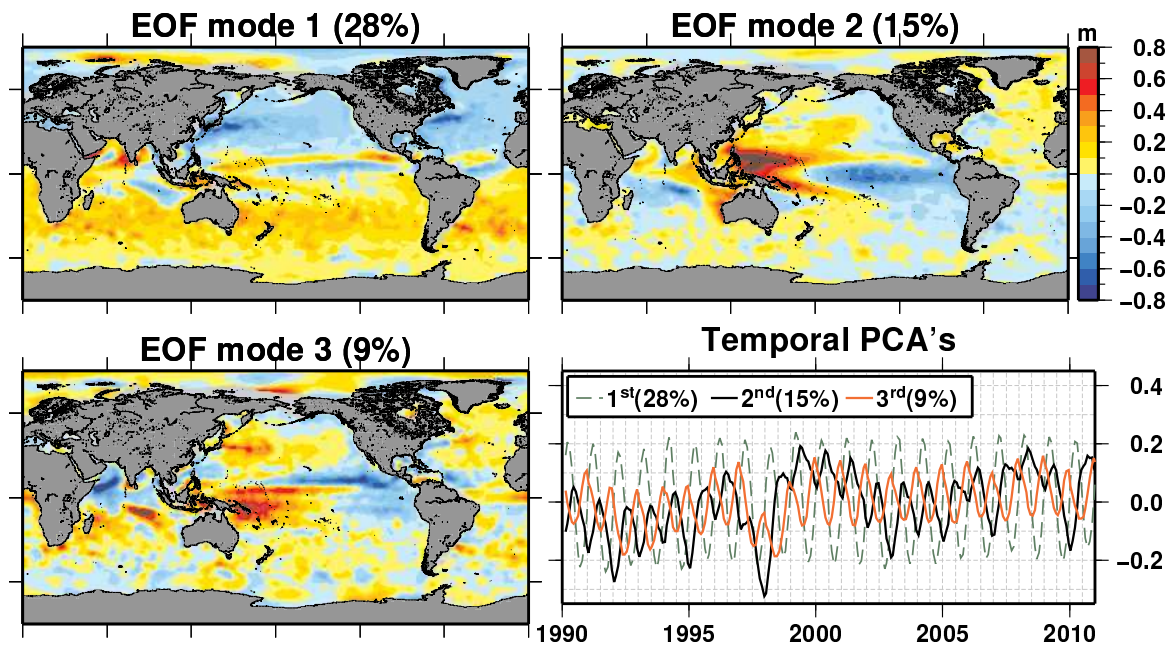
Figure 4.13: The first three spatial and temporal EOF modes of the steric height variations derived from Ishii and Kimoto (2009) data. The percentages in the legend indicate the variance explained by the mode.

The first 3 spatial and temporal modes of the steric sea level changes are shown in Fig. 4.13. Since the steric heights are provided on an equidistant grid, an additional weighting by the cell area has been applied to prevent overweighting the data at higher latitudes. Besides the seasonal variation which is visible as a north-south oscillation in the first mode, it is clear that the El Niño La Niña cycle is apparent in the second and third modes (and in other modes not shown here). The percentage of variance explained by the modes levels off only slowly with the amount of EOFs. The first three modes only explain 52% of the variance in the ARGO-derived steric sea level. For that reason, 100 EOF modes are accounted for in the inversion which explain almost 99% of the steric height variations.

---

[3]also known as Empirical Orthogonal Function analysis

Bootstrapping Additional Steric Patterns from the Altimetry Residuals

Although placed before the combination step, this subsection is actually written in retrospect after the computation of a global combination (readers are referred to Sec. 4.2.3 for more information when confusion arises). The reason is that, after an initial inversion, significant large scale signals were present in the altimetry residuals, justifying an extension of the steric pattern space as proposed up to now. Since the complementary patterns here are essentially extracted from the data itself, this procedure is nicknamed as a 'bootstrapping' procedure.

To justify this procedure, I computed the along-track altimetry residuals by propagating the initial inversion results to the altimeter bins. The propagated solution contained all relevant mass loading and steric patterns and constant altimeter offsets. These include 16 Greenland patterns, 27 Antarctic patterns, all land glaciers cluster, 5 complementary GIA patterns, 60 hydrological patterns and 100 EOFs as obtained from the Ishii and Kimoto (2009) data.

From the along track altimetry, the propagated solution and the residuals, global mean sea level changes were computed. Furthermore, time varying grids were computed using gridding software from the gmt toolbox (Smith and Wessel, 1990). The resulting grids do not seem to be affected by altimetry specific (orbit) errors, so more advanced statistical interpolation routines (e.g. Le Traon et al., 1998) are not deemed necessary at the moment.
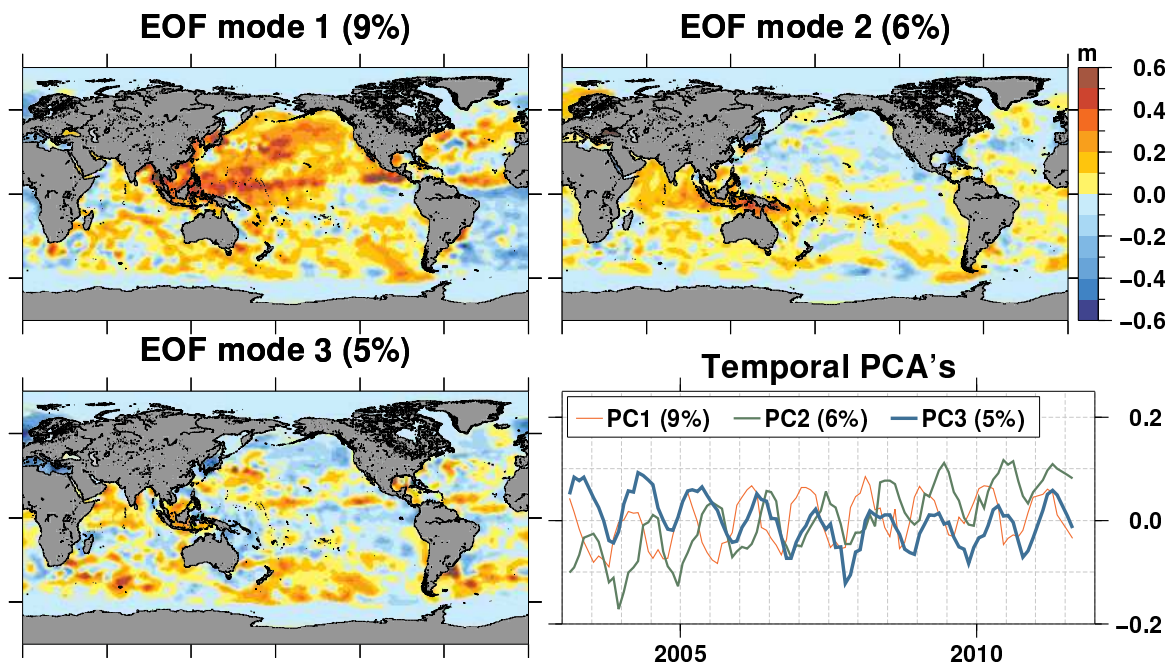
Figure 4.14: EOF modes obtained from the altimetry residuals

The global[4] mean sea level changes, are plotted in Fig. 4.15, where 'Inv1' denotes the inversion without the (to be computed) bootstrapping patterns. Alarming is that, although

---

[4]restricted by the region as covered by the altimetric footprints

the reconstructed total mean sea level change agrees to a large extent with the altimetry, the residuals (bottom subplot) are as large as the seasonal variability of the reconstructed steric sea level itself. Since the reconstructed steric sea level is in phase with the residual it leads to the suspicion that the inversion significantly underestimates the steric sea level. An alternative explanation could be that the estimated hydrological component, which is out of phase with its steric counterpart (see Fig. 5.13), is overestimated. This appears however less likely as the GRACE data constrains hydrology in a more direct sense.

To study the spatial nature of the altimetry residual, I applied a principal component analysis on the gridded residuals. However, since PCA may be strongly affected by few grid points with large variances I filtered the residuals with a Gaussian filter with a half-width of 200 km. This procedure reduces the variances in highly dynamic, but localized, regions, such as those associated with boundary currents, whereas the relative strength of large scale effects, which are of interest in the present context, increase.
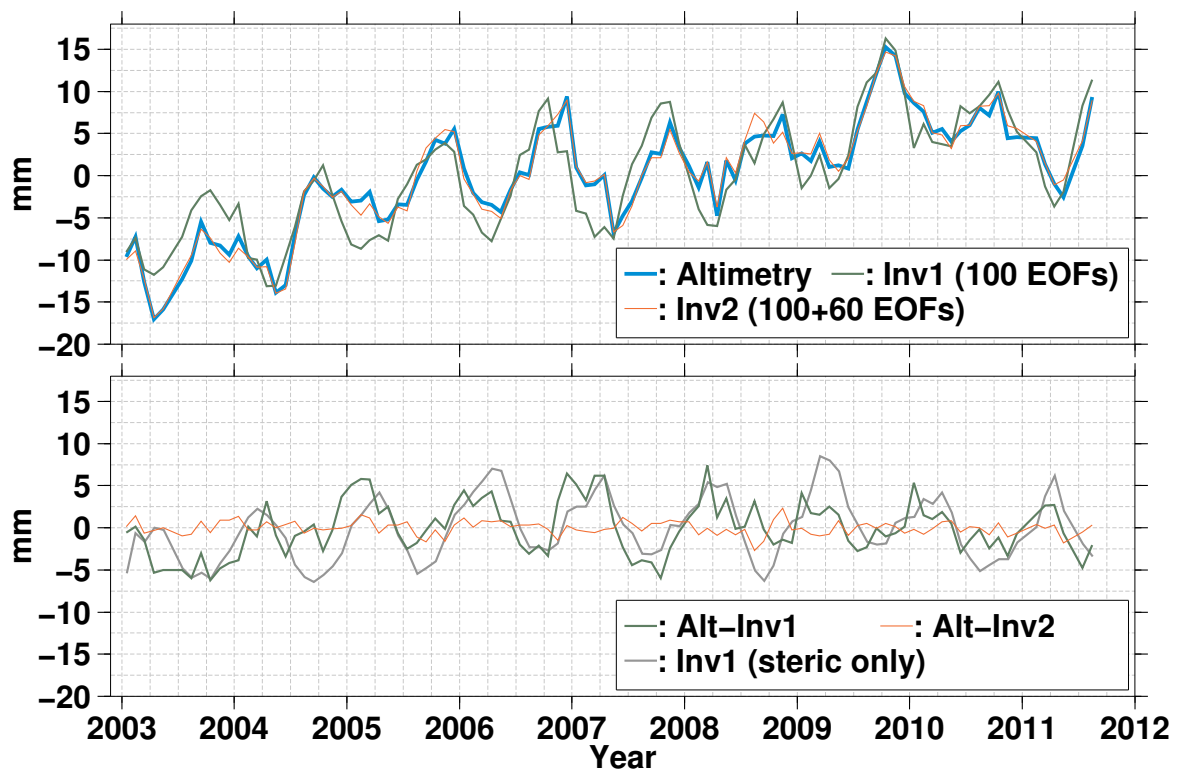
Figure 4.15: Geocentric mean sea level of the altimetry and residual

The first three resulting modes, explaining only 20% of the variance, are displayed in Fig. 4.14. Clearly, the spatial nature of the patterns hint to remaining steric signals lying *outside* the solution space of the Ishii-EOF modes, which are derived from gridded products in the upper 700 m of the ocean. The most obvious explanation, is that these signals arise from effects occurring in the deeper layers of the ocean. Sampling problems with the ARGO drifters are a less likely explanation as the signals are widespread compared to the ARGO sampling. Finally, it is also possible that remaining errors in the background models

are reflected in these patterns. Errors in wind-stress, inducing erroneous bottom pressure changes through Ekman pumping, may potentially leak into the residuals. It should be stressed that, since the first order effect is already subtracted from the altimetry data by using the reference ocean model (OMCT), the remaining effects are expected to be at the level of the *error* of the ocean model itself.

The time dependency of the principal components is dominated by seasonal behavior overlying strong trends. This suggests that neglecting these modes potentially introduces errors in the reconstructed sea level from the inversion. Indeed Fig. 4.15 clearly shows that when 60[5] 'bootstrapping' modes, explaining 86% of the variance, are introduced in the inversion (denoted by 'Inv2') the residual significantly decreases to an acceptable level.

It is worth noticing that natural oscillations such as the El Niño -La Niña cycle and the pacific decadal oscillations are not apparent from the modes. The typical horse shoe structures are difficult to spot in the spatial modes and the time variations also appear to reflect mainly seasonal variations and trends.

In summary, the steric patterns are obtained in a step-wise approach. Initially, only the patterns reflecting changes in the shallow ocean are used in the inversion. These are then augmented by deeper steric patterns which are obtained from an analysis of the altimetric residuals.

Terrestrial Hydrology

A prominent source of mass variations originate from the dynamics of the terrestrial hydrological water cycle. In the fingerprint inversion, such variations must either be reduced a priori or co-estimated in the inversion. The latter approach, pursued in this thesis, requires a set of base functions which parametize the most dominant water storage signals occurring in the terrestrial water cycle.. Similar to the steric height variations, these patterns are obtained from a principal component analysis of the simulated total water storage from WGHM (Döll et al., 2003). The model output also contains water storage variations in regions where there are also land glaciers. This can potentially disturb the estimated land glacier factors as the same glacier signal is contained in both the hydrological and glacier fingerprints. For that reason, I excluded the glacier cluster regions from the principal component analysis. Also excluded from the analysis are the ocean region, Greenland and Antarctica where the model provides no reliable data.

The first 60 EOFs are extracted from WGHM for further analysis. Since the EOFs represent mass changes on land, they also induce a self consistent sea level response. As with the ice sheet variations and the glaciers clusters, I construct a global self-consistent response of the ocean to each EOF. The resulting global patterns are then used as base functions in the inversion. The global surface load of the first three modes are plotted in Fig. 4.16. Compared to the continental load, the oceanic variations are an order of magnitude smaller. Nevertheless large scale, ocean-wide are visible which may affect the low degree coefficients of the gravity field.

---

[5]a total of 100 EOFs were computed.

76
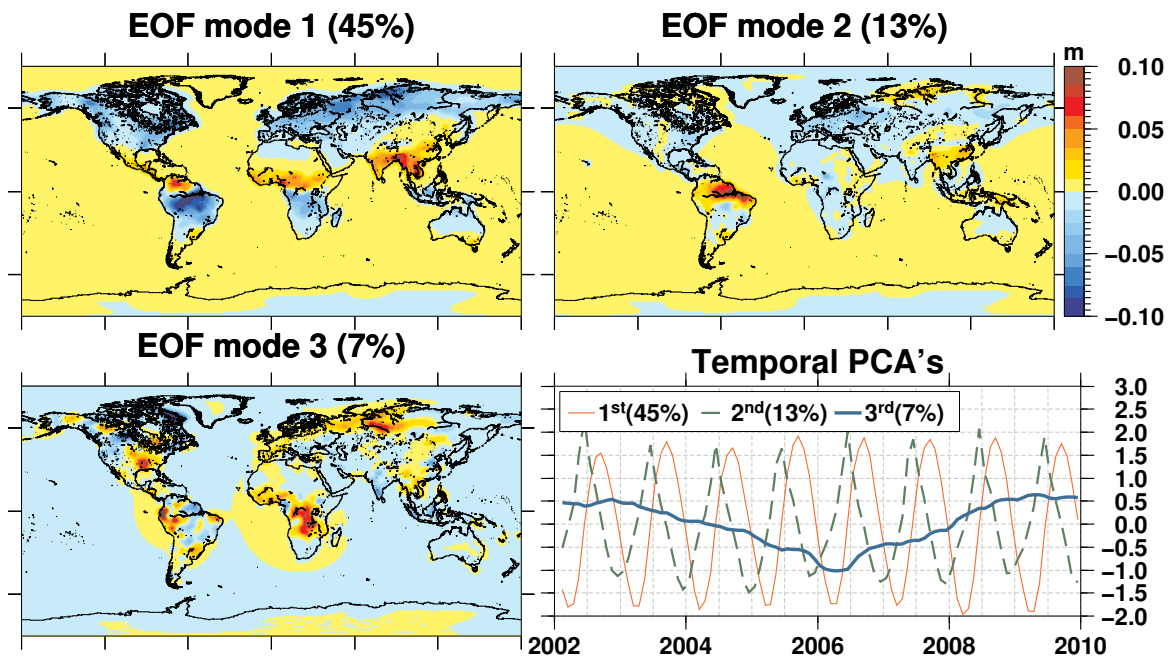
Figure 4.16: The self consistent surface load as computed from the first three hydrological EOFs from WGHM (Döll et al., 2003), and the associated time variations of the principal components. The sign of the modes is adapted such that each EOF is associated with a positive contribution to the ocean.

GIA

Finally, secular variations in geoid height, uplift and relative sea level are induced by glacial isostatic adjustment. In this thesis, 5 different GIA simulations (present day rates) are used, which were computed using a spectral finite element code(Martinec, 2000; Klemann and Martinec, 2009)(simulations courtesy of Volker Klemann).

The applied ice history and the radially symmetric incompressible Earth model correspond to ICE-5G (Peltier, 2004) and the associated VM2-2 model. Six different forcing scenarios are available to the inversion: (1) the total effect of the entire ice-history, and a partitioning in 5 different ice loads: (2) Laurentide, (3) Fennoscandia, (4) Antarctica, (5) Greenland and (6) complementary sources. The truncation degree for this simulation is relatively low ($l_{max} = 64$), but since most of the GIA signal has long wave-length characteristics this is not expected to be problematic.

The individual contributions, in terms of uplift are shown in Fig. 4.17. Since the ocean function is time dependent, the model runs from the single sources do not add up to the results of the model run forced with the combined glacial load. The net difference is comparably small and is shown in the bottom right subplot of Fig. 4.17, although in some parts it has the same order of magnitude as the uplift induced by the complementary sources. Nevertheless, considering that there is a considerable spread in contemporary GIA simulations, realistic GIA signals may be constructed by adding the contributions together, as is assumed within the fingerprint inversion. Recent efforts, such as those within the Ice

sheet Mass Balance Inter-comparison Exercise (IMBIE), aim at harmonizing available GIA models in order to obtain more realistic estimates of the mass changes of the Earth's ice sheets (Shepherd et al., 2012; Spada et al., 2011).
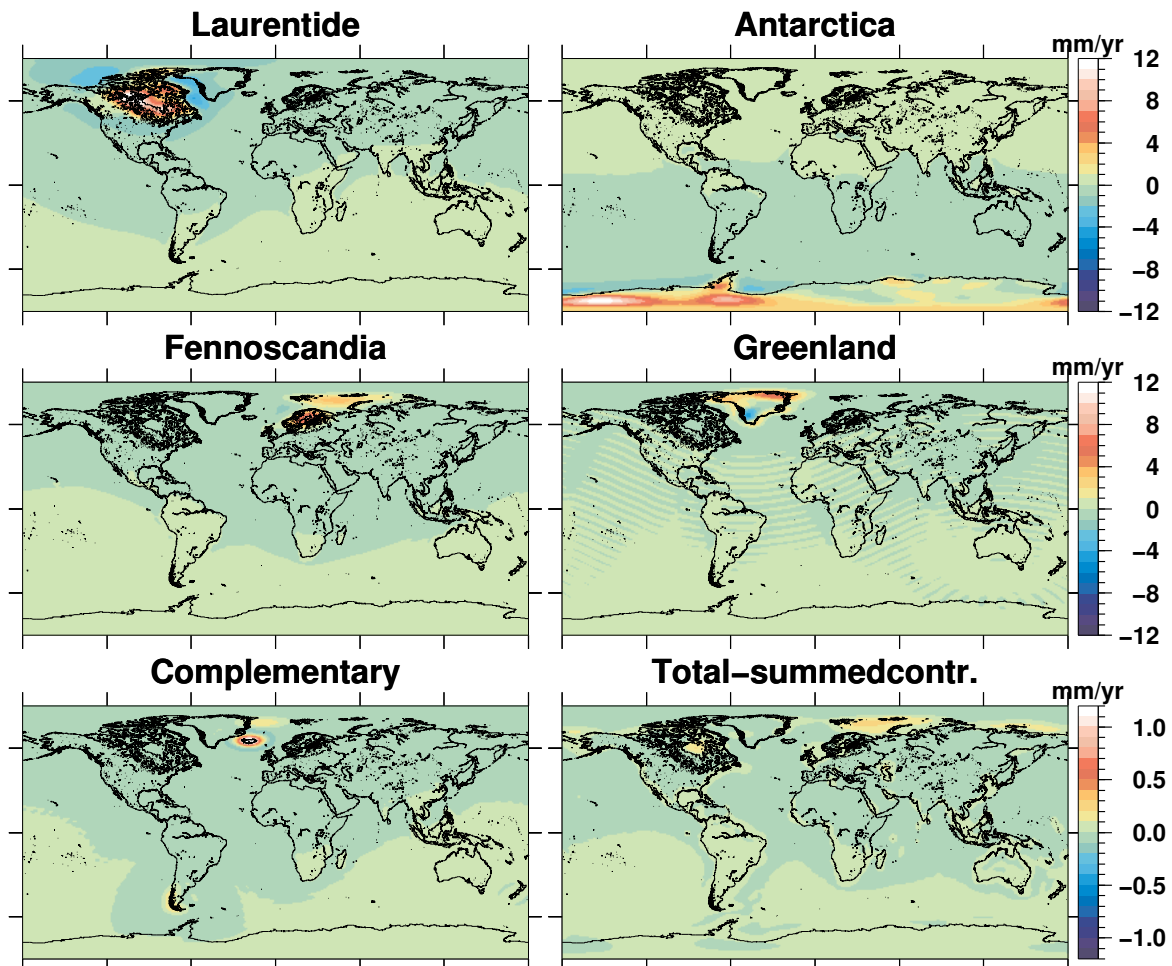
Figure 4.17: GIA uplift in $^{mm}/_{yr}$ for the 5 different patterns used in the inversion. The bottom right subplot indicates the difference between the total GIA pattern (model forced with the combined glacial sources) minus the reconstructed total uplift (adding the contribtions from the isolated sources). Note the scale difference of the bottom two subplots.

Using the theory from Sec. 2.3, I converted the simulated geoid and deformation rate from the CM to the CF frame, which is possible since the degree 1 signal from all three observables (geoid, vertical and horizontal deformation) are provided. This step is done since the (instantaneous) CF frame lies more closely to the reference frame origin of the altimetry data compared to the CM.

The degree 0 coefficients of the geoid, and (horizontal and vertical) deformation were initially set to zero. However, GIA induced changes in the volume of the ocean basin also induce uniform shifts of the sea level which are sensed by an altimeter. A correction, ap-

plicable to the observation equation of the altimeter, can however be computed as follows. As discussed in in Sec. 3.2.1 an altimeter will sense changes in geocentric sea level

$$\tilde{S} + U = N + \frac{\Delta\phi}{g}. \tag{4.24}$$

The uniform shift, $\frac{\delta\phi}{g}$, manifesting itself as the degree 0 coefficient of the quasi spectral sea level $\tilde{S}$, can be computed by imposing that the ocean mean of the GIA induced relative sea level is zero:

$$\bar{S}_{oce} = 0 = \frac{1}{A_{Oce}} \int_{Oce} \tilde{S} d\omega. \tag{4.25}$$

Substituting Eq. 4.24 and isolating $\frac{\Delta\phi}{g}$ yields

$$\frac{\Delta\phi}{g} = -\frac{1}{A_{Oce}} \int_{Oce} (N - U) d\omega. \tag{4.26}$$

In the spherical harmonic domain, this correction is computed from the fully normalized Stokes coefficients C_{nm} and the uplift coefficients U_{nm} which then simply reduces to [6]:

$$\tilde{S}_{00} = -\frac{1}{O_{00}} \sum_{n=1}^{l_{max}} \sum_{m=-n}^{n} O_{nm}(aC_{nm} - U_{nm}). \tag{4.27}$$

Underlying this correction is the assumption that the ocean mean of the relative sea level rise is zero. This assumption is quite realistic as the present day mass flux of the ICE-5G ice history model is virtually zero. Or in other words, the mass content of the ocean does not change due to GIA as the ice history does not exhibit a present day rate of melting.

4.2.2 Observation Equations of the Fingerprint Inversion

GRACE
Changes in the Stokes coefficients from GRACE are linked to the mass related components of the fingerprints. The unknown time varying magnitude can be linearly linked to the Stokes coefficients of GRACE:

$$\begin{bmatrix} \delta C_{20} \\ \vdots \\ \delta C_{n_{max}n_{max}} \end{bmatrix} = \mathbf{A} \begin{bmatrix} \mathbf{x}_{ice} \\ \mathbf{x}_{glac} \\ \mathbf{x}_{hydro} \\ \mathbf{x}_{gia} \end{bmatrix} + \epsilon. \tag{4.28}$$

Since mass is conserved globally, and the GRACE data has its reference frame origin in the center of mass of the Earth system, only coefficients with degrees larger than 1 are considered. This automatically transforms all of the fingerprints to the CM frame. The unknown time varying magnitudes, are grouped in different mass contributions. $\mathbf{x}_{ice}$ represents the factors associated with the ice sheets in Greenland and Antarctica, $\mathbf{x}_{glac}$ contain the magnitudes of the remaining (clusters of) land glaciers, and $\mathbf{x}_{hydro}$ is linked to the terrestrial

---

[6]see also Eq. 4.13 for the spectral representation of a basin average

hydrological variations. The variations due to glacial isostatic adjustment effects are contained in the vector $\mathbf{x}_{gia}$.

The columns of the design matrix $\mathbf{A}$ are composed of the corresponding fingerprints expressed in terms of normalized Stokes coefficients:

$$\mathbf{A}(t) = \begin{bmatrix} \delta C_{20}^{Greenland1} & \delta C_{20}^{Greenland2} & \cdots & \delta C_{20}^{gia_N}(t-t_0) \\ \vdots & \vdots & & \vdots \\ \delta C_{n_{max}n_{max}}^{Greenland1} & \delta C_{n_{max}n_{max}}^{Greenland2} & \cdots & \delta C_{n_{max}n_{max}}^{gia_N}(t-t_0) \end{bmatrix}. \tag{4.29}$$

For convenience, the fingerprints of the ice sheets and the land glaciers are normalized such that its mass contribution represents 1 Gton. In this way, the unknown factors $\mathbf{x}$ can be directly interpreted as eustatic sea level contributions in the units Gtons. It should be noted that no such normalization is applied in the case of the GIA contribution. Since the present day GIA component of relative sea level rise is zero, a division by zero would be the result. Furthermore, a normalization is also not recommended when using EOFs as base functions (which is the case for the hydrological and steric parameters). Often, there are EOFs which have a (almost) zero contribution to sea level. A normalization would then induce large scale differences between the columns of $\mathbf{A}$.

The GIA induced signal has a secular nature, the corresponding GIA potential rates are therefore scaled by the time difference with respect to the reference time t_0. For the release 05 GRACE data, the 1st of January 2005 is used, which is the reference time of the static background model Eigen-6c. Currently, the GIA component is the only time dependent factor in the design matrix. It is therefore smarter to store only the time independent part, without $(t-t_0)$, of the matrix and introduce this time dependency at the level of the normal equations as described in App. C.5.

Monthly normal equations of GRACE release 05 are available up to degree and order 180. In addition to the standard de-aliasing models, the time variable component of the Eigen-6C is removed a priori (in the standard GRACE solutions, this signal is restored). To make the signal consistent with the altimetry data, the time varying component is restored on the normal equation level in accordance with App. C.3. On top of that, I also apply an a priori correction which ensures that the background de-aliasing model has a zero mean over the ocean. This makes the signal content consistent with that of the altimeters, and it prevents the background models to introduce artificial changes in the ocean mean. The latter potentially cause (systematic) errors in the estimated parameters.

This large truncation degree of the normal equation systems does not allow a direct solution of all the Stokes coefficients. However using the transformation method of App. C.5, the normal equation systems may be transformed in terms of fingerprint magnitudes, without the need for solving but with retaining the full information up to degree and order 150. Coefficients with degrees larger than 150 are eliminated from the normal equation systems.

$$\mathbf{N}_{GRC}^{\dagger} = \mathbf{A}^T \mathbf{N} \mathbf{A},$$

$$\mathbf{b}_{GRC}^{\dagger} = \mathbf{A}^T \mathbf{b}, \tag{4.30}$$

$$[\mathbf{1}^T \mathbf{P} \mathbf{1}]^{\dagger} = \mathbf{1}^T \mathbf{P} \mathbf{l}. \tag{4.31}$$

The transformation operation drastically reduces the amount of unknowns, and thus the storage requirements, of the normal equation system from approximately 23000 to only about 125 (the number of mass related fingerprints).

Altimetry

As explained in Sec. 3.2.1, an altimeter is sensitive to changes in the geoid height. In addition, the range measurement is also affected by changes in the volume of the ocean basin and ocean-wide shifts due to the changing ocean mass. The altimetric observable for each surface loading fingerprint therefore consists of the (elastic) term $\tilde{S} + U$. The GIA component has the same form.

Similar to GRACE, a linear observation equation can be constructed for the corrected altimetry data (see Eq. 3.7):

$$\begin{bmatrix} \Delta h_i \\ \vdots \\ \Delta h_M \end{bmatrix} = \mathbf{YB} \begin{bmatrix} \mathbf{x}_{ice} \\ \mathbf{x}_{glac} \\ \mathbf{x}_{hydro} \\ \mathbf{x}_{gia} \end{bmatrix} + \mathbf{KC} \begin{bmatrix} \mathbf{x}_{ster} \end{bmatrix} + \mathbf{P} \begin{bmatrix} t_x \\ t_y \\ t_z \end{bmatrix}_{CN-CF} + \epsilon. \tag{4.32}$$

The columns of matrix $\mathbf{B}$ contain the geocentric sea level changes associated with the unknown patterns:

$$\mathbf{B}(t) = \begin{bmatrix} \tilde{S}_{00}^{Greenland1} & \tilde{S}_{00}^{Greenland2} & \cdots & \tilde{S}_{00}^{gia_N}(t-t_0) \\ a\delta C_{10}^{Greenland1} & a\delta C_{10}^{Greenland2} & \cdots & a\delta C_{10}^{gia_N}(t-t_0) \\ \vdots & \vdots & & \vdots \\ a\delta C_{n_{max}n_{max}}^{Greenland1} & a\delta C_{n_{max}n_{max}}^{Greenland2} & \cdots & a\delta C_{n_{max}n_{max}}^{gia_N}(t-t_0) \end{bmatrix}. \tag{4.33}$$

here, the Stokes coefficients scaled by the Earth radius a represent the induced geoid changes. To be as close to the altimeter reference system as possible, the geoid changes are provided in the CF system, by choosing the appropriate degree 1 coefficients. The matrix $\mathbf{Y}$ maps the patterns, expressed in spherical harmonics, to the locations of the altimeter measurements:

$$\mathbf{Y} = \begin{bmatrix} \bar{Y}_{00}(\theta_1, \lambda_1) & \cdots & \bar{Y}_{n_{max}n_{max}}(\theta_1, \lambda_1) \\ \vdots & \vdots & \vdots \\ \bar{Y}_{00}(\theta_M, \lambda_M) & \cdots & \bar{Y}_{n_{max}n_{max}}(\theta_M, \lambda_M) \end{bmatrix}. \tag{4.34}$$

The amount of rows of $\mathbf{Y}$ can reach several hundred thousand. From a storage perspective it is therefore advised not to compute the matrix $\mathbf{Y}$ explicitly.

The steric EOFs, provided on a geographic grid, are stacked in the matrix $\mathbf{C}$. These are then interpolated to the altimeter points by means of the (sparse) bi-linear interpolation

matrix $\mathbf{K}$.

Finally, a set of correction parameters is introduced, which may absorb remaining differences between the origin of the altimeter measurements (a CN frame) and the CF frame. The estimated offset is expected to be small as the origin of the reference system of the altimeters is expected to be close to the center of surface figure (CF). This issue is further elaborated upon in Sec 4.2.4. For each observation, the translation vector, $\begin{bmatrix} t_x & t_y & t_z \end{bmatrix}^T_{CN-CF}$, is projected onto the local radial direction by matrix $\mathbf{P}$

$$\mathbf{P} = \begin{bmatrix} \mathbf{e}^T_{1,h} \\ \vdots \\ \mathbf{e}^T_{M,h} \end{bmatrix} = \begin{bmatrix} \sin\theta_1\cos\lambda_1 & \sin\theta_1\sin\lambda_1 & \cos\theta_1 \\ \vdots & \vdots & \vdots \\ \sin\theta_M\cos\lambda_M & \sin\theta_M\sin\lambda_M & \cos\theta_M \end{bmatrix}. \tag{4.35}$$

When all the unknowns are stacked in one vector the resulting observation equation is described by:

$$\begin{bmatrix} \Delta h_i \\ \vdots \\ \Delta h_M \end{bmatrix} = \begin{bmatrix} \mathbf{YB} & \mathbf{KC} & \mathbf{P} \end{bmatrix} \begin{bmatrix} \mathbf{x}_{ice} \\ \mathbf{x}_{glac} \\ \mathbf{x}_{hydro} \\ \mathbf{x}_{gia} \\ \mathbf{x}_{ster} \\ \mathbf{t}_{CN-CF} \end{bmatrix} + \epsilon = \mathbf{D} \begin{bmatrix} \mathbf{x}_{ice} \\ \mathbf{x}_{glac} \\ \mathbf{x}_{hydro} \\ \mathbf{x}_{gia} \\ \mathbf{x}_{ster} \\ \mathbf{t}_{CN-CF} \end{bmatrix} + \epsilon. \tag{4.36}$$

For each altimeter, the normal equations can now be build by using the range error as a diagonal error-covariance, $\mathbf{C}_{alt} = \text{diag} \begin{bmatrix} \sigma\Delta h_1^2 \cdots \sigma\Delta h_M^2 \end{bmatrix}$. Similar to the GRACE processing, the introduction of the secular time dependency is postponed until after the assembly of the normal equations. It now also becomes clear what the advantage of the OpenADB altimeter data is. In the so-called 'BINS' format, the altimeter data is sampled in bins which do not change position in time. This means that for each mission (here Jason 1, Jason 1 extended mission, and Jason 2), a design matrix $\mathbf{D}$ can be precomputed (each one is approximately 700 Mb) and stored on disk. The normal equation systems are transformed according to

$$N_{alt} = \mathbf{D}^T \mathbf{C}_{alt}^{-1} \mathbf{D}, \tag{4.37}$$

$$\mathbf{b}_{alt} = \mathbf{D}^T \mathbf{C}_{alt}^{-1} \Delta\mathbf{h}, \tag{4.38}$$

$$[\mathbf{l}_0^T \mathbf{P} \mathbf{l}_0]_{alt} = \Delta\mathbf{h}^T \mathbf{C}_{alt}^{-1} \Delta\mathbf{h}. \tag{4.39}$$

A screening of the data has been performed, before the assembly of the normal equation systems to reduce the effect of outliers and seasonal sea-ice at the higher latitudes. For this means, data with excessive large sea level anomalies and range errors (magnitudes larger than 1 m), have been excluded. In addition, a sea-ice mask, derived from the maximum sea-ice extent (Cavalieri et al., 1996) has been applied to the data. This step removes valid measurements in the summer months, and reduces the maximum latitude reached. At the same time however, a potential seasonal aliasing of high latitude signal is also avoided (data at the higher latitudes is constrained only during the summer months).

4.2.3 Combination and Weighting of Altimetry and GRACE

Merging basins on the normal equation level
Once the normal equation systems have been build, a variety of solution scenarios can be implemented. Apart from eliminating certain parameters, it is desirable to be able to merge the effect of neighboring basins and consider the resulting parameter as a mean change in the combined basin. Consider a uniform change, x_{merge}, in a basin which encompasses N other basins. When expressed in Gton this uniform change will induce the following mass changes in the sub-basins $x_1, x_2, ..$ (again in Gt):

$$\begin{bmatrix} x_1 \\ x_2 \\ \vdots \\ x_N \end{bmatrix} = \frac{1}{\sum_{i=1}^{N} A_i} \begin{bmatrix} A_1 \\ A_2 \\ \vdots \\ A_N \end{bmatrix} \begin{bmatrix} x_{merge} \end{bmatrix} = \mathbf{M} \begin{bmatrix} x_{merge} \end{bmatrix}. \tag{4.40}$$

Where A_i denotes the area of the sub-basin i. Consequently, the merging operation can be written as a transformation of the normal equation system using matrix $\mathbf{M}$ (See App. C.5).

Combining Altimetry and GRACE
The monthly normal equation systems from altimetry and GRACE contain common (e.g. trend and mean) parameters which can only be solved for when data from the entire interval is included. A simultaneous inversion would therefore require the assembly of a rather large normal equation system containing the common parameters and a set of time varying scales for each month. With the current setup, this would result in a normal matrix with close to 30000 unknowns. Nowadays, a solution of such a matrix poses no real problem on a medium sized multi-core machine with enough memory.

However, the same problem can also be easily solved on smaller sized machines when realizing that the monthly systems are uncorrelated which results in a very sparse and almost block diagonal normal equation system:

$$\mathbf{N} = \begin{bmatrix} \mathbf{N}_{rr} & \mathbf{N}_{rc} \\ \hline \mathbf{N}_{rc}^T & \mathbf{N}_{cc} \end{bmatrix} = \left[\begin{array}{cccc|c} \mathbf{N}_{rr}^{(1)} & 0 & \dots & 0 & \mathbf{N}_{rc}^{(1)} \\ 0 & \mathbf{N}_{rr}^{(2)} & \dots & 0 & \mathbf{N}_{rc}^{(2)} \\ \vdots & \vdots & \ddots & \vdots & \vdots \\ 0 & 0 & \dots & \mathbf{N}_{rr}^{(i)} & \mathbf{N}_{rc}^{(i)} \\ \hline \mathbf{N}_{rc}^{(1)T} & \mathbf{N}_{rc}^{(2)T} & \dots & \mathbf{N}_{rc}^{(i)T} & \sum \mathbf{N}_{cc}^{i} \end{array} \right],$$

$$\mathbf{b} = \begin{bmatrix} \mathbf{b}_r \\ \hline \mathbf{b}_c \end{bmatrix} = \begin{bmatrix} \mathbf{b}_r^{(1)} \\ \mathbf{b}_r^{(2)} \\ \vdots \\ \mathbf{b}_r^{(i)} \\ \hline \sum \mathbf{b}_c^{(i)} \end{bmatrix}. \tag{4.41}$$

Here the superscripts denote the individual months. The subscript 'c' and 'r' denote the common and time varying parameters respectively.

The solution system for the common parameters, $\hat{\mathbf{x}}_c$, can be constructed by reducing all time varying parameters as described in App. C.2.

$$\left(\mathbf{N}_{cc} - \mathbf{N}_{rc}^T \mathbf{N}_{rr}^{-1} \mathbf{N}_{rc}\right) \hat{\mathbf{x}}_c = \mathbf{b}_c - \mathbf{N}_{rc}^T \mathbf{N}_{rr}^{-1} \mathbf{b}_r. \tag{4.42}$$

The block diagonal structure of $\mathbf{N}_{rr}$ allows this system to be written as the sum of the individual monthly systems, each separately reduced for its time varying coefficients:

$$\sum \left(\mathbf{N}_{cc}^{(i)} - \mathbf{N}_{rc}^{(i)T} \mathbf{N}_{rr}^{(i)-1} \mathbf{N}_{rc}^{(i)}\right) \hat{\mathbf{x}}_c = \sum \left(\mathbf{b}_c^{(i)} - \mathbf{N}_{rc}^{(i)T} \mathbf{N}_{rr}^{(i)-1} \mathbf{b}_r^{(i)}\right). \tag{4.43}$$

Once the common parameters are estimated, they can be fixed to these values in each of the monthly systems (according to App. C.3 and C.4). This procedure guarantees that the solution vector $\hat{\mathbf{x}}_r$ is the same as would have been obtained from solving the assembled system from Eq. 4.41.

Although, numerically efficient, the drawback of this procedure is that the monthly error-covariances will be too optimistic. During the fixing step, the common parameters are assumed to be known, and the corresponding part of the normal matrix is ignored. To obtain the correct error-covariance matrix for month k, a post-processing step can be performed to obtain the full error-covariance as follows:

$$\mathbf{C}^{(k)} = \left(\begin{bmatrix} \mathbf{N}_{rr}^{(k)} & \mathbf{N}_{rc}^{(k)} \\ \hline \mathbf{N}_{rc}^{(k)T} & \mathbf{N}_{cc}^{(k)} \end{bmatrix} + \begin{bmatrix} 0 & 0 \\ \hline 0 & \sum_{i \notin k} \left(\mathbf{N}_{cc}^{(i)} - \mathbf{N}_{rc}^{(i)T} \mathbf{N}_{rr}^{(i)-1} \mathbf{N}_{rc}^{(i)}\right) \end{bmatrix}\right)^{-1}. \tag{4.44}$$

In this expression, the block diagonal structure seen in Eq. 4.41 has been exploited. The first term on the right hand side is simply the normal matrix of the month k. The second term is the combined and reduced matrix using data from all months except for month k, whose contribution is already included in the first term.
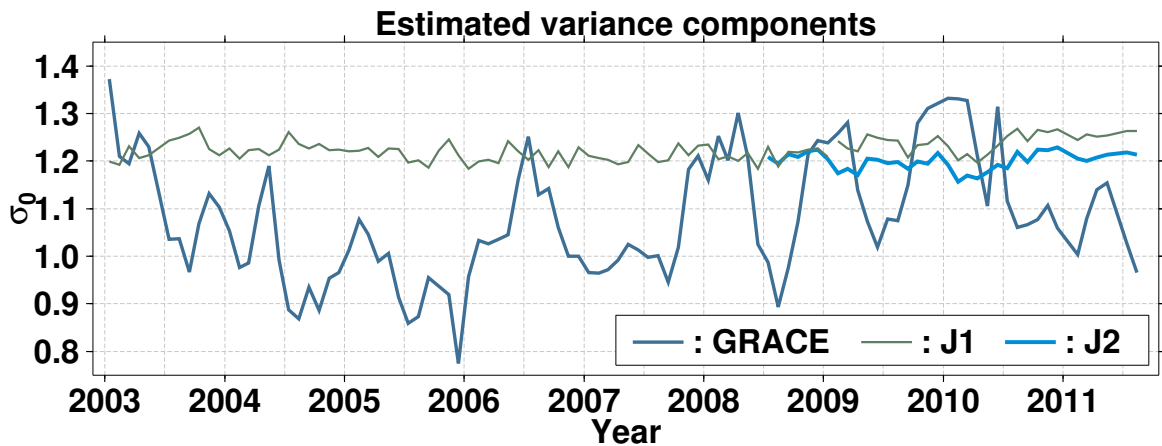
Figure 4.18: Estimated VCE component (square root), in the fingerprint inversion for the contributions of GRACE, and the Jason-1 and Jason-2 missions. The discontinuity in the Jason-1 curve at the start of 2009 indicates the migration to the extended mission.

To compute the relative weighting of the GRACE and altimetry normal equation systems, its variance components were estimated (App. C.6). It should be remarked that the variance components themselves were estimated without applying constraints and while keeping the common parameters fixed to their reference values. The GIA parameters were fixed to 1, which implies that the a priori GIA model was removed from the systems. Fig. 4.18 shows the estimated variance components. The variance component associated with the altimeters remains relatively constant at the level of $(1.2)^2$ times the formal variances, where Jason-2 appears to be more accurate compared to Jason-1. The variance factor for GRACE fluctuates more strongly but exhibits the same time behavior as when estimated for the surface loading inversion as indicated in Fig. 4.2.
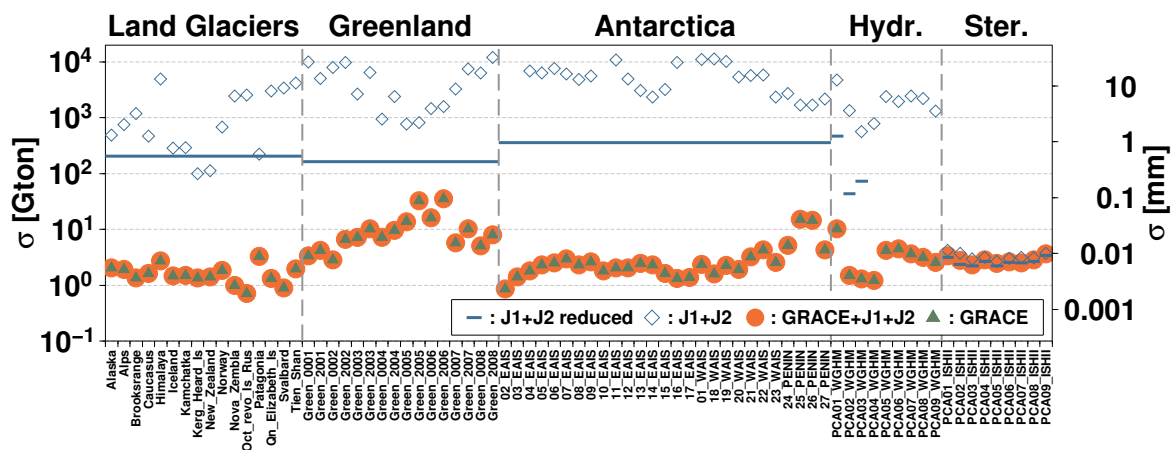
Figure 4.19: Monthly formal errors of the fingerprint inversion (September 2008), for several combinations of Jason-1, Jason-2, and GRACE. The solution of the 'reduced' altimetry-only inversion contain the total effect of Greenland, Antarctica and the land glaciers as single parameters, and the first three hydrological modes. All errors are expressed in terms of their ocean mass change and eustatic sea level contribution.

The formal errors of the time varying coefficients (diagonal of **C**) are plotted in Fig. 4.19, for the month September 2008. The errors are obtained from an unconstrained inversion of the combination, a GRACE-only solution and a altimetry-only inversion. In addition the errors of a simplified altimetry-only inversion are shown. In the latter setup, the drainage basins in Greenland and Antarctica are merged to represent uniform changes. Furthermore, the combined effect of all the land glaciers, and the parameterization of the GIA are represented by single parameters.

Although, the formal errors are still expected to be too small compared to the true errors, they are still a good relative measure of the obtainable accuracy. For example, from the combination, it can be seen that the land glaciers can be estimated relatively well, compared to the other mass parameters. Small narrow basins in Greenland (number 2005, 2006) and on the Antarctic peninsula (number 25, 26), are associated with much larger errors compared to their larger counterparts.

It is also clear that the errors of the mass related parameters are almost entire deter-

mined by the GRACE contribution. Consequently, the altimetry, shows virtually no skill in determining these parameters. Errors for the altimetry-only inversion are so large that no usable results can be expected from such an inversion. Even when the parameterization is strongly simplified, the altimetry-only errors are still several hundreds of Gton. The reason for this unstable behavior is that the altimeter can only indirectly sense the continental mass changes. The associated sea level changes are much weaker compared to the direct effect of the mass on the potential field, and generally decrease as one moves away from the mass source.
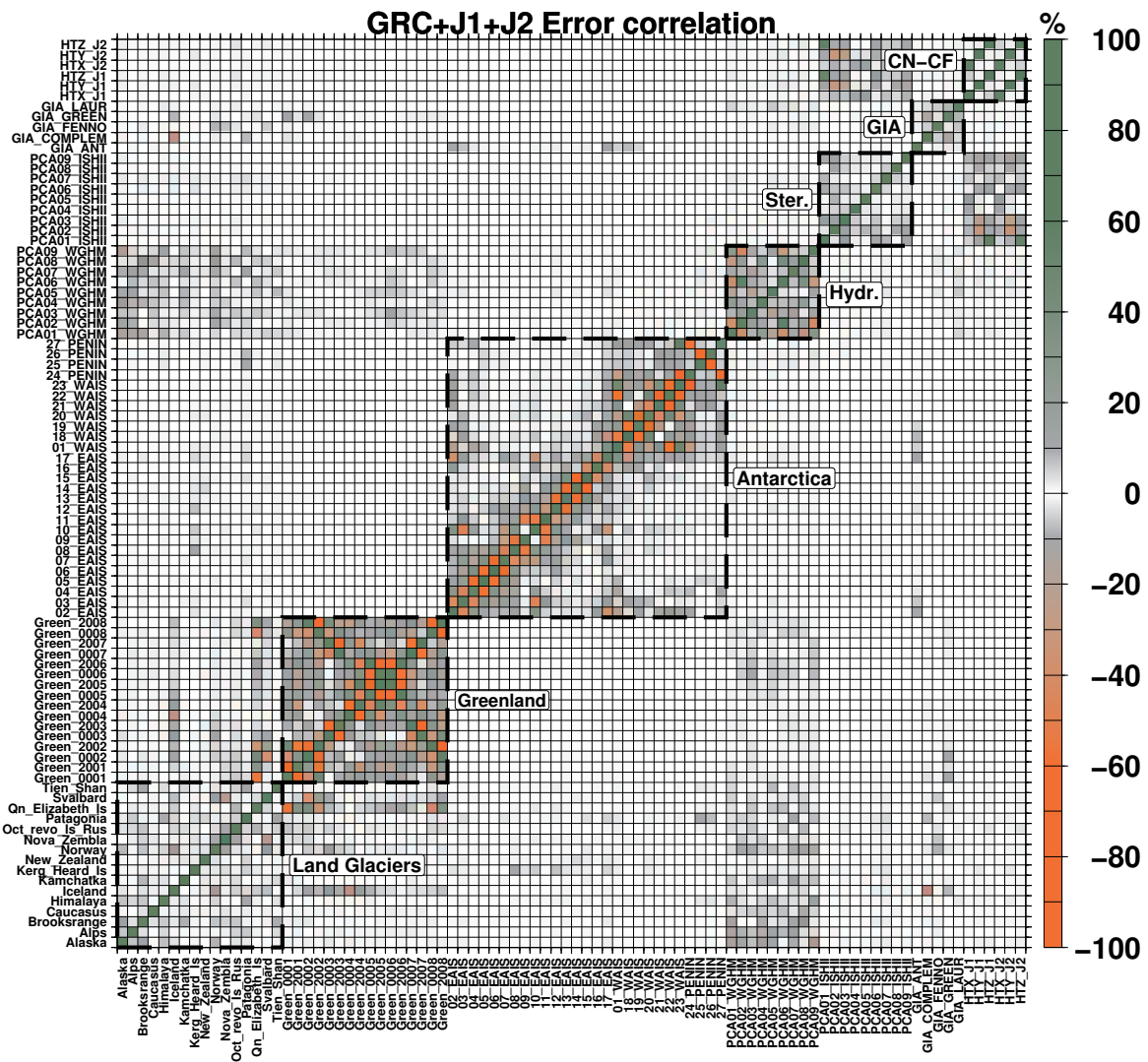
Figure 4.20: Formal error correlation of the estimated parameter scales, at full resolution, for September 2008. The GIA parameters (trends) are constrained by data over the entire time interval.

In contrast, the errors associated with the steric patterns, are very well constrained by the altimetry data. This is also the reason why the estimation of 160 steric parameters can

be performed without problems.

From the above, it would be tempting to conclude that in order to estimate steric sea level change it would suffice to compute the mass component from GRACE only and remove it in a post-processing step from the altimetry. Principally, there is nothing wrong with this procedure. However when one compares GRACE-only solutions with the combination solutions (not shown here), one sees that the addition of altimetry data do cause significant changes of the mass related parameters as well. The leverage, which the altimetry has on the mass parameters, can obviously not be easily spotted from the diagonal of the error-covariance, which stays approximately constant regardless of the addition of altimetry.

The correlation matrix of $\mathbf{C}$ can also provide useful insight in the stability of the inversion problem. Wherever correlations occur, one can expect separability issues between the parameters. The correlations reflect (1) the similarity of the used fingerprint patterns, and (2) an unfavorable sampling by GRACE and/or altimetry. Fig. 4.20 shows a section of the monthly correlation matrix for September 2008.

From the correlation matrix we see that the strongest correlations ($|\rho| > 0.7$) occur for drainage basins which are small and in each other vicinity. The land glaciers appear to be well separable but some smaller correlations exist with Greenland for neighboring glacier clusters such as Iceland, Svalbard and Queen Elizabeth Is. Furthermore, although the glacier cluster areas were excluded from the hydrology patterns, one can still see some correlations with the hydrological parameters.

Problems also occur for the CF offsets of the altimetry, when estimated for each month and per satellite separately. In particular the Z component is expected to cause problems due to its correlation with the steric parameters. This can be expected as the Z-component is ill-constrained by the altimetry as the sampling is limited to $\pm 66°$ latitude and outside the maximum sea ice mask. For this reason, the altimeter offsets will be estimated as mean parameter over the entire time interval as will be explained below.

At first sight, the correlations of the GIA parameters (estimated as trends) appear not so large. However,these correlation are especially problematic, as they can strongly influence the secular behavior of affected basins. For example, the Antarctic component of the GIA, is correlated with the mass pattern of the Antarctic basins (1, 2, 3, 17, 18, 19). Furthermore, the complementary GIA patterns is strongly correlated to the glaciers in Iceland, and correlations also occur with the Greenland basins. These correlations are very problematic for the inversion and require additional constraints to be applied to the GIA. The choice of these constraints will be discussed in the following section.

4.2.4 Constraining the Solution

Unfortunately, a straightforward inversion of the solution produces unsatisfactory results (large non-physical correlations between parameters, unacceptably large GIA components). Some of these problem can be mitigated by merging the smaller and badly constrained basins into larger ones, using the method of the previous section. However, when appro-

priate constraints are applied one can still exploit the data's ability to discriminate between basins. Furthermore, constraints are necessary to keep the GIA parameters at acceptable values.

Estimating Altimeter CN-CF Offsets
Firstly, the estimated altimeter offset vectors are considered. From the previous section, it was already clear that these geometrical offsets are not well estimated when allowed to vary per satellite and per month.

The altimeter origin (CN) is expected to approximate the center of surface figure, at the level of a few mm (Melachroinos et al., 2013), since it is linked to a network of tracking stations. Furthermore, Siegismund et al. (2011) obtained a geocenter motion from steric corrected altimetry which agreed well with Rietbroek et al. (2009) and Swenson et al. (2008). Underlying their analysis was the assumption that the altimeter origin (CN) coincided with the CF. Their finding also demonstrates that this assumption can be trusted to a large extent.
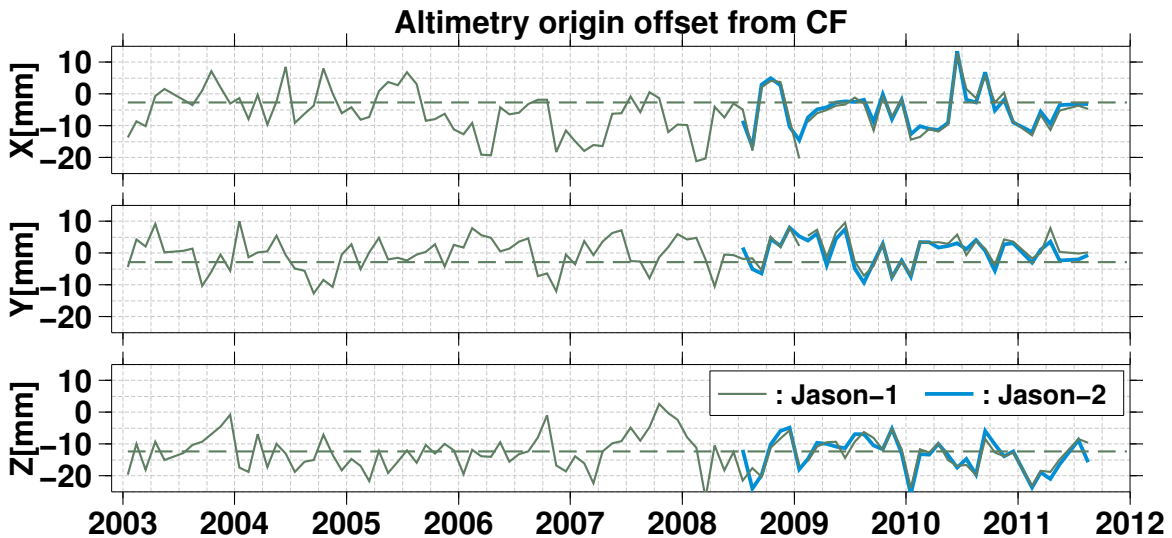
Figure 4.21: Estimated monthly offset of the altimeter (Jason-1&2) frame origin relative to the center of surface figure CF. The dashed lines indicate the estimated offsets when the parameters are assumed to be constant over the entire time interval and when the missions are combined.

Fig. 4.21 shows the time variation of the estimated CN-CF offsets. Clearly the monthly variations of the offset are larger then expected, but a bias in the Z direction can still be recognized. The cause of this shift remains unclear, it may be related to the altimetry orbit (with radial corrections applied), or it is possibly introduced through the subtraction of the mean sea surface (CLS01, Hernandez and Schaeffer, 2001) which is computed by averaging over an earlier time period. Furthermore, the variation of the Jason-1 and Jason-2 offsets is virtually the same, such that the offsets of the mission can safely be combined in a single set of parameters. The time variations of the offset (monthly, but also a secular signal) may potentially absorb geophysical signal from the estimated steric components. For that reason, and the observation that the CF assumption of the altimeter origin is realistic, it was

decided to estimate the altimeter offset as a constant vector over the entire time period. The estimated values are indicated by the dashed line in Fig. 4.21.

Inter-basin Regularization

There are several basins, whose parameters are difficult to separate in the inversion. The most problematic are the high-elevation Greenland basins 5 and 6, and the narrow drainage basins 25 and 26 on the tip of the Antarctic peninsula. For these basins, Fig. 4.22, shows their unconstrained time varying estimates in terms of Gtons. It is obvious that the unconstrained estimates are strongly negatively correlated. Their combined contribution is much less than their individual counterparts.

At first thought, it might be an option to constrain the estimated parameters towards zero. This would however also bias the combined mass change of the basins towards zero. Such a regularization can also have disastrous effect on the combined trend. On a global scale, it is of primary interest to get the trend right, which renders such a regularization technique unacceptable.
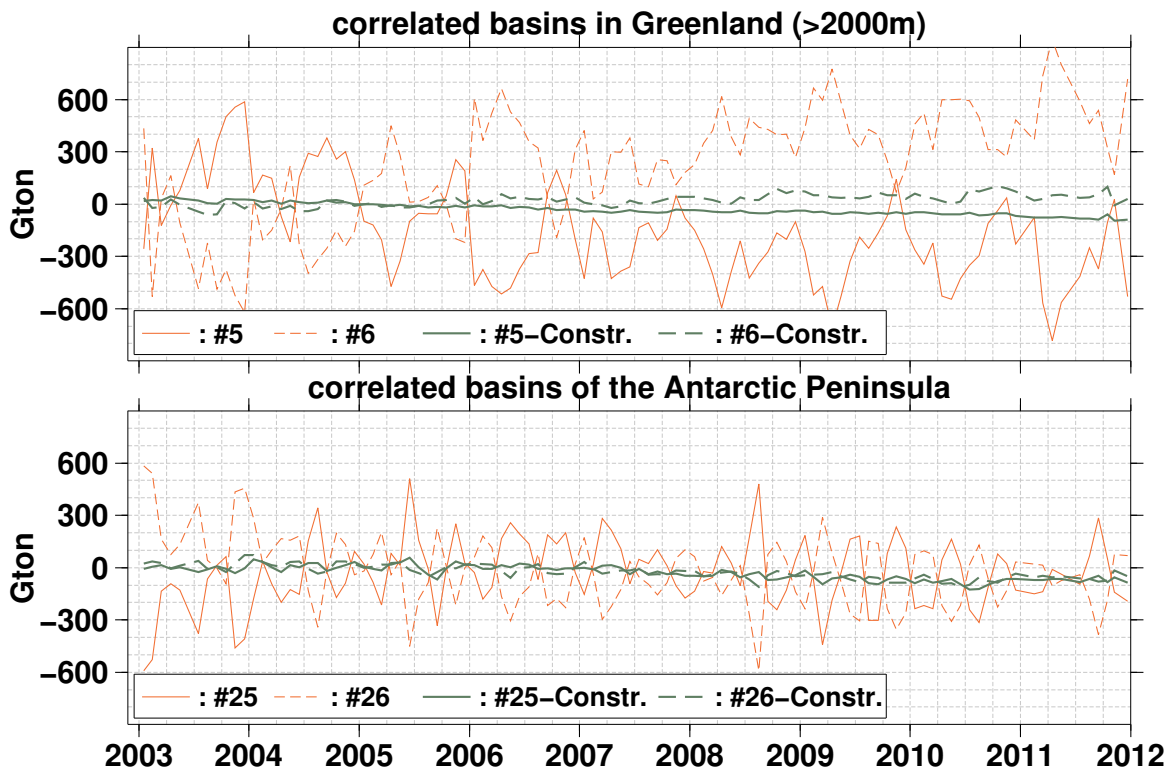
Figure 4.22: Unconstrained and constrained estimates of basins in southern Greenland (top figure) and on the tip of the Antarctic peninsula (bottom). The inter-basin constraint penalizes surface loading differences between basins which have a large formal error correlation ($|\rho| > 0.7$). The basins can be located in Fig. 4.11 by their corresponding numbers.

A more advanced regularization can be constructed by realizing that the basin estimates are strongly negatively correlated. This effect can be decreased by regularization the *dif-*

ference between the basins. In this way, the common time variation of the basins is still unconstrained. In terms of equivalent water height, the difference between two basins, Δh_i, can be written as a function of the estimated parameters in Gton:

$$\Delta h_i = \frac{x_{i_1}}{\rho_w A_{i_1}} - \frac{x_{i_2}}{\rho_w A_{i_2}} = \begin{bmatrix} 0 & \cdots & \frac{1}{\rho_w A_{i_1}} & -\frac{1}{\rho_w A_{i_2}} & \cdots & 0 \end{bmatrix} \mathbf{x}_{ice} = \mathbf{b}_i \mathbf{x}_{ice}. \tag{4.45}$$

To each monthly normal matrix, $\mathbf{N}_k$, a regularization matrix can now be added:

$$\tilde{\mathbf{N}}_k = \mathbf{N}_k + \alpha \boldsymbol{\Phi} \tag{4.46}$$

Where the matrix $\boldsymbol{\Phi}$ is constructed by constraining n basin differences:

$$\boldsymbol{\Phi} = \begin{bmatrix} \mathbf{b}_1^T \\ \vdots \\ \mathbf{b}_n^T \end{bmatrix} \begin{bmatrix} \mathbf{b}_1 \ldots \mathbf{b}_n \end{bmatrix} \tag{4.47}$$

In this thesis, a regularization matrix was constructed from those basin combinations in Greenland and Antarctica were a strong correlation ($|\rho| > 0.7$) was found in the formal-error correlation matrix (see Fig. 4.20). Under this criteria, 6 and 14 basin combinations were constrained in Antarctica and Greenland respectively[7].

The regularization parameter is empirically chosen as $\alpha = 20$. This implies that the induced basin differences, Δh, are associated with a variance of $(22cm)^2$. The impact of the regularization can be seen in Fig. 4.22. The chosen regularization effectively removes most of the sub-annual variations, while still allowing some difference in the estimated trends. A further increase of the regularization parameter will push the estimated trend difference towards zero, with the disadvantage that the signal is smeared out between the basins.

Constraining GIA Parameters

A particular challenge of the joint inversion is the separation of the GIA induced components from the present day mass changes. In particular, the GIA signal in Antarctica is spatially similar to the Antarctic basins, making it difficult to objectively split up the components based on geodetic data. This was realized already in many GRACE mass balance studies (e.g. Velicogna and Wahr, 2006b; Horwath and Dietrich, 2009; Wu et al., 2010)

To find a suitable set of constraints, the monthly mass and steric parameters, and the constant altimeter offset from the combined normal equation system from Eq. 4.41 are reduced. The resulting normal equation system contains only the five GIA parameters (Antarctica, Laurentide, Fennoscandia, Greenland, and complementary sources). An unconstrained inversion causes in particular the Greenland component and the complementary component (e.g. Iceland and Patagonia) to become unacceptably large (see Table 4.2).

The estimated GIA parameters are unitless factors, which indicate to what extent the reference model is adjusted. Consequently, when all GIA values are estimated as zero, the

---

[7]The total amount of possible combinations amounts to $\frac{(n-1)n}{2}$, implying 120 combinations within Greenland and 351 combinations within Antarctica

initial GIA model needs no adjusting. Likewise, when the Antarctic component is associated with a value of value of -0.2, the Antarctic component of the GIA signal is 20% smaller compared to the background model from Klemann and Martinec (2009).

Descr.	Ant.	Laur.	Fen.	Gre.	Compl.
TR($1 \cdot 10^0$)	-1.08	0.11	-0.95	-3.77	24.31
TR($1 \cdot 10^2$)	-1.08	0.12	-0.97	-3.47	11.13
TR($1 \cdot 10^3$)	-1.08	0.12	-0.97	-2.95	1.84
TR($1 \cdot 10^4$)	-1.05	0.13	-0.86	-1.43	0.18
TR($5 \cdot 10^4$)	-0.90	0.12	-0.55	-0.44	0.03
TR($1 \cdot 10^5$)	-0.77	0.11	-0.38	-0.24	0.02
TR($2 \cdot 10^5$)	-0.59	0.10	-0.24	-0.12	0.01
TR($1 \cdot 10^6$)	-0.21	0.06	-0.06	-0.03	0.00
TR($1 \cdot 10^7$)	-0.03	0.01	-0.01	-0.00	0.00
TR($1 \cdot 10^8$)	-0.00	0.00	-0.00	-0.00	0.00
TSVD(5)	-1.08	0.11	-0.95	-3.78	24.60
TSVD(4)	-1.09	0.12	-0.99	-3.29	-0.06
TSVD(3)	-1.10	0.14	-1.01	-0.01	0.00
TSVD(2)	-1.11	0.12	-0.01	-0.00	0.00
TSVD(1)	0.00	0.11	0.00	-0.00	0.00
Tuned	**-0.31**	**0.12**	**-0.14**	**-0.08**	**0.08**
α	($6 \cdot 10^5$)	($1 \cdot 10^0$)	($4 \cdot 10^5$)	($3 \cdot 10^5$)	($2 \cdot 10^4$)

Table 4.2: Variation of the GIA parameters under different constraints, relative to the reference model. TR(α) denotes a Tikhonov regularization using the identity matrix with the regularization parameter in brackets. TSVD(N) indicates a pseudo inverse based on a truncated singular value decomposition keeping N eigenvectors. The tuned diagonal regularization uses a different regularization for each GIA parameter.

Several types of constraint have been tried in this work. To obtain a first idea of the sensitivity of the 5 parameters to the regularization strength an identity matrix is used in a Tikhonov regularization. The regularization parameter is then allowed to vary between 1 and $1 \cot 10^8$. The results are visualized in Fig. 4.23 using a so-called L-curve, which is a log-log plot of the 2-norm of the solution vector plotted against the 2-norm of the posteriori (weighted) residual (Hansen, 1999). In the plot shown on the left, the norm of the estimated GIA parameters are normalized by $\sqrt{5}$ (inducing only a vertical shift on the log axis), such that it represents the RMS of the solution vector. This eases interpretation, as the magnitudes on the Y-axis can be regarded as the fractional change of the reference GIA model. In the same figure, the absolute values of the individual estimates from Tab. 4.2 are also plotted using light gray curves.

Alternatively, in the right subplot of Fig. 4.23, the effect of the regularization has also been plotted in terms of the spatial root mean square of the estimated uplift (i.e. the adjustment to the reference model). To this means, the five estimated GIA adjustment parameters are used to compute the weighted root mean square of the GIA adjustment pattern according to

$$WRMS_{GIA} = \sqrt{\sum_{i=0}^{n_{lat}} \sum_{j=0}^{n_{lon}} \frac{\Delta U_{GIA}^2(\phi_i . \lambda_j) \cos(\phi)}{n_{lat} n_{lon}}}, \tag{4.48}$$

$$\text{where} \quad \Delta U_{GIA}(\phi_i . \lambda_j) = \sum_{k=1}^{5} U_{GIA_k}(\phi_i . \lambda_j) x_{GIA_k}. \tag{4.49}$$

The five indivual GIA uplift components, U_{GIA_k}, are multiplied by the estimated corrections, x_{GIA_k}, before the latitude weighted root mean square is computed over the entire

globe, discretized by a 1x1 degree grid. The same can be done for the individual GIA components which are plotted in grey in the righthand side subplot of Fig. 4.23.
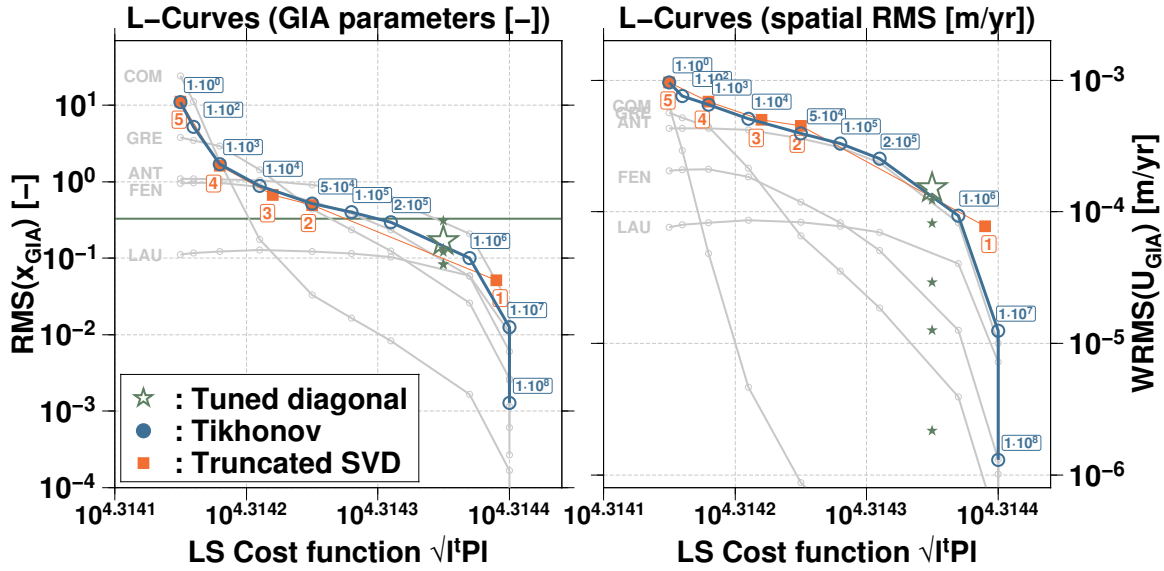
Figure 4.23: 'L-Curves' of the estimated GIA parameters under constraints. Three types of regularization are tried: (1) a Tikhonov regularization with various strengths, (2) a truncated singular value approach, (3) a diagonal regularization where the diagonals are individually tuned. The left subplot has the least squares cost functional plotted against the root mean square of the estimated GIA parameters, which reflect residuals relative to the reference model and are unitless. The green line (33%) serves as a prior, indicating a boundary below which acceptable values may be obtained. The curves of the 5 separate GIA components underlie in grey. The same results are also shown in the right subplot, but the latitude weighted rms of the estimated GIA uplift adjustment is now mapped on the Y-axis.

As suggested by Hansen (1999), a well-shaped L-curve would initially drop steeply as the regularization gains strength, effectively decreasing the solution without affecting the residual norm to much. Then a sharp turn would occur and the curve would level off horizontally, whereby virtually only the norm of the residual would be increasing. The regularization associated with the corner of this L-curve would then be chosen to be the 'optimal' regularization.

Disappointingly, from the inspection of Fig. 4.23 one has to conclude that such a L-shaped curve is *non-existent* in both visualizations. In fact, the L-curve as depicted in the right of Fig. 4.23 is even smoother as most of its behavior is determined by the Antarctic correction, which is the largest component and varies only smoothly.

The curve closest to a 'L' comes from the variation of the complementary GIA parameter, but a distinct corner can not be spotted. From the curves, a regularization parameter of 10^3 seems to be on the point with the strongest curvature, but the estimated GIA parameters associated with this value are simply too large (corresponding to changes in the order of

10% to 300 % of the GIA reference model).

Alternatively, a truncated singular value approach was tried to constrain the solution (see Matsu'ura and Hirata, 1982 for a discussion). In this approach only the N most stable eigen modes of the normal matrix are used to construct a pseudo-inverse. Since 5 parameters are estimated here, 5 truncation levels can be tried, which are also plotted in Fig. 4.23. Unfortunately, none of the truncation levels yields satisfactory results (see Tab. 4.2). While Greenland, and the complementary GIA parameter, quickly drop to zero as the truncation level increases, the values for Antarctica and Fennoscandia still remain too large.

The observations above underline once again the problem that 'separating GIA from the present day surface loading' is a very difficult task. This issue was also noted by Wu et al. (2010) who separated GIA from the present mass trends using GRACE and GPS, but their results are still considered controversial.

In conclusion, an objective constraint based only on the data can not be constructed. However a workable solution can still be constructed by applying more a priori (but admittingly fuzzy) knowledge. Paulson et al. (2007) considered a variety of GIA ensembles with variations of the glacial ice loads in the order of 20% to be realistic. Although such a number can be disputed, it gives a general guide as to where one must be looking for the true GIA values. Firstly, I decided to reject all estimated GIA parameters which have absolute values above the 33% level (indicated by the green line in Fig. 4.23). Secondly, one can expect that the GIA signal of Fennoscandia is better known than that from Antarctica as the regional measurement infrastructure is better in Scandinavia. Thirdly, the complementary and Greenland patterns are potentially disturbing the Glacier estimates so they are not allowed to change by more than 10%. Under these constraints, a tuned diagonal regularization matrix has been constructed (see the 'tuned' entries in Tab. 4.2). These constraints are then used in the final inversion results of this study.

Arguably, once can propose to simply remove the GIA parameters from the inverse problem and use only the a priori model. However, I still feel that the data provides some ability to separate the GIA from the present day mass changes. With the chosen regularization, I trust the GIA model at the 33% percent level but let the data decide whether the signal is weaker or stronger than the a priori model. In any case, the 12% increase of the Laurentide component seems to be a robust feature.

5 Results from the Global Inversions

5.1 Inversion for Global Surface Loading

In the following sections, the results from the inversion scheme described in Sec. 4.1 will be discussed. The inversion results span the period from January 2003 to December 2010, whereas the GPS-only inversion results span a somewhat longer period from January 2002 to Spring of 2012. The discussion will cover the estimated geocenter motion (CM-CE, in this case) and the seasonal and non-seasonal spatial distribution of the signal. Furthermore, the (residual) surface deformations at the GPS station locations are compared with the inversion results, and the oceanic mass variations are validated using time series of in situ bottom pressure recorders (BPRs). The estimated Helmert parameters are expected to absorb any remaining residual network defects and are shown to be small compared to the geocenter motion. Hydrological mass variations in selected watersheds are compared for different methods (GRACE, combination solution and GPS only).

5.1.1 Geocenter Motion

A major advantage of using the GPS station deformations in the inversion, is that it enables the estimation of the degree 1 surface loading components which can be linked to the geocenter motion. In line with Eq. 2.62, the geocenter (CM) can be computed from the estimated degree 1 surface loading coefficients in a chosen (isomorphic) frame:

$$\mathbf{x}_{CM} - \mathbf{x}_{CX} = \sqrt{3}a\frac{(1 + k_1^{'CX})\rho_w}{\rho_e}\begin{bmatrix} T_{11} \\ T_{1-1} \\ T_{10} \end{bmatrix}. \tag{5.1}$$

Fig. 5.1 shows the center of common mass as seen from the center of solid Earth frame (setting $k_1^{'CE} = 0$ above). The combination solution as well as a GPS-only solution are plotted. For comparison, monthly independent geocenter estimates from Swenson et al. (2008) and Cheng et al. (2010) are plotted as well. Here it must be noted that the estimates from SLR are slightly different, because they reflect the offset of the CM from the center of network (close to the ITRF2005 origin). The background de-aliasing model (GRACE GAC product) is not restored. As can be seen from the last column of Tab. 5.2, this introduces additional signal in the time series which limits the comparison of the different estimates. Generally, the series agree to a large extent, and the remaining discrepancies reflect the current level of understanding of the geocenter motion. This level remains however above the computed errors, which suggests that correlated and technique specific errors are more dominant.

The dominant signal in the geocenter motion corresponds to a seasonal variation for which the amplitudes and phases are tabulated (Tables 5.1 and 5.2). The GPS-only estimate

generally contains more high frequency noise, compared to the combination solution (see the last column of Tab 5.1). In comparison with the results from Rietbroek et al. (2012b), a reduction of noise in the X and Z component can be seen from the residual RMS. Furthermore, the GPS-only solution displays stronger inter-annual fluctuations reflected in the X (and Y) component of the geocenter motion. The inter-annual variation of these two components appears to be negatively correlated ($\rho = -0.45$, for a half year long running mean filter on the non-seasonal residual) and is consequently difficult to resolve by a GPS-only solution. It also depends on the applied ocean mass constraint (not shown here).
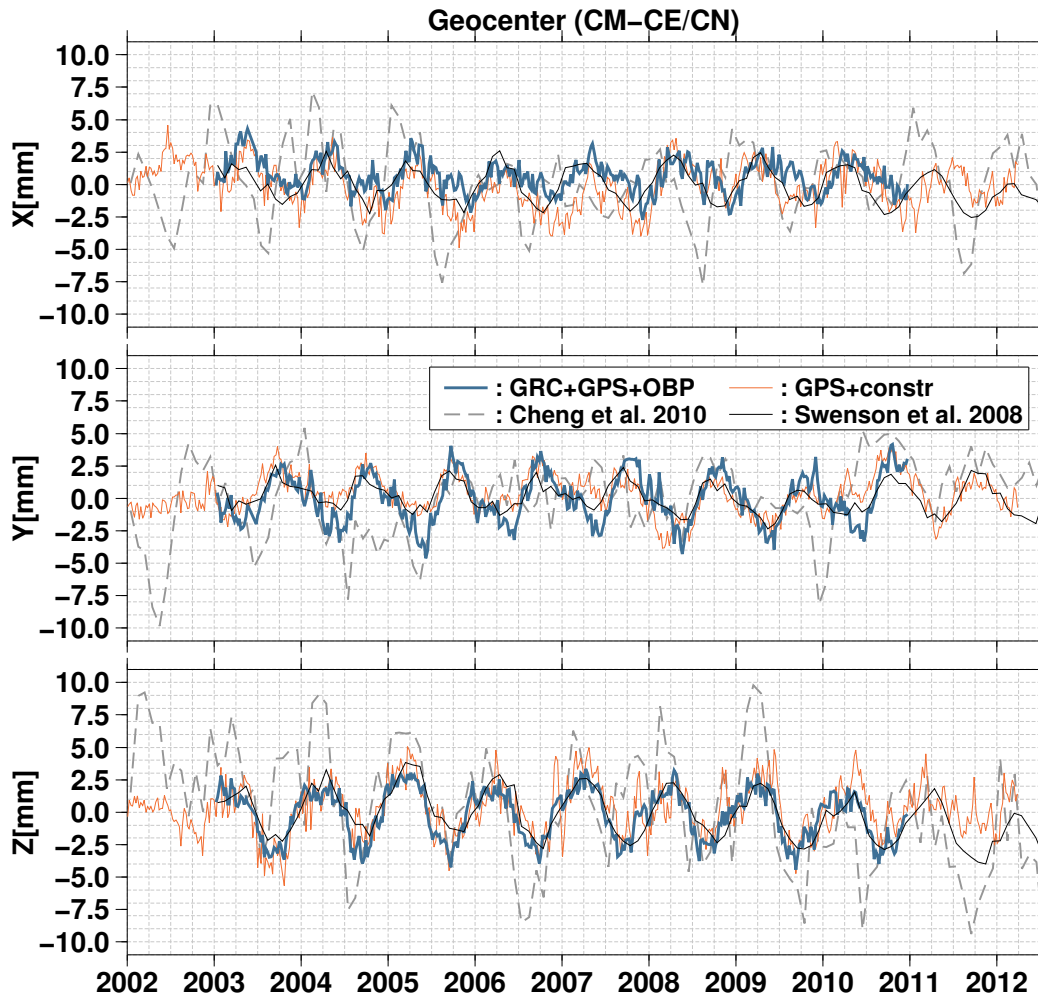
Figure 5.1: Time variation of the Cartesian components of the geocenter motion ($\mathbf{x}_{CM} - \mathbf{x}_{CE}$) for different estimates. The time series are relative to the release 05 Ocean-Atmosphere (GAC) product. The SLR based series represents the offset relative to the SLR network origin.

Unfortunately, a simple eye-balling of the three Cartesian components of geocenter motion contributes little to the physical comprehension. For that reason, the geocenter motion is plotted in 'polar form' in Fig. 5.2. This representation, also used in Rietbroek et al. (2012b), depicts the geographical location where the 3 dimensional CM-CE offset vector is

	Annual		Semiann.		RMS
	A[mm]	t_a[doy]	S[mm]	t_s[doy]	post.[mm]
GRC+GPS+OBP (X)	1.3 (± 0.06)	137 (± 3)	0.6 (± 0.06)	95 (± 3)	0.8
(Y)	2.2 (± 0.06)	304 (± 2)	0.8 (± 0.06)	77 (± 2)	0.7
(Z)	2.5 (± 0.06)	72 (± 1)	0.6 (± 0.06)	151 (± 3)	0.7
GRC+GPS+OBP(δh only) (X)	1.0 (± 0.05)	141 (± 3)	0.6 (± 0.05)	94 (± 3)	0.7
(Y)	2.0 (± 0.05)	306 (± 2)	0.7 (± 0.05)	77 (± 2)	0.7
(Z)	2.1 (± 0.05)	67 (± 1)	0.4 (± 0.05)	143 (± 3)	0.6
GPS (constr.) (X)	1.5 (± 0.09)	125 (± 4)	0.3 (± 0.09)	101 (± 9)	1.3
(Y)	1.4 (± 0.07)	278 (± 3)	0.5 (± 0.07)	91 (± 4)	0.9
(Z)	2.2 (± 0.11)	84 (± 3)	0.6 (± 0.11)	134 (± 6)	1.5
Swenson et al. (2008) (X)	1.7 (± 0.07)	99 (± 3)	0.1 (± 0.07)	57 (± 18)	0.5
(Y)	1.2 (± 0.07)	283 (± 4)	0.5 (± 0.07)	64 (± 4)	0.4
(Z)	2.3 (± 0.10)	93 (± 3)	0.1 (± 0.10)	132 (± 22)	0.6
Rietbroek et al. (2012b) (X)	1.5 (± 0.07)	107 (± 3)	0.2 (± 0.07)	142 (± 8)	1.1
(Y)	2.2 (± 0.05)	305 (± 1)	0.3 (± 0.05)	64 (± 6)	0.7
(Z)	2.3 (± 0.09)	32 (± 2)	0.7 (± 0.09)	151 (± 4)	1.2
Cheng et al. (2010) (X)	2.8 (± 0.35)	40 (± 7)	1.0 (± 0.34)	133 (± 10)	2.2
(Y)	0.6 (± 0.39)	318 (± 36)	0.5 (± 0.39)	57 (± 25)	2.5
(Z)	4.4 (± 0.48)	50 (± 6)	1.7 (± 0.48)	92 (± 8)	2.9
GAC RL05 (X)	1.4 (± 0.08)	10 (± 3)	0.5 (± 0.08)	165 (± 5)	1.0
(Y)	1.7 (± 0.06)	355 (± 2)	0.4 (± 0.06)	143 (± 4)	0.9
(Z)	0.9 (± 0.11)	348 (± 7)	0.6 (± 0.11)	86 (± 6)	1.5

Table 5.1: (Semi-)Seasonal amplitude and phase of the geocenter motion (CM-CE). The dealiasing model (release 05) is not restored, but the coefficients of its seasonal harmonic are provided for completeness in the last 3 rows of the table. The fitted model follows $f(t) = mean + trend(t - t_0) + A \cos(\Omega_{annual}(t - t_a)) + S \cos(2\Omega_{annual}(t - t_s))$, such that the phase can be interpreted as the time where the maximum occurs. The data flowing in the estimates are restricted to the period 2003-2009 (7 years). The provided errors are the formal errors rescaled by the a posteriori σ_0 (App. C.1). The entry with "δh only", denotes a solution where the horizontal deformation solution is excluded, and where no Helmert rotations are estimated. The residual RMS of the time series is provided in the last column.

	Annual		Semiann.		RMS
	A[mm]	t_a[doy]	S[mm]	t_s[doy]	post.[mm]
GRC+GPS+OBP (X)	1.2 ($\pm$ 0.08)	73 ($\pm$ 3)	0.4 ($\pm$ 0.07)	120 ($\pm$ 6)	1.0
(Y)	3.5 ($\pm$ 0.06)	326 ($\pm$ 1)	0.6 ($\pm$ 0.06)	96 ($\pm$ 3)	0.8
(Z)	2.7 ($\pm$ 0.12)	52 ($\pm$ 3)	0.4 ($\pm$ 0.12)	119 ($\pm$ 8)	1.5
GRC+GPS+OBP(δh only) (X)	1.1 ($\pm$ 0.07)	62 ($\pm$ 4)	0.4 ($\pm$ 0.07)	119 ($\pm$ 6)	0.9
(Y)	3.3 ($\pm$ 0.06)	329 ($\pm$ 1)	0.5 ($\pm$ 0.06)	100 ($\pm$ 3)	0.8
(Z)	2.5 ($\pm$ 0.12)	45 ($\pm$ 3)	0.5 ($\pm$ 0.11)	109 ($\pm$ 7)	1.5
GPS (constr.) (X)	1.6 ($\pm$ 0.11)	73 ($\pm$ 4)	0.4 ($\pm$ 0.11)	143 ($\pm$ 9)	1.5
(Y)	2.4 ($\pm$ 0.09)	320 ($\pm$ 2)	0.5 ($\pm$ 0.09)	116 ($\pm$ 5)	1.2
(Z)	2.3 ($\pm$ 0.15)	60 ($\pm$ 4)	0.7 ($\pm$ 0.15)	110 ($\pm$ 6)	2.0
Swenson et al. (2008) (X)	2.2 ($\pm$ 0.13)	61 ($\pm$ 4)	0.3 ($\pm$ 0.13)	171 ($\pm$ 12)	0.8
(Y)	2.3 ($\pm$ 0.09)	326 ($\pm$ 2)	0.2 ($\pm$ 0.09)	89 ($\pm$ 14)	0.6
(Z)	2.2 ($\pm$ 0.18)	70 ($\pm$ 5)	0.5 ($\pm$ 0.18)	95 ($\pm$ 10)	1.1
Rietbroek et al. (2012b) (X)	1.9 ($\pm$ 0.09)	62 ($\pm$ 3)	0.7 ($\pm$ 0.09)	157 ($\pm$ 4)	1.4
(Y)	3.4 ($\pm$ 0.07)	327 ($\pm$ 1)	0.2 ($\pm$ 0.07)	128 ($\pm$ 9)	1.0
(Z)	3.0 ($\pm$ 0.14)	19 ($\pm$ 3)	0.6 ($\pm$ 0.14)	128 ($\pm$ 7)	1.8
Cheng et al. (2010) (X)	4.1 ($\pm$ 0.36)	30 ($\pm$ 5)	1.3 ($\pm$ 0.36)	144 ($\pm$ 8)	2.3
(Y)	2.1 ($\pm$ 0.40)	345 ($\pm$ 11)	0.1 ($\pm$ 0.39)	111 ($\pm$ 120)	2.5
(Z)	4.8 ($\pm$ 0.48)	40 ($\pm$ 6)	2.2 ($\pm$ 0.47)	92 ($\pm$ 6)	2.9

Table 5.2: As in table 5.1, but now including the ocean and atmosphere from the de-aliasing product.

Orientation and magnitude of the CM–CE offset
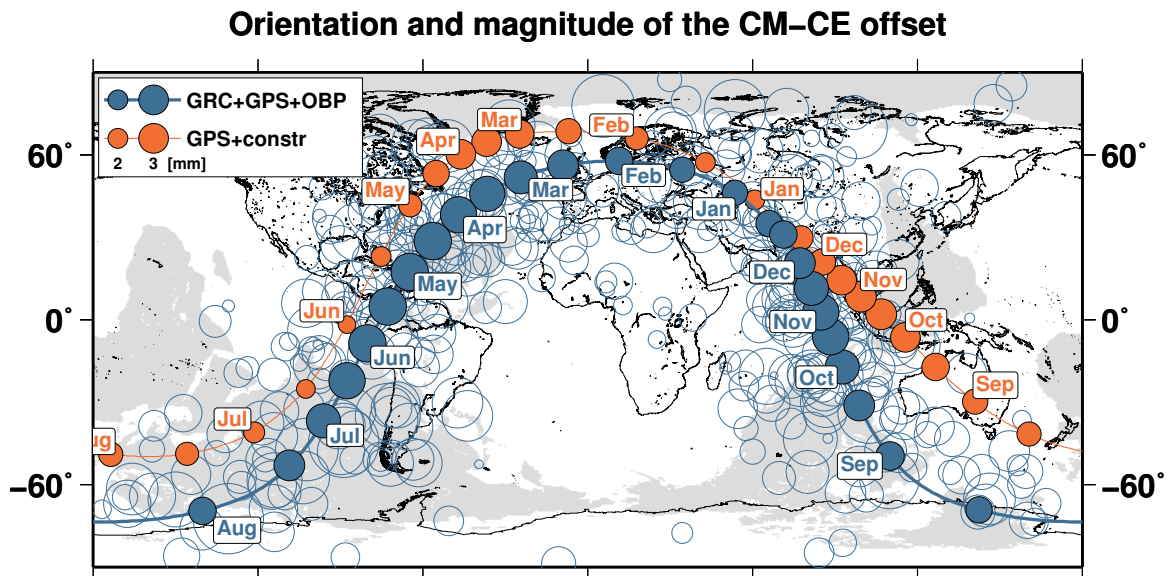
Figure 5.2: Orientation and magnitude of the seasonal geocenter motion, for a combination with GRC+GPS+OBP and for the (constrained) GPS-only solution. The release 05 Ocean-Atmosphere (GAC) product has been restored. Empty circles indicate weekly geocenter motion locations (from the combination).

directed to. The magnitude of the offset is visualized with the size of the marker.

Figure 5.2 depicts the seasonal variation of the geocenter motion, on top of the weekly geocenter estimates together with a seasonal estimate of the GPS-only solution. The time series include the oceanic and atmospheric background models. As can be seen from the figure, the geocenter offset revolves around the Earth, very roughly approximating a great circle, while the total CM-CE offset does not decrease below 2.5 mm. The seasonal variation from the GPS-only solution is similar, although the position of the peaks is shifted, and the magnitude is smaller.

5.1.2 Estimated Helmert Parameters

In the combination solution, 7 weekly Helmert parameters are estimated simultaneously with the surface loading coefficients. In the ideal case, where almost all of the deformations are explained by the surface load, those will remain small.

Fig. 5.3 shows the estimated Helmert parameters. The shifts at the Earth's surface, caused by the translation and rotation parameters, roughly remain below 0.5 mm. A somewhat larger variation (≈ 1 mm) is induced by the scale parameter, which predominantly exhibits a seasonal behavior.

However, compared to earlier results from Rietbroek et al. (2012b), a notable decrease in the scale amplitude is observed. The decrease is mainly caused by the removal of the GPS network constraints (see Sec. 3.3.1), which were also applied to the combination solutions of Rietbroek et al. (2012b). A further decrease may be caused by the VCE weighting scheme in combination with newer GRACE and OBP data, which is applied in this study. The use of high frequency ocean/and atmospheric surface loading as a background model in the GPS processing did not cause a notable change of the estimated scale parameter. This has been tested by running the inversion with a GPS version with and without a priori surface loading removed.

A variety of errors is expected to create apparent scale variations in the estimated GPS network. Of these, solar radiation pressure forces acting on the satellite are thought to play an important role. Similar to Collilieux et al. (2011a), some peaks in the power spectral density of the scale parameter (see Fig. 5.4) appear at the harmonics of the draconitic frequency of the GPS orbits (multiples of 1.04 cycles per year). In a so-called draconitic year the orientation of the GPS constellation relative to the sun repeats itself. These frequencies are consequently related to the solar illumination of the satellites, and may affect the solar radiation pressure, and consequently the estimated GPS orbits. As a remark, it must be noted that the time series is not long enough to allow for a finer frequency resolution to be more conclusive. Lavallée et al. (2006) suggested that an imperfect GPS network may induce aliasing of surface loading signal. However, since the surface loading signals are estimated simultaneously and are strongly constrained by GRACE this is not expected to explain the remaining scale variations. A similar conclusion has been reached by Collilieux et al. (2011b).
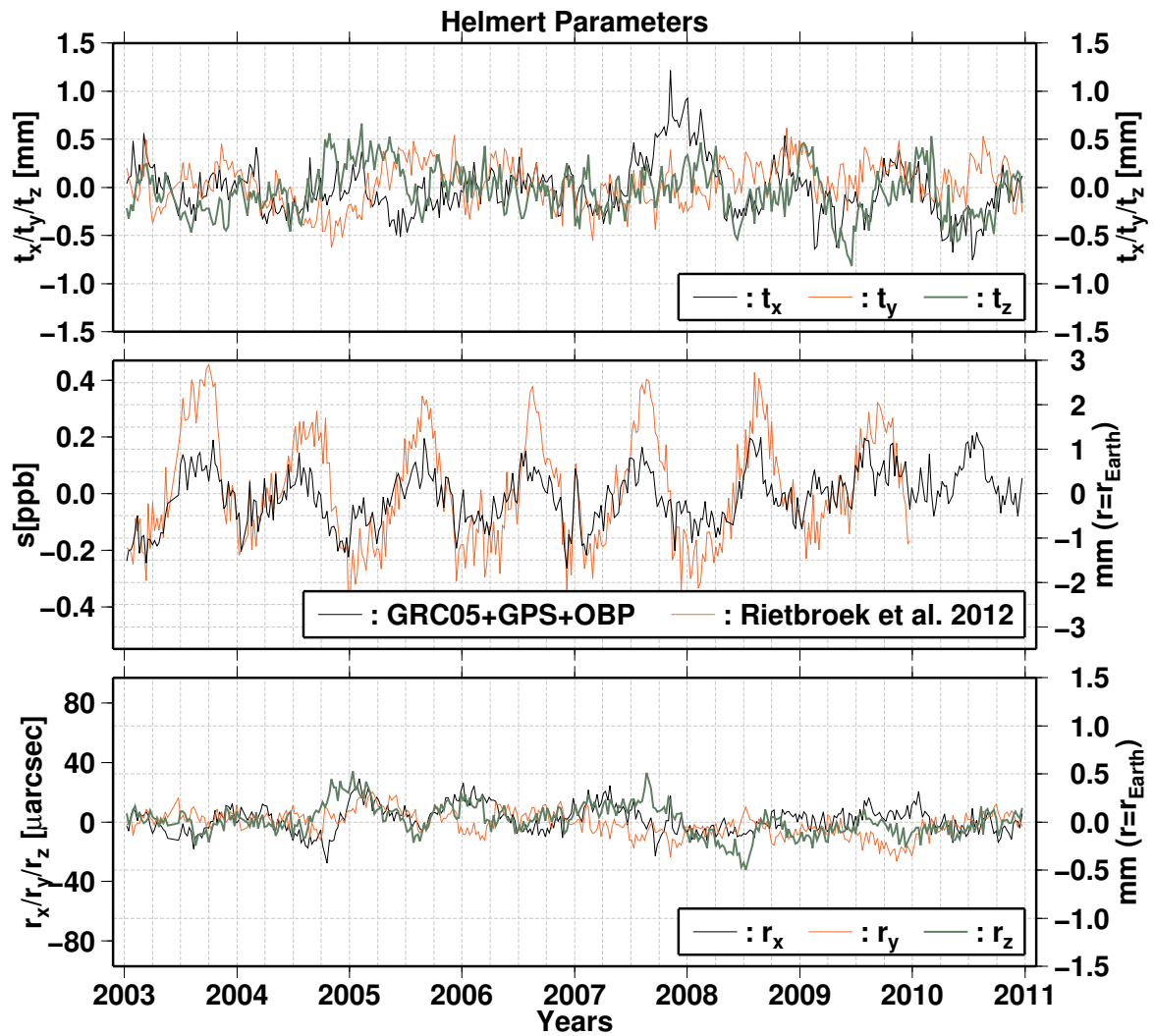
Figure 5.3: Weekly Helmert parameters from the combination solution. An earlier estimate of the scale parameter is also plotted.
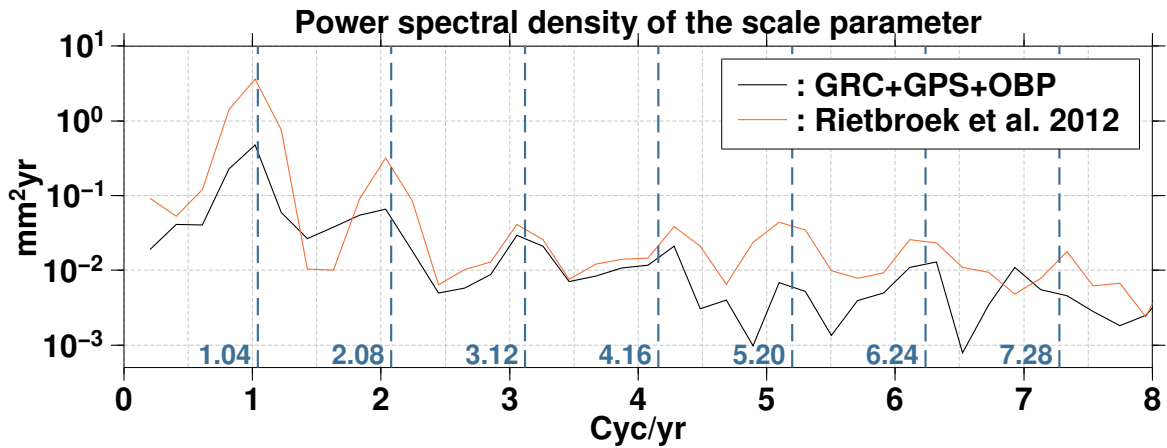
Figure 5.4: Power spectral density of the estimated scale parameter. Other harmonics of the draconitic GPS year (351.4 days) are indicated as vertical dashed lines. The scale parameter of Rietbroek et al. (2012b) is noisier over most of the spectrum.

5.1.3 GPS Station Residuals

It is interesting to asses how much of the GPS station deformation can be explained by the estimated surface load. To this means I've computed weekly station deformations from the GPS normal equation systems. It is important to note that, in order to mitigate some (near) rank defects in the GPS normal equation system, one needs to apply network constraints (Sec. 3.3.1) to obtain sensible deformation time series. Here, the following constraints, $\sigma_{t_{xyz}} = 20$mm, $\sigma_{r_{xyz}} = 10\mu$arcsec and $\sigma_s = 0.1$ppb, were applied to a core network of 132 well-distributed stations. The consequence of this procedure is that a certain stiffness is introduced, which is not present in the combination solution, such that, strictly speaking, the residual can not be considered a pure measurement residual. The surface loading from the combination solutions have been propagated to the station locations using Eq. 4.3, and are subsequently removed from the normal equation systems before the inversion (see App. C.3).

Fig. 5.5 shows the reduction in RMS of the deformation components when the combination solution is removed a priori. As can be expected, the reduction is most prominent in the *up* component of the deformation, which is about 3 times more sensitive to surface loading variations as the horizontal components. This is also visible from the lower right subplot from Fig. 5.5, where the sorted RMS of the station deformation is depicted. The reduction in the East and North components is significantly less, and for many stations no significant reduction is visible.

In the time domain, this typical behavior has also been plotted for a selected set of GPS stations in Fig. 5.6. The displayed stations cover well performing stations (WILL, GRAZ), but also some which perform marginally or even bad (KOUR, OSN1, EIL1). The height component of the stations generally show reduced seasonal behavior when the combination solution is subtracted, except for station EIL1 which in fact shows an increase in RMS. The horizontal components show little or no reduction, and the associated variations are
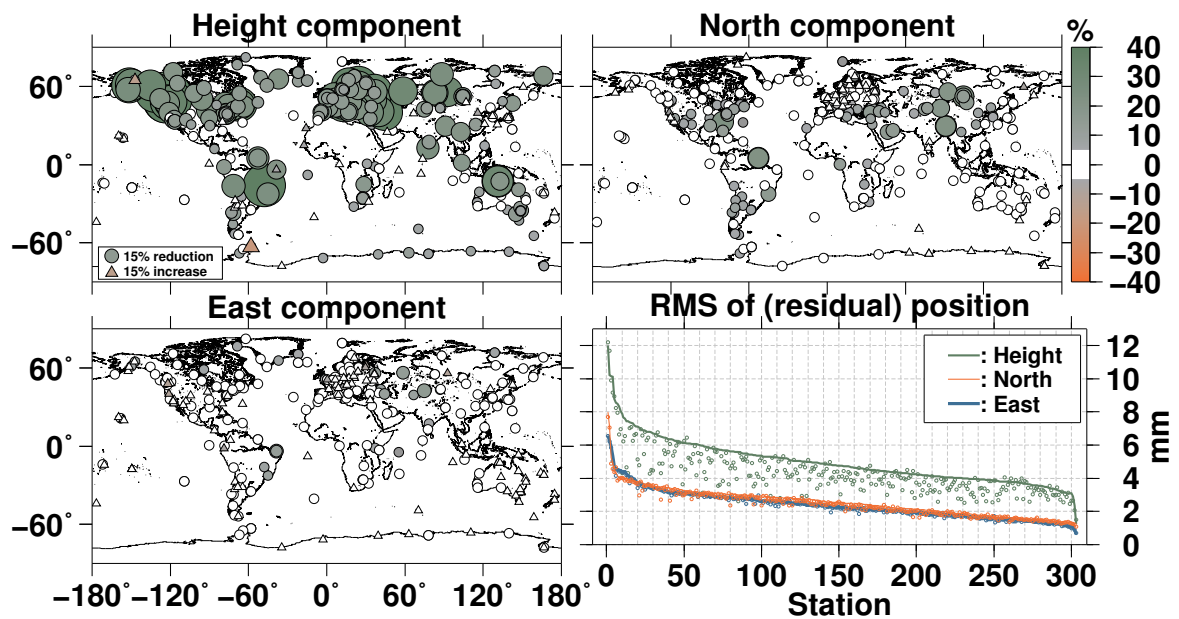
Figure 5.5: Reduction of the local station deformation components after removing the combination solution a priori from the GPS normal equations. The circles denote the decrease/increase in the RMS of the components. The lower right subplot indicate the original RMS (solid lines, sorted according to magnitude), whereas the dots denote the RMS of the corresponding residuals.

also not absorbed in the combination solution.

Naïvely, one may therefore suggest to exclude the horizontal deformations in the combination solution all together. However by doing so, the long wavelength coefficients may be affected. For example, the geocenter motion exhibits a decrease in seasonal amplitude when excluding the horizontal information (see Tables 5.1 and 5.2). For this reason, it is still advisable to include the horizontal information in the combination solutions.

5.1.4 Seasonal and Inter-annual Surface Loading

The estimated surface loading, without restoring the background models, mainly respresent hydrological signal. However, as the background models are not perfect, oceanic and atmospheric modelling errors are also reflected in the surface mass loads.

Fig. 5.7, shows the estimated Cosine and Sine amplitudes (peaking in the end of Dec and March respectively) of the combination solution. Clearly, most of the signal is related to the hydrological seasonal cycle, with the well-known maxima in the tropical regions. However, in the Southern Ocean, we see residual seasonal signal peaking in the winter. The removal of the seasonal fit (and trend), also reveals signals (5.7 bottom right) on other time scales. These may be caused by accelerations (Greenland, Alaska, Antarctic peninsula), sub-annual signals (Southern Ocean) or also episodic and inter-annual variations (High latitude regions in Asia, Dronning Maud land, Wilkes Land).
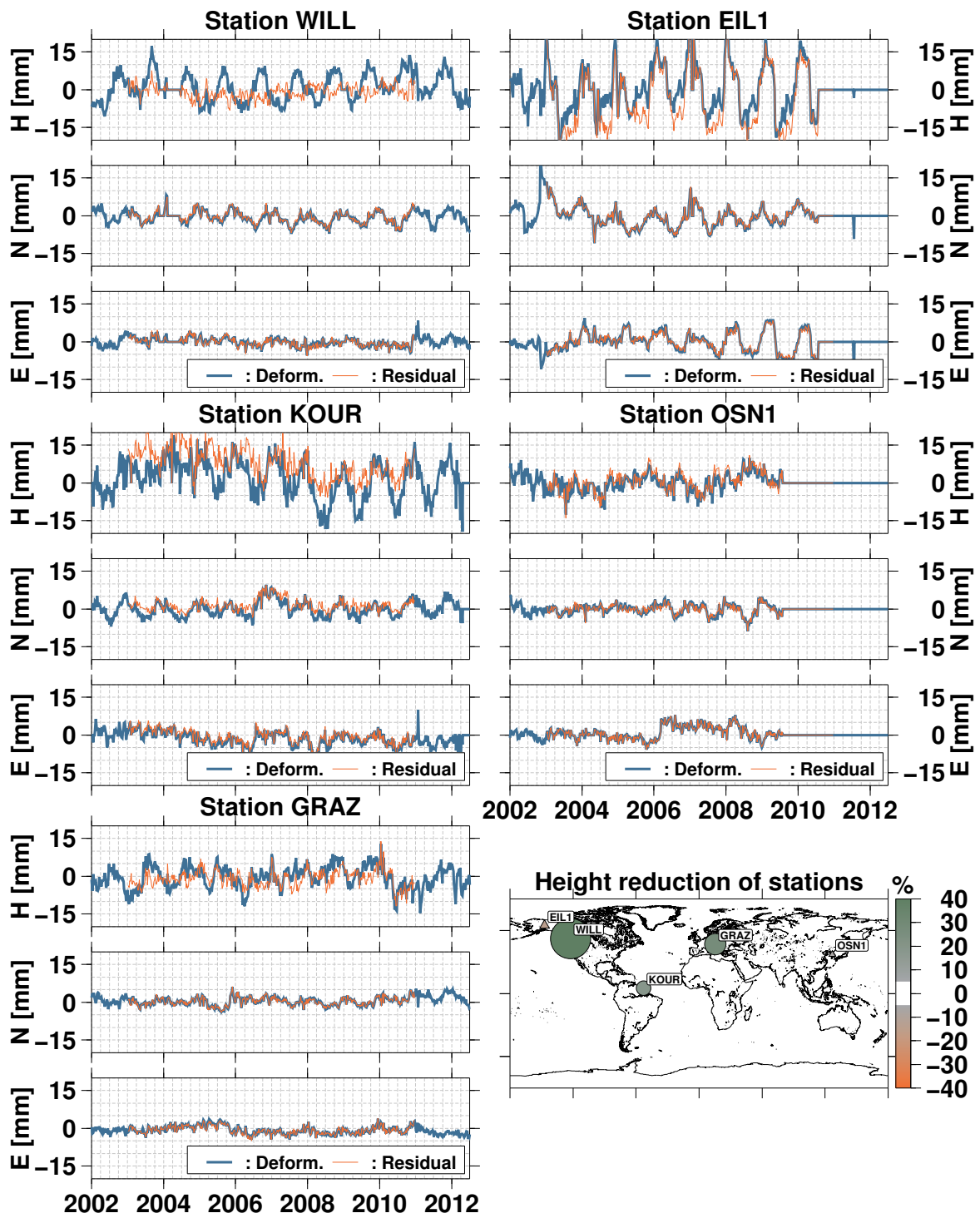
Figure 5.6: GPS station time series
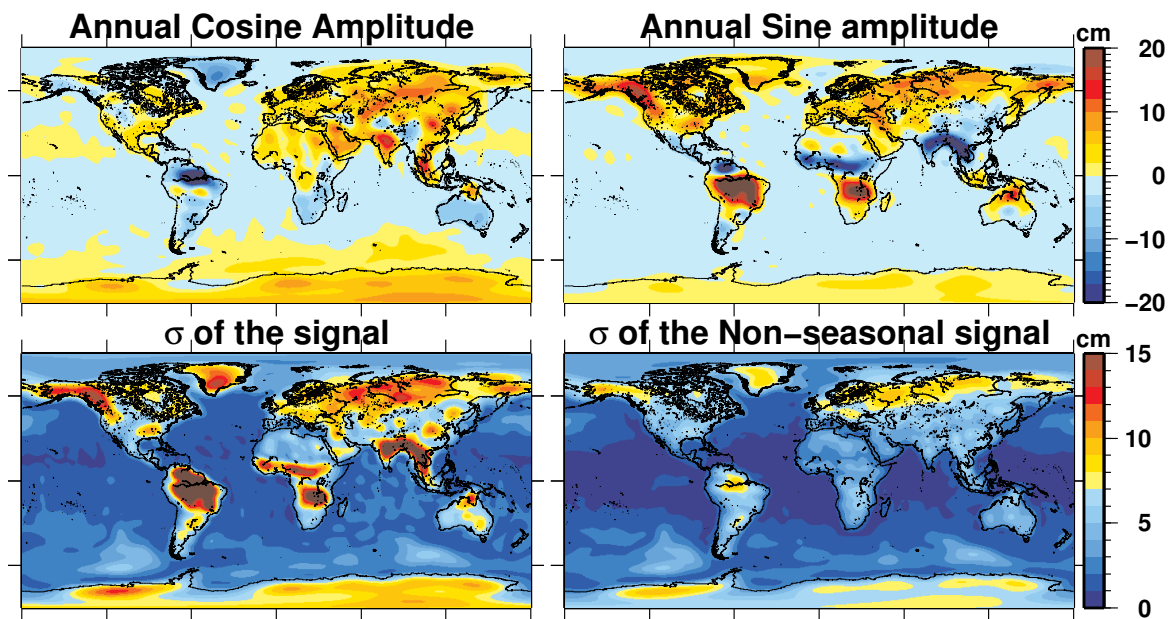
Figure 5.7: Seasonal amplitudes and standard deviations of the combination solution (no background models restored). The bottom figures depict the RMS of the surface load with and without seasonal signal.

5.1.5 Comparison with In Situ OBP

When studying oceanographic signals, the background (ocean/atmosphere) models need to be restored. The surface load from the inversion, can be directly compared with in situ measurements of ocean bottom pressure. The in situ data have not been used in the inversion or in the FESOM model, so they can be considered as an independent validation set.

In a first approach, the correlation between the in situ OBP series and the OBP from the combination solution has been computed. Fig. 5.8 shows the location and correlation of the combination solution with the in situ time series. For comparison, the correlation with the background model has also been computed (the right subplot). Compared to the GAC product, the combination solution shows improvements in correlation in the central Atlantic, the Southern Ocean and the Fram Strait. However there are also other areas, such as near the Aleutian trench and the West Coast of the US, where the combination solution now yield decreasing or even insignificant correlations. This is most likely due to the leakage of seasonal continental signal the coastal areas. In the well-sampled KESS array to east of Japan (Park et al., 2008), only small changes in correlations are found (both negative and positive). In contrast to the results from Macrander et al. (2010), the combination solution performs relatively well in the central Atlantic and the Drake passage. This is most likely the result of the simulated OBP which flows in the joint inversion, stabilizing the solution over the ocean. As a remark, the release 5 of the OMCT model (Dobslaw and Thomas, 2007b; Dobslaw et al., 2013), seems to perform better than the earlier release 4 model. When comparing the new model with the in situ series, the correlation improves at about 2 thirds of the recorders.
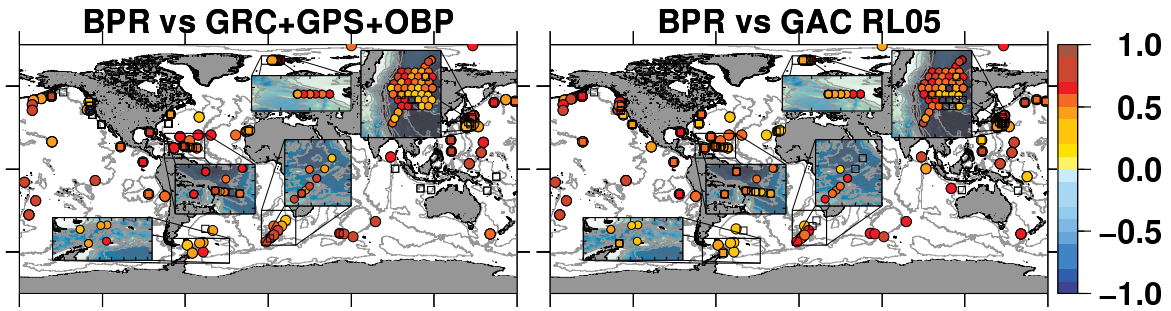
Figure 5.8: Correlation of the inversion solution with in situ bottom pressure series. Circles and triangles denote positive and negative correlations respectively. Empty squares indicate insignificant correlations (based on p-values larger than 0.05, which commonly arise because of a limited time span). Both the combination solution and the GAC product are evaluated up to degree and order 30.

By comparing correlations only, one introduces a potential pitfall. Just because two signals correlate well, it does not necessarily mean that the magnitude of the signals are comparable. To put the correlations in a better perspective an approximate signal to noise ratio is also plotted in Fig. 5.9. Here the signal to noise ratio is approximated as:

$$SNR_{comb} = \frac{\sum_i T_{BPR}(t_i)^2}{\sum_i (T_{BPR}(t_i) - T_{comb}(t_i))^2} \tag{5.2}$$

This measure allows the comparison of the power of the signal (from the local bottom pressure T_{BPR}) against the approximated noise level (the combination solution, T_{comb}, subtracted from the local series). For values of $SNR_{comb} > 1$, the combination solution explains a significant fraction of the variation of the in situ series.
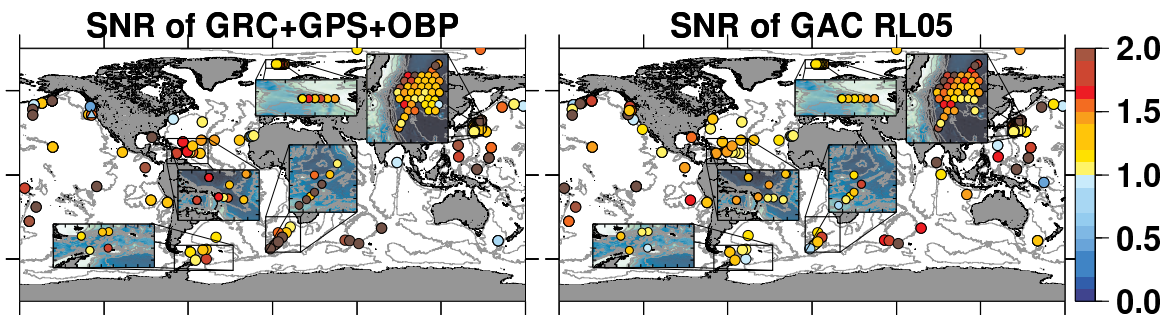
Figure 5.9: Approximate signal to noise ratio of the local OBP signal relative to the residual signal (combination solution on the left, and the GAC product on the right). As in Fig. 5.8, circles and triangles come from comparisons with significant positive and negative correlations.

The in situ measurements are band-unlimited measurements at single locations, whereas the combination results are associated with a band-limited expansion of spherical harmonics. The difference in spatial resolution makes a comparison inherently difficult. A good

match is therefore only expected when the in situ time series reflect ocean bottom pressure variations occurring in a much larger area surrounding the recorder. Indeed, several local OBP series in the Southern Ocean were shown to be significantly correlated to GRACE-derived OBP in areas far away from the recorder itself (Rietbroek, 2007).
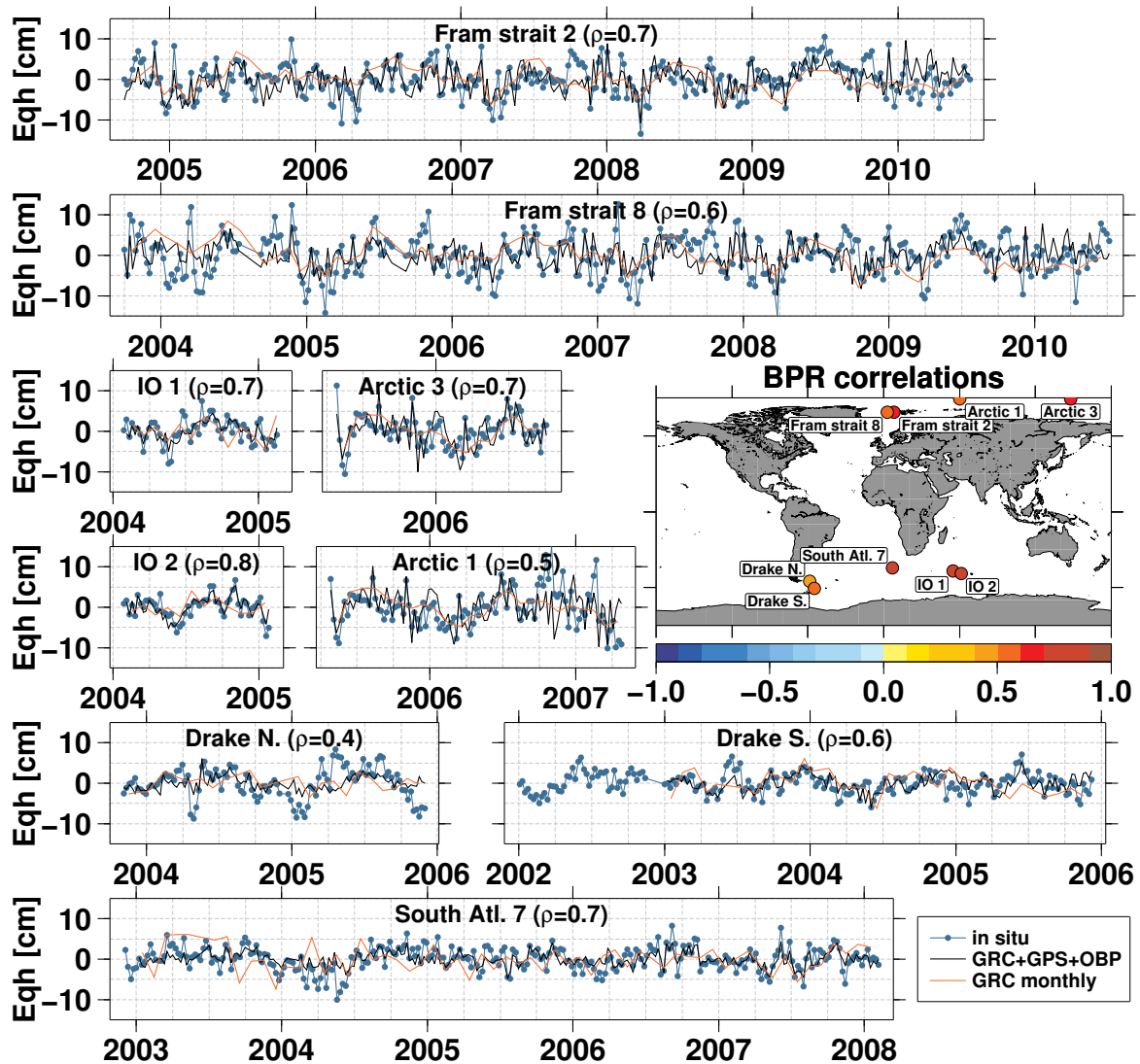
Figure 5.10: Highlighted set of bottom pressure time series plotted against the joint inversion solution and a monthly GRACE (GFZ RL05) solution. The longer series (Fram strait, Drake passage, South Atlantic) are composites of multiple BPR deployments. The corresponding correlations between the joint inversion and the local series is indicated in the subplot titles.

When looking at the signal to noise ratios, one finds that the combination solutions generally show large signal to noise ratios where the correlations are also improved. However, there are several locations, where one finds SNR values lower than 1, whereas the correlation is significant and positive. At those locations, the combination solution does not

necessarily yield an improvement. It must be noted however, that additional spatial filters may yield more optimal results. Although much less than GRACE-only solutions, the oceanic signal of the combination is still affected by some leftover striping, which may be decreased by applying an appropriate filter.

Fig. 5.10 depicts, for selected recorders, the local time series versus the results from the joint inversion. In addition, the (standard) monthly GRACE solution (GFZ RL05), is also plotted. Signals on sub-monthly scales are captured in both the joint inversion results and the local series. This demonstrates the potential of the joint inversion to resolve sub-monthly signals as well. In fact, the local bottom pressure signal is often associated with large (spatial) correlation lengths, and is therefore detectable in the lower harmonics of surface loading (Böning et al., 2008).

5.1.6 Hydrological Variations in Selected Watersheds

The low degree part of the surface load contains large scale hydrological variations, which can studied on basin-wide scale. In the spectral domain, Eq. 4.14 can be used to compute the spatial mean of the basin. For large watersheds, it is in many cases also possible to retrieve the hydrological signal using a GPS-only inversion. Since it cannot be expected that the GRACE mission overlaps a GRACE follow-on, a gap in between the mission will most likely occur. Using a GPS-only solution has the potential to fill such a gap. Although the accuracy will be much less than that of GRACE.

This section covers the comparison of basin averages from (1) the joint inversion, (2) a GRACE-only weekly solution, and (3) a GPS-only inversion. Nine basins, of varying sizes, and covering various climatological regions, are investigated in terms of watershed variations. In the computation of the basin average, a (weak) Gaussian filter with a half-width of 200 km is applied. This reduces some of the remaining noise in the solution, without attenuating the solution too much.

The GPS-only solution uses constraints over the ocean as described in Sec. 4.1.3, and is resolved up to degree and order 10. The weekly GRACE solution and the combination are both resolved up to degree and order 30. The rescaling factors, to account for signal leakage in and out of the basin averages, are computed according to Sec. 4.1.4. All solutions have no background models restored such that the signal represents hydrological mass variation only.

Fig. 5.11 shows the three solutions plotted along side, for the considered basins. It is obvious that, although resolved up to a lower degree, the GPS only solution is more noisy (last column of Tab. 5.3). There are two effects which intermingle here. Firstly, the errors in the surface loading coefficients are larger, and the propagated error in terms of basin average will consequently increase. Secondly, the lower truncation of the GPS-only solution causes a different, and in most cases larger, rescaling factor. This will additionally change the noise level of the GPS-only series.

From Fig. 5.11 it is obvious that, on watershed scale, the GRACE solution follows that of the combination closely. Changes can however be seen in the annual amplitudes (see
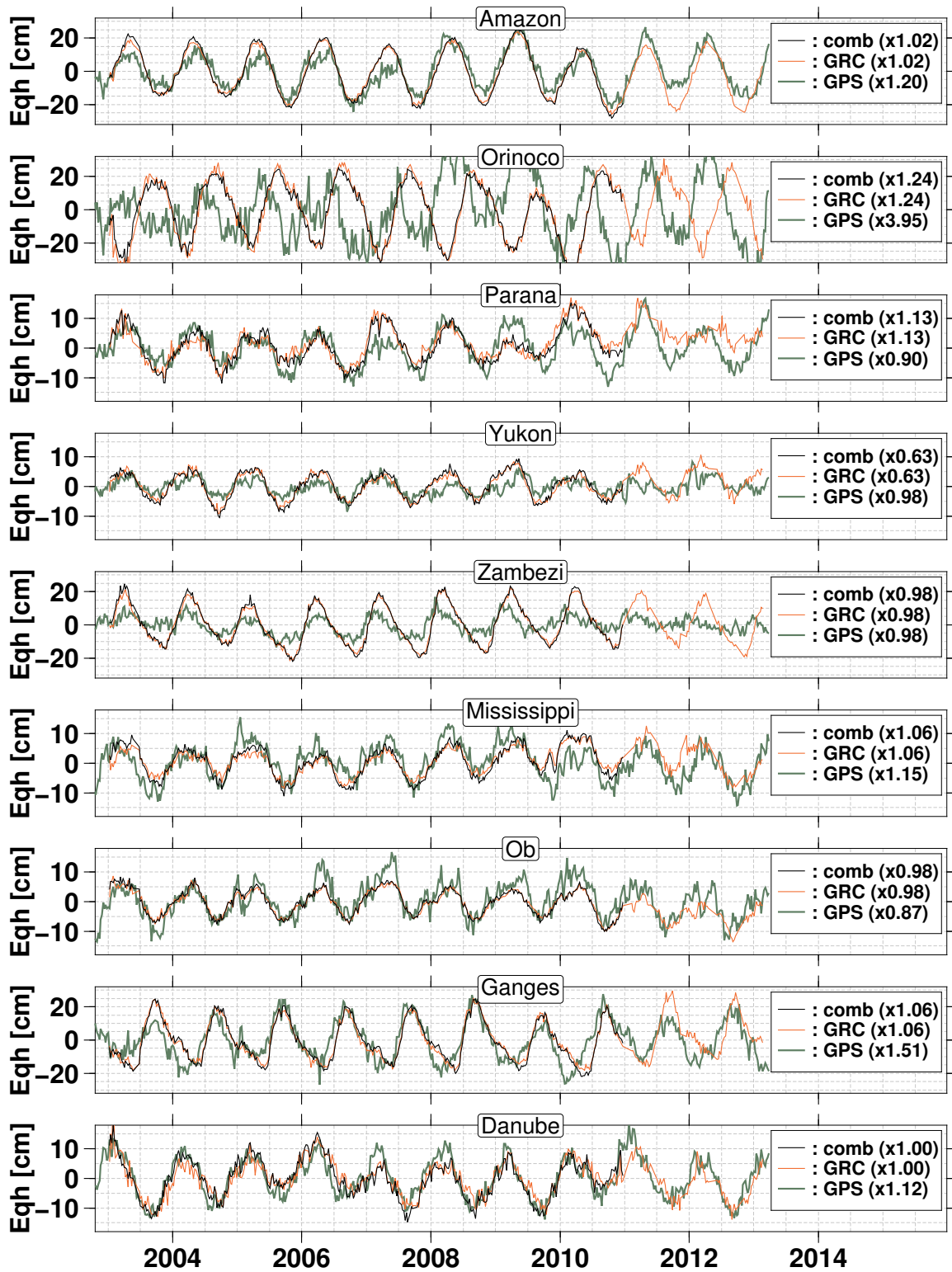
Figure 5.11: Total water storage variations in various hydrological watersheds.
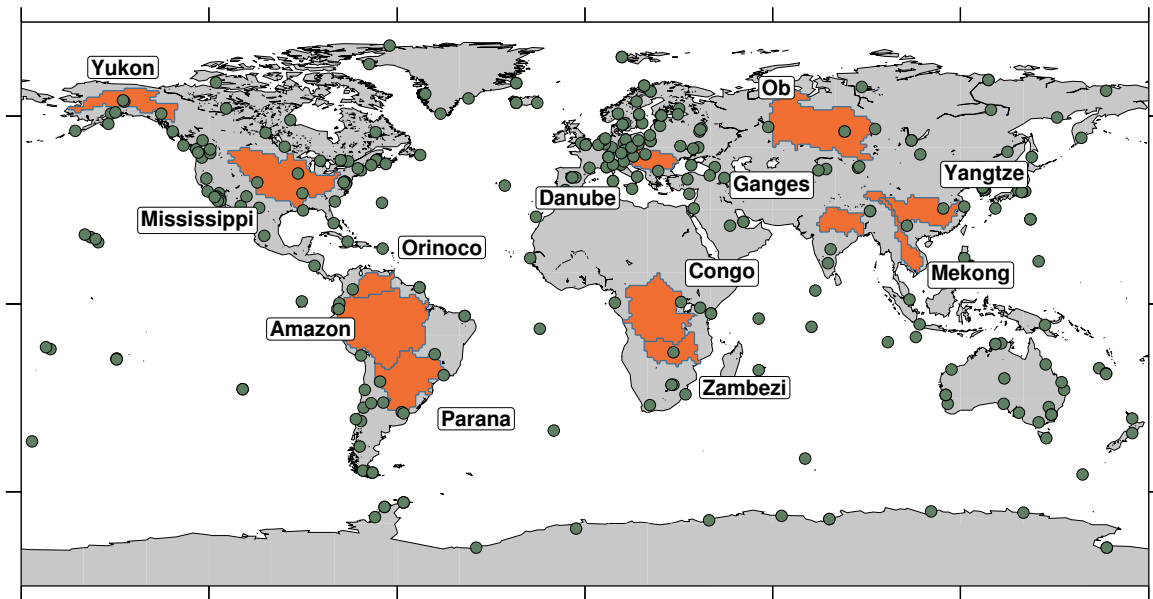
Figure 5.12: GPS station coverage of selected hydrological watersheds.

Tab. 5.3). A large part of the remaining differences are explained by the missing geocenter motion in the GRACE-only solution.

The coverage of the watersheds by GPS stations is shown in Fig. 5.12. Watersheds with a dense GPS coverage, such as the Danube and the Mississippi, show a good agreement of the GPS-only solution and the combination solution. The annual amplitude agrees to within (± 1 cm) and the phase to within a week.

In the Amazon, the largest watershed considered, the GPS-only solution agrees well in phase but displays a weaker annual amplitude (13 cm versus 19 cm). This may be related to the relative sparse GPS coverage, which shows no GPS receivers in the center of the Amazon, where the signal is strongest.

The Orinoco basin, situated right next to the Amazon basin, is much smaller, and its seasonal behavior largely out of phase (134 days) compared to that in the Amazon basin (Tab. 5.3). Clearly, Fig. 5.11 shows that the GPS-only solution breaks down in this region. On the one hand, the size of the basin is too small, resulting in larger errors and signal leakage out of the estimate. On the other hand out of phase signal from the Amazon is leaking into the estimate. Even from the pure annual modeled WGHM signal (column 2 in Tab. 5.3), we find that the filtered signal in the Orinoco basin suffers from the largest phase shift (42 days ahead of the unfiltered signal). The rescaling factor which needs to be applied is also excessively large (≈ 4), exaggerating both leakage effects and the noise level.

Although only slightly larger, the Ganges basin, shows a much better agreement between the GPS-only solution and the joint inversion. Although the coverage by GPS stations is rather sparse, the strong monsoonal signal obviously result in better skill for the GPS-only

solution. In Bangladesh, monsoonal flooding has already been succesfully detected using a GPS array (Steckler et al., 2010).

Some of the scaling factors, in Tab. 5.3 and Fig. 5.11 are smaller than 1. Although intuitively, one expects an attenuation of the signal, and hence a factor larger than 1, it is apparent that sometimes the signal leaking into the estimate is larger than the signal which is leaking out.

The discussion above demonstrates that there is definitely potential for the use of GPS-only inversions to cover a future GRACE mission gap. On the other hand the interpretation of hydrological signal from such inversions is highly heterogenous, depending on the GPS coverage and the leakage associated with the surrounding signal.

	WGHM	Annual		Semiann.		RMS
	$f_\vartheta\ (\delta t_a)$	A[cm]	t_a [doy]	S[cm]	t_s [doy]	post.[cm]
Amazon GPS	1.20 (2)	12.9 ($\pm$ 0.4)	121 ($\pm$ 2)	1.5 ($\pm$ 0.4)	9 ($\pm$ 7)	5.7
GPS+GRC+OBP	1.02 (0)	22.3 ($\pm$ 0.2)	119 ($\pm$ 1)	1.3 ($\pm$ 0.2)	152 ($\pm$ 5)	3.5
GRC	1.02 (0)	20.6 ($\pm$ 0.2)	117 ($\pm$ 1)	1.1 ($\pm$ 0.2)	157 ($\pm$ 6)	3.3
Congo GPS	1.27 (-5)	4.7 ($\pm$ 0.4)	100 ($\pm$ 5)	0.3 ($\pm$ 0.4)	115 ($\pm$ 46)	5.8
GPS+GRC+OBP	1.01 (3)	5.9 ($\pm$ 0.2)	63 ($\pm$ 2)	1.3 ($\pm$ 0.2)	128 ($\pm$ 5)	3.2
GRC	1.01 (3)	5.7 ($\pm$ 0.2)	54 ($\pm$ 2)	1.6 ($\pm$ 0.2)	141 ($\pm$ 4)	2.9
Danube GPS	1.12 (-1)	8.4 ($\pm$ 0.2)	59 ($\pm$ 1)	0.7 ($\pm$ 0.2)	107 ($\pm$ 8)	2.9
GPS+GRC+OBP	1.00 (0)	8.2 ($\pm$ 0.3)	66 ($\pm$ 2)	0.4 ($\pm$ 0.3)	147 ($\pm$ 22)	4.3
GRC	1.00 (0)	7.2 ($\pm$ 0.3)	75 ($\pm$ 2)	1.0 ($\pm$ 0.3)	28 ($\pm$ 8)	4.1
Ganges GPS	1.51 (-9)	14.9 ($\pm$ 0.4)	255 ($\pm$ 2)	2.4 ($\pm$ 0.4)	62 ($\pm$ 5)	5.6
GPS+GRC+OBP	1.06 (-3)	22.0 ($\pm$ 0.3)	280 ($\pm$ 1)	9.1 ($\pm$ 0.3)	65 ($\pm$ 1)	3.9
GRC	1.06 (-3)	21.2 ($\pm$ 0.3)	275 ($\pm$ 1)	8.0 ($\pm$ 0.3)	64 ($\pm$ 1)	4.3
Mekong GPS	1.70 (0)	8.9 ($\pm$ 0.3)	255 ($\pm$ 2)	1.6 ($\pm$ 0.3)	52 ($\pm$ 5)	3.6
GPS+GRC+OBP	1.14 (3)	28.0 ($\pm$ 0.4)	276 ($\pm$ 1)	3.0 ($\pm$ 0.4)	89 ($\pm$ 4)	5.4
GRC	1.14 (3)	27.0 ($\pm$ 0.4)	274 ($\pm$ 1)	3.9 ($\pm$ 0.4)	92 ($\pm$ 3)	5.6
Mississippi GPS	1.15 (-7)	6.3 ($\pm$ 0.3)	89 ($\pm$ 2)	1.3 ($\pm$ 0.3)	5 ($\pm$ 6)	3.6
GPS+GRC+OBP	1.06 (0)	6.9 ($\pm$ 0.2)	94 ($\pm$ 1)	1.1 ($\pm$ 0.2)	169 ($\pm$ 5)	2.4
GRC	1.06 (0)	4.9 ($\pm$ 0.2)	94 ($\pm$ 2)	0.8 ($\pm$ 0.2)	164 ($\pm$ 6)	2.2
Ob GPS	0.87 (3)	6.4 ($\pm$ 0.2)	92 ($\pm$ 2)	1.8 ($\pm$ 0.2)	145 ($\pm$ 4)	3.2
GPS+GRC+OBP	0.98 (-1)	4.8 ($\pm$ 0.1)	86 ($\pm$ 1)	1.1 ($\pm$ 0.1)	151 ($\pm$ 2)	1.4
GRC	0.98 (-1)	4.5 ($\pm$ 0.1)	90 ($\pm$ 1)	1.1 ($\pm$ 0.1)	156 ($\pm$ 2)	1.3
Orinoco GPS	3.95 (-42)	17.0 ($\pm$ 0.9)	145 ($\pm$ 3)	3.3 ($\pm$ 0.9)	180 ($\pm$ 8)	12.9
GPS+GRC+OBP	1.24 (-2)	70.2 ($\pm$ 1.2)	253 ($\pm$ 1)	14.1 ($\pm$ 1.2)	182 ($\pm$ 2)	17.0
GRC	1.24 (-2)	77.3 ($\pm$ 1.3)	255 ($\pm$ 1)	13.2 ($\pm$ 1.3)	7 ($\pm$ 3)	18.0
Parana GPS	0.90 (-9)	7.0 ($\pm$ 0.2)	103 ($\pm$ 2)	0.9 ($\pm$ 0.2)	19 ($\pm$ 6)	2.9
GPS+GRC+OBP	1.13 (-2)	5.3 ($\pm$ 0.2)	103 ($\pm$ 2)	0.1 ($\pm$ 0.2)	49 ($\pm$ 35)	2.5
GRC	1.13 (-2)	4.4 ($\pm$ 0.2)	87 ($\pm$ 3)	0.2 ($\pm$ 0.2)	43 ($\pm$ 27)	2.7
Yangtze GPS	0.87 (9)	6.6 ($\pm$ 0.2)	255 ($\pm$ 2)	1.6 ($\pm$ 0.2)	47 ($\pm$ 4)	3.3
GPS+GRC+OBP	1.10 (2)	3.5 ($\pm$ 0.1)	231 ($\pm$ 2)	0.6 ($\pm$ 0.1)	53 ($\pm$ 6)	1.7
GRC	1.10 (2)	4.1 ($\pm$ 0.1)	222 ($\pm$ 1)	0.4 ($\pm$ 0.1)	53 ($\pm$ 8)	1.5
Yukon GPS	0.98 (3)	2.4 ($\pm$ 0.1)	90 ($\pm$ 3)	1.1 ($\pm$ 0.1)	146 ($\pm$ 3)	1.7
GPS+GRC+OBP	0.63 (4)	9.0 ($\pm$ 0.1)	82 ($\pm$ 1)	1.7 ($\pm$ 0.1)	153 ($\pm$ 2)	2.0
GRC	0.63 (4)	8.0 ($\pm$ 0.1)	83 ($\pm$ 1)	1.0 ($\pm$ 0.1)	146 ($\pm$ 4)	2.0
Zambezi GPS	0.98 (-2)	5.8 ($\pm$ 0.2)	69 ($\pm$ 2)	0.9 ($\pm$ 0.2)	62 ($\pm$ 8)	3.6
GPS+GRC+OBP	0.98 (0)	15.4 ($\pm$ 0.2)	97 ($\pm$ 1)	4.4 ($\pm$ 0.2)	64 ($\pm$ 2)	3.4
GRC	0.98 (0)	14.7 ($\pm$ 0.2)	96 ($\pm$ 1)	3.6 ($\pm$ 0.2)	64 ($\pm$ 2)	3.2

Table 5.3: Seasonal amplitudes (in cm) and phases (in day of year) for selected watersheds in the time period (2003-2011). The amplitudes and phases are defined as in table 5.1. The applied scale factor, and the expected phase shift (not applied) of the filtered estimate is tabulated in the second column.

5.2 Inversion for Fingerprint Magnitudes

From the combination of GRACE and altimetry data, the inversion scheme described in Sec. 4.2 yields primarily time series which are associated with the predefined patterns ('fingerprints'). The estimated factors, associated with the ice-sheet drainage basins and glaciers can straightforwardly be interpreted as mass changes in Gton. In the spatial domain, different linear functionals may be constructed by scaling the appropriate fingerprints by their estimated factors and summing the results. This section will discuss a variety of extracted functionals, such as mean sea level changes, estimated GIA uplift, steric sea level changes, geocenter motion, and time variation of the ice sheets and glaciers. The results shown here are by no means exhaustive, as many (combinations of) observables can be extracted, but do provide an insight in the quality and possibilities of the inversion.

Unless explicitly stated otherwise, the results shown here were estimated using constraints on the inter-basin variations and the 5 (secular) GIA parameters as discussed in Sec. 4.2.4. Three Cartesian network biases were estimated for the altimeters, using data from the entire interval. In accordance with Tab. 4.1, the ice sheets and glaciers were parameterized using a total of 59 monthly parameters. In addition, 60 parameters describing the hydrological storage change and 160 steric parameters (100 from Ishii and Kimoto, 2009 and 60 bootstrapped patterns from altimetry residuals) were estimated each month.

5.2.1 Global Mean Sea Level Change

The fingerprint inversion allows a partitioning of the sea level into different contributions. A closure of the sea level budget is enforced in a least squares sense through the inversion scheme. Furthermore, the inversion is not restricted to secular effects but inter-annual variations are detected as well. The latter property is important to assess the significance of the trends and to quantify superimposed (natural) oceanic oscillations, such as the El Niño - La Niña cycle, the Pacific Decadal Oscillation (PDO) and the Arctic Oscillation (AO).

Fig. 5.13 depicts the estimated relative sea level change grouped in contributions from Greenland, Antarctica, land glaciers, hydrology and the steric components. As stated by Eq. 4.25, the contribution of the present day GIA to relative sea level is zero. Worth noting is that the annual cycle of the steric component is out of phase with the hydrological component (see also Tab. 5.4). In addition, from the posteriori RMSs from table 5.4, it becomes clear that, in the total sea level, some of the inter-annual noise in the steric sea level is canceled out by the hydrological component.

The interplay between the hydrological and steric component introduces the strongest inter-annual variations in the total sea level. Consequently, the trend estimates are expected to strongly depend on the chosen time interval. For the hydrologic component, a trend of -0.2 mm/yr is estimated, this value is consistent with Jensen et al. (2013) (-0.2 mm/yr) and Llovel et al. (2010)-0.22 mm/yr and to a lesser extent with Riva et al. (2010)-0.1 mm/yr. However, from the inspection of Fig. 5.13 it is not surprising that other trend estimates have been reported. For example, Ramillien et al., 2008 reported a positive trend of 0.19 mm/yr over the period from 2003-2006.

The estimated steric variation of the sea level is split up in a component which is linked to the first 100 EOFs of the upper 700m of the ocean and a component which is linked to the 60 bootstrapped patterns (see Sec. 4.2.1). Remarkable is that the 'bootstrapped' component exhibits a much larger trend of $1\,\mathrm{mm/yr}$ compared to the upper '700m' patterns ($0.17\,\mathrm{mm/yr}$). In fact, from inspecting Table 5.4, one sees that the trend from the interpolated ARGO data from Ishii and Kimoto (2009) can not explain the total steric sea level changes ($1.2\,\mathrm{mm/yr}$).
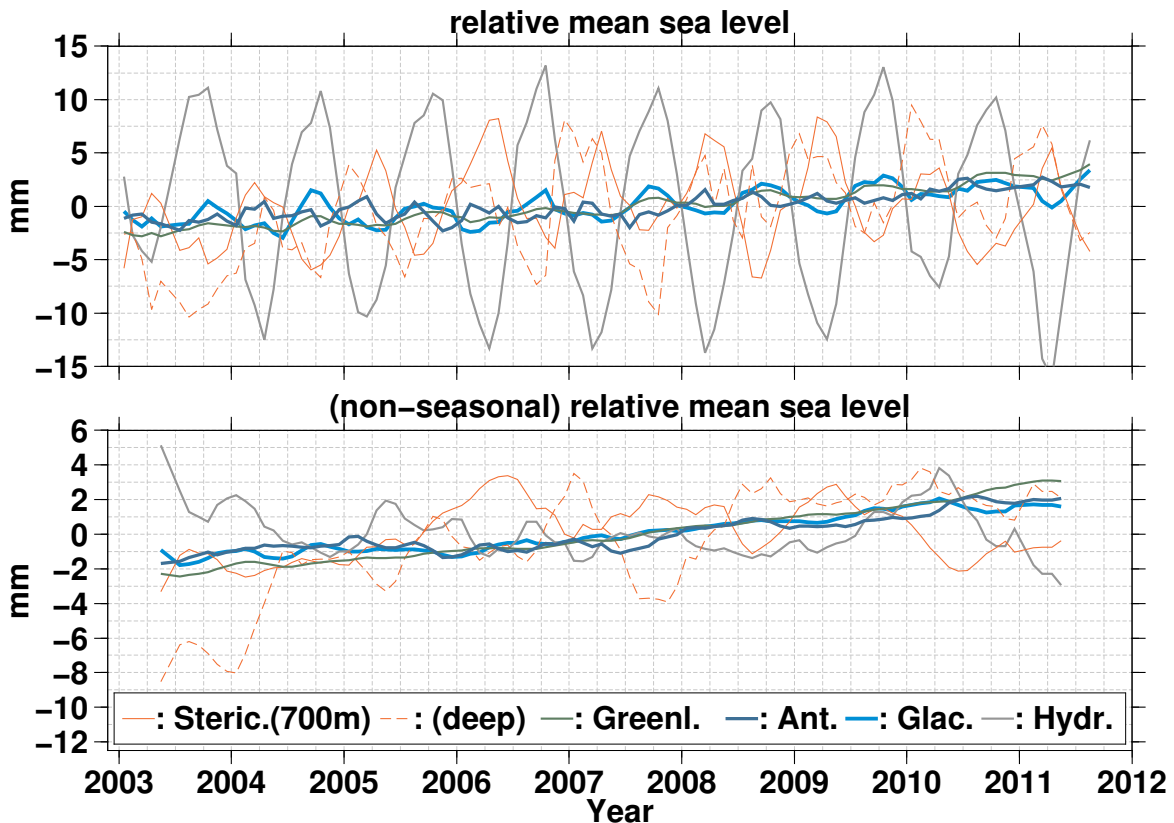
Figure 5.13: Estimated contributions to global relative sea level rise. The contributions are separated in the contributions from Greenland, Antarctica, land, glaciers, hydrology, and steric effects. The curves in the bottom figure have their annual harmonic fits removed and are filtered with a half year long boxcar filter.

The results suggests that deeper part of the ocean may be responsible for a large warming component, which has also been suggested by Balmaseda et al. (2013). When considering the Earth's radiation budget, a deep ocean warming has also been expected as the observed upper ocean layer cannot account for the excess heat by itself (Trenberth and Fasullo, 2010).

The trends associated with the glaciers and ice sheets are more significant as they display less inter-annual behavior. Greenland, shows the largest trend ($0.66\pm0.01\,\mathrm{mm/yr}$) while its residual variations are twice as small compared to the variations from Antarctica and the land glaciers. Combined, they account with $1.3\,\mathrm{mm/yr}$ for slightly more than half of the estimated global sea level rise ($2.5\pm0.11\,\mathrm{mm/yr}$).

	Annual		Trend	RMS
	A[mm]	t_a[doy]	mm/yr	post.[mm]
Antarctica RSL	0.3 ($\pm$ 0.09)	78 ($\pm$ 17)	0.40 ($\pm$ 0.03)	0.6
Antarctica GSL	0.3 ($\pm$ 0.09)	78 ($\pm$ 17)	0.38 ($\pm$ 0.03)	0.6
Greenland RSL	0.5 ($\pm$ 0.04)	282 ($\pm$ 5)	0.66 ($\pm$ 0.01)	0.3
Greenland GSL	0.5 ($\pm$ 0.04)	282 ($\pm$ 5)	0.64 ($\pm$ 0.01)	0.3
Hydrology RSL	11.1 ($\pm$ 0.28)	270 ($\pm$ 1)	-0.20 ($\pm$ 0.09)	2.2
Hydrology GSL	10.5 ($\pm$ 0.26)	270 ($\pm$ 2)	-0.19 ($\pm$ 0.08)	2.1
Glaciers RSL	1.2 ($\pm$ 0.07)	276 ($\pm$ 4)	0.43 ($\pm$ 0.02)	0.6
Glaciers GSL	1.2 ($\pm$ 0.07)	276 ($\pm$ 4)	0.42 ($\pm$ 0.02)	0.6
Steric(700m) RSL/GSL	4.2 ($\pm$ 0.29)	88 ($\pm$ 4)	0.17 ($\pm$ 0.08)	2.0
Steric(deep) RSL/GSL	4.3 ($\pm$ 0.35)	51 ($\pm$ 5)	1.03 ($\pm$ 0.10)	2.7
Steric RSL/GSL	8.1 ($\pm$ 0.48)	69 ($\pm$ 4)	1.20 ($\pm$ 0.14)	3.5
GIA GSL	-	-	-0.13 ($\pm$ 0.04)	-
Total RSL	5.3 ($\pm$ 0.37)	299 ($\pm$ 4)	2.50 ($\pm$ 0.11)	2.5
Total GSL	4.7 ($\pm$ 0.37)	303 ($\pm$ 5)	2.34 ($\pm$ 0.11)	2.5
Total @ J1+J2 (GSL)	4.2 ($\pm$ 0.43)	300 ($\pm$ 6)	2.16 ($\pm$ 0.12)	2.9
J1+J2 (GSL)	4.2 ($\pm$ 0.43)	302 ($\pm$ 6)	2.11 ($\pm$ 0.12)	2.9
Auxiliary				
MMA Colorado (GSL)	5.1 ($\pm$ 0.32)	288 ($\pm$ 4)	2.02 ($\pm$ 0.09)	3.9
Steric(Ishii)GSL/RSL	3.9 ($\pm$ 0.17)	88 ($\pm$ 3)	0.28 ($\pm$ 0.05)	1.2

Table 5.4: Trend, annual amplitude and phase of mean sea level changes, separated in different contributions over the time interval 2003-2011. RSL and GSL denote relative sea level and geocentric sea level respectively. The provided errors (within brackets) are the formal errors rescaled by the posteriori σ_0. An exception is the error of the GIA which is explicitly set to 33% of the trend value. The auxiliary multi mission altimetry (MMA) time series from Nerem et al. (2010) is readjusted with their GIA correction (-0.3mm/yr) to represent geocentric sea level, and is evaluated over the same time interval (2003-2011) as the inversion results. The entry with 'J1+J2', denotes the mean sea level as computed from along track Jason-1 and Jason-2 (thus excluding higher latitudes). Evaluated on the same altimetry tracks, the mean sea level change from the inversion is denoted by 'Total @ J1+J2'. The last column contains the root mean square of the residuals after the trend and annual fit have been removed from the time series.

From table 5.4 it becomes clear that the difference between the total geocentric sea level and relative sea level is in the order of -0.16 mm/yr. This is largely explained by the contribution of GIA (-0.13±0.04 mm/yr). Nerem et al. (2010) applied a larger GIA correction of -0.3 mm/yr to obtain relative sea level rise from multi-mission altimetry. Upon readjusting their series with their GIA correction, the trend in the their geocentric sea level is lower (2.02 mm/yr) compared to the estimated geocentric sea level trend from this study (2.34 mm/yr, see Tab. 5.4). This discrepancy can actually be explained by the contribution of the steric patterns in the Arctic. When the inversion results are propagated to the along track altimetry points, before estimating a uniform sea level rise, a smaller sea level rise is obtained as well (2.16±0.12 mm/yr). The latter value agrees to within the error bars with the estimate from Nerem et al. (2010) and with a GSL estimate using altimetry from this study (2.11±0.12 mm/yr).

5.2.2 Variations of the Ice Sheets

The mass variations of the major ice sheets are by no means uniform changes. The ice-sheets are constantly in motion, the marine terminating glacier are melting and drain in the ocean, while the mass is replenished through snow precipitation on the higher end of the glacier. A mass imbalance of the ice sheets will occur when either one of these processes outweigh the other. Mass losses occur at small spatial scales at the glacier outlets, and are associated with a combination of melting and an acceleration of the glaciers. Precipitation generally occurs at wider spatial scales, but may be strongly influenced by topography.

Within the inversion, the ice sheets are decomposed in several drainage basins, such that the estimated mass changes can be used to study the dynamics of the ice sheets.

Greenland

The ice dome in Greenland inclines relatively steeply in the vicinity of the coast before leveling off to about 2-3 km thickness. In the center of Greenland, the bedrock below the ice sheet is actually below the current sea level. The mass losses are therefore expected to occur in a narrow band in the vicinity of the coasts.

The discussion in Sec. 5.2.1 showed that the Greenland ice sheet contributes about 0.66 mm/yr to relative sea level rise. This implies that the total ice sheet is in imbalance by about -253 Gt/yr. Table 5.5 shows the partitioning of this value in its different contributions in terms of trends and annual amplitude and phase. The time series of the individual basins are plotted in Fig. 5.14. In the same figure, the trend is plotted in the spatial domain. To compare the trends, estimates from Wouters et al. (2008) and an ICEsat derived mass trend (Sørensen et al., 2011) are also tabulated. It must be noted that these trends are derived from shorter time intervals, as used in this thesis.

From the time variations of figure 5.14 one sees that, despite the applied inter-basin regularization, some curves are negatively correlated (e.g. within basin 1 and basin 3). It is therefore possible that the obtained trends will be exaggerated somewhat, but will partly compensate each other when combined. A simple 'solution' to this problem would be to crank up the strength of the regularization strength. However, this would at the same time also hide interesting features which are visible at the current regularization strength. For

this reason, I choose to set the strength of the regularization relatively low while acknowledging that inter-basin (error) correlations exist in the estimates.

	Annual		Trend	W08	ICEsat	RMS
	A [Gt]	t_a [doy]	[Gt/yr]	[Gt/yr]	[Gt/yr]	post.[Gt]
Green1 <2000m	57.1 (± 7.69)	118 (± 8)	-40.4 (± 2.2)	-12.0	-14.7	54.2
Green1 >2000m	37.9 (± 6.20)	321 (± 9)	15.8 (± 1.8)	-1.0	0.4	43.2
Green2 <2000m	14.8 (± 3.39)	115 (± 14)	-16.8 (± 1.0)	-6.0	-5.2	23.9
Green2 >2000m	11.5 (± 3.50)	47 (± 18)	18.3 (± 1.0)	19.0	3.0	24.7
Green3 <2000m	37.4 (± 5.78)	165 (± 9)	-16.8 (± 1.6)	-25.0	-12.2	40.4
Green3 >2000m	27.5 (± 5.11)	19 (± 11)	-1.1 (± 1.4)	-10.0	2.6	35.9
Green4 <2000m	5.7 (± 4.01)	61 (± 41)	-37.4 (± 1.2)	-49.0	-43.0	28.7
Green4 >2000m	16.8 (± 2.06)	111 (± 7)	-6.8 (± 0.6)	-7.0	-0.3	14.8
Green5 <2000m	60.1 (± 3.08)	115 (± 3)	-47.1 (± 0.9)	-51.0	-55.8	22.7
Green5 >2000m	2.1 (± 1.31)	5 (± 36)	-11.9 (± 0.4)	6.0	-4.2	9.1
Green6 <2000m	33.7 (± 6.41)	107 (± 11)	-26.2 (± 1.8)	-13.0	-24.9	45.6
Green6 >2000m	13.6 (± 3.25)	321 (± 14)	9.0 (± 0.9)	11.0	0.2	22.8
Green7 <2000m	18.1 (± 4.58)	131 (± 15)	-48.7 (± 1.3)	-14.0	-34.3	32.7
Green7 >2000m	14.0 (± 3.84)	364 (± 15)	18.1 (± 1.1)	2.0	-0.2	26.8
Green8 <2000m	29.0 (± 6.33)	93 (± 13)	-52.5 (± 1.8)	-16.0	-45.6	47.4
Green8 >2000m	11.8 (± 5.73)	244 (± 29)	-8.3 (± 1.7)	-13.0	-1.1	41.3
Total >2000m	76.9 (± 11.38)	356 (± 8)	33.4 (± 3.2)	7.0	0.4	78.6
Total <2000m	237.1 (± 21.74)	119 (± 5)	-286.0 (± 6.2)	-186.0	-235.6	154.4
Total	200.6 (± 15.03)	101 (± 4)	-252.5 (± 4.3)	-179.0	-235.2	109.0

Table 5.5: Annual mass changes and trends in Gtons for the resolved basins in Greenland. The trends are furthermore compared to (GRACE) trends from Wouters et al. (2008)(column, W08, using data from Feb 2003 - Jan 2008) and ICEsat derived trends from Sørensen et al. (2011)/Sasgen et al. (2012b), using data from 2003 until 2009.

Generally, we see that at higher elevations (above 2000m) a mass increase, while at the lower elevations a mass decrease is visible. Most obvious are the strong mass losses in the South East of Greenland and in basin 7 where the Jakobshaven glacier is located. At the higher elevations, we see the largest mass increases in the basins 1, 2 and 7. In particular the increase in the high elevation part of basin 1 seems to be a more recent phenomena starting from 2008. The positive mass trend (18.3 $^{Gt}/_{yr}$) of the upper 2000m of basin 2 seems to be a steady phenomena and is also in good agreement with the estimate obtained from ICEsat(19.0 $^{Gt}/_{yr}$).

Apart from the trends, it is clear from Fig. 5.14 that several interesting non-secular signals are visible. The low elevation part of basin number 5 in the South East exhibits for example a strong seasonal signal. This is not unexpected, since one expects strong seasonal fluctuations in that region associated with the transport of moist air from the Gulf stream. Table 5.5 also indicates a strong seasonal signal in the lower section of basin 1, however since the upper section of the basin shows an almost opposite phase, this can be probably be attributed to a correlated error.

The mass loss in many of the basins are accelerating, and some losses appear to be started only recently. When the trends are compared to those of Wouters et al. (2008), which are

derived from a shorter time interval (2003 until the start of 2008), one sees that for example basin 6, 7 and 8 exhibit a significantly larger trend. The acceleration is also confirmed by comparing the trends with those as derived from ICEsat, which uses a somewhat larger time interval (2003-2009). The total ice mass loss in Greenland is estimated to be -252 $^{Gt}/_{yr}$ over the considered time interval (Jan 2003 until Dec 2011).
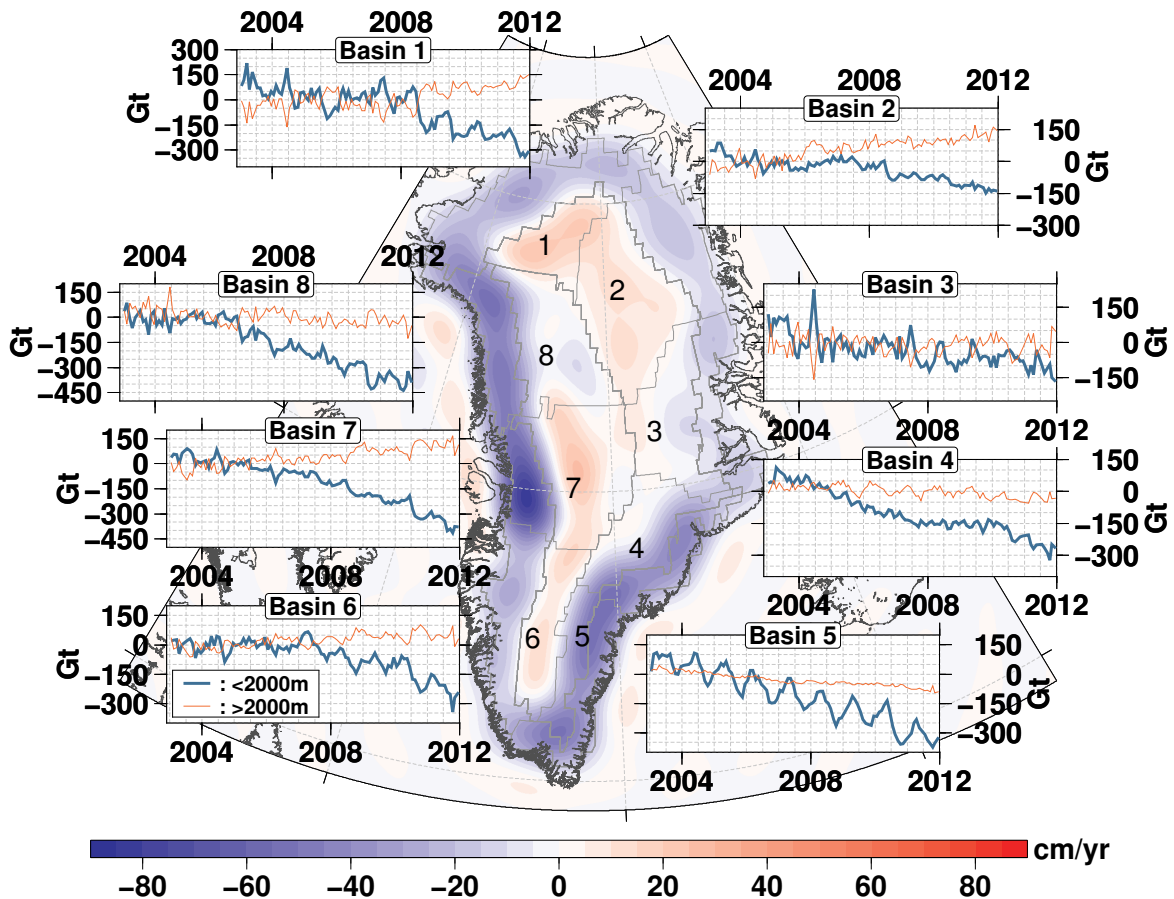
Figure 5.14: Estimated basin changes in Greenland in Gt. The background image depicts the computed trend in terms of equivalent water height. The trend is obtained by summing all basin contributions in terms of geoid height. Subsequently, a mean, trend and annual harmonic is fitted through each spherical harmonic coefficient. The obtained trend is then converted from geoid height to surface load and evaluated in the spatial domain.

Antarctica and GIA

As stated earlier in Sec. 4.2.4, the challenge in Antarctica is to separate the GIA signal from the present day mass changes in the drainage basins. It is therefore useful to discuss these topics together.

Similar to the discussion of the Greenland mass changes, a table (5.6) is provided where the annual fits and trends of the basins are assembled. To obtain an impression of the time

variations, the estimated basin curves have been plotted over time in Fig. 5.15. The estimated trend is plotted in the spatial domain in the same figure.

From Fig. 5.15, it is obvious that the most prominent changes occur in the Amundsen sea sector (basins 20-23). These basins exhibit mass losses from 30 to over 60 $^{Gt}/_{yr}$. It should be stressed that these changes are mainly related to the accelerating glacier velocities and melting in this region, and are virtually unaffected by the GIA signal, which only contributes an apparent 1-2 $^{Gt}/_{yr}$ per basin. Furthermore, although a significant annual signal is present, the long term signal is dominated by trends and more recent accelerations. Compared to the results of Sasgen et al. (2012a) the estimated trends from this study are consistently larger by about 10-30 $^{Gt}/_{yr}$. although the time period is similar. In the current study, the GRACE signal up to degree and order 150 is used, and only a weak inter-basin constraint is applied. This possibly allows more signal to propagate in the estimates, compared to using filtered GRACE RL04 data.
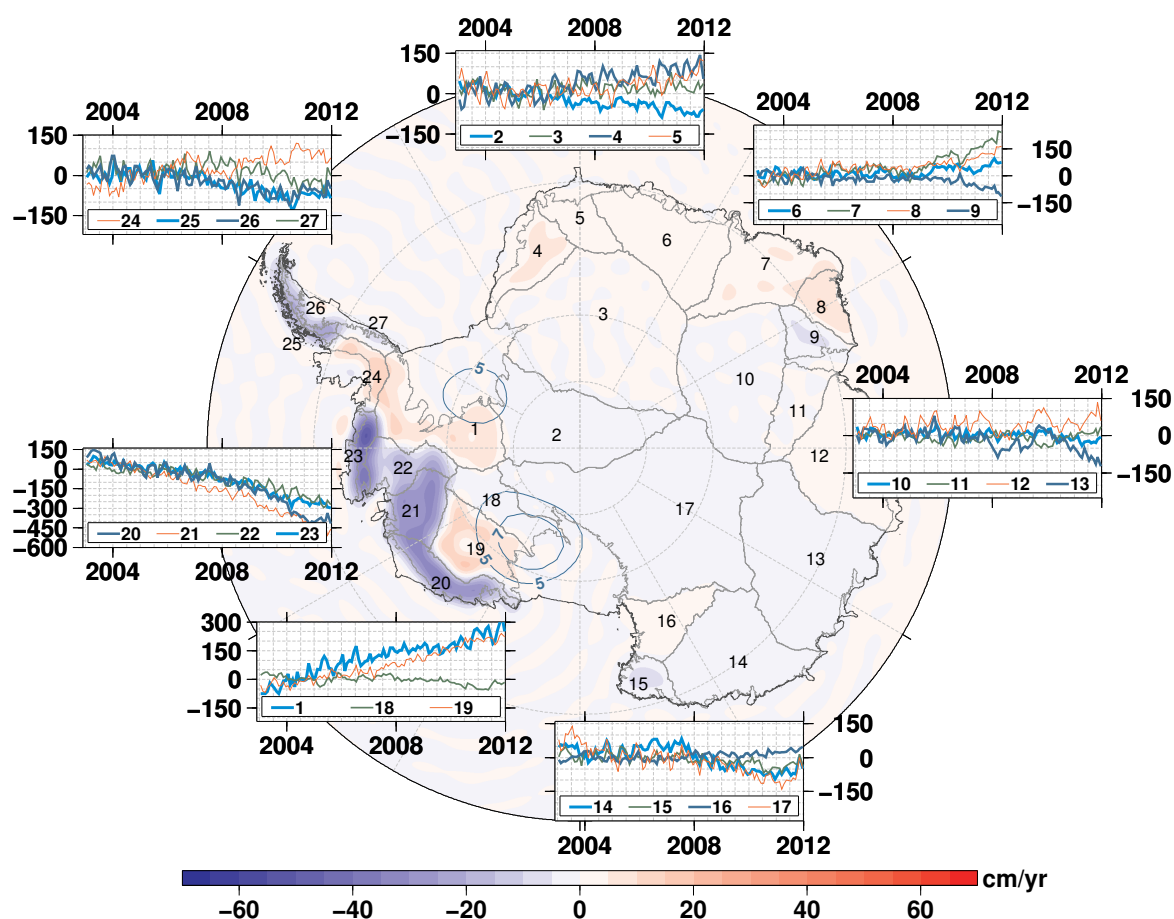
Figure 5.15: As in Fig. 5.14, but now for the Antarctic ice sheet. The blue contours indicate the estimated GIA uplift (see also Fig. 5.16).

The estimated GIA signal, in terms of present day uplift, is displayed in Fig. 5.16. The plot has been constructed by simply adjusting the spherical harmonic coefficients of the

	Annual		Trend	S12	GIA	RMS
	A (Gt)	t_a (doy)	Gt/yr	Gt/yr	Gt/yr	post.
02_EAIS	13.1 ($\pm$ 1.79)	286 ($\pm$ 8)	-11.5 ($\pm$ 0.5)	-6	9.0	12.9
03_EAIS	14.8 ($\pm$ 2.92)	261 ($\pm$ 12)	1.8 ($\pm$ 0.9)	4	8.0	21.1
04_EAIS	23.3 ($\pm$ 3.08)	203 ($\pm$ 7)	13.2 ($\pm$ 0.9)	12	1.0	21.5
05_EAIS	20.2 ($\pm$ 3.69)	11 ($\pm$ 10)	8.0 ($\pm$ 1.0)	5	0.0	27.2
06_EAIS	16.8 ($\pm$ 2.59)	235 ($\pm$ 9)	4.7 ($\pm$ 0.8)	5	2.0	18.8
07_EAIS	6.4 ($\pm$ 5.04)	336 ($\pm$ 45)	21.7 ($\pm$ 1.4)	13	2.0	35.0
08_EAIS	5.5 ($\pm$ 3.48)	360 ($\pm$ 35)	12.9 ($\pm$ 1.0)	15	1.0	25.2
09_EAIS	5.9 ($\pm$ 2.82)	180 ($\pm$ 27)	-7.0 ($\pm$ 0.8)	-1	1.0	19.9
10_EAIS	4.0 ($\pm$ 1.88)	292 ($\pm$ 28)	-2.7 ($\pm$ 0.6)	-1	5.0	13.9
11_EAIS	2.0 ($\pm$ 2.48)	250 ($\pm$ 73)	-0.1 ($\pm$ 0.7)	9	1.0	17.7
12_EAIS	19.5 ($\pm$ 3.62)	275 ($\pm$ 11)	4.1 ($\pm$ 1.1)	-8	4.0	26.1
13_EAIS	14.4 ($\pm$ 4.21)	251 ($\pm$ 17)	-9.7 ($\pm$ 1.2)	-8	5.0	30.4
14_EAIS	11.0 ($\pm$ 4.72)	215 ($\pm$ 25)	-14.3 ($\pm$ 1.4)	-8	2.0	31.8
15_EAIS	5.7 ($\pm$ 2.48)	96 ($\pm$ 26)	-6.5 ($\pm$ 0.7)	-2	0.0	17.8
16_EAIS	6.0 ($\pm$ 1.83)	355 ($\pm$ 17)	3.7 ($\pm$ 0.5)	-5	1.0	12.4
17_EAIS	19.1 ($\pm$ 3.84)	253 ($\pm$ 12)	-18.8 ($\pm$ 1.1)	-4	13.0	27.6
01_WAIS	6.1 ($\pm$ 4.13)	68 ($\pm$ 40)	33.2 ($\pm$ 1.2)	9	6.0	29.8
18_WAIS	7.9 ($\pm$ 2.17)	272 ($\pm$ 17)	-5.0 ($\pm$ 0.6)	8	6.0	15.6
19_WAIS	10.5 ($\pm$ 2.64)	235 ($\pm$ 15)	31.7 ($\pm$ 0.8)	8	6.0	18.9
20_WAIS	5.6 ($\pm$ 7.37)	185 ($\pm$ 74)	-56.1 ($\pm$ 2.1)	-38	1.0	49.7
21_WAIS	8.3 ($\pm$ 4.03)	311 ($\pm$ 28)	-62.4 ($\pm$ 1.2)	-51	2.0	29.5
22_WAIS	9.8 ($\pm$ 5.18)	253 ($\pm$ 32)	-31.1 ($\pm$ 1.5)	-25	2.0	36.4
23_WAIS	5.0 ($\pm$ 4.51)	175 ($\pm$ 50)	-41.4 ($\pm$ 1.3)	-12	0.0	31.4
24_PENIN	10.8 ($\pm$ 3.77)	263 ($\pm$ 21)	13.9 ($\pm$ 1.1)	4	1.0	26.6
25_PENIN	5.3 ($\pm$ 3.21)	72 ($\pm$ 36)	-12.4 ($\pm$ 0.9)	-25	0.0	22.8
26_PENIN	14.0 ($\pm$ 3.13)	27 ($\pm$ 13)	-12.0 ($\pm$ 0.9)	-	0.0	21.9
27_PENIN	9.3 ($\pm$ 3.94)	102 ($\pm$ 25)	-4.5 ($\pm$ 1.1)	-	1.0	27.4
PENIN	14.4 ($\pm$ 7.55)	43 ($\pm$ 30)	-15.1 ($\pm$ 2.1)	-21	2.0	53.4
WAIS	29.1 ($\pm$ 16.86)	247 ($\pm$ 34)	-131.2 ($\pm$ 4.9)	-102	22.0	119.4
EAIS	107.6 ($\pm$ 20.28)	262 ($\pm$ 11)	-0.5 ($\pm$ 6.0)	19	57.0	146.9
Total	123.0 ($\pm$ 33.64)	263 ($\pm$ 16)	-147.0 ($\pm$ 9.9)	-103	81.0	237.9

Table 5.6: Annual mass changes and trends in Gtons for the drainage basins in Antarctica. The column denoted with S12 denote the values as published by Sasgen et al. (2012a), who used the same basin delineation. The apparent mass change as would have been induced by the estimated GIA model is tabulated in the column marked with 'GIA'. These values are computed by means of basin averaging the estimated GIA signal.

reference GIA uplift using the estimated GIA parameters. In the spectral domain, such a rescaling is justified since the relationship between the GIA-induced Stokes coefficients and the associated uplift coefficients is approximately linear (Wahr et al., 2000, Purcell et al., 2011).
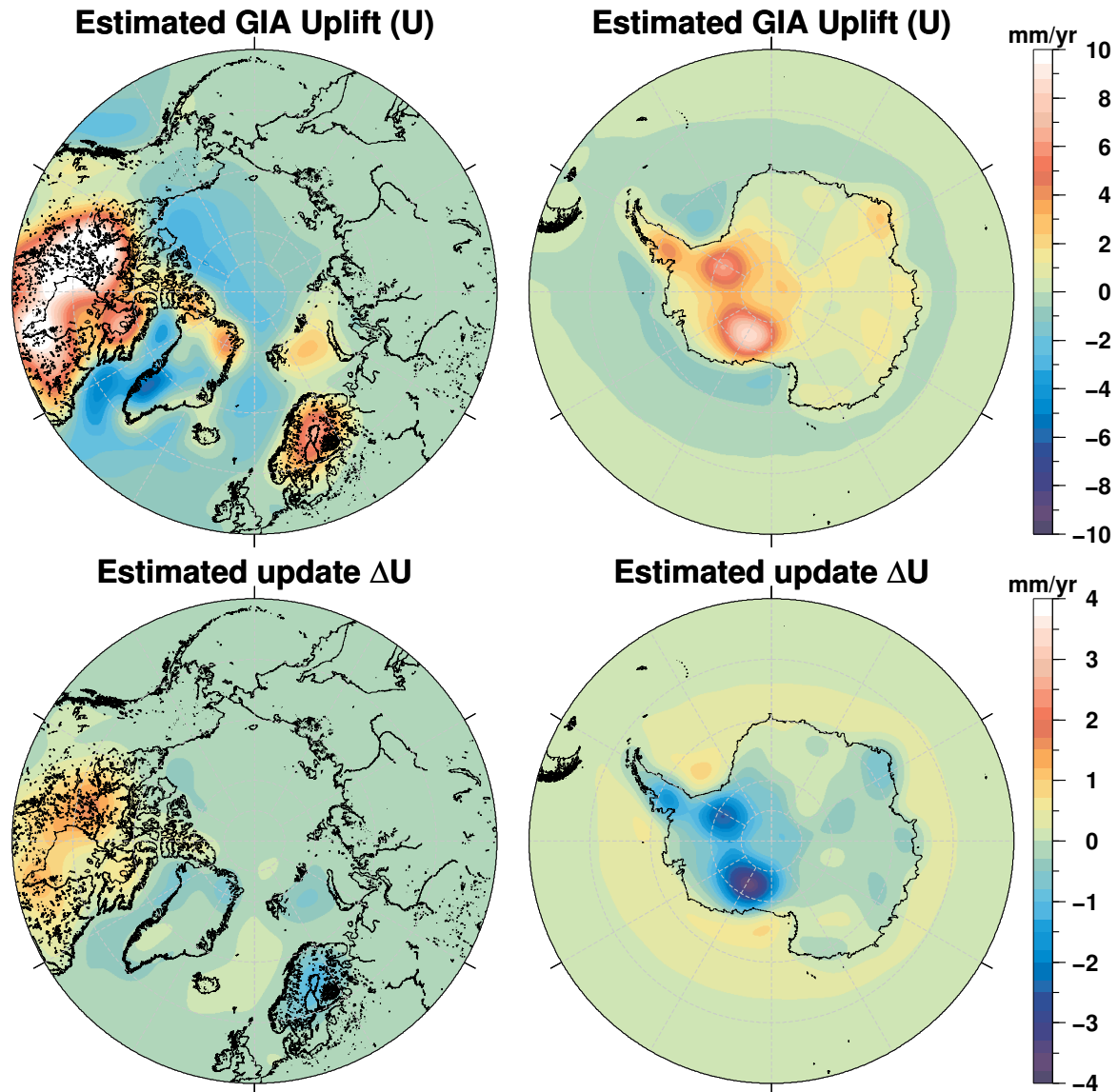
Figure 5.16: Estimated GIA uplift in the northern and southern hemisphere. The bottom two figures, indicate the change relative to the a priori model (ICE-5G, with VM2 earth model).

Compared to the reference GIA model in Antarctica, the estimated model shows 31% smaller amplitudes. Smaller GIA signals were also found by Whitehouse et al. (2012) and Sasgen et al. (2012a). In particular, Sasgen et al. (2012a) suggested that the GIA signal is much smaller than previously assumed. Integrated over Antarctica they found an appar-

ent mass change of 48 Gt/yr which is roughly twice as small as the value estimated here 81 Gt/yr. Accordingly, this difference is also reflected in the total present day mass change. Interesting is that, when the GIA constraints , applied in this study, would be loosened such values would also be obtained. It is therefore likely that the GIA constraint over Antarctica might still be too strong, but a more detailed study is not within the scope of this work.

One thing that would speak against this, is that the basins 1 and 19, which are now associated with a strong positive trend (roughly 30 Gt/yr), would be even stronger when the GIA component was decreased. Alternatively, it could be that a different GIA pattern, whose maximum values are shifted towards the centers of basin 1 and 19, would fit the data better.

The basins which are most affected by the GIA signal lie on the boundary between West and East Antarctica (basins 1, 2, 3, 17, 18, 19). Although the GIA signal in basins 2, 3 and 17 are not strong in value, they may still falsely contribute to the mass imbalance of Antarctica, since the basins are so large. It should be remarked that the ice loading history of ICE5-G results in significantly more signal in east Antarctica compared to the ice loading histories from Ivins and James (2005), Whitehouse et al. (2012), Shepherd et al. (2012).

Compared to the trends, inter-annual variations play a more important role in East Antarctica and on the Antarctic peninsula. These are likely associated with atmospheric events. For example the recent changes in Dronning Maud land (basins 4-7) have been associated with large scale snow fall events (Böning et al., 2012).

5.2.3 Variations of Land Glaciers and Terrestrial Hydrology

Besides the mass changes of the major ice sheets, estimates of the land glaciers and hydrology can be extracted. In terms of global mean sea level, this has been discussed in Sec. 5.2.1, but the inversion also allows a finer resolution.

Variations in the Glacier Clusters

Similar to the discussion on the ice sheets, Figs. 5.17 and 5.18, display the time variation of the glaciers clusters in terms of mass change overlying the induced trend in the spatial domain. The fitted annual amplitudes, phases, and trends are tabulated in Tab. 5.7.

From the table and figures it is clear that the glaciers are considerably affected by (inter)annual signals. The annual amplitude, associated with the total glacier contributions, is more than twice as large as that of Greenland and more than three times as large as the antarctic contribution. Strong annual amplitudes are present in Alaska and Kamchatka.

Overall, no doubt exists that the glaciers are losing ice (-149±9 l/Gtyr). The strongest mass losses occur in Patagonia (-41 Gt/yr) and Alaska (-44 Gt/yr). A relative strong trend (-29 Gt/yr) is also seen on the Queen Elizabeth islands (main contributor Ellesmere Island). The northern most Artic Islands and Iceland all show a consistent mass loss. Although more affected by inter-annual variations, the Alps in central Europe are losing mass with -4.6 Gt/yr.

The largest and most significant positive trend is only 5.5±1.2 Gt/yr, and is found in the
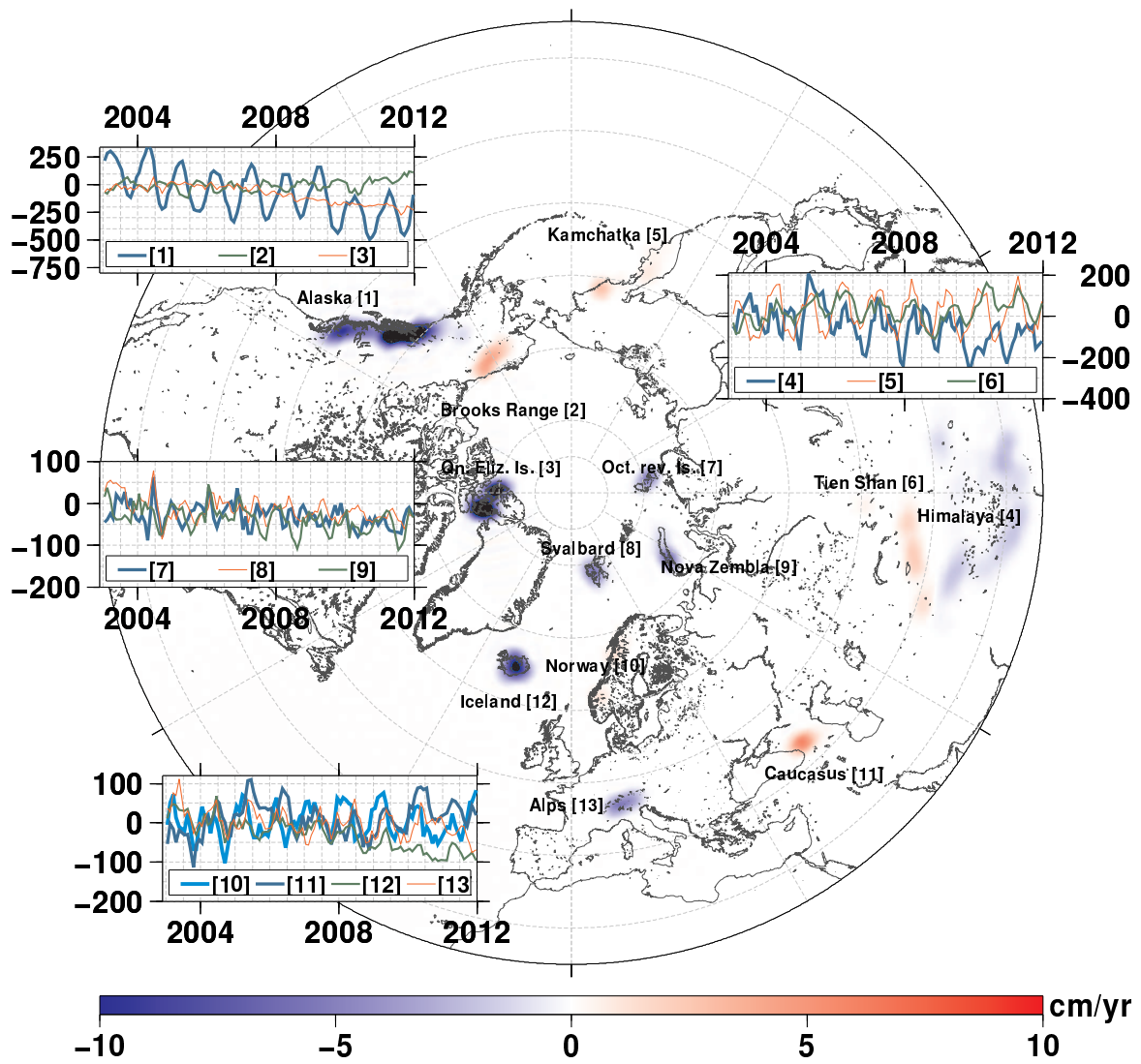
Figure 5.17: As in Fig. 5.14 but now for the glacier clusters in the northern hemisphere.

Brooks range in Northern Alaska. Compared to the other Alaska glaciers a much weaker annual signal is found.

An interesting contrast can be found between the Himalayas and the Tien Shan mountain ranges. From the time variation in Fig. 5.17, one sees that the curves are diverging in more recent times. This is also reflected in the trends which have opposite sign (Himalayas: -16.6±2.4 Gt/yr, Tien Shan: (4.3±1.6 Gt/yr). After removing the fits, a large amount of signal remains in the signal (RMS of 42-59 Gt), making it difficult to assess the robustness of the trends in Tien Shan mountains.
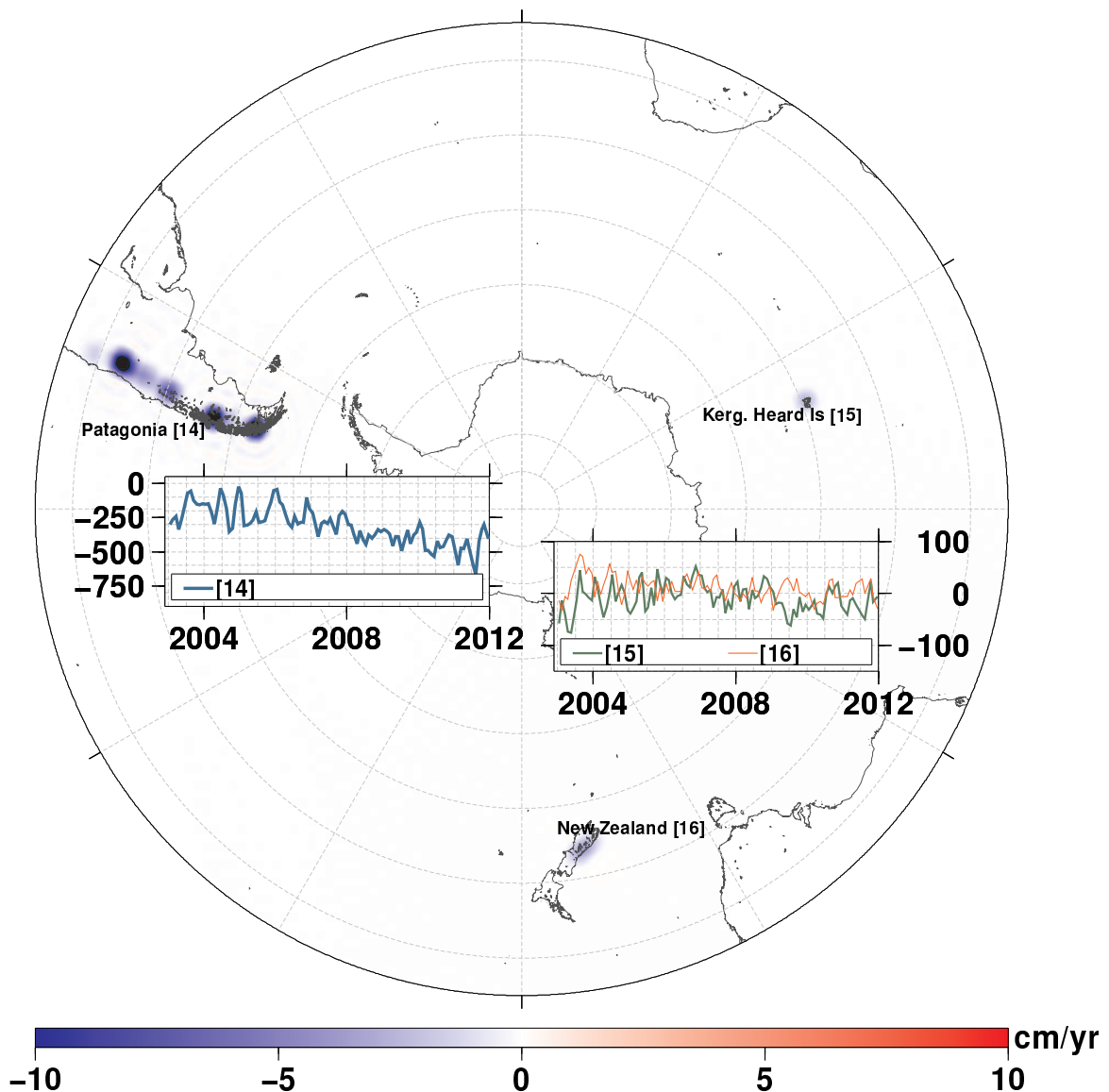
Figure 5.18: As in Fig. 5.17 but now for the glacier clusters in the southern hemisphere.

In relation to the errors, all estimated trends are significant. However, considering the

residual variations, one can suspect that some of the smaller trends may change beyond their error bars, when different time intervals are used. For example, the clusters in the Alps, Norway, Caucasus, New Zealand, Kerguelen&Heard is., and Kamchatka, are all heavily affected by strong inter-annual variations.

	Annual		Trend	RMS
	A (Gt)	t_a (doy)	Gt/yr	post.
Alaska	216.4 ($\pm$ 8.39)	91 ($\pm$ 2)	-44.1 ($\pm$ 2.5)	61.3
Alps	25.9 ($\pm$ 2.98)	153 ($\pm$ 7)	-4.6 ($\pm$ 0.9)	21.8
Brooksrange_Alaska	46.0 ($\pm$ 4.18)	288 ($\pm$ 5)	5.5 ($\pm$ 1.2)	31.7
Caucasus	33.5 ($\pm$ 4.52)	138 ($\pm$ 8)	3.1 ($\pm$ 1.3)	32.3
Himalaya	61.9 ($\pm$ 8.37)	147 ($\pm$ 8)	-16.6 ($\pm$ 2.4)	59.3
Iceland	19.0 ($\pm$ 2.12)	119 ($\pm$ 7)	-12.1 ($\pm$ 0.6)	15.1
Kamchatka	113.5 ($\pm$ 4.53)	74 ($\pm$ 2)	2.0 ($\pm$ 1.3)	33.5
Kerg_Heard_Is	12.4 ($\pm$ 3.42)	304 ($\pm$ 16)	-1.8 ($\pm$ 1.0)	25.7
New_Zealand	11.5 ($\pm$ 2.47)	213 ($\pm$ 12)	-3.5 ($\pm$ 0.7)	17.9
Norway	37.5 ($\pm$ 3.99)	60 ($\pm$ 6)	2.2 ($\pm$ 1.2)	28.7
Nova_Zembla	27.5 ($\pm$ 2.38)	30 ($\pm$ 5)	-4.9 ($\pm$ 0.7)	17.5
Oct_revo_Is_Rus	16.2 ($\pm$ 3.01)	284 ($\pm$ 11)	-3.9 ($\pm$ 0.9)	22.1
Patagonia	47.9 ($\pm$ 9.92)	336 ($\pm$ 12)	-41.4 ($\pm$ 2.8)	73.5
Qn_Elizabeth_Is	7.8 ($\pm$ 4.85)	85 ($\pm$ 37)	-28.5 ($\pm$ 1.4)	37.0
Svalbard	19.6 ($\pm$ 2.49)	117 ($\pm$ 8)	-4.3 ($\pm$ 0.7)	18.1
Tien_Shan	52.3 ($\pm$ 5.53)	111 ($\pm$ 6)	4.3 ($\pm$ 1.6)	41.8
Total	433.1 ($\pm$ 28.81)	92 ($\pm$ 4)	-148.7 ($\pm$ 8.5)	224.2

Table 5.7: Estimated mass variations of the land glacier clusters

Variations in Hydrology

In the inversion, the principal components, associated with the first 60 hydrological EOFs from WGHM, are estimated from the GRACE and altimetry data. This allows a direct comparison with the principal components coming from the analysis of WGHM. For the first 18 modes, explaining 94% of the total variance, these curves are plotted against each other in Fig. 5.19.

Compared to WGHM, the seasonal amplitudes in the first two modes, are larger for the inversion. For the other modes, we generally see an increased variability of the estimated curves. The increase in amplitude and variability is in agreement with the calibration study of Werth and Güntner (2010). In the tropical realm of WGHM, they found the model underestimating the seasonal amplitude and variability compared to GRACE. In contrast, at higher latitude regions, they found that the model overestimated GRACE. However, such a latitudinal dependency can not be spotted from Fig. 5.19, and the displayed variations are likely to be dominated by the tropical component of the model, which is more important in terms of variance.

From the secular modes 7 and 9, one can also observe that the inversion generally yields larger trends. This would suggest that GRACE data may play an important role for correcting the trends in assimilation schemes (Eicker et al., 2014).
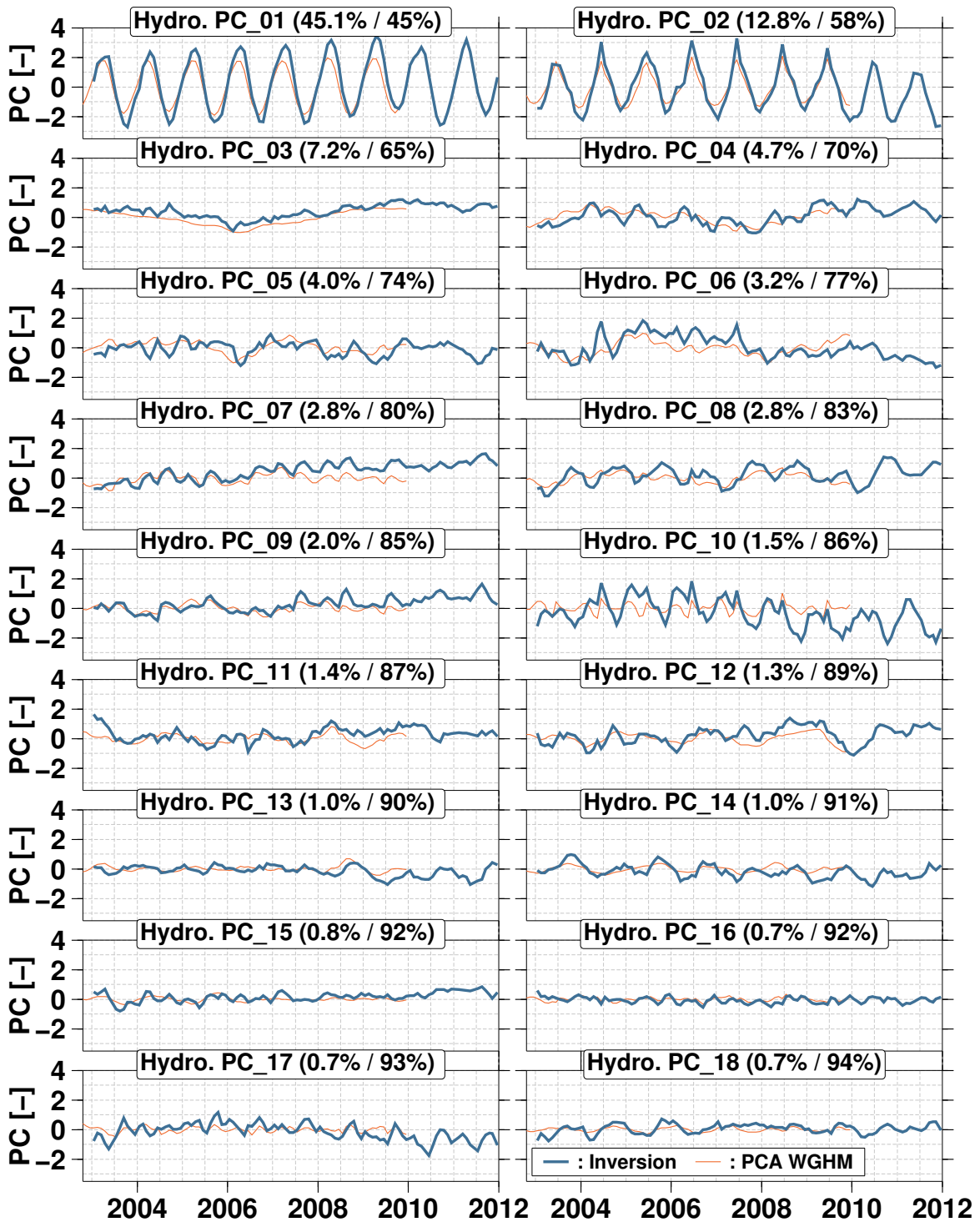
Figure 5.19: Time variation of the first 18 principal components of the changes in terrestrial total water storage. The scales, as estimated by the inversion, are plotted along the principal components which were computed from the PCA of the dataset from WGHM Döll et al. (2003). The percentages denote the variance explained (per mode/cumulative).

5.2.4 Geocenter Motion from the Fingerprint Inversion

All the patterns, which flow into the observation equations are available in the CF frame. Consequently, the estimated scales, can be propagated in terms of geocenter motion (here CM-CF), by using the degree 1 coefficients of the patterns.
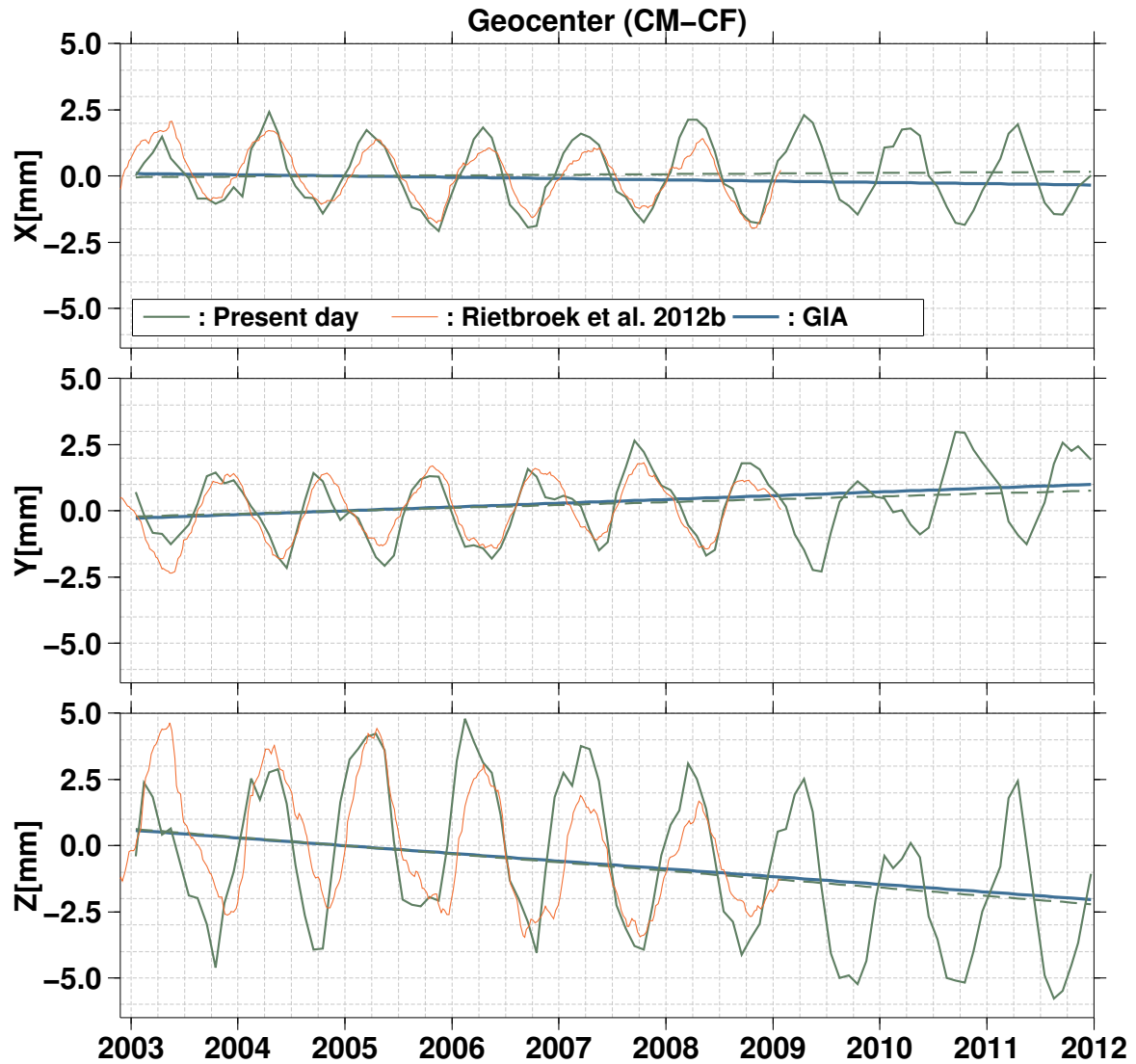
Figure 5.20: Geocenter motion (CM-CF) as obtained from the fingerprint inversion estimates. The signal is split up in a present day component (all ice-sheets, glaciers and hydrology) and a GIA component. For comparison the solution from an earlier inversion (Rietbroek et al., 2012a) is also shown. The contribution of the atmosphere and modelled ocean mass is not included.

The present day component, estimated from the inversion is plotted in Fig. 5.20. Furthermore, the geocenter motion is also decomposed in a contribution from Greenland, Antarctica, hydrology, land glaciers, and GIA. The corresponding annual amplitudes, phases and

	Annual		Trend	RMS
	A (mm)	t_a (doy)	mm/yr	post.
Antarctica (X)	0.02 (± 0.01)	249 (± 19)	0.02 (± 0.01)	0.04
(Y)	0.03 (± 0.01)	256 (± 15)	0.03 (± 0.01)	0.06
(Z)	0.18 (± 0.03)	67 (± 10)	0.10 (± 0.02)	0.32
Greenland (X)	0.07 (± 0.01)	101 (± 9)	-0.09 (± 0.01)	0.06
(Y)	0.04 (± 0.01)	284 (± 9)	0.05 (± 0.01)	0.04
(Z)	0.23 (± 0.04)	99 (± 10)	-0.28 (± 0.02)	0.21
Hydrology (X)	1.51 (± 0.19)	93 (± 5)	0.14 (± 0.04)	0.42
(Y)	1.47 (± 0.18)	307 (± 7)	-0.02 (± 0.05)	0.48
(Z)	2.27 (± 0.31)	67 (± 6)	-0.10 (± 0.07)	1.02
Glaciers (X)	0.04 (± 0.02)	233 (± 26)	-0.02 (± 0.01)	0.07
(Y)	0.08 (± 0.03)	150 (± 27)	0.05 (± 0.01)	0.11
(Z)	0.57 (± 0.06)	94 (± 4)	-0.08 (± 0.02)	0.14
Total(PD) (X)	1.54 (± 0.19)	95 (± 5)	0.03 (± 0.04)	0.40
(Y)	1.42 (± 0.19)	303 (± 7)	0.12 (± 0.05)	0.50
(Z)	3.16 (± 0.35)	75 (± 4)	-0.31 (± 0.08)	1.11
GIA (X)	-	-	-0.05 (± 0.02)	-
(Y)	-	-	0.14 (± 0.05)	-
(Z)	-	-	-0.29 (± 0.10)	-
Rietbroek et al. (2012a)(PD) (X)	1.28 (± 0.02)	104 (± 1)	-0.14 (± 0.01)	0.22
(Y)	1.36 (± 0.02)	303 (± 1)	0.12 (± 0.01)	0.33
(Z)	2.64 (± 0.05)	108 (± 1)	-0.38 (± 0.02)	0.68
Rietbroek et al. (2012a)(GIA) (X)	-	-	-0.14 (± 0.05)	-
(Y)	-	-	0.31 (± 0.10)	-
(Z)	-	-	-0.71 (± 0.23)	-
Wu et al. (2010)(PD) (X)	-	-	-0.08 (± 0.04)	-
(Y)	-	-	0.29 (± 0.05)	-
(Z)	-	-	-0.16 (± 0.07)	-
Wu et al. (2010)(GIA) (X)	-	-	-0.10 (± 0.01)	-
(Y)	-	-	0.11 (± 0.02)	-
(Z)	-	-	-0.72 (± 0.06)	-
Swenson et al. (2008)(PD) (X)	1.67 (± 0.05)	96 (± 2)	-0.14 (± 0.01)	0.56
(Y)	1.31 (± 0.05)	288 (± 2)	-0.06 (± 0.01)	0.54
(Z)	2.25 (± 0.05)	93 (± 1)	-0.29 (± 0.01)	0.72

Table 5.8: Annual amplitude, phase and trend of the geocenter motion (CM-CF) from the fingerprint inversion. For comparison, the geocenter estimates from Rietbroek et al. (2012a), Wu et al. (2010) and Swenson et al. (2008) are also provided. 'PD' denotes present day effects.

trends can be found in Table 5.8.

Similar, to the discussion on the mean sea level changes in Sec 5.2.1, the hydrologic component is responsible for most of the variability in the geocenter motion. The majority of the seasonal signal and residual variability and in the present day geocenter motion, is caused by hydrology.

From Table 5.8 and Fig. 5.20 it is clear that the results from Rietbroek et al. (2012a) have a somewhat smaller seasonal amplitude. This is mainly because I obtained these earlier estimates from an 11 week running mean. In the Z component, which is the most difficult component to estimate, a larger discrepancy can be found. The exact cause for this remains unclear, but it should be sought in processing differences between the current study and that of Rietbroek et al. (2012a).

From all the sources, hydrology exhibits the largest trend in the X direction ($0.14 \, \mathrm{mm/yr}$). It must be said however that this trend is compensated by the negative X-trends from Greenland and the land glaciers, yielding an insignificant trend for the total present day X component. Earlier results from Wu et al. (2010) and Rietbroek et al. (2012a), showed negative trends for the X component. A likely explanation for this discrepancy is that the inter-annual variation of hydrology may yield different X-trends depending on the time interval used.

In the Z direction, the present day mass changes are associated with a trend of -0.31 ± 0.08 $\mathrm{mm/yr}$. The main contributor to these changes are actually caused by the Greenland ice sheet, which alone contributes already $^{-0.28}/\mathrm{mm}\mathrm{yr}$.

Considering the GIA induced trends, these are roughly a factor two smaller than those estimated in Rietbroek et al. (2012a). The reason is that the mantle viscosity of the a priori GIA model is different, which causes smaller amplitudes in the geocenter motion (Klemann and Martinec, 2009). The largest component is, as expected, the Z-direction, on which the dissapearance of the Laurentide glacial has a large role. Wu et al. (2010) observed that the a priori GIA Z-component changed from $-0.48 \, \mathrm{mm/yr}$ to an estimated $-0.72 \, \mathrm{mm/yr}$. Considering the discussion, above the strong estimated GIA signal in Greenland may have also contributed to this trend, while in Rietbroek et al. (2012a), the lower mantle viscosity was a more likely explanation.

5.2.5 Steric Sea Level Changes

Similar to the hydrological parameters, the estimated steric principal components from the inversion, can be compared to the ones as computed from the steric height changes derived from Ishii and Kimoto (2009) (see Section 4.2.1). The time variation of the first 18 modes, explaining 81% of the variance, is plotted in Fig. 5.21.

From Fig 5.21, it is clear that the estimated principal components follow the original ones closely. In particular, the inter-annual variations are well captured by the inversion. Peculiar is that the higher modes from the Ishii data are more susceptible to oscillations

compared to their estimated counterparts. One can suspect that these oscillations point to spatial-temporal sampling problems in the original ARGO data. Clearly, the inversion results do not seem to be affected by this, and the altimeter data yields smoothly varying estimates.

From the inversion, steric sea level can be reconstructed by multiplying the estimated PCs with their corresponding EOFs. Here, both the EOFs from Ishii and Kimoto (2009) as well as the 'bootstrapped' patterns are used. As discussed in Sec. 4.2.1, these bootstrapped patterns are necessary to extract all the relevant signals from the altimetry, and prevent an underestimation of the steric signal.

For each grid point of the reconstructed steric height, an annual harmonic and trend is fitted. The corresponding trend and the RMS of the residual are plotted at the top of Figure 5.22. The reconstructed trend is very similar to the sea level trend from Jason-1 only (see Fig. 5.22). The typical structure in the North Pacific points to the influence of the Pacific Decadal Oscillation, which has been entering a cooling phase since 2003. The strong negative trend in the equatorial Pacific also points to the strong La Niña, which occurred in 2010. Residual effects of the El Niño Southern Oscillation (ENSO) can still be spotted in the spatial RMS. Both oscillations have spatially similar patterns and are therefore difficult to separate on these time scales.

To study the steric changes in the deeper part of the ocean, the steric component of the upper 700m of the ocean from the Ishii data is subtracted from the . The remaining sea level variations should provide some hints on the structures which are associated with deep ocean changes. Similar as above, the fitted trend, and residual σ is plotted in the middle section of Fig. 5.22. Although smaller in magnitude, the resulting trend has a much more uniform structure. In particular, the large negative trend in the equatorial Pacific has now become positive. Furthermore, a strong reduction of the RMS can be observed in the equatorial Pacific, which hints to the removal of a large part of the ENSO.

Finally, the total reconstructed sea level has been subtracted from the gridded altimetry data. The associated trend and residual RMS is shown at the bottom of Fig. 5.22. The remaining trend shows little or no large scale signals, which suggests that most of the altimetry trend signal has been absorbed in the unknowns. The standard deviation of the residual, on the other hand still shows regions with large variability originating from the altimetry data. However, these variations can be mostly attributed to dynamic effects such as meso- scale eddies and planetary rossby waves. Such features are in fact expected to end up in the altimetry residuals.

Regarding the retrieval of steric variations, the fingerprint inversion pursued in this thesis come with a set of advantages compared to the more straightforward approach to derive steric changes from the difference of altimetry and GRACE (e.g. Lombard et al., 2007).

Firstly, in the inversion approach, the mass induced component and steric induced component are estimated simultaneously from GRACE and Altimetry. Although, the altimetry appear to have little influence on the mass-related parameters from a formal perspective (see Sec. 4.2.3), it does change the estimated hydrology in terms of the associated mean sea
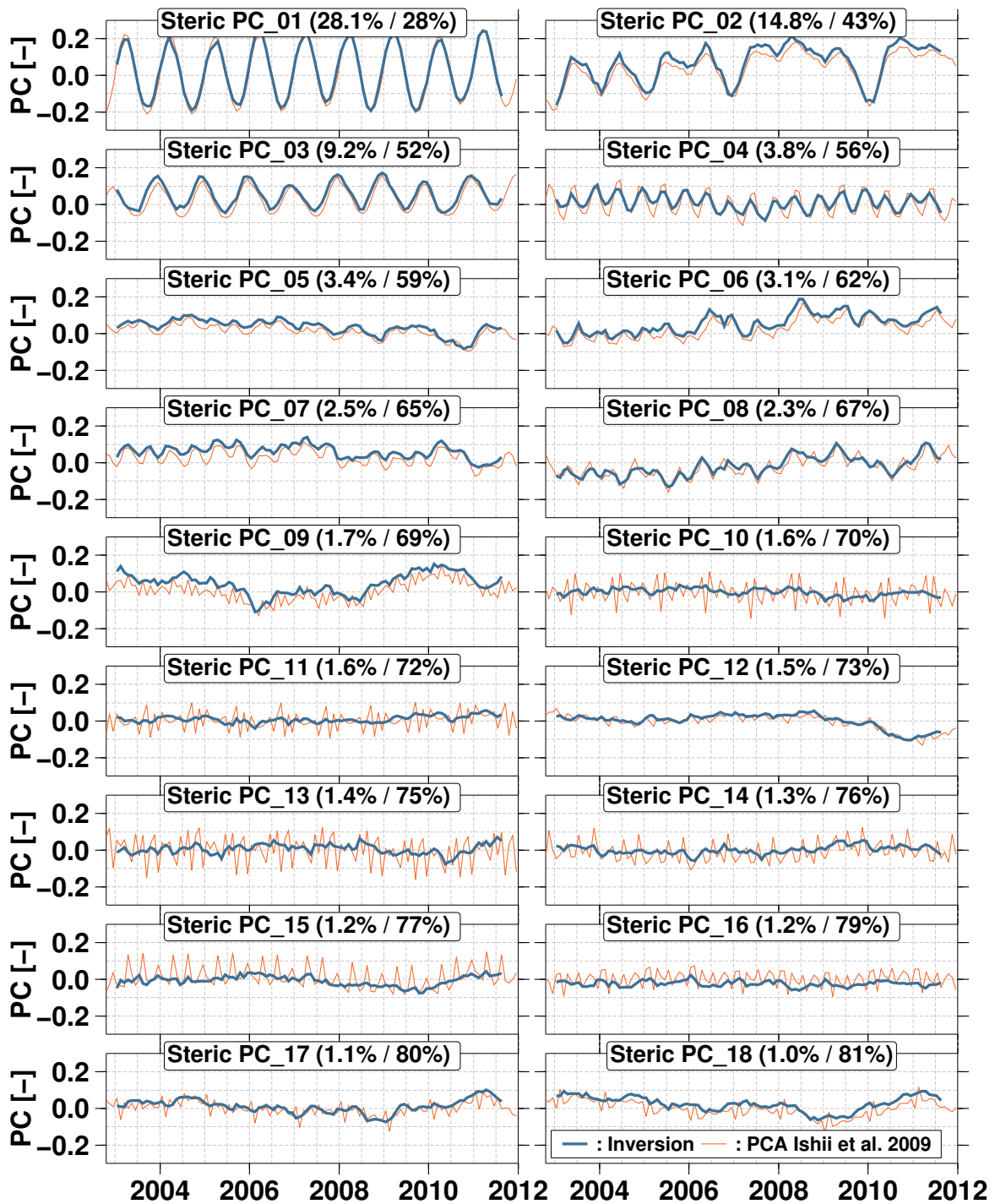
Figure 5.21: Time variation of the first 18 principal components of the steric sea level changes. The scales, as estimated by the inversion, are plotted along the principal components which were computed from the PCA of the dataset from Ishii and Kimoto (2009). The percentages denote the variance explained (per mode/cumulative).
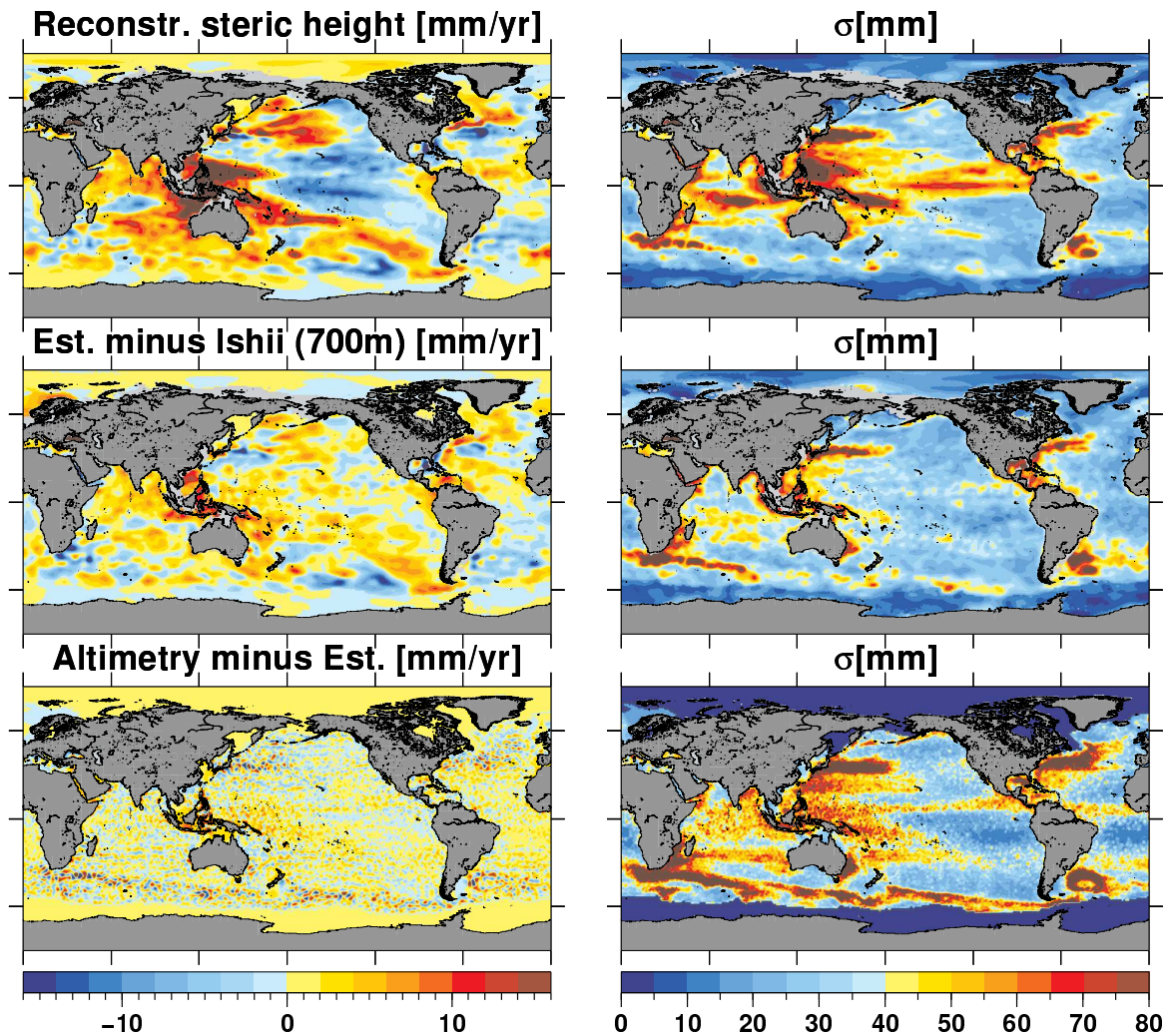
Figure 5.22: Reconstructed steric sea level trend and the standard deviation of the residual (after removing the mean, trend and annual harmonic curve per grid point). The middle plots shows the trend and standard deviation of the reconstructed steric sea level but now with the gridded steric height from the upper 700m of Ishii and Kimoto (2009) removed. The bottom plots display the trend and the standard deviation of the altimetric residual after removing the total fit (mass-induced, GIA and steric sea level and the effect of the nuisance parameters).

level change (not shown here).

Another advantage stems from the step-wise parameterization of the steric variations in the inversion, where the initial 100 EOFs from the Ishii data are augmented with an additional 60 bootstrapping EOFs derived from the altimetry residuals. This step-wise approach allows a decomposition of the steric component into a shallow and a residual deep ocean component. Such decompositions provide valuable insights in the ongoing discussion of the deep ocean warming which is expected from the radiation imbalance of the Earth system. The results here are consistent with a signaificant warming in the deeper ocean.

Finally, in the straightforward approach (Altimetry minus GRACE), a large and uncertain GIA correction has been applied to GRACE (~1.7 $\mathrm{mm/yr}$ in terms of ocean-averaged equivalent water height), whereas the altimetry needs to be corrected only by ~0.3 $\mathrm{mm/yr}$ (Lombard et al., 2007). The GIA correction in the inversion approach is consistently co-estimated from the data. Furthermore, since the mass induced sea level in the inversion is parameterized by equipotential surfaces, the effect of the GIA error remains small compared to the situation where equivalent water heights are computed directly from GRACE.

6 Conclusions and Outlook

6.1 Conclusions

The motivation for this thesis work was to investigate whether the joint inversion of geodetic observations is of benefit to the accuracy and separability of estimated surface loading. For that means, I've investigated two types of joint inversion schemes. On the one hand, GRACE data, GPS network deformations, and modelled OBP were combined to resolve for weekly spherical harmonic coefficients of surface loading. On the other hand, observations from GRACE and Jason-1 and 2 have been jointly inverted for steric sea level changes, GIA and time varying mass changes of the ice sheets, glaciers and hydrology.

The combination of different types of observation remains an exciting but challenging exercise. In the weighing of the different observation types, careful consideration must be given to both the technique specific signal content as well as the nature of their errors.

The provided results and the methodology are relevant to a wide range of studies. On the one hand, the results of the weekly inversion shed light on sub-annual and annual surface loading variations. These are in particular important to better understand the hydrological water cycle. The inclusion of GPS data in the inversion also ensures that reference frame issues are treated in a consistent way, and allows the study of the center of mass of the Earth's system relative to other more 'intuitive' reference system origins such as for example the center of surface figure of the Earth.

The results of the fingerprint inversion provide valuable insights into the behavior of the Earth's Ice-sheets, and furthermore allow a consistent separation of present day sea level variations. In addition to providing estimates of mean sea level changes, spatially varying sea level changes are also addressed which play an significant role when studying coastal sea level changes.

From a methodological perspective, this work describes a theoretical framework, which can serve as a start for future inversion schemes, possibly incorporating more data from auxiliary sources.

Improvement of Accuracy

From a formal error perspective, it is not always obvious that an increase in accuracy is obtained from the joint inversion. For example, in the inversion of weekly surface loading, the GPS data appears to play only a minor role in terms of its formal (error) contribution. However, to conclude that the inversion results are not affected by GPS, would be simply wrong. The GPS data provide important information (e.g. degree 1 information, land coverage w.r.t. OBP), which are absent in the other datasets. Furthermore, the off-diagonal elements of the error-covariance do have a significant influence on the estimated parameters. A GPS+GRACE derived geocenter motion is more accurate than one obtained from GPS only, even though GRACE can not directly observe the geocenter motion.

A similar conclusion can be reached for the fingerprint inversion results. The formal errors of Fig. 4.19 seem to indicate that the altimetry data has no effect on the mass related parameters. Although not shown here explicitly, the altimetry data however do seem to have leverage on the mass related parameters, in particular the parameters related to terrestrial hydrology.

Improvement of Separability

The most important advantage of the joint inversion approach, is that the complementariness of the used data can be exploited, while ensuring consistency. The geocenter motion from a joint inversion is less noisy than using GPS only. In the joint inversion, the addition of GRACE data serves as a strong constraint on the higher degrees preventing higher degree loading effects to alias in the geocenter motion.

The nature of the 'fingerprint' inversion makes it in particular very suitable for separability problems. The combination of GRACE with altimetry, results in a physically consistent treatment of the time varying geoid over the ocean. Accordingly, steric changes in the ocean can therefore be separated from the mass induced variations, without the need for assumptions on the geoid.

Furthermore, the inversion allows the decomposition of the sea level contributions, in their major components (Greenland, Antarctica, land glaciers, hydrology, and GIA). The use of self-consistent sea level fingerprints furthermore allows non-uniform sea level change to be studied. This latter aspect is important for the planning and policy regarding coastline defense.

Geophysical Interpretation of the Weekly Surface Loading

It has been frequently mentioned that the joint inversion of GPS, GRACE and modeled ocean bottom pressure yields an estimate of the geocenter motion. When the ocean and atmosphere is included, the geographical position of the geocenter roughly traverses a great circle every season, crossing cental Asia in Winter and then passing over Europe and the Atlantic in spring. Over the year the magnitude of the CM-CE offset, varies seasonally between 1.8 mm to 3.2 mm. In terms of Cartesian components, the Y component exhibits the largest amplitude (3.5 mm). However, when the atmospheric and oceanic background models are removed, the series contain less high frequency variation and the Z component is larger than the X and Y component. It should be noted that the surface load are very sensitive to changes in the geocenter motion. A geocenter motion offset of 1 mm manifests itself as a equivalent water height of 3.1 mm.

Within the inversion, 7 Helmert parameters were fitted to the GPS network every week. These are intended to absorb residual network errors of the GPS stations and can be safely estimated simultaneously with the degree 1 surface loading coefficients. In terms of translations and rotations, the terms remain small (generally below 0.5 mm at the Earth's surface). Somewhat larger network changes (about 1 mm) are caused by the estimated scale parameter, which is thought to be more sensitive to errors in the solar radiation pressure model,

as applied to the GPS satellites.

The inversion results have been propagated and subtracted from the GPS station deformations. As expected, the inversion results are responsible for a significant part of the deformation in zenith direction for most of the stations. The horizontal components seem to show only little or no reduction when the propagated inversion results are subtracted.

A comparison of the estimated ocean bottom pressure with data from in situ recorders, generally shows an improvement in correlation over the OBP from the background model. Agreements on sub-monthly time scales are also visible for well-performing recorders.

For a variety of watersheds, the time variable basin averages have been computed from the joint inversion results. Additionally, equivalent series have been computed from a constrained GPS-only surface loading inversion. Good agreements between the GPS-only solution and the joint inversion were found for some basins well covered by GPS stations (e.g. Danube). However, truncation problems, leakage effects, and sparse GPS sampling caused large discrepancies in other watersheds, most notably the Orinoco basin.

Geophysical Interpretation of the Fingerprint Inversion Results

The 'fingerprint' inversion, where observed gravity and altimetric sea level is linked through unknown time varying scales through a set of predefined patterns, yields to a variety of geophysical insights.

The total mean sea level rise over the period from Jan 2003 to Dec 2011, has been estimated as 2.5 ± 0.11 mm/yr. The mass induced contributions can be further decomposed into the mass induced sea level contributions: 0.66 ± 0.01 mm/yr (Greenland), 0.40 ± 0.03 mm/yr (Antarctica), 0.43 ± 0.02 mm/yr (Land glaciers), and -0.20 ± 0.09 mm/yr (Hydrology). From these contributions, the hydrological component exhibits the strongest (inter)annual variations. Consequently, this is also the component which introduces the largest errors in the trends. Compared to the modeled hydrological variations from WGHM, the inversion point to stronger seasonal amplitudes.

The contribution of the steric sea level is estimated to be 1.2 ± 0.14 mm/yr. This contribution can be further split up in two components. The patterns and scales, representative for the upper 700 m of the ocean, yield 0.17 ± 0.08 mm/yr. The other component, representative for complementary effects (e.g. the deeper part of the ocean), yields a much stronger value of 1.03 ± 0.10 mm/yr. This large trend is therefore a serious indication that the deeper part of the ocean is warming significantly. Alternatively, I've subtracted the spatial steric variations of the upper 700 m of the ocean from the steric variations of the inversion. The remaining trend exhibits basin-wide trends in the Pacific and Indian Ocean. It is worth noting that natural oscillations such as the El Niño - La Niña cycle and the Pacific decadal oscillation mainly seem to be confined to the upper layers of the ocean.

The second set of steric pattern is obviously important. In the course of this work, it turned out that a parameterization, using only the EOF modes derived from the steric heights from Ishii and Kimoto (2009), did not suffice to explain the altimetric observations.

Although the estimated principal components from the inversion compare very well with the computed principal components from the ARGO data, large scale signals were visible in the residuals which were in the same order of the estimated steric variations itself. For this reason, an additional set of steric (bootstrapping) patterns was created based on an EOF analysis of the initial altimetry residuals. It is possible that some residual bottom pressure effects due to wind stress errors of the a priori ocean model are contained within these bootstrapping modes. Different wind stress fields may cause regionally different ocean bottom pressure changes through the mechanism of Ekman pumping. However, on a global scale, such effects are unable to explain the large trend found in the global mean sea level.

From the estimated GIA signal, the inferred geocentric correction to global mean sea level is estimated to be -0.16 mm/yr, which is about half of the correction which is commonly applied (-0.3 mm/yr from Douglas and Peltier, 2002). However this feature is mostly related to the set up of the GIA model. Relatively, strong constraints need to be applied to the GIA parameters, in order to obtain realistic values. The results from the inversion indicate that the Laurentide GIA signal is underestimated in the a priori model, while the Antarctic component is over estimated. Unfortunately, the trend of the Antarctic GIA component is highly correlated with some drainage variations in Antarctica, making it difficult to separate the contributions. This has also been observed in other studies which used GRACE data (e.g. Velicogna and Wahr, 2006b; Horwath and Dietrich, 2009; Wu et al., 2010).

The mass losses over the entire Greenland ice sheet total -253±4.3 Gt/yr (2003-2011), where it should be noted that the uncertainties coming from the GIA component may be somewhat understimated because of the applied constraints. The inversion indicates that the losses are confined to the coastal regions with lower elevations, while some of regions at higher elevations exhibit positive trends. The estimated mass losses are smaller than earlier estimates, using shorter time spans, confirming an acceleration of the mass loss in Greenland. This is also obvious from the estimated time variations in the drainage basins.

The mass loss of the Antarctic Ice sheet, totaling -147 Gt/yr, largely originates from the Amundsen sea sector. In this region, the GIA signal is expected to be small, such that these are clearly significant losses. However there are several basins which are strongly affected by the GIA signal. For example Sasgen et al. (2012a) found a significantly smaller total trend (-103 Gt/yr) for Antarctica. The discrepancy can be attributed to a different GIA strength. Interesting is, that when I would apply weaker constraints to the Antarctic GIA component, the results of this study would move towards those of Sasgen et al. (2012a). Compared to the variations in Greenland, the time variations in the Antarctic exhibit more fluctuations, which are likely related to precipitation events in the coastal zones.

The land glaciers are losing mass with a rate of -149±9 Gt/yr, which is comparable with the Antarctic contribution and confirms the findings of Jacob et al. (2012). Many glacier clusters exhibit considerable (inter)annual variations, although annual variations of the Arctic clusters appear to be somewhat smaller. Highly significant are the mass losses on the Alaska coast -44.1 ±2.5 Gt/yr, Patagonia -41.1 ±2.8 Gt/yr and on the Queen Elizabeth Island (-28.5±1.4 Gt/yr mainly from Ellesmere Island). Although much smaller and not as significant, the largest positive trend (5.5±1.2 Gt/yr), is found in the Brooks range in north-

ern Alaska.

The geocenter motion as inferred from the inversion results, are indicating significant trends in both the present day contributions as well as the GIA contributions. Considering the GIA contribution, we see that the X and Z trends are about a factor of 2 smaller compared to the estimates of Rietbroek et al. (2012a) and Wu et al. (2010). On the one hand, the difference can be sought in the lower mantle viscosity of the a priori GIA earth models, which affects the magnitude of the geocenter trend strongly. Another effect may come from the contribution of Greenland, which is shown to be relatively large for the Z trend. The Greenland signals found by Wu et al. (2010) (large GIA signal and a relatively small present day loss) may therefore also hav an effect on their estimated geocenter trend.

The present day trend of the geocenter (with the components: X 0.03 ± 0.04 mm/yr, Y 0.12 ± 0.05 mm/yr, Z -0.31 ± 0.08 mm/yr), is too large to be simply ignored in GRACE-only studies of Antarctica. If the associated degree 1 trends are averaged over Antarctica a positive gain of 20 Gt/yr is obtained. The net effect of the geocenter trend on the Greenland mass balance is much less, simply because the area of Greenland is smaller, amounting only to -3 Gt/yr. The gross of the Greenland mass loss is therefore contained within the higher degree coefficients.

The seasonal geocenter component agrees to within 0.8 mm amplitude and 40 days of phase with the results of the weekly surface loading inversion, when considering the same time span. This discrepancy exceeds the formal error estimates, and is likely related to the way the ocean is treated. Whereas the ocean bottom pressure in the fingerprint inversion is induced by an equipotential surface, bottom pressure variations from a non-equipotential ocean response are also present in the weekly solutions.

6.2 Outlook

The inversion schemes developed in this thesis are promising tools which may be improved for future studies. Both schemes, estimating generic surface loading coefficients versus estimating scales from tuned fingerprints, have their advantages and disadvantages.

A major improvement of the GPS+GRACE+OBP scheme, would be the inclusion of trends in the inversion. Up to now, a secular reference frame has been subtracted from the GPS station deformations, and the GRACE and OBP data have been detrended. The challenge of including the trends, will be that a GIA signal has to be co-estimated. This will be very difficult in regions where the present day loading patterns look similar to the GIA. Furthermore, trends in the GPS data may also be caused by geophysical signals in the solid Earth which are neither of GIA or surface loading origin.

Both schemes can be improved by incorporating additional data sources. The GPS data may be used in the fingerprint inversion, and the altimetry may be a helpful ocean constraint for the weekly surface loading. Furthermore SLR data may be added to constrain the lowest gravity coefficients. Tide gauges may provide constraints at the coastlines as

long as they are not dominated by local signals. And data from gravimeters may provide important information as well. Volumetric measurements of the ice sheet (e.g. ICEsat and Cryosat2) are interesting candidates, although additional problems (and opportunities) with firn density may be introduced at the same time. In addition, Cryosat2 potentially offers information on the thickness of the sea-ice, which would allow an extension of the method into the Arctic.

The addition of new data sources potentially allows the extension of time series of mass storage changes beyond or before the GRACE time span. For example Nerem and Wahr (2011) showed that SLR-derived changes in the Earth's oblateness are related to mass losses of the major ice sheets, and that SLR can aid in studies of Greenland and Antarctica before the GRACE era.

Furthermore, a low degree time varying gravity field from GPS and LEO satellites in the past decades, would be a great tool to reprocess and improve past altimeter orbits such a those from TOPEX. In the near future, joint inversion techniques, may also aid in bridging the gap between GRACE and its follow on mission (Rietbroek et al., 2014).

The weekly sets of spherical harmonic surface loading coefficients, are resolved up to degree 30 only. This limitation is induced by the density of the ground track patterns of GRACE. To resolve higher resolution signals, more data from outside the week is needed. A promising techniques to do this is to apply a Kalman filter/smoother approach (Kurtenbach et al., 2009). An additional benefit is that the higher resolution will at the same time also decrease the truncation error which is made in the surface loading Green's functions.

In the fingerprint inversion, all of the currently used patterns are standing waves which oscillate in time but not in space. However, a variety of geophysical signals exist which are associated with patterns which move in time. A relevant example is for example the ocean's response to the computed meltwater input. The associated steric effects have been demonstrated to propagate along the boundary currents in time (Brunnabend et al., 2012). The use of patterns with propagating features is challenging but may offer interesting geophysical insights, and avoid signals to be split up in too many modes.

The orthogonality of the spatial EOFs is numerically advantageous when applied as base functions in the fingerprint inversion. However, single EOF modes are very difficult to interpret physically, as geophysical phenomena are not necessarily orthogonal. Future work may therefore benefit from a decomposition which is derived from Independent Component Analysis (ICA, Forootan and Kusche, 2012). In the ICA method, the EOFs are rotated based on their higher order statistical moments, in such a way that the modes are statistically independent in either the time or spatial domain. Most of the time, the resulting independent modes are easier to interpret physically. On a regional scale, a fingerprint inversion, using the spatial information from an independent component analysis, has already provided valuable physical insight in water resource problematics in Iran (Forootan et al., 2014).

The current parameterization of the GIA signal, silently postulates that the true GIA signal can be represented by a linear combination of GIA components. In reality this approximation may be (partly) incorrect. Roughly speaking, changes in the most uncertain

components, namely ice mass and mantle viscosity, appear as scaling effects in the GIA induced geoid and uplift. However, a different spatial structure of the ice history, which may be the case in for example Antarctica, will also induce spatially different GIA responses. Furthermore, changes in the rigidity and thickness of the crust may affect the position of the peripheral bulge in the vicinity of the ice sources. To parameterize such effects in terms of (linear) fingerprints is at least challenging, and is further complicated by the fact that additional degrees of freedom of the GIA parameterization render the inverse problem even more ill-posed than that it is already.

In the current inversion scheme, the altimeter and GPS orbits are derived from gravity fields which are not consistent with GRACE. Ultimately, a unification is desirable where a 'grand' inversion scheme allows only a single gravity field to affect all the relevant orbits.

The Artic contribution to (mean) sea level appears to be significant ($0.18\,\mathrm{mm/yr}$ in terms of mean sea level rise). However, besides the GRACE data, no observational constraints on the sea level are entering the fingerprint inversion. Consequently, the steric sea level change in the Artic should be considered as an extrapolation using the steric modes obtained from the data from Ishii and Kimoto (2009). This approach can potentially be improved by applying observational or modeling constraints in the Artic region. Unfortunately, observational monitoring data in this region is hardly available.

Bibliography

Z. Altamimi, L. Métivier, and X. Collilieux. Itrf2008 plate motion model. *Journal of Geophysical Research*, 117(B7):B07402, 2012.

D. F. Argus, R. G. Gordon, and C. DeMets. Geologically current motion of 56 plates relative to the no-net-rotation reference frame. *Geochemistry Geophysics Geosystems*, 12(11): Q11001, 2011.

M. A. Balmaseda, K. E. Trenberth, and E. Källén. Distinctive climate signals in reanalysis of global ocean heat content. *Geophysical Research Letters*, 40(9):1754–1759, May 2013. doi: 10.1002/grl.50382. URL http://dx.doi.org/10.1002/grl.50382.

O. Baur, M. Kuhn, and W. Featherstone. Grace-derived ice-mass variations over greenland by accounting for leakage effects. *Journal of Geophysical Research: Solid Earth (1978–2012)*, 114(B6), 2009.

R. Biancale and A. Bode. *Mean annual and seasonal atmospheric tide models based on 3-hourly and 6-hourly ECMWF surface pressure data*. GeoForschungsZentrum, 2006.

N. Bindoff, J. Willebrand, V. Artale, A. Cazenave, J. Gregory, S. Gulev, K. Hanawa, C. Le Quere, S. Levitus, Y. Nojiri, et al. *Observations: oceanic climate change and sea level in Climate Change 2007: The Physical Science Basis. Contribution of Working Group I to the Fourth Assessment Report of the Intergovernmental Panel on Climate Change*. Cambridge University Press, 2007. ISBN 9780521880091.

G. Blewitt. Self-consistency in reference frames, geocenter definition, and surface loading of the solid earth. *Journal of Geophysical Research*, 108(B2):2103, 2003. ISSN 0148-0227.

G. Blewitt and P. Clarke. Inversion of earth's changing shape to weigh sea level in static equilibrium with surface mass redistribution. *Journal of Geophysical Research (Solid Earth)*, 108:2311, jun 2003. doi: 10.1029/2002JB002290.

G. Blewitt, D. Lavallée, P. Clarke, and K. Nurutdinov. A new global mode of earth deformation: seasonal cycle detected. *Science*, 294(5550):2342–5, 2001. doi: 10.1126/science. 1065328.

C. Böning, R. Timmermann, A. Macrander, and J. Schröter. A pattern-filtering method for the determination of ocean bottom pressure anomalies from grace solutions. *Geophysical Research Letters*, 35(18):L18611, Sept 2008. doi: 10.1029/2008GL034974.

C. Böning, M. Lebsock, F. Landerer, and G. Stephens. Snowfall-driven mass change on the east antarctic ice sheet. *Geophysical Research Letters*, 39(21), 2012.

C. Böning, J. K. Willis, F. W. Landerer, R. S. Nerem, and J. Fasullo. The 2011 la niña: So strong, the oceans fell. *Geophys. Res. Lett.*, 39(19):L19602–, Oct. 2012. ISSN 0094-8276. URL http://dx.doi.org/10.1029/2012GL053055.

W. Bosch and R. Savcenko. Satellite altimetry: multi-mission cross calibration. In *Dynamic Planet*, pages 51–56. Springer, 2007.

R. Bouchard, S. McArthur, W. Hansen, K. J. Kern, and L. Locke. Operational performance of the second generation deep-ocean assessment and reporting of tsunamis (dart trade ii). In *OCEANS 2007*, pages 1–6. IEEE, 2007.

F. Bouillé, A. Cazenave, J. M. , Lemoine, and J. F. Crétaux. Geocentre motion from the doris space system and laser data to the lageos satellites: comparison with surface loading data. *Geophysical Journal International*, 143(1):71–82, 2000. doi: 10.1046/j.1365-246x.2000. 00196.x.

S.-E. Brunnabend. *Sea Level Variations derived from Mass Conserving Finite Element Sea-Ice Ocean Model*. PhD thesis, Bremen, Univ., Diss., 2011.

S.-E. Brunnabend, R. Rietbroek, R. Timmermann, J. Schröter, and J. Kusche. Improving mass redistribution estimates by modelling ocean bottom pressure uncertainty. *Journal of Geophysical Research*, 116(C8):C08037, 2011. doi: 10.1029/2010JC006617.

S.-E. Brunnabend, J. Schröter, R. Timmermann, R. Rietbroek, and J. Kusche. Modeled steric and mass-driven sea level change caused by greenland ice sheet melting. *Journal of Geodynamics*, 59-60(0):219 –225, 2012. ISSN 0264-3707. doi: 10.1016/j. jog.2011.06.001. URL http://www.sciencedirect.com/science/article/pii/ S0264370711000615. Mass Transport and Mass Distribution in the System Earth.

G. Cambiotti, Y. Ricard, and R. Sabadini. Ice age true polar wander in a compressible and non-hydrostatic earth. *Geophysical Journal International*, 183(3):1248–1264, 2010.

L. Carrère and F. Lyard. Modeling the barotropic response of the global ocean to atmospheric wind and pressure forcing - comparisons with observations. *Geophysical Research Letters*, 30:8–1, mar 2003.

D. J. Cavalieri, C. L. Parkinson, P. Gloersen, and H. Zwally. Sea ice concentrations from nimbus-7 smmr and dmsp ssm/i-ssmis passive microwave data, 1996. Boulder, Colorado USA: NASA DAAC at the National Snow and Ice Data Center, updated yearly.

A. Cazenave and W. Llovel. Contemporary sea level rise. *Annual Review of Marine Science*, 2:145–173, 2010. doi: 10.1146/annurev-marine-120308-081105.

D. P. Chambers, J. Wahr, and R. S. Nerem. Preliminary observations of global ocean mass variations with grace. *Geophysical Research Letters*, 31(13), jul 2004.

J. L. Chen, C. R. Wilson, R. J. Eanes, and R. S. Nerem. Geophysical interpretation of observed geocenter variations. *Journal of Geophysical Research*, 104:2683–2690, 1999. doi: 10.1029/1998JB900019.

M. Cheng, B. Tapley, and J. Ries. Geocenter variations from analysis of slr data. iag commission 1 symposium 2010. *Reference Frames for Applications in Geosciences (REFAG2010), Marne-La-Vallee, France*, pages 4–8, 2010.

J. Church and N. White. A 20th century acceleration in global sea-level rise. *Geophysical Research Letters*, 33(1):L01602, 2006.

J. Church and N. White. Sea-level rise from the late 19th to the early 21st century. *Surveys in Geophysics*, pages 1–18, 2011.

J. G. Cogley. Geodetic and direct mass-balance measurements: comparison and joint analysis. *Annals of Glaciology*, 50(50):96, 2009. doi: 10.3189/172756409787769744.

X. Collilieux, Z. Altamimi, J. Ray, T. van Dam, and X. Wu. Effect of the satellite laser ranging network distribution on geocenter motion estimation. *Journal of Geophysical Research*, 114 (B4):B04402, 2009.

X. Collilieux, L. Métivier, Z. Altamimi, T. van Dam, and J. Ray. Quality assessment of gps reprocessed terrestrial reference frame. *GPS solutions*, 15(3):219–231, 2011a.

X. Collilieux, T. van Dam, J. Ray, D. Coulot, L. Métivier, and Z. Altamimi. Strategies to mitigate aliasing of loading signals while estimating gps frame parameters. *Journal of Geodesy*, pages 1–14, 2011b.

J. F. Crétaux, L. Soudarin, F. J. M. Davidson, M. C. Gennero, M. Bergé-Nguyen, and A. Cazenave. Seasonal and interannual geocenter motion from slr and doris measurements: Comparison with surface loading data. *Journal of Geophysical Research (Solid Earth)*, 107, dec 2002. doi: 10.1029/2002JB001820.

F. A. Dahlen. The passive influence of the oceans upon the rotation of the earth. *Geophysical Journal of the Royal Astronomical Society*, 46(2):363–406, 1976.

J. L. Davis, P. Elósegui, J. X. Mitrovica, and M. E. Tamisiea. Climate-driven deformation of the solid earth from grace and gps. *Geophys. Res. Lett*, 31:24, 2004.

S. D. Desai. Observing the pole tide with satellite altimetry. *Journal of Geophysical Research*, 107(C11):3186, 2002. doi: 10.1029/2001JC001224.

R. Dill. Hydrological model lsdm for operational earth rotation and gravity field variations. Scientific technical report; 08/09, Helmholtz-Zentrum Potsdam Deutsches Geo-ForschungsZentrum, 2008.

H. Dobslaw and M. Thomas. Impact of river run-off on global ocean mass redistribution. *Geophysical Journal International*, 168:527–532, feb 2007a. doi: 10.1111/j.1365-246X.2006. 03247.x.

H. Dobslaw and M. Thomas. Simulation and observation of global ocean mass anomalies. *Journal of Geophysical Research: Oceans (1978–2012)*, 112(C5), 2007b.

H. Dobslaw, F. Flechtner, I. Bergmann-Wolf, C. Dahle, R. Dill, S. Esselborn, I. Sasgen, and M. Thomas. Simulating high-frequency atmosphere-ocean mass variability for dealiasing of satellite gravity observations: Aod1b rl05. *Journal of Geophysical Research: Oceans*, 118(7):3704–3711, Jul 2013. doi: 10.1002/jgrc.20271. URL http://dx.doi.org/10.1002/jgrc.20271.

P. Döll, F. Kaspar, and B. Lehner. A global hydrological model for deriving water availability indicators: model tuning and validation. *Journal of Hydrology*, 270(1-2):105–134, 2003.

D. Dong, J. Dickey, Y. Chao, and M. Cheng. Geocenter variations caused by atmosphere, ocean and surface ground water. *Geophysical research letters*, 24(15):1867–1870, 1997.

B. C. Douglas and W. R. Peltier. The puzzle of global sea-level rise. *Physics Today*, 55(3): 35–41, 2002.

A. Dziewonski. Preliminary reference earth model. *Physics of The Earth and Planetary Interiors*, 25(4):297, 1981. doi: 10.1016/0031-9201(81)90046-7.

R. Eanes, S. Kar, S. Bettadapur, and M. Watkins. Low-frequency geocenter motion determined from slr tracking. *Eos Trans. AGU*, 78:46, 1997.

A. Eicker, J. Schall, and J. Kusche. Regional gravity modelling from spaceborne data: case studies with goce. *Geophysical Journal International*, Dec 2013. doi: 10.1093/gji/ggt485. URL http://dx.doi.org/10.1093/gji/ggt485.

A. Eicker, M. Schumacher, J. Kusche, P. Döll, and H. Müller-Schmied. Calibration/data assimilation approach for integrating GRACE data into the WaterGAP Global Hydrology Model (WGHM) using an ensemble Kalman filter . *Surveys in Geophysics (submitted)*, 2014.

W. E. Farrell. Deformation of the earth by surface loads. *Reviews of Geophysics and Space Physics*, 10:761, aug 1972.

W. E. Farrell and J. A. Clark. On postglacial sea level. *Geophysical Journal of the Royal Astronomical Society*, 46(3):647–667, 1976. ISSN 1365-246X.

M. Feissel-Vernier, K. Le Bail, P. Berio, D. Coulot, G. Ramillien, and J. J. Valette. Geocentre motion measured with doris and slr, and predicted by geophysical models. *Journal of Geodesy*, 80(8):637–648, November 2006. doi: 10.1007/s00190-006-0079-z.

L. Fenoglio-Marc, J. Kusche, and M. Becker. Mass variation in the mediterranean sea from grace and its validation by altimetry, steric and hydrologic fields. *Geophysical Research Letters*, 33(19):L19606, oct 2006. doi: 10.1029/2006GL026851.

L. Fenoglio-Marc, R. Rietbroek, S. Grayek, M. Becker, J. Kusche, and E. Stanev. Water mass variation in the mediterranean and black sea. *Journal of Geodynamics*, 59-60(0): 168 – 182, 2012. ISSN 0264-3707. doi: 10.1016/j.jog.2012.04.001. URL http://www.sciencedirect.com/science/article/pii/S0264370712000622. Mass Transport and Mass Distribution in the System Earth.

E. Forootan and J. Kusche. Separation of global time-variable gravity signals into maximally independent components. *Journal of Geodesy*, pages 1–21, 2012.

E. Forootan, R. Rietbroek, J. Kusche, M. Sharifi, J. Awange, M. Schmidt, P. Omondi, and J. Famiglietti. Separation of large scale water storage patterns over iran using grace, altimetry and hydrological data. *Remote Sensing of Environment*, 140(0):580 – 595, 2014. ISSN 0034-4257. doi: http://dx.doi.org/10.1016/j.rse.2013.09.025. URL http://www.sciencedirect.com/science/article/pii/S0034425713003623.

W. Förstner. Ein verfahren zur schätzung von varianz-und kovarianzkomponenten. *Allgemeine Vermessungsnachrichten*, 86(11-12):446–453, 1979.

M. Fritsche, R. Dietrich, C. Knöfel, A. Rülke, S. Vey, M. Rothacher, and P. Steigenberger. Impact of higher-order ionospheric terms on gps estimates. *Geophysical Research Letters*, 32(23):L23311, 2005.

M. Fritsche, R. Dietrich, A. Rülke, M. Rothacher, and P. Steigenberger. Low-degree earth deformation from reprocessed gps observations. *GPS Solutions*, 14(2):165, 2009. doi: 10.1007/s10291-009-0130-7.

L. Fu and A. Cazenave. *Satellite altimetry and earth sciences: a handbook of techniques and applications*, volume 69. Academic Press, 2001.

M. Gebler. *Detection and analysis of oceanic motion using pressure inverted echo sounders (PIES)*. PhD thesis, Universität Oldenburg, 2013. URL http://oops.uni-oldenburg.de/1448/.

G. Giacaglia and M. Burša. Transformations of spherical harmonics and applications to geodesy and satellite theory. *Studia Geophysica et Geodaetica*, 24(1):1–11, 1980.

A. E. Gill. *Atmosphere-ocean dynamics*. Academic Press New York, 1982.

GRASS Development Team. *Geographic Resources Analysis Support System (GRASS GIS) Software*, 2008. URL http://grass.osgeo.org. http://grass.osgeo.org.

R. J. Greatbatch. A note on the representation of steric sea level in models that conserve volume rather than mass. *Journal of Geophysical Research*, 99(C6):12767, jun 1994. doi: 10.1029/94JC00847.

S.-C. Han, C. Shum, M. Bevis, C. Ji, and C.-Y. Kuo. Crustal dilatation observed by grace after the 2004 sumatra-andaman earthquake. *Science*, 313(5787):658–662, 2006.

P. C. Hansen. *The L-curve and its use in the numerical treatment of inverse problems*. IMM, Department of Mathematical Modelling, Technical Universityof Denmark, 1999.

W. A. Heiskanen and H. Moritz. *Physical Geodesy*. W. H. Freeman and Co., 1967.

F. Hernandez and P. Schaeffer. The cls01 mean sea surface: A validation with the gsfc00 surface. *CLS Ramonville St Agne, France*, 2001.

M. Horwath and R. Dietrich. Signal and error in mass change inferences from grace: the case of antarctica. *Geophysical Journal International*, 177(3):849, 2009. doi: 10.1111/j.1365-246X.2009.04139.x.

M. Horwath, B. Legrésy, F. Rémy, F. Blarel, and J. Lemoine. Consistent patterns of antarctic ice sheet interannual variations from envisat radar altimetry and grace satellite gravimetry. *Geophysical Journal International*, 2012.

S. Hosoda, T. Ohira, and T. Nakamura. A monthly mean dataset of global oceanic temperature and salinity derived from argo float observations. *JAMSTEC Rep. Res. Dev*, 8:47–59, 2008.

C. W. Hughes, V. N. Stepanov, L. L. Fu, B. Barnier, and G. W. Hargreaves. Three forms of variability in argentine basin ocean bottom pressure. *Journal of Geophysical Research*, 112, jan 2007. doi: 10.1029/2006JC003679.

K. Huybers and G. H. Roe. Spatial patterns of glaciers in response to spatial patterns in regional climate. *Journal of Climate*, 22(17):4606–4620, 2009.

M. Ishii and M. Kimoto. Reevaluation of historical ocean heat content variations with time-varying xbt and mbt depth bias corrections. *Journal of Oceanography*, 65(3):287–299, 2009.

M. Ishii, M. Kimoto, K. Sakamoto, and S.-I. Iwasaki. Steric sea level changes estimated from historical ocean subsurface temperature and salinity analyses. *Journal of Oceanography*, 62(2):155, 2006. doi: 10.1007/s10872-006-0041-y.

E. R. Ivins and T. S. James. Antarctic glacial isostatic adjustment: a new assessment. *Antarctic Science*, 17(04):541–553, 2005.

T. Jacob, J. Wahr, W. Pfeffer, and S. Swenson. Recent contributions of glaciers and ice caps to sea level rise. *Nature*, 2012.

M. J. F. Jansen, B. C. Gunter, and J. Kusche. The impact of grace, gps and obp data on estimates of global mass redistribution. *Geophysical Journal International*, 177(1):1, 2009. doi: 10.1111/j.1365-246X.2008.04031.x.

C. Jekeli. *Alternative methods to smooth the Earth's gravity field*. The Ohio State University, dec 1981.

L. Jensen, R. Rietbroek, and J. Kusche. Land water contribution to sea level from grace and jason measurements. *Journal of Geophysical Research: Oceans*, 2013.

Y. Jiang, T. H. Dixon, and S. Wdowinski. Accelerating uplift in the north atlantic region as an indicator of ice loss. *Nature Geoscience*, 3(6):404, 2010. doi: 10.1038/ngeo845.

S. Jin and W. Zhu. A revision of the parameters of the nnr-nuvel-1a plate velocity model. *Journal of Geodynamics*, 38(1):85–92, 2004.

T. Kanzow, F. Flechtner, A. Chave, R. Schmidt, P. Schwintzer, and U. Send. Seasonal variation of ocean bottom pressure derived from gravity recovery and climate experiment (grace): Local validation and global patterns. *Journal of Geophysical Research*, 110, 2005. doi: 10.1029/2004JC002772.

R. A. Kendall, J. X. Mitrovica, and G. A. Milne. On post-glacial sea level–ii. numerical formulation and comparative results on spherically symmetric models. *Geophysical Journal International*, 161(3):679–706, 2005.

B. Kennett, E. Engdahl, and R. Buland. Constraints on seismic velocities in the earth from traveltimes. *Geophysical Journal International*, 122(1):108–124, 1995.

R. Klees, E. Revtova, B. Gunter, P. Ditmar, E. Oudman, H. Winsemius, and H. Savenije. The design of an optimal filter for monthly grace gravity models. *Geophysical Journal International*, 175(2):417–432, 2008.

V. Klemann and Z. Martinec. Contribution of glacial-isostatic adjustment to the geocenter motion. *Tectonophysics (online first, doi:10.1016/j.tecto.2009.08.031)*, 2009. doi: 10.1016/j.tecto.2009.08.031.

K.-R. Koch. *Parameter estimation and hypothesis testing in linear models*. Springer-Verlag New York, Inc., 1988.

K.-R. Koch and J. Kusche. Regularization of geopotential determination from satellite data by variance components. *Journal of Geodesy*, 76(5):259–268, 2002.

J. Kuhlmann, H. Dobslaw, and M. Thomas. Improved modeling of sea level patterns by incorporating self-attraction and loading. *Journal of Geophysical Research: Oceans*, 116 (C11):n/a–n/a, 2011. ISSN 2156-2202. doi: 10.1029/2011JC007399. URL http://dx.doi.org/10.1029/2011JC007399.

E. Kurtenbach, T. Mayer-Gürr, and A. Eicker. Deriving daily snapshots of the earth's gravity field from grace l1b data using kalman filtering. *Geophysical Research Letters*, 36(17): L17102, 2009.

J. Kusche. A monte-carlo technique for weight estimation in satellite geodesy. *Journal of Geodesy*, 76(11):641–652, 2003.

J. Kusche. Approximate decorrelation and non-isotropic smoothing of time-variable grace-type gravity field models. *Journal of Geodesy*, 81(11):733, nov 2007. doi: 10.1007/s00190-007-0143-3.

J. Kusche and E. J. O. Schrama. Surface mass redistribution inversion from global gps deformation and gravity recovery and climate experiment (grace) gravity data. *Journal of Geophysical Research (Solid Earth)*, 110(B9):9409, sep 2005. doi: 10.1029/2004JB003556.

J. Kusche, R. Schmidt, S. Petrovic, and R. Rietbroek. Decorrelated grace time-variable gravity solutions by gfz, and their validation using a hydrological model. *Journal of Geodesy*, 83(10):903, 2009. doi: 10.1007/s00190-009-0308-3.

F. Landerer, J. Jungclaus, and J. Marotzke. Regional dynamic and steric sea level change in response to the ipcc-a1b scenario. *Journal of physical oceanography*, 37(2):296–312, 2007.

D. A. Lavallée, T. van Dam, G. Blewitt, and P. J. Clarke. Geocenter motions from gps: A unified observation model. *Journal of Geophysical Research*, 111(B5):B05405, 2006. doi: 10.1029/2005JB003784.

P. Y. Le Traon, F. Nadal, and N. Ducet. An improved mapping method of multisatellite altimeter data. *Journal of Atmospheric and Oceanic Technology*, 15, apr 1998. URL http://dx.doi.org/10.1175/1520-0426(1998)015<0522:AIMMOM>2.0.CO;2.

E. W. Leuliette and L. Miller. Closing the sea level rise budget with altimetry, argo, and grace. *Geophysical Research Letters*, 36(4):–04608, 2009.

W. Llovel, M. Becker, A. Cazenave, J.-F. Crétaux, and G. Ramillien. Global land water storage change from grace over 2002–2009; inference on sea level. *Comptes Rendus Geosciences*, 342(3):179–188, 2010. doi: 10.1016/j.crte.2009.12.004.

N. Loeb, J. Lyman, G. Johnson, R. Allan, D. Doelling, T. Wong, B. Soden, and G. Stephens. Observed changes in top-of-the-atmosphere radiation and upper-ocean heating consistent within uncertainty. *Nature Geoscience*, 5(2):110–113, 2012.

A. Lombard, D. Garcia, G. Ramillien, A. Cazenave, R. Biancale, J. M. Lemoine, F. Flechtner, R. Schmidt, and M. Ishii. Estimation of steric sea level variations from combined grace and jason-1 data. *Earth and Planetary Science Letters*, 254(1-2):194–202, 2007. ISSN 0012-821X. doi: DOI:10.1016/j.epsl.2006.11.035.

A. Love. The yielding of the earth to disturbing forces. *Proceedings of the Royal Society of London. Series A*, 82(551):73–88, 1909.

J. Luscombe and M. Luban. Simplified recursive algorithm for wigner 3j and 6j symbols. *Physical Review E*, 57(6):7274, 1998.

F. Lyard, F. Lefevre, T. Letellier, and O. Francis. Modelling the global ocean tides: modern insights from fes2004. *Ocean Dynamics*, 56(5):394–415, 2006.

J. Lyman, J. Willis, and G. Johnson. Recent cooling of the upper ocean. *Geophysical Research Letters*, 33:L18604, 2006.

J. Lyman, S. Good, V. Gouretski, M. Ishii, G. Johnson, M. Palmer, D. Smith, and J. Willis. Robust warming of the global upper ocean. *Nature*, 465(7296):334–337, 2010.

A. Macrander, C. Böning, O. Boebel, and J. Schröter. Validation of grace gravity fields by in-situ data of ocean bottom pressure. In L. Stroink, V. Mosbrugger, G. Wefer, F. M. Flechtner, T. Gruber, A. Güntner, M. Mandea, M. Rothacher, T. Schöne, and J. Wickert, editors, *System Earth via Geodetic-Geophysical Space Techniques*, chapter Advanced Technologies in Earth Sciences, pages 169–185. Springer Berlin Heidelberg, 2010. ISBN 978-3-642-10228-8.

Z. Martinec. Spectral-finite element approach to three-dimensional viscoelastic relaxation in a spherical earth. *Geophysical Journal International*, 142(1):117–141, 2000.

M. Matsu'ura and N. Hirata. Generalized least-squares solutions to quasi-linear inverse problems with a priori information. *Journal of Physics of the Earth*, 30(6):451–468, 1982.

T. Mayer-Gürr et al. *Gravitationsfeldbestimmung aus der Analyse kurzer Bahnbögen am Beispiel der Satellitenmissionen CHAMP und GRACE*. PhD thesis, Universitäts-und Landesbibliothek Bonn, 2006.

D. D. McCarthy and G. Petit. Iers conventions (2003). Technical report, DTIC Document, 2004.

T. J. McDougall and P. Barker. Getting started with teos-10 and the gibbs seawater (gsw) oceanographic toolbox. *SCOR/IAPSO WG*, 127:1–28, 2011.

M. Meier, M. Dyurgerov, U. Rick, S. O'Neel, W. Pfeffer, R. Anderson, S. Anderson, and A. Glazovsky. Glaciers dominate eustatic sea-level rise in the 21st century. *Science*, 317 (5841):1064, 2007.

S. Melachroinos, F. Lemoine, N. Zelensky, D. Rowlands, S. Luthcke, and O. Bordyugov. The effect of geocenter motion on jason-2 orbits and the mean sea level. *Advances in Space Research*, 51(8):1323 – 1334, 2013. ISSN 0273-1177. doi: http://dx.doi.org/10.1016/j.asr.2012.06.004. URL http://www.sciencedirect.com/science/article/pii/S0273117712003778.

D. Melini, G. Spada, and A. Piersanti. A sea level equation for seismic perturbations. *Geophysical Journal International*, 180(1):88–100, 2010.

A. Messiah. Quantum mechanics, vol. 1/2, 1961.

L. Miller and B. Douglas. Mass and volume contributions to twentieth-century global sea level rise. *Nature*, 428(6981):406–409, 2004.

G. A. Milne and J. X. Mitrovica. Postglacial sea-level change on a rotating earth. *Geophysical Journal International*, 133(1):1–19, 1998.

J. X. Mitrovica and G. A. Milne. On post-glacial sea level: I. general theory. *Geophysical Journal International*, 154(2):253–267, 2003.

J. X. Mitrovica, M. E. Tamisiea, J. L. Davis, and G. A. Milne. Recent mass balance of polar ice sheets inferred from patterns of global sea-level change. *Nature*, 409(6823):1026–9, 2001. doi: 10.1038/35059054.

J. X. Mitrovica, J. Wahr, I. Matsuyama, and A. Paulson. The rotational stability of an ice-age earth. *Geophysical Journal International*, 161(2):491–506, 2005. doi: 10.1111/j.1365-246X. 2005.02609.x.

J. Morison, J. Wahr, R. Kwok, and C. Peralta-Ferriz. Recent trends in arctic ocean mass distribution revealed by grace. *Geophysical Research Letters*, 34(7):L07602, apr 2007. doi: 10.1029/2006GL029016.

W. H. Munk and G. J. MacDonald. The rotation of the earth; a geophysical discussion. *Cambridge [Eng.] University Press, 1960.*, 1, 1960.

M. Nakada and J. Okuno. Perturbations of the earth's rotation and their implications for the present-day mass balance of both polar ice caps. *Geophysical Journal International*, 152 (1):124–138, 2003. ISSN 1365-246X. doi: 10.1046/j.1365-246X.2003.01831.x. URL http://dx.doi.org/10.1046/j.1365-246X.2003.01831.x.

R. Nerem and J. Wahr. Recent changes in the earth's oblateness driven by greenland and antarctic ice mass loss. *Geophysical Research Letters*, 38(13), 2011.

R. Nerem, D. Chambers, C. Choe, and G. Mitchum. Estimating mean sea level change from the topex and jason altimeter missions. *Marine Geodesy*, 33(S1):435–446, 2010. Data available from http://sealevel.colorado.edu/.

NSIDC. Word glacier inventory (updated 2009), 1999. URL http://nsidc.org/data/docs/noaa/g01130_glacier_inventory. World Glacier Monitoring Service and National Snow and Ice Data Center/World Data Center for Glaciology. Boulder, CO. Digital media.

S. D. Pagiatakis. The response of a realistic earth to ocean tide loading. *Geophysical Journal International*, 103(2):541–560, 1990. ISSN 1365-246X. doi: 10.1111/j.1365-246X.1990. tb01790.x. URL http://dx.doi.org/10.1111/j.1365-246X.1990.tb01790.x.

J.-H. Park, D. R. Watts, K. A. Donohue, and S. R. Jayne. A comparison of in situ bottom pressure array measurements with grace estimates in the kuroshio extension. *Geophysical Research Letters*, 35(17), 2008. ISSN 1944-8007. doi: 10.1029/2008GL034778. URL http://dx.doi.org/10.1029/2008GL034778.

A. Paulson, S. Zhong, and J. Wahr. Inference of mantle viscosity from grace and relative sea level data. *Geophysical Journal International*, 171(2):497, 2007. doi: 10.1111/j.1365-246X.2007.03556.x.

W. Peltier. Global glacial isostasy and the surface of the ice-age earth: The ice-5g (vm2) model and grace. *Annual Review of Earth and Planetary Sciences*, 32(1):111, 2004. doi: 10.1146/annurev.earth.32.082503.144359.

W. R. Peltier and S. B. Luthcke. On the origins of earth rotation anomalies: New insights on the basis of both "paleogeodetic" data and gravity recovery and climate experiment (grace) data. *Journal of Geophysical Research*, 114(B11):B11405, 2009. doi: 10.1029/2009JB006352.

H. P. Plag and H. U. Jüttner. Inversion of global tide gauge data for present-day ice load changes. *Mem Natl Inst Polar Res Spec Issue*, 54:301–317, 2001.

R. W. Preisendorfer and C. D. Mobley. *Principal component analysis in meteorology and oceanography*. Developments in Atmospheric Science 17. Elsevier, Amsterdam, 1988.

A. Purcell, A. Dehecq, P. Tregoning, E.-K. Potter, S. McClusky, and K. Lambeck. Relationship between glacial isostatic adjustment and gravity perturbations observed by grace. *Geophysical Research Letters*, 38(18):L18305, 2011.

G. Ramillien, S. Bouhours, A. Lombard, A. Cazenave, F. Flechtner, and R. Schmidt. Land water storage contribution to sea level from grace geoid data over 2003–2006. *Global and Planetary Change*, 60(3):381–392, 2008.

B. Raup, A. Racoviteanu, S. Khalsa, C. Helm, A. R, and Y. Arnaud. The glims geospatial glacier database: A new tool for studying glacier change. *Global and Planetary Change*, 56 (1-2):101, 2007. doi: 10.1016/j.gloplacha.2006.07.018.

R. Rietbroek. Validation of oceanic mass changes derived from grace gravimetry. Master's thesis, TU Delft, 2007. URL http://repository.tudelft.nl/view/ir/uuid:f0e6cd75-50e8-4066-98c4-199881d2ce1a.

R. Rietbroek, P. LeGrand, B. Wouters, J. M. Lemoine, G. Ramillien, and C. W. Hughes. Comparison of in situ bottom pressure data with grace gravimetry in the crozet-kerguelen region. *Geophysical Research Letters*, 33, 2006. doi: 10.1029/2006GL027452.

R. Rietbroek, S. E. Brunnabend, C. Dahle, J. Kusche, F. Flechtner, J. Schröter, and R. Timmermann. Changes in total ocean mass derived from grace, gps, and ocean modeling with weekly resolution. *Journal Of Geophysical Research-Oceans*, 114(C11004):C11004, 2009. doi: 10.1029/2009JC005449.

R. Rietbroek, S. E. Brunnabend, J. Kusche, and J. Schröter. Resolving sea level contributions by identifying fingerprints in time-variable gravity and altimetry. *Journal of*

Geodynamics, 59:72–81, 2012a. doi: DOI:10.1016/j.jog.2011.06.007. URL http://www.sciencedirect.com/science/article/pii/S0264370711000779.

R. Rietbroek, M. Fritsche, S. E. Brunnabend, I. Daras, J. Kusche, J. Schröter, F. Flechtner, and R. Dietrich. Global surface mass from a new combination of grace, modelled obp and reprocessed gps data. *Journal of Geodynamics*, 59-60(0):64 – 71, 2012b. ISSN 0264-3707. doi: 10.1016/j.jog.2011.02.003. URL http://www.sciencedirect.com/science/article/pii/S0264370711000305. Mass Transport and Mass Distribution in the System Earth.

R. Rietbroek, L. Jensen, S.-E. Brunnabend, J. Kusche, and J. Schröter. To what extent are altimetry residuals explained by mass redistribution and steric changes? In *20 years of progress in radar altimetry, Venice*, Esa Publications divisions, 2012c.

R. Rietbroek, M. Fritsche, C. Dahle, S.-E. Brunnabend, M. Behnisch, J. Kusche, F. Flechtner, J. Schröter, and R. Dietrich. Can gps-derived surface loading bridge a grace mission gap? *Surveys in Geophysics*, pages 1–17, 2014. ISSN 0169-3298. doi: 10.1007/s10712-013-9276-5. URL http://dx.doi.org/10.1007/s10712-013-9276-5.

M. Rio and F. Hernandez. A mean dynamic topography computed over the world ocean from altimetry, in situ measurements, and a geoid model. *J. Geophys. Res*, 109(12):C12032, 2004.

R. E. M. Riva, J. L. Bamber, D. A. Lavallée, and B. Wouters. Sea-level fingerprint of continental water and ice mass change from grace. *Geophysical Research Letters*, 37(19):L19605, 2010. doi: 10.1029/2010GL044770.

M. Rodell, I. Velicogna, and J. S. Famiglietti. Satellite-based estimates of groundwater depletion in india. *Nature*, 460(7258):999–1002, 2009.

V. Rosmorduc, J. Benveniste, O. Lauret, C. Maheu, M. Milagro, and N. Picot. Radar altimetry tutorial. *http://www. altimetry. info*, 2009.

M. Rothacher, G. Beutler, T. A. Herring, and R. Weber. Estimation of nutation using the global positioning system. *Journal of Geophysical Research*, 104:4835–4860, 1999.

A. Rülke, R. Dietrich, M. Fritsche, M. Rothacher, and P. Steigenberger. Realization of the terrestrial reference system by a reprocessed global gps network. *J. Geophys. Res.*, 113 (B08403), 2008. doi: 10.1029/2007JB005231.

R. Sabadini and B. Vermeersen. *Global dynamics of the Earth: Applications of normal mode relaxation theory to solid-earth geophysics*, volume 20. Springer, 2004.

I. Sasgen, Z. Martinec, and J. Bamber. Combined grace and insar estimate of west antarctic ice mass loss. *Journal of Geophysical Research*, 115(F4):F04010, 2010.

I. Sasgen, H. Konrad, E. Ivins, M. Broeke, J. Bamber, Z. Martinec, and V. Klemann. Antarctic ice-mass balance 2002 to 2011: regional re-analysis of grace satellite gravimetry measurements with improved estimate of glacial-isostatic adjustment. *The Cryosphere Discussions*, 6(5):3703–3732, 2012a.

I. Sasgen, M. van den Broeke, J. L. Bamber, E. Rignot, L. S. Sørensen, B. Wouters, Z. Martinec, I. Velicogna, and S. B. Simonsen. Timing and origin of recent regional ice-mass loss in greenland. *Earth and Planetary Science Letters*, 333:293–303, 2012b.

R. Savcenko and W. Bosch. Eot11a–empirical ocean tide model from multi-mission satellite altimetry. *DGFI report*, 89, 2012.

A. Schettino. Computational methods for calculating geometric parameters of tectonic plates. *Computers & Geosciences*, 25(8):897–907, 1999.

M. Schmeer, M. Schmidt, W. Bosch, and F. Seitz. Separation of mass signals within grace monthly gravity field models by means of empirical orthogonal functions. *Journal of Geodynamics*, 59:124–132, 2012.

R. Schmidt, F. Flechtner, R. König, U. Meyer, K. H. Neumayer, C. Reigber, M. Rothacher, S. Petrovic, S. Y. Zhu, and A. Güntner. *Dynamic Planet*, chapter GRACE Time-Variable Gravity Accuracy Assessment, pages 237–243. Springer Berlin Heidelberg, 2007b. doi: 10.1007/978-3-540-49350-1_36.

R. Schmidt, F. Flechtner, U. Meyer, K.-H. Neumayer, C. Dahle, R. König, and J. Kusche. Hydrological signals observed by the grace satellites. *Surveys in Geophysics*, 29(4-5):319, 2008. doi: 10.1007/s10712-008-9033-3.

E. Schrama, B. Wouters, and R. Rietbroek. A new global mascon approach to assess ice sheet and glacier mass balances from grace data. *Submitted to Journal of Geophysical Research*, 2014.

E. J. O. Schrama and B. Wouters. Revisiting Greenland ice sheet mass loss observed by GRACE. *Journal of Geophysical Research (Solid Earth)*, 116(B15):B02407, feb 2011. doi: 10.1029/2009JB006847.

C. Schwatke, W. Bosch, R. Savcenko, and D. Dettmering. Openadb: An open database for multi-mission altimetry. *EGU Geophysical research abstracts, http://openadb.dgfi.badw.de*, 2010.

A. Shepherd, E. R. Ivins, A. Geruo, V. R. Barletta, M. J. Bentley, S. Bettadpur, K. H. Briggs, D. H. Bromwich, R. Forsberg, N. Galin, et al. A reconciled estimate of ice-sheet mass balance. *Science*, 338(6111):1183–1189, 2012.

F. Siegismund, V. Romanova, A. Köhl, and D. Stammer. Ocean bottom pressure variations estimated from gravity, nonsteric sea surface height and hydrodynamic model simulations. *Journal of Geophysical Research: Oceans (1978–2012)*, 116(C7), 2011.

S. Singh and A. Ben-Menahem. On the summation of certain legendré series. *Journal of Engineering Mathematics*, 2(3):275–282, 1968.

A. Slangen, C. Katsman, R. Van de Wal, L. Vermeersen, and R. Riva. Towards regional projections of twenty-first century sea-level change based on ipcc sres scenarios. *Climate dynamics*, 38(5-6):1191–1209, 2012.

W. Smith and P. Wessel. Gridding with continuous curvature splines in tension. *Geophysics*, 55(3):293–305, 1990.

Y. Song and F. Colberg. Deep ocean warming assessed from altimeters, gravity recovery and climate experiment, in situ measurements, and a non-boussinesq ocean general circulation model. *J. Geophys. Res*, 116:C02020, 2011.

L. S. Sørensen, S. Simonsen, K. Nielsen, P. Lucas-Picher, G. Spada, G. Adalgeirsdottir, R. Forsberg, and C. Hvidberg. Mass balance of the greenland ice sheet (2003-2008) from icesat data-the impact of interpolation, sampling and firn density. *Cryosphere*, 5(4):173–186, 2011.

G. Spada. Alma, a fortran program for computing the viscoelastic love numbers of a spherically symmetric planet. *Computers & Geosciences*, 34(6):667–687, 2008.

G. Spada and P. Stocchi. Selen: A fortran 90 program for solving the "sea-level equation". *Computers & Geosciences*, 33(4):538–562, 2007.

G. Spada, V. Barletta, V. Klemann, R. Riva, Z. Martinec, P. Gasperini, B. Lund, D. Wolf, L. Vermeersen, and M. King. A benchmark study for glacial isostatic adjustment codes. *Geophysical Journal International*, 185(1):106–132, 2011.

M. S. Steckler, S. L. Nooner, S. H. Akhter, S. K. Chowdhury, S. Bettadpur, L. Seeber, and M. G. Kogan. Modeling earth deformation from monsoonal flooding in bangladesh using hydrographic, GPS, and gravity recovery and climate experiment (grace) data. *Journal of Geophysical Research*, 115(B8), Aug 2010. doi: 10.1029/2009JB007018. URL http://dx.doi.org/10.1029/2009JB007018.

P. Steigenberger, M. Rothacher, R. Dietrich, M. Fritsche, A. Rülke, and S. Vey. Reprocessing of a global gps network. *Journal of Geophysical Research*, 111(B5):B05402, 2006.

S. Swenson and J. Wahr. Post-processing removal of correlated errors in grace data. *Geophysical Research Letters*, 33, 2006. doi: 10.1029/2005GL025285.

S. Swenson, D. Chambers, and J. Wahr. Estimating geocenter variations from a combination of grace and ocean model output. *J. Geophys. Res.*, 113(B08410), 2008. doi: 10.1029/2007JB005338.

Y. Tanaka, V. Klemann, Z. Martinec, and R. Riva. Spectral-finite element approach to viscoelastic relaxation in a spherical compressible earth: application to gia modelling. *Geophysical Journal International*, 184(1):220–234, 2011.

B. D. Tapley, S. Bettadpur, J. C. Ries, P. F. Thompson, and M. M. Watkins. Grace measurements of mass variability in the earth system. *Science*, 305:503–506, jul 2004. doi: 10.1126/science.1099192.

R. Timmermann, S. Danilov, J. Schröter, C. Böning, D. Sidorenko, and K. Rollenhagen. Ocean circulation and sea ice distribution in a finite element global sea ice-ocean model. *Ocean Modelling*, 27(3-4):114–129, 2009. ISSN 1463-5003. doi: 10.1016/j.ocemod.2008.10.009. URL http://www.sciencedirect.com/science/article/B6VPS-4V70RFF-1/2/89e91ce1980bce3d64e4d43bfca51c14.

P. Tregoning, C. Watson, G. Ramillien, H. McQueen, and J. Zhang. Detecting hydrologic deformation using grace and gps. *Geophysical Research Letters*, 36, 2009.

K. E. Trenberth and J. T. Fasullo. Tracking earth's energy. *Science*, 328(5976):316–317, Apr 2010. doi: 10.1126/science.1187272. URL http://dx.doi.org/10.1126/science. 1187272.

A. Trupin, M. Meier, and J. Wahr. Effect of melting glaciers on the earth's rotation and gravitational field: 1965–1984. *Geophysical journal international*, 108(1):1–15, 1992.

T. van Dam, J. Wahr, and D. Lavallée. A comparison of annual vertical crustal displacements from gps and gravity recovery and climate experiment (grace) over europe. *Journal of Geophysical Research*, 112(B3):B03404, 2007. doi: 10.1029/2006JB004335.

J. van Loon. *Functional and stochastic modelling of satellite gravity data*, volume 67. NCG, Nederlandse Commissie Voor Geodesie, 2008. Ph. D. thesis.

I. Velicogna. Increasing rates of ice mass loss from the greenland and antarctic ice sheets revealed by grace. *Geophysical Research Letters*, 36(19):L19503, 2009. doi: 10.1029/ 2009GL040222.

I. Velicogna and J. Wahr. Acceleration of greenland ice mass loss in spring 2004. *Nature*, 443(7109):329–331, 2006a. doi: 10.1038/nature05168.

I. Velicogna and J. Wahr. Measurements of time-variable gravity show mass loss in antarctica. *Science*, 311(5768):1754–1756, 2006b.

J. Wahr, M. Molenaar, and F. Bryan. Time variability of the earth's gravity field: Hydrological and oceanic effects and their possible detection using grace. *Journal of Geophysical Research*, 103:30205–30230, dec 1998. doi: 10.1029/98JB02844.

J. Wahr, D. Wingham, and C. Bentley. A method of combining icesat and grace satellite data to constrain antarctic mass balance. *Journal of Geophysical Research: Solid Earth (1978–2012)*, 105(B7):16279–16294, 2000.

H. Wang, L. Xiang, L. Jia, L. Jiang, Z. Wang, B. Hu, and P. Gao. Load love numbers and green's functions for elastic earth models prem, iasp91, ak135, and modified models with refined crustal structure from crust 2.0. *Computers & Geosciences*, 2012.

S. Werth and A. Güntner. Calibration analysis for water storage variability of the global hydrological model wghm. *Hydrol. Earth Syst. Sci*, 14:59–78, 2010.

P. L. Whitehouse, M. J. Bentley, G. A. Milne, M. A. King, and I. D. Thomas. A new glacial isostatic adjustment model for antarctica: calibrated and tested using observations of relative sea-level change and present-day uplift rates. *Geophysical Journal International*, 190(3):1464–1482, 2012. ISSN 1365-246X. doi: 10.1111/j.1365-246X.2012.05557.x. URL http://dx.doi.org/10.1111/j.1365-246X.2012.05557.x.

J. K. Willis, D. P. Chambers, and R. S. Nerem. Assessing the globally averaged sea level budget on seasonal to interannual timescales. *Journal of Geophysical Research (Oceans)*, 113 (C12):6015, jun 2008. doi: 10.1029/2007JC004517.

R. Woodward. On the form and position of mean sea level. *Geological Survey Bulletin*, 48: 87–170, 1888.

B. Wouters and E. J. O. Schrama. Improved accuracy of grace gravity solutions through empirical orthogonal function filtering of spherical harmonics. *Geophysical Research Letters*, 34(23):L23711, 2007. doi: 10.1029/2007GL032098.

B. Wouters, D. Chambers, and E. J. O. Schrama. Grace observes small-scale mass loss in greenland. *Geophysical Research Letters*, 35(20):L20501, 2008. doi: 10.1029/2008GL034816.

P. Wu and W. R. Peltier. Pleistocene deglaciation and the earth's rotation: a new analysis. *Geophysical Journal of the Royal Astronomical Society*, 76(3):753–791, 1984.

X. Wu, D. F. Argus, M. B. Heflin, E. R. Ivins, and F. H. Webb. Site distribution and aliasing effects in the inversion for load coefficients and geocenter motion from gps data. *Geophysical Research Letters*, 29(24):2210, 2002. doi: 10.1029/2002GL016324.

X. Wu, M. B. Heflin, E. R. Ivins, and I. Fukumori. Seasonal and interannual global surface mass variations from multisatellite geodetic data. *Journal of Geophysical Research (Solid Earth)*, 111(B10):9401, sep 2006. doi: 10.1029/2005JB004100.

X. Wu, M. B. Heflin, H. Schotman, B. L. A. Vermeersen, D. Dong, R. S. Gross, E. R. Ivins, A. W. Moore, and S. E. Owen. Simultaneous estimation of global present-day water transport and glacial isostatic adjustment. *Nature Geoscience*, 3(9):642, 2010. doi: 10.1038/ngeo938.

X. Wu, J. Ray, and T. van Dam. Geocenter motion and its geodetic and geophysical implications. *Journal of Geodynamics*, 58:44–61, 2012.

H. Zwally and M. Giovinetto. Overview and assessment of antarctic ice-sheet mass balance estimates: 1992–2009. *Surveys in geophysics*, 32(4):351–376, 2011.

A Translation of the Geopotential Field

The external potential at a shifted position, $\mathbf{r}_2 = \mathbf{r}_1 + \mathbf{x}$, may be expressed by a spherical harmonic expansion. In contrast to Eq. 2.3, it is convenient to use normalized complex spherical harmonics[1]. These have the properties

$$\bar{Y}_n^m(\theta, \lambda) = \sqrt{(2n+1)\frac{(n-m)!}{(n+m)!}} P_{nm}(\cos\theta)e^{im\lambda}, \tag{A.1}$$

$$\bar{Y}_n^{m*}(\theta, \lambda) = (-1)^m \bar{Y}_n^{-m}(\theta, \lambda), \tag{A.2}$$

$$\oint_\Omega \bar{Y}_n^m(\omega)\bar{Y}_{n'}^{m'*}(\omega)d\omega = 4\pi\delta_{nn'}\delta_{mm'}. \tag{A.3}$$

where the asterisk denotes the complex conjugate.

The potential at position $\mathbf{r}_2$ may now be written using complex Stokes coefficients C_n^m:

$$\phi(\mathbf{r}_2) = \frac{GM}{a}\sum_{n=0}^{\infty}\sum_{m=-n}^{n}\left(\frac{a}{|\mathbf{r}_2|}\right)^{n+1}C_n^m\bar{Y}_n^m(\Omega_2). \tag{A.4}$$

The real valued Stokes coefficients can be derived from the relations:

$$\begin{aligned}
C_n^m &= \frac{1}{\sqrt{2}}\left(C_{nm} - iC_{n-m}\right), \quad m > 0, \\
C_n^0 &= C_{n0}, \quad m = 0, \\
C_n^m &= (-1)^m C_n^{-m*}, \quad m < 0.
\end{aligned} \tag{A.5}$$

The irregular solid spherical harmonic base functions on the right hand side of Eq. A.4 may be written in terms of a reference system shifted by, $\mathbf{x}$. Applying the proper normalization one obtains from Giacaglia and Burša (1980) the following relation

$$\frac{1}{r_2^{n+1}}\bar{Y}_n^m(\Omega_2) = \sum_{n',m'}^{\infty}A_{n,m,n',m'}\frac{1}{|\mathbf{x}|^{n+1}}\left(\frac{|\mathbf{x}|}{|\mathbf{r}_1|}\right)^{n'+1}\bar{Y}_{n'}^{m'}(\Omega_1)\bar{Y}_{n'-n}^{m'-m*}(\Omega_{\mathbf{x}}), \quad |\mathbf{r}_1| > |\mathbf{x}|, \tag{A.6}$$

where,

$$A_{n,m,n',m'} = (-1)^{n+n'}\frac{\sqrt{\frac{(2n+1)}{(2n'+1)}\frac{(n'+m')!(n'-m')!}{(n+m)!(n-m)!}}}{\sqrt{(2n'-2n+1)(n'-n+m'-m)!(n'-n-m'+m)!}}, \tag{A.7}$$

and Ω_1 and Ω_x are the angles associated with $\mathbf{r}_1$ and $\mathbf{x}$ respectively. Substituting A.6 in A.4 and changing the order of summation yields after some manipulation:

$$\phi(\mathbf{r}_2) = \frac{GM}{a}\sum_{n'=0}^{\infty}\sum_{m'=-n'}^{n'}\left(\frac{a}{|\mathbf{r}_1|}\right)^{n'+1}\tilde{C}_{n'}^{m'}\bar{Y}_{n'}^{m'}(\Omega_1). \tag{A.8}$$

---

[1] using vertically positioned degree and order

A.154

The transformed Stokes coefficients, $\tilde{C}_{n'}^{m'}$, are now linearly dependent on the original coefficients C_n^m:

$$\tilde{C}_{n'}^{m'} = \sum_{n=0}^{n'} \sum_{m=-\frac{n'-m'}{2}}^{\frac{n'+m'}{2}} C_n^m \left(\frac{|\mathbf{x}|}{a}\right)^{n'-n} A_{n,m,n',m'} \bar{Y}_{n'-n}^{m'-m*}(\Omega_{\mathbf{x}}). \qquad (A.9)$$

The start and end indices are changed due to the restrictions of the degree and order. Only a limited combination of n and m yield non-zero values as is depicted by the shaded region in Fig. A.1.

Non–zero combinations of n,m
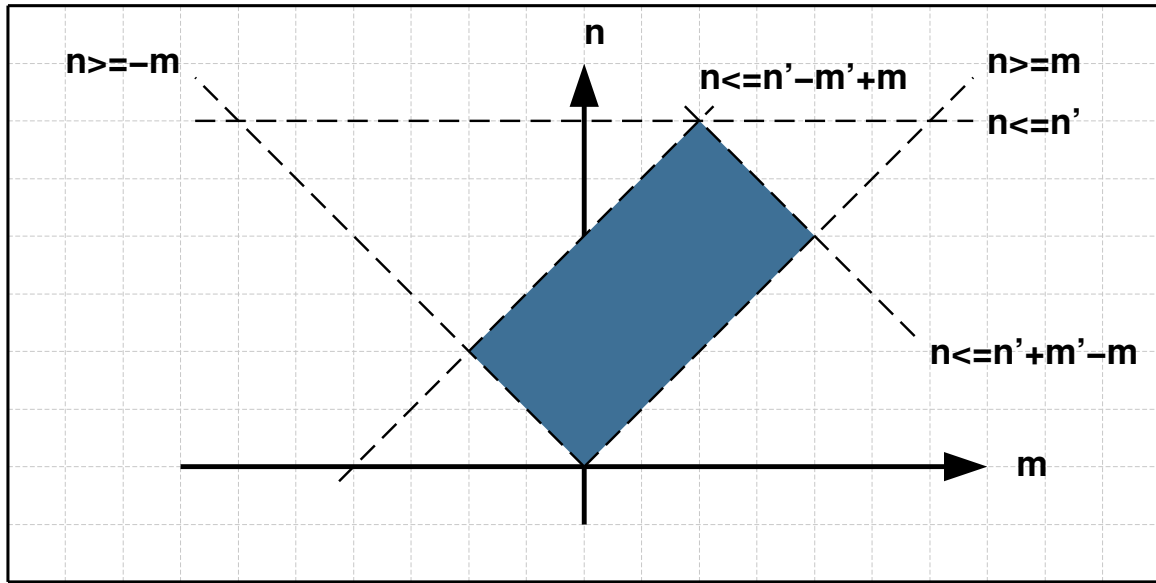
Figure A.1: Obeying four constraints, the double summation from Eq. A.9 will only yield non-zero combinations for n and m in the shaded area.

A.1 Position of the Center of Mass of the Earth System

The center of mass of the Earth system is the position, $\mathbf{x}_{CM}$ where the degree 1 Stokes coefficients of the translated potential field vanish. From Eq. A.9 one can derive for $n' = 1$, $m' = 0, 1$ the following relation:

$$\tilde{C}_1^{m'} = 0 = -\frac{1}{3} C_0^0 \frac{|\mathbf{x}_{CM}|}{a} \bar{Y}_1^{m'*}(\Omega_x) + C_1^{m'} \bar{Y}_0^0. \qquad (A.10)$$

Substituting $C_0^0 = 1$ (the central gravity term) and $\bar{Y}_0^0 = 1$, and observing that in Cartesian coordinates:

$$\mathbf{x}_{CM} = |\mathbf{x}_{CM}| \begin{bmatrix} \sin(\theta)\cos(\lambda) \\ \sin(\theta)\sin(\lambda) \\ \cos(\theta) \end{bmatrix} = |\mathbf{x}_{CM}| \frac{1}{\sqrt{3}} \begin{bmatrix} \mathrm{Re}\{\bar{Y}_1^{1*}(\Omega_x)\}\sqrt{2} \\ -\mathrm{Im}\{\bar{Y}_1^{1*}(\Omega_x)\}\sqrt{2} \\ \bar{Y}_1^0(\Omega_x) \end{bmatrix}, \qquad (A.11)$$

one finds:

$$\mathbf{x}_{CM} = \sqrt{3}a \begin{bmatrix} \mathrm{Re}\{C_1^1\}\sqrt{2} \\ -\mathrm{Im}\{C_1^1\}\sqrt{2} \\ C_1^0 \end{bmatrix} = \sqrt{3}a \begin{bmatrix} C_{11} \\ C_{1-1} \\ C_{10} \end{bmatrix}. \tag{A.12}$$

A similar proof can be found in Klemann and Martinec (2009).

A.2 Small Translations of the Potential Field

As Eq. A.9 shows, *all* of the Stokes coefficients will change under a translation. However for small geocenter related offsets, typically smaller than 1 cm, $|\mathbf{x}| << a$. First order terms in Eq. A.9 will only occur for $n' - n \leq 1$. Furthermore, besides the central gravity term, the second largest term in the gravity field is related to oblateness of the Earth (degree 2 and order 0). When the Earth gravity field is approximated by an ellipsoid only the zero order terms ($m = 0$) are non-zero. Ignoring higher order terms, we see that the Stokes coefficients of the translated ellipsoid can be written as:

$$\tilde{C}_n^0 = C_n^0 - C_{n-1}^0 \sqrt{\frac{n^2}{3}} \sqrt{\frac{2n-1}{2n+1}} \left(\frac{|\mathbf{x}|}{a}\right) \bar{Y}_1^0, \tag{A.13}$$

$$\tilde{C}_n^1 = C_n^1 - C_{n-1}^0 \sqrt{\frac{(n+1)n}{3 \cdot 2}} \sqrt{\frac{2n-1}{2n+1}} \left(\frac{|\mathbf{x}|}{a}\right) \bar{Y}_1^{1*}.$$

Or in terms of the translation vector and real Stokes coefficients:

$$\begin{bmatrix} \tilde{C}_{n1} \\ \tilde{C}_{n-1} \\ \tilde{C}_{n0} \end{bmatrix} = \begin{bmatrix} C_{n1} \\ C_{n-1} \\ C_{n0} \end{bmatrix} -$$

$$\frac{C_{n-10}}{a} n \sqrt{\frac{2n-1}{2n+1}} \begin{bmatrix} \sqrt{\frac{(n+1)}{2n}} & 0 & 0 \\ 0 & \sqrt{\frac{(n+1)}{2n}} & 0 \\ 0 & 0 & 1 \end{bmatrix} \mathbf{x}. \tag{A.14}$$

Besides the degree 1 coefficients, the translated bulge will appear as a 'pear shape' of the Earth (Stokes coefficients C_{30}, C_{31}, S_{31}). However, for seasonal variations of the geocenter motion (Rietbroek et al., 2012b), the effect is in the order of $5e^{-13}$ (see Fig. A.2), which about an order of magnitude smaller as the current accuracy of the monthly degree 3 coefficients obtainable by GRACE (GFZ Release 05: $\approx 4e^{-12}$).

Therefore, as long as the translations are small, one may in practice translate a potential by merely applying Eq. A.14 to the degree 1 coefficients.
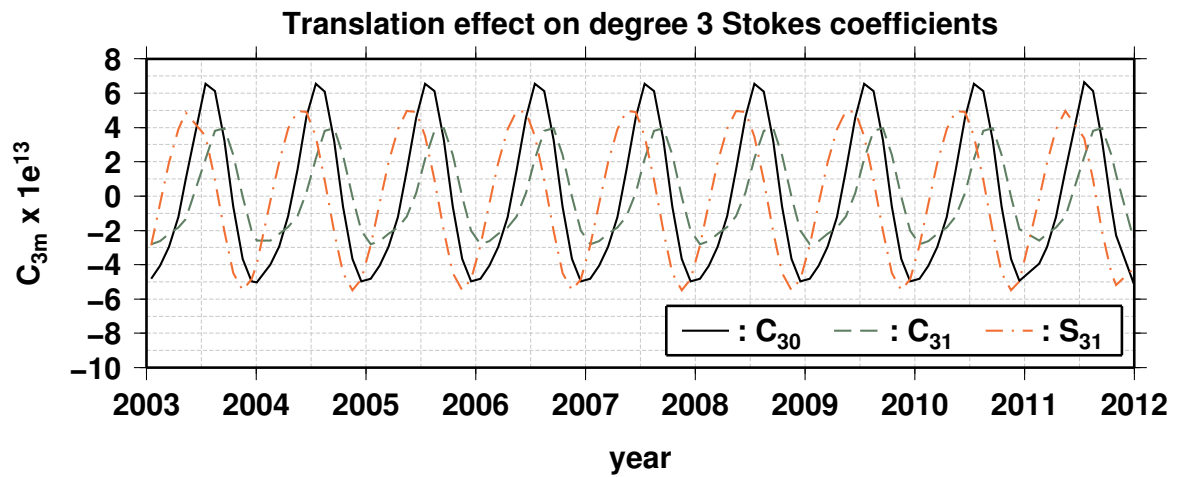
Figure A.2: Translational effect of the equatorial bulge on the degree 3 Stokes coefficients due to the seasonal geocenter motion as computed by Rietbroek et al. (2012b) (4.5 mm annual amplitude).

B Product to Sum Operator

B.1 Formulation with Complex Spherical Harmonics

The product of two functions expressed as spherical harmonic expansions, $\tilde{S}$, O can by itself be expressed in an SH expansion[1]:

$$S(\theta, \lambda) = O(\theta, \lambda)\tilde{S}(\theta, \lambda). \tag{B.1}$$

The spherical harmonic coefficients of $\tilde{S}$ are truncated at degree and order N. In order to simplify the derivation, it is convenient to initially use the same complex notation as in App. A leading to

$$\tilde{S}(\theta, \lambda) = \sum_{n=0}^{N} \sum_{m=-n}^{n} \tilde{S}_n^m \bar{Y}_n^m(\theta, \lambda).$$

The coefficients S_{nm} can be obtained by multiplying Eq. B.1 by the conjugate, $\bar{Y}_n^{m*}$, and integrating over the unit sphere:

$$S_{nm} = \frac{1}{4\pi}\int_\Omega S(\omega)\bar{Y}_n^{m*}(\omega)d\omega = \frac{1}{4\pi}\int_\Omega O(\omega)\tilde{S}(\omega)(-1)^m \bar{Y}_n^{-m}(\omega)d\omega. \tag{B.2}$$

Or when expanding the functions:

$$\begin{aligned}
S_n^m &= \frac{1}{4\pi}\int_\Omega \sum_{n_1,m_1}^{N} \sum_{n_2,m_2}^{\infty} O_{n_2}^{m_2}\tilde{S}_{n_1}^{m_1}(-1)^m \bar{Y}_n^{-m}\bar{Y}_{n_1}^{m_1}\bar{Y}_{n_2}^{m_2}d\omega \\
&= \sum_{n_1,m_1}\sum_{n_2,m_2} O_{n_2}^{m_2}\tilde{S}_{n_1}^{m_1}\frac{(-1)^m}{4\pi}\int_\Omega \bar{Y}_n^{-m}\bar{Y}_{n_1}^{m_1}\bar{Y}_{n_2}^{m_2}d\omega \\
&= \sum_{n_1,m_1}^{N}\sum_{n_2,m_2}^{\infty} (-1)^m O_{n_2}^{m_2}\tilde{S}_{n_1}^{m_1}A_{-mm_1m_2}^{nn_1n_2}.
\end{aligned} \tag{B.3}$$

In this work, the triple integral, $A_{mm_1m_2}^{nn_1n_2}$, also known as the Gaunt coefficient is computed explicitly in terms of Wigner-3j symbols (e.g. Messiah (1961)):

$$A_{-mm_1m_2}^{nn_1n_2} = \sqrt{(2n+1)(2n_1+1)(2n_2+1)}\begin{pmatrix} n & n_1 & n_2 \\ 0 & 0 & 0 \end{pmatrix}\begin{pmatrix} n & n_1 & n_2 \\ -m & m_1 & m_2 \end{pmatrix}. \tag{B.4}$$

The Wigner-3j symbols itself can be computed by recursive formulas (Luscombe and Luban, 1998)[2]. In fact, most combination of the Wigner-3j symbols will be zero except

---

[1] although the notation used here corresponds to notations for the ocean function and Sea level, the actual functions may be arbitrary.

[2] This algorithm has been implemented in the Fortran library SHTOOLS. In this work, the routine has been modified to enable parallel execution with openMP

when the following conditions are satisfied:

$$
\begin{aligned}
|n - n_1| &\le n_2 \le n + n_1, \\
m_2 &= m - m_1, \\
-n &\le m \le n, \\
-n_1 &\le m_1 \le n_1, \\
-n_2 &\le m_2 \le n_2.
\end{aligned}
\tag{B.5}
$$

Furthermore for odd combinations of $n + n_1 + n_2$

$$
\begin{pmatrix} n & n_1 & n_2 \\ 0 & 0 & 0 \end{pmatrix} = 0, \quad n + n_1 + n_2 = 2p + 1, p \in \mathbb{N}.
\tag{B.6}
$$

This implies that most of the terms in the summation from Eq. B.3 are zero and the inner sum can be simplified:

$$
\begin{aligned}
S_n^m &= \sum_{n_1, m_1}^{N} \left[\sum_{\substack{n_2 = |n - n_1| \\ n + n_1 + n_2 = 2p}}^{n + n_1} (-1)^m O_{n_2}^{m - m_1} A_{-m m_1 (m - m_1)}^{n n_1 n_2} \right] \tilde{S}_{n_1}^{m_1} \\
&= \sum_{n_1, m_1}^{N} B_{n_1 m_1}^{nm} \tilde{S}_{n_1}^{m_1}.
\end{aligned}
\tag{B.7}
$$

B.2 Formulation with Real Spherical Harmonics

Eq. B.7 may be implemented in matrix form. If the function O is constant, the matrix entries, $B_{m m_1}^{n n_1}$, can be stored for reuse. Furthermore, for a given truncation degree N the coefficients, O_n^m, need only to be computed until $2N$. However, when the functions O and $\tilde{S}$ are real-valued, a 50 % reduction in matrix size can be achieved. Since in that case, a symmetric matrix with real, instead of complex, entries can be constructed.

For this purpose, it is convenient to sort the coefficients according to their order, and define the following two vectors:

$$
\begin{aligned}
\mathbf{s}_1^T &= \begin{bmatrix} S_N^{-N} & \cdots & S_2^{-2} & \cdots & S_N^{-2} & S_1^{-1} & \cdots & S_N^{-1} \end{bmatrix}, \\
\mathbf{s}_2^T &= \begin{bmatrix} S_0^0 & \cdots & S_N^0 & S_1^1 & \cdots & S_N^1 & \cdots & S_N^N \end{bmatrix}.
\end{aligned}
$$

Similarly, the coefficients denoted with the tilde are expanded and the product to sum operation is written as:

$$
\begin{bmatrix} \mathbf{s}_1 \\ \hline \mathbf{s}_2 \end{bmatrix} = \begin{bmatrix} \mathbf{B}_{11} & \mathbf{B}_{12} \\ \hline \mathbf{B}_{21} & \mathbf{B}_{22} \end{bmatrix} \begin{bmatrix} \tilde{\mathbf{s}}_1 \\ \hline \tilde{\mathbf{s}}_2 \end{bmatrix}.
\tag{B.8}
$$

The symmetry relations from Eq. A.5 can be used to write the lower section ($m \ge 0$) of matrix vector operation as follows:

$$
\begin{aligned}
S_n^m &= \sum_{n_1 = 0}^{N} \left[\sum_{m_1 = -n_1}^{-1} B_{m m_1}^{n n_1} \tilde{S}_{n_1}^{m_1} + \sum_{m_1 = 0}^{n_1} B_{m m_1}^{n n_1} \tilde{S}_{n_1}^{m_1} \right] \\
&= \sum_{n_1 = 0}^{N} \sum_{m_1 = 0}^{n_1} \left[(-1)^{m_1} (1 - \delta_{0 m_1}) B_{m - m_1}^{n n_1} \tilde{S}_{n_1}^{m_1 *} + B_{m m_1}^{n n_1} \tilde{S}_{n_1}^{m_1} \right].
\end{aligned}
\tag{B.9}
$$

In order to establish the relation between the complex and real coefficients, it is convenient to use a matrix notation for the complex numbers:

$$a + ib = \begin{bmatrix} a & b \\ -b & a \end{bmatrix}, \quad (a + ib)^* = \begin{bmatrix} a & -b \\ b & a \end{bmatrix}. \tag{B.10}$$

This consequently yields for each entry in the summation over n_1 and m_1:

$$\frac{1}{\sqrt{2 - \delta_{0m}}} \begin{bmatrix} S_{nm} & -S_{n-m} \\ S_{n-m} & S_{nm} \end{bmatrix} =$$

$$\sum_{n_1=0}^{N} \sum_{m_1=0}^{n_1} \begin{bmatrix} \mathrm{Re}\{B_{nn_1}^{m-m_1}\} & \mathrm{Im}\{B_{nn_1}^{m-m_1}\} \\ -\mathrm{Im}\{B_{nn_1}^{m-m_1}\} & \mathrm{Re}\{B_{nn_1}^{m-m_1}\} \end{bmatrix} \frac{(-1)^{m_1}(1 - \delta_{0m_1})}{\sqrt{2 - \delta_{0m_1}}} \begin{bmatrix} \tilde{S}_{n_1 m_1} & \tilde{S}_{n_1 - m_1} \\ -\tilde{S}_{n_1 - m_1} & \tilde{S}_{n_1 m_1} \end{bmatrix} \tag{B.11}$$

$$+ \sum_{n_1=0}^{N} \sum_{m_1=0}^{n_1} \begin{bmatrix} \mathrm{Re}\{B_{nn_1}^{mm_1}\} & \mathrm{Im}\{B_{nn_1}^{mm_1}\} \\ -\mathrm{Im}\{B_{nn_1}^{mm_1}\} & \mathrm{Re}\{B_{nn_1}^{mm_1}\} \end{bmatrix} \frac{1}{\sqrt{2 - \delta_{0m_1}}} \begin{bmatrix} \tilde{S}_{n_1 m_1} & -\tilde{S}_{n_1 - m_1} \\ \tilde{S}_{n_1 - m_1} & \tilde{S}_{n_1 m_1} \end{bmatrix}.$$

The rightmost columns of the matrix multiplication may be ignored because of the symmetry relation, and a rewriting yields:

$$\begin{bmatrix} S_{nm} \\ S_{n-m} \end{bmatrix} = \sum_{n_1=0}^{N} \sum_{m_1=0}^{n_1} \mathbf{D}_{nn_1}^{mm_1} \begin{bmatrix} \tilde{S}_{n_1 m_1} \\ \tilde{S}_{n_1 - m_1} \end{bmatrix}. \tag{B.12}$$

For clarity, the real coefficients are stacked in vectors, $\mathbf{s}$, $\tilde{\mathbf{s}}$, according to the following scheme:

$$\mathbf{s}^T = \begin{bmatrix} S_{00} & \cdots & S_{N0} & S_{11} & S_{1-1} & \cdots & S_{N1} & S_{N-1} & \cdots & S_{N-N} \end{bmatrix}. \tag{B.13}$$

In this way the entire matrix operation looks like:

$$\mathbf{s} = \mathbf{D}\tilde{\mathbf{s}}, \tag{B.14}$$

in the real domain.

Where each entry, $\mathbf{D}_{nn_1}^{mm_1}$, is by itself a 2x2 matrix[3]:

$$\mathbf{D}_{n_1 m_1}^{nm} = \frac{\sqrt{2 - \delta_{0m}}}{\sqrt{2 - \delta_{0m_1}}} \left\{ (-1)^{m_1}(1 - \delta_{0m_1}) \begin{bmatrix} \mathrm{Re}\{B_{nn_1}^{m-m_1}\}+ & -\mathrm{Im}\{B_{nn_1}^{m-m_1}\} \\ -\mathrm{Im}\{B_{nn_1}^{m-m_1}\} & -\mathrm{Re}\{B_{nn_1}^{m-m_1}\} \end{bmatrix} + \right.$$

$$\left. \begin{bmatrix} \mathrm{Re}\{B_{nn_1}^{mm_1}\}+ & \mathrm{Im}\{B_{nn_1}^{mm_1}\} \\ -\mathrm{Im}\{B_{nn_1}^{mm_1}\} & \mathrm{Re}\{B_{nn_1}^{mm_1}\} \end{bmatrix} \right\}. \tag{B.15}$$

Which can be built using the relation from Eq. B.7:

$$B_{nn_1}^{m-m_1} = \sum_{\substack{n_2=|n-n_1| \\ n+n_1+n_2=2p}}^{n+n_1} (-1)^m O_{n_2}^{m+m_1} A_{-m-m_1(m+m_1)}^{nn_1 n_2}, \tag{B.16}$$

$$B_{nn_1}^{mm_1} = \sum_{\substack{n_2=|n-n_1| \\ n+n_1+n_2=2p}}^{n+n_1} (-1)^m O_{n_2}^{m-m_1} A_{-mm_1(m-m_1)}^{nn_1 n_2}, \quad m \geq m_1, \tag{B.17}$$

$$B_{nn_1}^{mm_1} = \sum_{\substack{n_2=|n-n_1| \\ n+n_1+n_2=2p}}^{n+n_1} (-1)^{m_1} O_{n_2}^{m_1-m*} A_{-mm_1(m-m_1)}^{nn_1 n_2}, \quad m < m_1. \tag{B.18}$$

---

[3]For $m = 0$ and/or $m_1 = 0$, the second row and/or column is removed

Although, not obvious from the above, the matrix $\mathbf{D}$ is symmetric with size $(N+1)^2 \times (N+1)^2$. Compared to the complex case, which yields a Hermitian matrix a 50% reduction in matrix memory is obtained. For example, storing the lower triangle of a matrix with $N = 150$, takes up 1.9 Gb instead of 3.9 Gb. More importantly, the matrix can be applied directly to real spherical harmonic coefficients, which are much more common in geodesy.

For practical use, the lower triangle of the product to sum matrix, $\mathbf{D}$, may be computed from Eqs. B.12 until B.17 in combination with Eq. B.4. Although not critical for most applications, the computation has been implemented with a parallelization using openMP, since all the matrix entries can be computed separately.

Alternatively, Blewitt and Clarke (2003) provide formulas in the case of unnormalized real spherical harmonic coefficients, by separating the integrals of latitude and longitude. Due to the absence of normalization, the resulting matrix will however not be symmetric, and it is possible that entries for high degrees suffer from numerical overflow problems.

C Operations on Normal Equation Systems

This appendix describes a set of operations which may be applied to systems of normal equations. Most of these operations are commonly applied in the field of Geodesy, and can be found in for example (Koch, 1988). Nevertheless, they are described here for completeness and follow the notation as used throughout this thesis. The methods focus on the manipulation of the normal equation systems, without the need to have information at the original observation level.

C.1 Least Squares Solution of a Linear Inverse Problem

Let a set of unknown parameter residuals, stacked in a vector $\mathbf{x}$, be linearly related to a set of observations $\mathbf{d}$:

$$\mathbf{A}(\mathbf{x} + \mathbf{x}_0) = \mathbf{d} + \epsilon. \tag{C.1}$$

The correlated measurements noise, ϵ, is described by the error-covariance matrix, $\mathbf{Q}_{dd} = \mathbf{P}_{dd}^{-1}$. The vector $\mathbf{x}_0$ is an approximate solution which is already available before the inversion.

From this observation equation one may compute the well known least squares estimate by solving the normal equation system for $\hat{\mathbf{x}}$:

$$\mathbf{N}\hat{\mathbf{x}} = \mathbf{b}. \tag{C.2}$$

Where the normal matrix, $\mathbf{N}$, the right hand side, $\mathbf{b}$, and the parameter residual, $\hat{\mathbf{x}}$ are build up as follows:

$$\mathbf{N} = \mathbf{A}^T\mathbf{P}\mathbf{A},$$
$$\mathbf{b} = \mathbf{A}^T\mathbf{P}(\mathbf{d} - \mathbf{A}\mathbf{x}_0). \tag{C.3}$$

The solution minimizes the weighted measurement residuals or quadratic cost function:

$$(\mathbf{d} - \mathbf{A}\mathbf{x}_0 - \mathbf{A}\hat{\mathbf{x}})^T\mathbf{P}(\mathbf{d} - \mathbf{A}\mathbf{x}_0 - \mathbf{A}\hat{\mathbf{x}}) = \mathbf{l}^T\mathbf{P}\mathbf{l}. \tag{C.4}$$

The error-covariance of the estimated parameters is given by

$$\mathbf{Q}_{xx} = \mathbf{N}^{-1}. \tag{C.5}$$

Based on the residuals, one may estimate an a posteriori variance factor, σ_0 to obtain the a posteriori error covariance $\tilde{\mathbf{Q}}_{xx}$:

$$\tilde{\mathbf{Q}}_{xx} = \sigma_0^2\mathbf{Q}_{xx}, \quad \text{with} \quad \sigma_0^2 = \frac{\mathbf{l}^T\mathbf{P}\mathbf{l}}{n_d - n_x}. \tag{C.6}$$

The amount of observations, n_d, minus the amount of unknown parameters, n_x are the degrees of freedom of the overdetermined system, being solved here.

In order to estimate the unknown parameters and an a posteriori covariance scale, one only needs to store the following normal equation system elements:

$$\mathbf{N}, \ \mathbf{b}, \ \mathbf{x}_0, \ n_x, \ n_d,$$
$$\mathbf{l}_0^T \mathbf{Pl}_0 = (\mathbf{d} - \mathbf{Ax}_0)^T \mathbf{P}(\mathbf{d} - \mathbf{Ax}_0). \tag{C.7}$$

Without knowledge of the original design matrix or the observations, the value of the quadratic optimization functional can be obtained by an update of $\mathbf{l}_0^T \mathbf{Pl}_0$:

$$\mathbf{l}^T \mathbf{Pl} = \mathbf{l}_0^T \mathbf{Pl}_0 - 2\hat{\mathbf{x}}^T \mathbf{b} + \hat{\mathbf{x}}^T \mathbf{N}\hat{\mathbf{x}} = \mathbf{l}_0^T \mathbf{Pl}_0 - \hat{\mathbf{x}}^T \mathbf{b}. \tag{C.8}$$

C.2 Reduction of Unknown Parameters

Often, there are parameters in an inverse problem which need to be solved, but are not of particular interest. These so-called nuisance parameters may be eliminated from the solution space of a normal equation system, while still being solved implicitly. This procedure is generally referred to as the reduction of parameters (see for example Kusche (2003))

The normal equation system may be partitioned into nuisance parameters, $\mathbf{x}_r$ and the remaining parameters of interest, $\mathbf{x}_c$:

$$\mathbf{N} = \begin{bmatrix} \mathbf{N}_{rr} & \mathbf{N}_{rc} \\ \mathbf{N}_{rc}^T & \mathbf{N}_{cc} \end{bmatrix},$$
$$\mathbf{b} = \begin{bmatrix} \mathbf{b}_r \\ \mathbf{b}_c \end{bmatrix}, \tag{C.9}$$
$$\hat{\mathbf{x}} = \begin{bmatrix} \hat{\mathbf{x}}_r \\ \hat{\mathbf{x}}_c \end{bmatrix}.$$

Furthermore, the inverse of the partitioned normal matrix may be written as:

$$\begin{bmatrix} \mathbf{N}_{rr} & \mathbf{N}_{rc} \\ \mathbf{N}_{rc}^T & \mathbf{N}_{cc} \end{bmatrix}^{-1} =$$
$$\begin{bmatrix} \mathbf{N}_{rr}^{-1} + \mathbf{N}_{rr}^{-1}\mathbf{N}_{rc}(\mathbf{N}_{cc} - \mathbf{N}_{rc}^T\mathbf{N}_{rr}^{-1}\mathbf{N}_{rc})^{-1}\mathbf{N}_{rc}^T\mathbf{N}_{rr}^{-1} & -\mathbf{N}_{rr}^{-1}\mathbf{N}_{rc}(\mathbf{N}_{cc} - \mathbf{N}_{rc}^T\mathbf{N}_{rr}^{-1}\mathbf{N}_{rc})^{-1} \\ -(\mathbf{N}_{cc} - \mathbf{N}_{rc}^T\mathbf{N}_{rr}^{-1}\mathbf{N}_{rc})^{-1}\mathbf{N}_{rc}^T\mathbf{N}_{rr}^{-1} & (\mathbf{N}_{cc} - \mathbf{N}_{rc}^T\mathbf{N}_{rr}^{-1}\mathbf{N}_{rc})^{-1} \end{bmatrix}. \tag{C.10}$$

From the lower part of the matrix , the solution $\mathbf{x}_c$ may now be extracted:

$$\hat{\mathbf{x}}_c = -(\mathbf{N}_{cc} - \mathbf{N}_{rc}^T\mathbf{N}_{rr}^{-1}\mathbf{N}_{rc})^{-1}\mathbf{N}_{rc}^T\mathbf{N}_{rr}^{-1}\mathbf{b}_r$$
$$+(\mathbf{N}_{cc} - \mathbf{N}_{rc}^T\mathbf{N}_{rr}^{-1}\mathbf{N}_{rc})^{-1}\mathbf{b}_c. \tag{C.11}$$

Which may again be written as a reduced normal equation system:

$$\tilde{\mathbf{N}}\hat{\mathbf{x}}_c = \tilde{\mathbf{b}},$$
$$\tilde{\mathbf{N}} = (\mathbf{N}_{cc} - \mathbf{N}_{rc}^T \mathbf{N}_{rr}^{-1} \mathbf{N}_{rc}),$$
$$\tilde{\mathbf{b}} = \mathbf{b}_c - \mathbf{N}_{rc}^T \mathbf{N}_{rr}^{-1} \mathbf{b}_r, \qquad \text{(C.12)}$$
$$\widetilde{\mathbf{l}_0^T \mathbf{P} \mathbf{l}_0} = \mathbf{l}_0^T \mathbf{P} \mathbf{l}_0 - \mathbf{b}_r^T \mathbf{N}_{rr}^{-1} \mathbf{b}_r,$$
$$\tilde{n}_x = n_x, \; \tilde{n}_d = n_d.$$

The degrees of freedom of the system do not change for a reduction, since no observations are added or removed and the amount of parameters remains constant (but some are now implicitly solved).

C.3 Changing the a Priori Solution

It is desirable to be able to change the a priori solution $\mathbf{x}_0$ in a normal equation system, without having to resort to the original measurements. This step is necessary, when different normal equation systems are to be combined and their signal content needs to be made consistent. In addition, it is sometimes desirable to fix certain parameters to other a priori values when they cannot be (accurately) estimated.

Imagine that the a priori values are slightly adapted to a new value $\tilde{\mathbf{x}}_0$:

$$\tilde{\mathbf{x}}_0 = \mathbf{x}_0 + \delta \mathbf{x}_0. \qquad \text{(C.13)}$$

In the special case, where the design matrix is not dependent on the to be estimated parameters, a change in the a priori vector will only affect the right-hand side and the a priori cost functional, but has no influence on the normal matrix nor does it change the degrees of freedom of the system:

$$\tilde{\mathbf{N}}\hat{\mathbf{x}} = \tilde{\mathbf{b}},$$
$$\tilde{\mathbf{N}} = \mathbf{N},$$
$$\tilde{\mathbf{b}} = \mathbf{A}^T \mathbf{P}(\mathbf{d} - \mathbf{A}\tilde{\mathbf{x}}_0) = \mathbf{b} - \mathbf{N}\delta\mathbf{x}_0,$$
$$\widetilde{\mathbf{l}_0^T \mathbf{P} \mathbf{l}_0} = \mathbf{l}_0^T \mathbf{P} \mathbf{l}_0 - 2\delta\mathbf{x}_0^T \mathbf{b} + \delta\mathbf{x}_0^T \mathbf{N}\delta\mathbf{x}_0, \qquad \text{(C.14)}$$
$$\tilde{n}_x = n_x, \; \tilde{n}_d = n_d.$$

C.4 Fixing Parameters to their a Priori Values

A subset, say n_f, of the parameters may be fixed to their a priori values and subsequently removed from the normal equation system. A partitioning of the normal equation system into parameter which are to be fixed (with subscript 'f') and those which will be kept (with symbol 'k') is again useful:

$$\mathbf{N}\mathbf{x} = \begin{bmatrix} \mathbf{N}_{kk} & \mathbf{N}_{kf} \\ \mathbf{N}_{kf}^T & \mathbf{N}_{ff} \end{bmatrix} \begin{bmatrix} \mathbf{x}_k \\ \mathbf{x}_f \end{bmatrix} = \begin{bmatrix} \mathbf{b}_k \\ \mathbf{b}_f \end{bmatrix}. \qquad \text{(C.15)}$$

Fixing the parameters to their a priori values implies simply $\mathbf{x}_f = \mathbf{0}$, and the adapted normal equation system is a cross section of the original system:

$$\tilde{\mathbf{N}}\hat{\mathbf{x}}_k = \tilde{\mathbf{b}},$$
$$\tilde{\mathbf{N}} = \mathbf{N}_{kk},$$
$$\tilde{\mathbf{b}} = \mathbf{b}_k, \tag{C.16}$$
$$\widetilde{\mathbf{l}_0^T\mathbf{P}\mathbf{l}_0} = \mathbf{l}_0^T\mathbf{P}\mathbf{l}_0,$$
$$\tilde{n}_x = n_x - n_f, \tilde{n}_d = n_d.$$

When fixing the parameters, the degrees of freedom of the system is increased as n_x is decreased by n_f.

C.5 Linear Transformation of the Parameters

In many problems in this thesis, situations arise when a set of normal equation system are available but the parameter set which is of interest is linearly dependent on the unknowns of the system itself. For this type of transformation, the original normal equation systems may be transferred in the new solution space.

Let the new solution vector, $\tilde{\mathbf{x}}$ be linearly related to the unknowns of the normal equation system:

$$\mathbf{x} = \mathbf{B}\tilde{\mathbf{x}}. \tag{C.17}$$

The matrix $\mathbf{B}$ does not need to be invertible or square. The new solution space amounts to the number of columns of matrix $\mathbf{B}$: n_c. The observation equation from C.1 now reads:

$$\mathbf{AB}\tilde{\mathbf{x}} = \mathbf{d} - \mathbf{Ax}_0 + \epsilon. \tag{C.18}$$

Which can be used to build the following normal equation system:

$$\tilde{\mathbf{N}}\hat{\tilde{\mathbf{x}}} = \tilde{\mathbf{b}},$$
$$\tilde{\mathbf{N}} = \mathbf{B}^T\mathbf{A}^T\mathbf{PAB} = \mathbf{B}^T\mathbf{NB},$$
$$\tilde{\mathbf{b}} = \mathbf{B}^T\mathbf{A}^T\mathbf{P}(\mathbf{d} - \mathbf{Ax}_0) = \mathbf{B}^T\mathbf{b}, \tag{C.19}$$
$$\widetilde{\mathbf{l}_0^T\mathbf{P}\mathbf{l}_0} = \mathbf{l}_0^T\mathbf{P}\mathbf{l}_0,$$
$$\tilde{n}_x = n_c, \tilde{n}_d = n_d.$$

The new a priori vector, $\tilde{\mathbf{x}}_0$, may be obtained by solving:

$$\mathbf{B}\tilde{\mathbf{x}}_0 = \mathbf{x}_0. \tag{C.20}$$

Which poses a problem when $\mathbf{B}$ cannot be inverted. In that case, it is often possible to apply an approximation by reverting to a generalized inverse. Alternatively, when the absolute values of the problem are not of any particular interest, one may simply force $\tilde{\mathbf{x}}_0 = 0$ and continue with the interpretation of the residuals only.

When $\mathbf{B}$ is an invertible matrix, the least squares solution of the old and new system are simply related by the inverse transformation. When the original normal matrix is diagonalized with a singular value decomposition, the estimated vector now follows from:

$$
\begin{aligned}
\hat{\tilde{\mathbf{x}}} &= \tilde{\mathbf{N}}^{-1}\tilde{\mathbf{b}}, \\
&= (\mathbf{B}^T\mathbf{D}^T\mathbf{\Lambda}\mathbf{D}\mathbf{B})^{-1}\mathbf{B}^T\mathbf{b}, \\
&= (\mathbf{B}^{-1}\mathbf{D}^T\mathbf{\Lambda}^{-1}\mathbf{D}\mathbf{B}^{-T})\mathbf{B}^T\mathbf{b}, \\
&= \mathbf{B}^{-1}\hat{\mathbf{x}}.
\end{aligned}
\tag{C.21}
$$

In practice, there can however be situations where $\mathbf{N}$ is (nearly) singular, whereas the inverse of $\hat{\mathbf{N}}$ is much more stable. In that case, the better choice would be to transform the normal equations before the solving step.

A common example where normal equation system transformations can be useful is the introduction of a (linear) time dependency for the unknown parameters. When a normal equation system holds data for a certain epoch, t, one can introduce a mean and a trend for each parameter using the (sparse) transformation matrix $\mathbf{B}_t$:

$$
\mathbf{B}_t = \begin{bmatrix} 1 & (t-t_0) & 0 & 0 & \cdots \\ 0 & 0 & 1 & (t-t_0) & \cdots \\ \vdots & \vdots & \vdots & \vdots & \vdots \end{bmatrix}.
\tag{C.22}
$$

Of course, in this case , normal equation systems from other epochs are required in a combination to solve the newly introduced parameters.

C.6 Combination and Variance Component Estimation

Combining multiple normal equation systems, which share common parameters, may improve the solution estimate and possibly mitigate (near) rank defects. The combination of two (or more) systems at the level of the normal equations is relatively straightforward. In addition, it is possible to estimate separate a posteriori variance factors for the input normal equation systems. The procedure is known as Variance Component Estimation (VCE) (Förstner, 1979; Koch and Kusche, 2002).

Let each normal equation system be associated with an a priori variance scale σ_i. The

combined normal equation system can be obtained as follows:

$$\tilde{\mathbf{N}}\hat{\mathbf{x}}_k = \tilde{\mathbf{b}},$$

$$\tilde{\mathbf{N}} = \sum_{i=1}^{N} \frac{1}{\sigma_i^2} \mathbf{N}_i,$$

$$\tilde{\mathbf{b}} = \sum_{i=1}^{N} \frac{1}{\sigma_i^2} \mathbf{b}_i, \tag{C.23}$$

$$\widetilde{\mathbf{l}_0^T \mathbf{Pl}_0} = \sum_{i=1}^{N} \frac{1}{\sigma_i^2} [\mathbf{l}_0^T \mathbf{Pl}_0]_i,$$

$$\tilde{n}_x = n_x, \quad \tilde{n}_d = \sum_{i=1}^{N} n_{d_i}.$$

The a posteriori variance components, $\hat{\sigma}_i$, may be estimated by:

$$\hat{\sigma}_i^2 = \frac{[\mathbf{l}^T \mathbf{Pl}]_i}{r_i}. \tag{C.24}$$

Where the redundancy r_i is described by:

$$r_i = n_{d_i} - \frac{1}{\sigma_i^2} \operatorname{trace}\{\mathbf{N}_i \tilde{\mathbf{N}}^{-1}\}. \tag{C.25}$$

Furthermore, the diagonal entries of the redundancy matrix, $\frac{1}{\sigma_i^2}\mathbf{N}_i\tilde{\mathbf{N}}^{-1}$, indicate the relative weight system i has in the estimation of the associated parameter. Accordingly, these values may be used to study the sensitivity of parameters w.r.t. the individual data sources. For a single system, the a posteriori factor simply reduces to Eq. C.6.

The estimation of $\hat{\sigma}_i^2$, with Eq. C.24 depends on the a priori values of σ_i^2, which are not necessarily the same. The values can however be made to converge (in most cases), when the procedure is applied iteratively:

Step 1: Approximate $\sigma_i = 1$, $i = 1, .., N$ (although better initial values yield faster convergence)

Step 2: Compute and solve the combined normal equation system ($\tilde{\mathbf{N}}$, $\tilde{\mathbf{b}}$, $\widetilde{\mathbf{l}_0^T \mathbf{Pl}_0}$, ..)

Step 3: Using the solution, compute an update of the system's weighted measurement residual (see Eq. C.14):
$$[\mathbf{l}^T \mathbf{Pl}]_i = [\mathbf{l}_0^T \mathbf{Pl}_0]_i - 2\mathbf{x}^T \mathbf{b}_i^T + \mathbf{x}^T \mathbf{N}_i \mathbf{x}^T.$$

Step 4: Compute $\hat{\sigma}_i^2$

Step 5: Check for convergence $\hat{\sigma}_i^2 / \sigma_i^2 \approx 1$, update $\sigma_i^2 = \hat{\sigma}_i^2$, $i = 1, .., N$, and possibly reiterate.

D Principal Component Analysis

Principal component analysis allows a time-space dataset to be decomposed in normalized spatial patterns coupled to a magnitude varying in time. Each of these so called 'modes', are orthogonal and are usually sorted according to their relative importance. In the framework of this thesis, PCA is used to parameterize the steric sea level variations and water variations from a hydrological model by a restricted set of dominant modes.

Mathematically, PCA can be derived from the Singular Value Decomposition (SVD) of a given (signal) covariance matrix $\mathbf{\Sigma}$

$$\mathbf{\Sigma} = \mathbf{X}^{\mathbf{T}}\mathbf{X} = \mathbf{U}\mathbf{\Lambda}\mathbf{U}^{\mathbf{T}}. \tag{D.1}$$

Here $\mathbf{X}$ is the n x p data matrix, containing p points (e.g. grid points) and n epochs. The columns of $\mathbf{X}$ must have a zero mean, which is equivalent to subtracting the time mean of the data per spatial node. Since the matrix $\mathbf{\Sigma}$ is symmetric it can be decomposed by the spectral decomposition theorem. This yields eigenvectors contained in the columns of matrix $\mathbf{U}$ and eigenvalues contained in the diagonal matrix $\mathbf{\Lambda}$. In practice, it is also possible to compute the SVD of the data matrix $\mathbf{X}$ and derive the matrices $\mathbf{U}$ and $\mathbf{\Lambda}$ from that.

Since the ortho-normality of $\mathbf{U}$ implies $\mathbf{U}\mathbf{U}^{\mathbf{T}} = \mathbf{I}$, one can write for $\mathbf{X}$:

$$\mathbf{X} = \mathbf{X}\mathbf{U}\mathbf{U}^{\mathbf{T}} = \mathbf{A}\mathbf{U}^{\mathbf{T}} \quad \text{(analysis)}, \tag{D.2}$$

$$\text{with} \quad \mathbf{A} \equiv \mathbf{X}\mathbf{U} \quad \text{(synthesis)}. \tag{D.3}$$

The columns of matrix, $\mathbf{U}$, are time independent and contain the spatial modes of the data. These are sorted according to their relative importance or equivalently their eigenvalues. A useful quantity are the eigenvalues divided by the trace of $\mathbf{\Lambda}$:

$$r_i = \frac{\Lambda_{i,i}}{\text{trace}\{\mathbf{\Lambda}\}} 100\%. \tag{D.4}$$

Where r_i denotes the the percentage of variance explained by mode i.

The time variation of each mode, the principal components, can be obtained from the columns of matrix $\mathbf{A}$, which essentially is a transformation of the data onto the spatial modes (the synthesis).

By choosing only the first N modes with the largest eigenvalues, the data matrix $\mathbf{X}$ may be approximated (the analysis) by:

$$\mathbf{X} \approx \tilde{\mathbf{A}}\tilde{\mathbf{U}}^{\mathbf{T}}. \tag{D.5}$$

Where the tilde denotes the reduction of the column space to only the first N modes.

Glossary

C_{nm}	Fully normalized Stokes coefficients [-]	15
G_X	Green's function of surface loading functional X (N, U or V)	20
G	Gravitational constant [$m^3kg^{-1}s^{-2}$]	15
H	Continental surface load [m of water]	34
M	Mass of the Earth [kg]	15
N	Geoid height [m]	15
P_{nm}	Associated Legendre function of degree n and order m	15
P_n	Legendre Polynomial of degree n	16
S	Salinity of sea water [-]	44
S	Relative sea level [m of water]	34
T_{nm}	Spherical harmonic surface loading coefficients [-]	17
T	Temperature of sea water [K]	44
T	Total surface load [m of water]	31, 34
U	Radial deformation of the Earth[m]	17
V	Tangential deformation of the Earth's surface [m]	17
ΔM_0	OBP model mass correction [m]	60
Λ	Centrifugal potential [m^2s^{-2}]	15
Ω_E	Rotational speed of the Earth [$rad\ s^{-1}$]	15
$\alpha^{A\rightarrow B}$	Isomorphic frame transformation parameter	28
$\bar{Y}_{nm}$	4π normalized spherical harmonic base function of degree n and order m	15
δJ_{i3}	Residual changes of the moments of intertia of the Earth	38
γ	Mean gravitational acceleration of the normal ellipsoid [m^2s^{-2}]	15
λ	Longitude angle	16
ϕ	Gravitational potential [m^2s^{-2}]	14, 15
ρ_e	Mean density of the Earth [kgm^{-3}]	17
ρ_{ice}	Mean density of ice [kgm^{-3}]	41
ρ_w	Mean density of (sea) water [kgm^{-3}]	17
ρ	Density of sea water [-]	43
σ_0	Chandler frequency	39
σ	Surface density of a load in a thin shell [kgm^{-2}]	16
D	Surface deformation vector field	18
I*	Ice thickness [m]	41
J	Mass inertia tensor of the Earth	38
O	Product to sum matrix of the ocean function	36
Q	Inertia tensor of a tectonic plate	33

V	Horizontal surface deformation vector field	21
h	Vectorized spherical harmonic coefficients of H [m of water]	64
$\mathbf{m}_L$	Moment vector of the surface load	25
o	Vectorized spherical harmonic coefficients of O	36
s	Vectorized spherical harmonic coefficients of S [m of water]	36
t	Vectorized spherical harmonic coefficients of T [-]	64
θ	Co-latitude angle	16
$\tilde{S}$	Quasi-spectral relative sea level [m of water]	36
$\tilde{U}$	Normal potential of the reference ellipsoid [m]	15
$\tilde{\mathbf{s}}$	Vectorized spherical harmonic coefficients of $\tilde{S}$ [m of water]	36
a	Mean Earth radius [m]	15, 17
g	Mean gravitational acceleration of the Earth [$m^2 s^{-2}$]	18
h'_n	Radial deformation Love number of degree n for a surface load	20
h_2	Radial deformation Love number of degree 2 for a tidal load	40
h_{mssh}	Mean sea surface height [m]	47
h_{ssh}	Sea surface height [m]	47
h_{steric}	Steric sea level height [m]	43
k'_n	Geoid change Love number of degree n for a surface load	20
k_2	Geoid change Love number of degree 2 for a tidal load	40
l'_n	Lateral deformation Love number of degree n for a surface load	20
m_i	Polar motion components [-]	38
AO	Arctic Oscillation	111
ARGO	Global array of drifting floats measuring temperature and salinity profiles	11, 75, 128
AWI	Alfred Wegener Institute	52
BPR	Bottom Pressure Recorder	52, 105
CE	Center of mass of the solid Earth	25
CF	Center of surface figure	23, 59, 78, 125
CM	Center of mass of the Earth system	23, 54, 59, 78, 125
CN	Center of Network	24, 59
CODE	Center for Orbit Determination in Europe	54
CTD	Conductivity Temperature Depth	11

DORIS	Doppler Orbitography and Radiopositioning Integrated by Satellite	9
ECCO	Estimation of the Circulation and Climate of the Ocean	9
ECMWF	European Centre for Medium-Range Weather Forecasts	50
ENSO	El Niño Southern Oscillation	111, 128
EOF	Empirical Orthogonal Function analysis (synonym for PCA)	73, 112, D.168
EOP	Earth Orientation Parameters	5, 55
FESOM	Finite Element Sea-Ice Model	5, 50
GAC	Ocean and atmosphere background de-aliasing models used in the standard GRACE processing	50
GFZ	Helmholtz-Zentrum Potsdam - Deutsches GeoForschungsZentrum GFZ	7
GIA	Glacial Isostatic Adjustment	7, 9, 70, 77, 127
GLIMS	Global Land Ice Measurements from Space	71
GNSS	Global Navigation Satellite System	4
GPS	Global Positioning Satellite System	4, 53
GRACE	Gravity Recovery and Climate Experiment	4
GSL	Geocentric Sea Level	113
IB	Inverted Barometer response	48
ICEsat	Ice, Cloud, and land Elevation Satellite	115
IERS	International Earth Rotation and reference systems Service	54
IGS	International GNSS Service	55
InSAR	Interferometric Synthetic Aperture Radar	12
ITRF	International Terrestrial Reference Frame	94
LSDM	Land Surface Discharge Model	50
NCEP	National Centers for Environmental Prediction	50
NEQ	Normal EQuation system	5, C.162
OBP	Ocean Bottom Pressure	5, 9, 59
OMCT	Ocean Model for Circulation and Tides	76
PCA	Principal Component Analysis (synonym for EOF)	6, 73, D.168
PDO	Pacific Decadal Oscillation	111
PREM	Preliminary Reference Earth Model	19
PSMSL	Permanent Service for Mean Sea Level	13

RSL	Relative Sea Level	113
SLR	Satellite Laser Ranging	9
SNR	Signal to Noise Ratio	105
SNREI	Spherically-symmetric Non-Rotating Elastic Isotropic	4, 17
TWS	Total Water Storage	6
UT1	Universal time [s]	54, 55
VCE	Variance Component Estimation	5, 60, C.166
VLBI	Very Long Baseline Interferometry	54
WGHM	WaterGAP Global Hydrology Model	76, 123
WGI	World Glacier Inventory	71
XBT	eXpendable BathyThermograph	11